

TOWARDS UNDERSTANDING NEUROPATHY FROM CANCER
CHEMOTHERAPY AND PATHOPHYSIOLOGY OF PAIN SENSATION: AN
ENGINEERING APPROACH

A Dissertation

Submitted to the Faculty

of

Purdue University

by

Parul Verma

In Partial Fulfillment of the

Requirements for the Degree

of

Doctor of Philosophy

May 2020

Purdue University

West Lafayette, Indiana

**THE PURDUE UNIVERSITY GRADUATE SCHOOL
STATEMENT OF DISSERTATION APPROVAL**

Dr. Doraiswami Ramkrishna, Chair

Davidson School of Chemical Engineering

Dr. Sangtae Kim

Davidson School of Chemical Engineering

Dr. John A. Morgan

Davidson School of Chemical Engineering

Dr. Wanqing Liu

Wayne State University

Approved by:

Dr. John A. Morgan

Head of Graduate Program

To my parents (Anoop Kumar and Renu Verma), my brother (Shivam Verma), and
my partner (Krishna Pillutla).

ACKNOWLEDGMENTS

This thesis would not have been possible without the constant support and mentorship of my advisor Prof. Doraiswami “Ramki” Ramkrishna. I want to thank him for believing in me throughout and for providing me complete freedom to steer my research projects in any direction that seemed interesting. I have learnt many virtues from him: being able to think and not worry when research does not go the way I had intended, to be rigorous and meticulous, and to question, among others. His teachings have deepened my interest in applied mathematics. I am always inspired by his passion for research and teaching and hope to follow his path in the future. I would also like to thank my committee members: Dr. Kim, Dr. Morgan, and Dr. Liu for their support and constructive feedback on my research projects.

There are many collaborators without whom this thesis would not have been possible. I would like to thank Dr. Jodi Skiles, Dr. Jamie Renbarger, and Dr. Tammy Sajdyk for helping with the clinical data, and Dr. Bruce Cooper for helping with metabolite profiling and training me to be able to use the relevant software. Dr. Cooper has been very patient in teaching me some of the metabolite profiling techniques. My collaborators from the MCMP department at Purdue: Muriel Eaton and Dr. Yang Yang, have been tremendously helpful with driving the CIPN mechanism project forward, as well. I want to thank Dr. Yang for having me attend some of his group meetings through which I learnt more about experimental neuroscience. Muriel has been very supportive and I want to thank her for believing that my results were worth validating in the first place. I feel most fortunate to have gotten an opportunity to collaborate with Dr. Achim Kienle and Dr. Dietrich Flockerzi from the Max Planck Institute. I have tremendously enjoyed collaborating with them and have learnt substantially about numerical bifurcation theory from them. Both

of them have a contagious level of enthusiasm. I totally cherish my two visits to Max Planck where I got an opportunity to work with them closely. I also want to thank Dr. Kienle for welcoming me to Magdeburg and making my stay comfortable. Furthermore, I want to thank Dr. Haroon Anwar from NJIT, for helping me during the start of the model building of DRG neuron when I was feeling lost and did not know how to proceed and enter the field of computational neuroscience. I would not have been able to start the DRG neuron modeling work without his support. Nisheet Patel and Dr. Andreas Voigt also provided ideas for my DRG neuron-related work. In addition, there are several others with whom I have discussed my research projects and sought feedback which have helped me in steering my research projects.

Next, I would like to thank current and previous group members. The older group members include Dr. Frank DeVilbiss, Dr. Conor Parks, and Dr. Vu Tran. They were very supportive during my starting years when I was just learning on how to conduct research. My current group members include Akancha Pandey, Lina Aboulmouna, Pelin Bulutoglu, Rubesh Raja, and newly joined member Sana Khanum. I especially want to thank Akancha, Lina, and Pelin for lifting the spirit of the lab and for those stimulating group discussions. I have truly enjoyed having them as my group members. All three of them have tremendously supported me throughout. Akancha has been my close friend from the very start; I especially want to thank her for being my pillar of support all these years and for introducing me to the SKY club at Purdue (mentioned later). Lina has been very supportive with helping me write my papers and applications. I would have never learnt writing any better. Our latest addition to the group meetings, Kunaal Joshi, also provided detailed feedback on my research projects.

Purdue chemical engineering department provides a very supportive environment. A special thanks to Bev Johnson, Corwin Green, Robin Waling, Lauren Hays, and Betty Guerrero, and the GSO members. All of them have been very helpful and kind. Bev is truly a mother to all.

This journey would not have been complete without many friends I had throughout, helping me through the darkest of the times. Some of my friends I had here are Ravi Joshi, Murtuza Shergadwala, and Kshitiz Swaroop. Ravi helped me grow both personally and professionally. I also want to thank my Tatvam band mates for keeping the music alive: Ananya Sheth, Anamika Shreevastava, Sai Prashanth Balachandran, and Janav Udani. My housemates: Ananya, Anamika, Prashanth, and Kanishka Misra, have been very supportive and created our apartment into a home away from home. My journey here became smoother also thanks to the Purdue SKY club; I learnt a breathing technique which kept me sane and energetic throughout and I also made some close friends who have supported me these years: Shamiek Mangipudi, Saurabh Misra, and my teachers Akshay Ponda and Annelies Richmond, among others. Purdue CAPS has also been supportive. Moreover, I want to thank Purdue karate club and my instructors Shihan Webb and Sensei Leaird; they encouraged me to seek perfection in every aspect of my life. My undergraduate friends Animesh, Anish, Manju, and Prateek have also always lifted my spirits and have always been just a phone call away.

My deepest thanks to my parents and my brother, Shivam, for all their sacrifices and support. I am here because of them. I also want to thank my brother for teaching me compassion and kindness. Finally, I want to thank my partner, Krishna Pillutla: the pillar of constant rock-solid support. Thank you for encouraging and supporting me all along. Without you, this thesis would not have been possible.

TABLE OF CONTENTS

	Page
LIST OF TABLES	xi
LIST OF FIGURES	xiv
SYMBOLS	xxi
ABBREVIATIONS	xxiii
ABSTRACT	xxv
1 INTRODUCTION	1
1.1 CIPN diagnosis and prediction	2
1.2 CIPN mechanism	3
1.3 Existing treatment strategies	8
1.4 Pain sensation	10
1.5 Objectives	13
2 A METABOLOMICS APPROACH FOR EARLY PREDICTION OF VINCRI- STINE-INDUCED PERIPHERAL NEUROPATHY	16
2.1 Introduction	16
2.2 Results	19
2.2.1 Pediatric ALL patient data description	19
2.2.2 Longitudinal versus independent analysis of metabolite profiles	21
2.2.3 Metabolite selection and model building	23
2.2.4 Metabolite structure identification	27
2.2.5 Pathway analysis	29
2.3 Discussion	31
2.4 Methods	36
2.4.1 ALL patient data collection [151]	36
2.4.2 Metabolomics sample preparation and extraction	37
2.4.3 HPLC-MS analysis of metabolomics samples [152]	37
2.4.4 Vincristine quantitation [153]	38
2.4.5 Metabolite profiling data analysis	39
3 USING BIFURCATION THEORY FOR EXPLORING PAIN	41
3.1 Introduction	41
3.2 The Neuroscience of Pain Sensation	43
3.3 Mathematical Model of a Pain-Sensing Neuron	47

	Page
3.4 Influence of external current I_{ext}	56
3.4.1 $Na_v1.7$ Channel Mutations	58
3.4.2 $Na_v1.8$ Channel Mutations	59
3.5 Influence of Ion Equilibrium Potentials at $I_{ext} = 0$	63
3.6 Discussions	65
3.7 Supplementary Information	67
4 COMPUTATIONAL ANALYSIS OF A 9D MODEL FOR A SMALL DRG NEURON	68
4.1 Introduction	69
4.2 Model description and first simulation results	71
4.3 Numerical bifurcation analysis	73
4.4 Mixed-mode oscillations	78
4.5 Discussion	89
5 A MATHEMATICAL INVESTIGATION OF CHEMOTHERAPY-INDUCED PERIPHERAL NEUROPATHY	93
5.1 Introduction	94
5.2 Results	95
5.2.1 Model description	95
5.2.2 Bifurcation analysis	98
5.2.3 Effect of Paclitaxel	103
5.2.4 Experimental validation results	108
5.3 Discussions	109
5.4 Materials and methods	115
5.4.1 Model parameter values	115
5.4.2 XPPAUT settings	115
5.4.3 MATCONT settings	116
5.4.4 Reagents	116
5.4.5 Primary Cell Culture	116
5.4.6 Micro/multielectrode Array (MEA)	117
5.4.7 Statistics	118
5.5 Supporting information	118
6 EXPLORING INTERACTIONS IN CIPN MECHANISMS	121
6.1 Calcium homeostasis	121
6.2 Oxidative stress	122
6.3 Inflammation	123
6.4 Axonal degeneration	123
7 CONCLUSIONS	125
8 FUTURE WORK	129
8.1 A comprehensive approach to investigate CIPN	129
8.2 Developing personalized treatment strategy for cancer patients	131

	Page
REFERENCES	133
A SUPPLEMENTARY MATERIAL FOR CHAPTER 2	163
A.1 Metabolite selection	163
A.2 Metabolite identification	165
A.3 Pathway analysis	166
A.4 Univariate analysis	166
A.4.1 Pathway analysis	168
B DESCRIPTION OF MODEL EQUATIONS AND PARAMETER SETTINGS	171
B.1 XPPAUT settings	171
B.2 Model equations	171
B.2.1 $\text{Na}_v1.8$ kinetics	173
B.2.2 K/KDR kinetics	175
B.2.3 KA kinetics	175
B.3 Non-dimensional equations	175
C MATHEMATICAL MODELING OF INOSITOL 1,4,5-TRIPHOSPHATE MEDIATED CALCIUM DYNAMICS: UNDERSTANDING PERTURBA- TIONS DUE TO EXTERNAL TOXICITY	178
C.1 Introduction	178
C.2 Methods	179
C.2.1 Data procurement and processing	179
C.2.2 Model development and parameter estimation	179
C.2.3 Sensitivity analysis	181
C.3 Results	181
C.4 Discussions	182
C.5 Conclusions	186
D OPTIMIZING VINCRISTINE INFUSION RATE	187
D.1 Introduction	187
D.2 Model	188
D.3 Results	192
D.4 Discussions	193
E MODELING VINCRISTINE TRANSPORT	194
E.1 Introduction	194
E.2 Data available	195
E.3 Model	195
E.4 Parameter estimation	198
E.5 Future work	199
F A LIPIDOMICS APPROACH TO INVESTIGATE NON-ALCOHOLIC FATTY LIVER DISEASE	204
F.1 Methods and materials	205

	Page
F.1.1 Data acquisition	205
F.1.2 Statistical analysis	205
F.2 Results	206
F.2.1 Clinical profile	206
F.2.2 Statistical results for hepatic lipids	207
F.2.3 Hepatic lipid signature	207
F.3 Discussions	210
VITA	213

LIST OF TABLES

Table	Page
1.1 A summary of potential mechanisms involved in CIPN due to the mentioned chemotherapy agents.	9
2.1 Patient characteristics were defined according to gender, age, and body mass index (BMI). For the day 8 treatment time point, 8 overall low neuropathy (LN) samples were available, while for day 29 and month 6 time points, 12 LN samples were available. 24 overall high neuropathy (HN) samples were available at all the three time points. Age and BMI correspond to that during the start of the treatment. Here, "HN" implies that the patient had a Total Neuropathy Score Pediatric Vincristine (TNS [©] -PV) greater than 8 at least once, and "LN" implies that the patient had a TNS [©] -PV less than 3 throughout the treatment. SD: standard deviation.	21
2.2 Metrics obtained by performing RFE on the data sets at the three time points. A: The set of metabolites found that can accurately predict overall neuropathy susceptibility (HN versus LN) at these time points before manual integration of the chromatogram peaks. B: The set of metabolites found that can accurately predict TNS [©] -PV intensity of either high or low at that specific time point. C: The set of metabolites that can accurately predict overall neuropathy susceptibility at the time points after manual integration of peaks. AUROC: Area Under Receiver Operating Characteristics Curve, AUROCSD: standard deviations for AUROC. See Supplementary Table S1 for sensitivity and specificity corresponding to each of these.	25
2.3 Cross validation accuracy metrics for the models with optimal tuning using the final selected metabolites. These metrics were calculated after choosing the probability thresholds for each of the time points. Cost = 4, 0.25, 0.25 for day 8, day 29, and month 6 models, respectively.	28
2.4 Identified metabolites that can accurately predict neuropathy susceptibility at the day 29 time point.	29
2.5 Identified metabolites that can accurately predict neuropathy susceptibility at the month 6 time point.	30
4.1 Values of I_{ext} at the cyclic limit points (CLP) and the period doubling bifurcation points (PD) in Fig. 4.6.	82

Table	Page
4.2	An illustration of MMOs solution sequences satisfying the Farey arithmetic. 88
5.1	Spontaneous neurons. Pax: Paclitaxel, Na _v 1.8-: Na _v 1.8 blocker, KDR+: KDR enhancer 109
5.2	Model parameter values 115
A.1	Metrics obtained by performing recursive feature elimination on the data sets at the three time points. A: Set of metabolites found that can accurately predict overall neuropathy susceptibility at these time points before manual integration of peaks. B: Set of metabolites found that can accurately predict TNS [⊙] -PV intensity at that specific time point. C: Set of metabolites that can accurately predict overall neuropathy susceptibility at the time points after manual integration of peaks. AUROC: Area Under Receiver Operating Characteristics Curve, Sens: Sensitivity, Spec: Specificity, AUROCS _D , Sens _{SD} , Spec _{SD} are standard deviations for AUROC, sensitivity and specificity. Sensitivity and specificity are calculated by keeping 0.5 probability as the threshold. Note: positive class is overall susceptibility to high neuropathy (HN) for A and C, and TNS [⊙] -PV greater than 8 for B. 164
A.2	Sample confusion matrix to explain terms used. 164
A.3	Confusion matrix generated after training the final models with the final selected thresholds for each time point. 165
A.4	Mass, retention time, and adduct information for the final set of Day 8 metabolites. None of them could be identified 165
A.5	Mass, retention time, and adduct information for the final set of day 29 metabolites. 4 of them could be identified. 166
A.6	Mass, retention time, and adduct information for the final set of month 6 metabolites. 9 of them could be identified. 167
A.7	Table generated from Metaboanalyst for day 29 metabolites 168
A.8	Table generated from Metaboanalyst for month 6 metabolites 168
A.9	Mass, retention time, adduct information, and HMDB guesses for the metabolites that were significantly associated with VIPN at day 8 time point of the treatment. 168
A.10	Pathway analysis with HMDB0010395 as the guess for Mass 543.3312 . . 169
A.11	Pathway analysis with HMDB0010396 as the guess for Mass 543.3312. . . 169
B.1	Voltage dynamics equation parameter values 172

Table	Page
B.2 Gating variables parameters	174
D.1 Model parameter and their values	191
D.2 Initial conditions and parameters for the transition and death rates . . .	191
E.1 V_{max}/K_m (ml/min/g) for different genotypic scores	196
F.1 Lipids and FDR value in discovery set, all negatively associated	208
F.2 Lipids and FDR value in validation set, all negatively associated	208
F.3 Significant unsaturated lipid families and FDR value in discovery set . .	208
F.4 Significant unsaturated lipid families and FDR value in validation set . .	208
F.5 List of lipids found as biomarkers (in order of importance)	209
F.6 Overlapping lipids between discovery and validation set	209

LIST OF FIGURES

Figure	Page
1.1 Parts of a myelinated DRG neuron that can get impacted due to chemotherapy agents. (Figure developed using Biorender (https://biorender.com/))	6
1.2 The pain sensation pathway starts from a noxious stimulus being detected by a small DRG neuron (nociceptor) at the skin. The input leads to the generation of action potentials which are then transmitted to the spinal cord. From the spinal cord, the input is further transmitted to the thalamus via the ascending pathway. The response is transmitted back to the spinal cord via the descending pathway. It is finally transmitted to the muscle cells via the motor neuron. The muscle cells respond in concordance with the signal. The DRG neuron consists of a cell body, an axon across which the action potential is transmitted, and ends at the synapse which transmits information from one neuron to the other.	12
2.1 A bar plot showing distribution of the neuropathy score of patients over time. A TNS [⊙] -PV less than 3 corresponds to low, a score between 3 and 8 corresponds to medium, and a score above 8 corresponds to high. The first group shows the overall susceptibility of patients to neuropathy (LN versus HN). The next three groups show the TNS [⊙] -PV intensity at that particular time point. Since patients with an overall medium TNS [⊙] -PV intensity were not considered in this study, the number of such patients is zero in the first group. Some HN patients had medium TNS [⊙] -PV intensity (TNS [⊙] -PV greater than 3 but lesser than 8) at some points during the treatment, as seen in the next three groups.	22
2.2 A dendrogram created based on the Euclidean distance shows that the metabolite profiles are clustered according to their corresponding time points. Day 8 and day 29 metabolite profiles belong to the same primary branch and are consequently closer to each other.	23
2.3 ROC plots for the final trained models at the three time points. a: Day 8, b: Day 29, c: Month 6. AUC: Area Under Curve. CI: Confidence Interval.	26

Figure	Page
2.4 A workflow showing a potential vincristine dose decision making strategy based on the trained SVC models. Blood samples of patients can be collected at day 8 and month 6 time points of the treatment. Samples can then be analyzed using mass spectrometry for metabolite profiling of the selected 2 and 21 metabolites at the day 8 and month 6 time points, respectively. The metabolite profile data can then be used to predict overall neuropathy susceptibility from the trained SVC models. If the model output probability is greater than a threshold value of 0.7, the patient might be susceptible to overall high neuropathy (HN). This strategy enables identification of patients susceptible to HN. The vincristine dose for HN patients may require adjustment.	33
3.1 A schematic of an action potential. When a stimulus is applied, an action potential is generated due to activation of sodium channels leading to the rise in membrane potential. Following this rise, sodium channels inactivate and potassium channels activate, leading to a decrease in the potential. Finally, all channels attain steady states and the membrane reverts back to the resting membrane potential (RMP).	45
3.2 A schematic of a neuronal membrane. The membrane consists of a lipid bilayer. The voltage-gated sodium and potassium channels are transmembrane pores. The extracellular concentration of sodium is greater, leading to an inflow of sodium ions when the channel opens. The intracellular concentration of potassium is greater, leading to an outflow of potassium ions when the channel opens.	46
3.3 Circuit diagram representing neuron membrane. V_{in} : intracellular potential; V_{out} : extracellular potential; $I_{1.7}, I_{1.8}, I_K, I_{KA}, I_l$: current due to $Na_v1.7, Na_v1.8$, delayed rectifier potassium, A-type transient potassium and leak channels respectively; I_{ext} : external stimulus current; $g_{1.7}, g_{1.8}, g_K, g_{KA}, g_l$: conductance of $Na_v1.7, Na_v1.8$, delayed rectifier potassium, A-type transient potassium and leak channels respectively; E_{Na}, E_K, E_l : equilibrium sodium, potassium and leak potentials respectively, C : membrane capacitance.	48
3.4 A: Action potential generated due to a constant external current $I_{ext} = 100$ pA, B: Dynamics of activation and inactivation state variables, C-F: Dynamics of potential-dependent time constants for the state variables. . .	52
3.5 Dynamic simulations for A: $I_{ext} = 102$ pA, B: $I_{ext} = 110$ pA, C: $I_{ext} = 150$ pA	54
3.6 Dynamic simulations for A: $E_{Na} = 125$ mV, B: $E_{Na} = 128.2$ mV, C: $E_{Na} = 130$ mV	54

Figure	Page
3.7 Dynamic simulations for A: $E_K = -74.5$ mV, B: $E_K = -74$ mV, C: $E_K = -73$ mV	55
3.8 Partial bifurcation diagram with I_{ext} as the bifurcation parameter. HB: Subcritical Hopf bifurcation point (at $I_{ext} = 102.99$ pA), LP: Limit point, CLP: Cyclic limit point (at $I_{ext} = 116.98$ pA for the stable periodic branch).	57
3.9 Two parameter continuation for v_0 in A: $\alpha_{m_{1.7}}(V)$ and B: $\beta_{m_{1.7}}(V)$. The plot shows how the bifurcation points vary upon changing v_0 . An approximately 300% increase or more in k_3 of $\alpha_{m_{1.7}}(V)$ and a 28% increase or more in k_3 of $\beta_{m_{1.7}}(V)$ shifts the bifurcation points.	59
3.10 There is a shift in $m_{1.7\infty}^3$ as a result of an increase in v_0	60
3.11 Two parameter continuation for v_0 in A: $\alpha_{m_{1.8}}(V)$ and B: $\beta_{m_{1.8}}(V)$. The plot shows how the bifurcation points vary upon changing v_0 . An approximately 170% increase or more in k_3 of $\alpha_{m_{1.8}}(V)$ and a 4% increase or more in k_3 of $\beta_{m_{1.8}}(V)$ shifts the bifurcation points.	61
3.12 There is a shift in $m_{1.8\infty}$ as a result of an increase in v_0	62
3.13 Bifurcation diagram with A: E_{Na} (HB at $E_{Na} = 128.04$ mV and CLP of stable periodic branch at $E_{Na} = 128.96$ mV) and B: E_K (HB at $E_K = -74.37$ mV and CLP of stable periodic branch at $E_K = -73.66$ mV) as primary bifurcation parameters. HB: Subcritical Hopf bifurcation point, CLP: Cyclic limit point	64
4.1 Dynamic simulations of action potentials. For higher values of $\bar{g}_{1.8}$, MMOs are observed. a.: Dynamic simulations for $\bar{g}_{1.8}$ at 7 mS/cm ² , and $I_{ext} = 100, 106, 120$ pA. b.: Dynamic simulations for $\bar{g}_{1.8}$ at 4.5 mS/cm ² , and $I_{ext} = 115, 215, 230$ pA. No MMOs are observed in this case.	72
4.2 Bifurcation diagrams for $\bar{g}_{1.8} = 4.5, 5, 7$ and 8 mS/cm ² for diagrams a, b, c and d, respectively. For lower values of $\bar{g}_{1.8}$ in diagram (a), MMOs are not observed, and there is a region of bistability between steady state and periodic firing of action potentials, as shown by the orange shaded region. This bistability is not present in diagrams b, c, d. Instead, MMOs are observed in these diagrams in the purple shaded region. MMOs solution branches will be discussed separately in section 3 and are not included in this figure. Note that the unstable blue periodic branch in diagram c ends before the LP ₂ point which is not evident from the figure because of the thickness of the branches. HB: Hopf bifurcation point, CLP: Cyclic limit point, LP: limit point	75

Figure	Page
4.3 Two parameter plot with $\bar{g}_{1.8}$ as the secondary continuation parameter. a.: Variation over a large interval of $\bar{g}_{1.8}$. b.: Zoomed in version of a. near the intersection of the HB point and the CLP ₃ point.	77
4.4 Two parameter plot with the following secondary continuation parameters: a.: $\bar{g}_{1.7}$, b.: \bar{g}_K and c.: \bar{g}_{KA}	78
4.5 Basic MMOs solutions of the type: a.: 1 ⁶ , b.: 1 ³ , and c.: 1 ¹ for selected values of I_{ext} . Upper row: temporal evolution of membrane voltage, lower row: orbits in the V, h_{ka}, n_K phase space.	80
4.6 Basic periodic solution branches with one action potential per period in the range of I_{ext} from 105 to 120 pA. Solid lines: stable periodic solutions, dashed line: unstable periodic solutions.	81
4.7 a.: MMOs for $I_{ext} = 102.992$ pA below the Hopf bifurcation point at $I_{ext} = 102.9935$ pA. b.: Representation of the solution in the V, h_{KA}, n_K phase diagram.	83
4.8 A sequence of concatenated periodic solutions. a.: 1 ² 1 ¹ at $I_{ext} = 112.9$ pA, b.: 1 ² (1 ¹) ² at $I_{ext} = 113.1$ pA, c.: 1 ² (1 ¹) ³ at $I_{ext} = 113.18$ pA, d.: 1 ² (1 ¹) ⁴ at $I_{ext} = 113.2$ pA.	84
4.9 Tree of selected periodic MMOs solutions. Numbers in parentheses are values of I_{ext} in pA corresponding to the solution on top of it. Solutions highlighted in yellow are shown in Figure 4.8.	86
4.10 Selected periodic MMOs patterns observed below but close to the cyclic limit point CLP ₃ in Figure 4.2c before small amplitude oscillations disappear. Numbers in parentheses are the corresponding values of I_{ext} in pA, corresponding to the solution on top of it.	87
4.11 Simulations before and after the period doubling bifurcation at $I_{ext} = 108.9962$ pA. Left column: $I_{ext} = 108.9$ pA, right column: $I_{ext} = 109$ pA. After the period doubling bifurcation, the system exhibits chaotic-like behavior which is evident in the dynamics of $s_{1.7}$	90
5.1 Dynamic simulations obtained by varying $\bar{g}_{1.8}$. A: One action potential followed by a steady state is observed for $\bar{g}_{1.8} = 10.2$ mS/cm ² , B: MMOs are observed for $\bar{g}_{1.8} = 10.45$ mS/cm ² , and C: Continuous firing of action potentials is observed for $\bar{g}_{1.8} = 11$ mS/cm ²	97

Figure	Page
5.2 A-D: Bifurcation diagrams obtained by keeping A: $\bar{g}_{1.7}$, B: $\bar{g}_{1.8}$, C: \bar{g}_{KDR} , and D: \bar{g}_{KA} as the bifurcation parameters. E-F: Frequency versus maximal conductance obtained in the periodic firing regime with E: $\bar{g}_{1.8}$ and F: \bar{g}_{KDR} as the bifurcation parameters. The frequency of firing increases with $\bar{g}_{1.8}$ and decreases with \bar{g}_{KDR} . The frequency of unstable periodic solutions tends towards zero, implying that the unstable branch is ending in a period-infinity solution.	101
5.3 Two parameter continuations performed for the Hopf bifurcation point HB, limit points LP ₁ and LP ₂ , and cyclic limit point CLP ₂ . A: Continuation plot for $\bar{g}_{1.7}$ versus $\bar{g}_{1.8}$ show that the bifurcation points generated by keeping $\bar{g}_{1.8}$ as the bifurcation parameter do not shift upon varying $\bar{g}_{1.7}$. B: HB and LP's of $\bar{g}_{1.8}$ bifurcation diagram do not shift upon varying \bar{g}_{KA} . CLP ₂ shift rightwards upon decreasing \bar{g}_{KA} . This implies that the MMOs region will be wider in this case. C: Bifurcation points of \bar{g}_{KDR} do not shift upon varying $\bar{g}_{1.7}$. D: HP and LP's of \bar{g}_{KDR} do not shift upon varying \bar{g}_{KA} . CLP ₂ shifts leftwards upon decreasing \bar{g}_{KA} . This implies that the MMOs region will become narrower in this case. E: A linear combinational effect is seen between $\bar{g}_{1.8}$ and \bar{g}_{KDR} . Note that the thin gap between stable steady state and continuous firing regimes is the MMOs region.	104
5.4 A: Bifurcation diagram obtained by treating paclitaxel concentration as the bifurcation parameter. B: A zoomed in version of the bifurcation diagram in A. HB ₁ : subcritical Hopf bifurcation point, HB ₂ : supercritical Hopf bifurcation point, LP ₁ and LP ₂ : limit points, CLP ₁ , CLP ₂ , CLP ₃ , and CLP ₄ : cyclic limit points, PD: periodic doubling bifurcation point. C: Frequency plot for the stable periodic firing region. Frequency first increases and then decreases upon increasing paclitaxel concentration. Left and right end points of this curve refer to CLP ₂ and PD, respectively. . .	107

5.5 Multielectrode array (MEA) firing summary shows amelioration of hyperexcitability after treatment of A-803467 (Na_v1.8 blocker) and PIP₂ (KDR enhancer). All parameters are reported as fold change (treatment over baseline of culture before treatment). A) Mean firing rate for different dosages of paclitaxel. B) Mean firing rate reveals a significant increase in paclitaxel firing from media control (p<0.0001), a decrease from paclitaxel when A-803467 and PIP₂ are administered separately (p=0.0449 and p<0.0001, respectively), but a significant increase from media when administered together (p<0.0001). C) Heatmap of representative MEA recordings with firing frequency of each active electrode colorcoded: warm colors (red, orange, yellow) represent high firing frequency (white=10Hz); cool colors (green, blue) represent low firing frequency (black=0Hz). Each circle represents a spontaneous firing neuron within the 8 X 8 electrode array. Top row is baseline at time 0 before treatment is added. Bottom row is 24 hours after treatment was added. Asterisks denote statistical significance from Mann-Whitney U test (*P<0.05, **P<0.01, ***P<0.001) 110

5.6 Effect of paclitaxel on conductances and firing. A: Effect of paclitaxel on $\bar{g}_{1.7,new}$ upon varying h_n and $\bar{G}_{Na,max}$. Increasing $\bar{G}_{Na,max}$ will widen the parameter range of $\bar{g}_{1.7,new}$. Increasing h_n alters the curve to become more sigmoidal. B: Similar effect is seen with $\bar{g}_{1.8,new}$. Decreasing $\bar{G}_{Na,max}$ will reduce the parameter range of $\bar{g}_{1.8,new}$. C: Increasing paclitaxel concentration decreases $\bar{g}_{KDR,new}$. As before, increasing h_n makes the curve more sigmoidal. Decreasing $\bar{G}_{K,min}$ increases the parameter range. D: Similar effect is seen for $\bar{g}_{KA,new}$. Increasing $\bar{G}_{K,min}$ decreases the parameter range in this case. The blue curves correspond to the parameter values that were considered for bifurcation analysis. Note that the blue and purple curves are overlapping in in D, thus the blue curve is not visible. 119

5.7 **Regions of stable steady state, MMOs, and continuous firing upon varying h_n , $\bar{G}_{Na,max}$, and $\bar{G}_{K,min}$ with paclitaxel concentration [P].** A: Continuation of Hill's coefficient h_n . Upon increasing h_n , the spontaneous firing regime becomes narrower. B: Continuation of $\bar{G}_{Na,max}$. Upon increasing $\bar{G}_{Na,max}$, the spontaneous firing regime becomes narrower. C: Continuation of $\bar{G}_{K,min}$. Upon increasing $\bar{G}_{K,min}$, the spontaneous firing regime becomes wider 120

6.1 Potential interactions between different CIPN-related mechanisms based on current literature. 123

Figure	Page
A.1 The three plots show the metrics evaluated at different probability thresholds. 1a, 2a and 3b show the plot of Youden's J statistic (J) and distance (dist) to best possible cutoff (i.e. sensitivity and specificity equal to 1) at different probability thresholds, at day 8, day 29 and Month 6 data respectively. The probability threshold is for high neuropathy. If the SVM model output is greater than the threshold, the sample is classified as high, and vice versa. 1b, 2b, and 3b show how the sensitivity and specificity varies as a function of probability threshold. Vertical line corresponds to the chosen threshold, based on minimum dist.	170
C.1 First subplot is the frequency plot for the low pass filter. The second subplot shows the raw and the filtered data. Order 5 and cutoff of 0.005 Hz was used.	182
C.2 Plot of simulated Ca^{2+} concentration (in blue) and the processed Ca^{2+} signal data (in green). Concentration is in μM . Though not evident from the plot, the simulated and observed concentration at time = 0 s is the same.	183
C.3 A heatmap showing the sensitivity of model parameters with Ca^{2+} peak. The diagonal elements show the sensitivities of individual parameters, and the non-diagonal elements show the sensitivities of paired parameters. Color closer to blue indicates low sensitivity, while color closer to red indicates high sensitivity. From this figure, c_0 and k_3 seem to be most sensitive to Ca^{2+} peak.	184
C.4 Ca^{2+} simulated with estimated model parameters (in blue), and with k_3 reduced by a factor of 1.1 (in green). There is a visible decrease in Ca^{2+} spike.	185
D.1 Vincristine mechanism in the cell cycle	189
D.2 Plot of number of remaining cancer cells as a function of infusion time	192
E.1 Vincristine PK/PD	197
E.2 PK profile for one patient	200
E.3 PK model validation for patients	201
E.4 Heat map showing sensitivity of parameters	202

SYMBOLS

V	Voltage
t	time
C	Capacitance
A	Area of DRG neuron membrane
c	Specific capacitance
I_{ext}	External stimulus current
$\bar{g}_{1.7}$	Maximal conductance of Na _v 1.7 channel
$\bar{g}_{1.8}$	Maximal conductance of Na _v 1.8 channel
\bar{g}_K/\bar{g}_{KDR}	Maximal conductance of delayed rectifier potassium channel
\bar{g}_{KA}	Maximal conductance of A-type transient potassium channel
g_l	Maximal conductance of leak channel
$m_{1.7}$	Activation variable of Na _v 1.7 channel
$h_{1.7}$	Inactivation variable of Na _v 1.7 channel
$s_{1.7}$	Slow inactivation variable of Na _v 1.7 channel
$m_{1.8}$	Activation variable of Na _v 1.8 channel
$h_{1.8}$	Inactivation variable of Na _v 1.8 channel
n_K/n_{KDR}	Activation variable of delayed rectifier potassium channel
n_{KA}	Activation variable of A-type transient potassium channel
h_{KA}	Inactivation variable of A-type transient potassium channel
E_{Na}	Equilibrium potential of sodium
E_K	Equilibrium potential of potassium
E_l	Equilibrium potential of leak channel
h_n	Hill's coefficient
[P]	Paclitaxel concentration (in nM)

$k_{0.5}$ Half maximal effective concentration

ABBREVIATIONS

CIPN	Chemotherapy-induced peripheral neuropathy
VIPN	Vincristine-induced peripheral neuropathy
ALL	Acute lymphoblastic Leukemia
TNS [©] -PV	Total Neuropathy Score Pediatric Vincristine
HN	High neuropathy
LN	Low neuropathy
BMI	Body mass index
LC-MS/MS	Liquid chromatography with tandem mass spectrometry
SVC	Support vector classifier
RFE	Recursive feature elimination
AUROC	Area under the receiver operating characteristics curve
AUROCSD	Standard deviation for AUROC
NIR	No Information Rate
m/z	Mass-to-charge ratio
HMDB	Human Metabolome Database
AMP	Adenosine 5'-monophosphate
CMM	CEU Mass Mediator
POG	Pediatric Oncology Group
ESI	Electrospray ionization
MRM	Multiple Reaction Monitoring
CE	Collision energy
KNN	K-nearest neighbours
DRG	Dorsal root ganglia
RMP	Resting membrane potential

K/KDR	Delayed rectifier potassium
KA	A-type transient potassium
MMOs	Mixed-mode oscillations
HB	Hopf bifurcation point
LP	Limit point
CLP	Cyclic limit point
MEA	Multi electrode array
PIP2	L-alpha-phosphatidyl-D-myo-inositol 4,5-diphosphate, dioc- tanoyl
ROS	Reactive oxygen species

ABSTRACT

Verma, Parul Ph.D., Purdue University, May 2020. Towards Understanding Neuropathy from Cancer Chemotherapy and Pathophysiology of Pain Sensation: An Engineering Approach. Major Professor: Doraiswami Ramkrishna.

This thesis addresses chemotherapy-induced peripheral neuropathy (CIPN)- a form of pain sensation and a prevalent dose-limiting side-effect of several chemotherapy agents such as vincristine, paclitaxel, and oxaliplatin. These agents are used for treating various cancers such as leukemia, brain tumor, lung cancer. Peripheral neuropathy is a numbing, tingling, and burning sensation felt in the palms and feet, which occurs due to damage to neurons (nerve cells). Prolonged CIPN can impact the quality of life of cancer patients. Occasionally, severe CIPN can result in termination of chemotherapy treatment altogether. Currently, there are no established strategies for treating CIPN due to a lack of understanding of its mechanisms. Moreover, different patients react differently to the same treatment; a subgroup of patient population may never experience CIPN, while another may experience severe CIPN for the same dose. In addition, there are no established strategies for predicting CIPN either. This thesis addresses both prediction and mechanisms of CIPN.

The following paragraphs reflect the organization of this thesis. Each paragraph introduces a research problem, the approaches taken to investigate it, and states the key results.

First, a metabolomics-based approach was used to investigate CIPN prediction. Blood samples of pediatric leukemic cancer patients who underwent treatment with a chemotherapy agent - vincristine were provided. These blood samples were analyzed at different treatment time points using mass spectrometry to obtain the metabolite profiles. Machine learning was then employed to identify specific metabolites that

can predict overall susceptibility to peripheral neuropathy in those patients at specific treatment time points. Subsequently, selected metabolites were used to train machine learning models to predict neuropathy susceptibility. Finally, the models were deployed into an open-source interactive tool- *VIPNp*- that can be used by researchers to predict CIPN in new pediatric leukemic cancer patients.

Second, the focus was shifted to the pathophysiology of pain and the pain-sensing neuron; specifically: (i) investigating pain sensation mutations and the dynamics of the pain-sensing neuron, and (ii) exploring chemotherapy-induced peripheral neuropathy mechanisms.

While pain is a common experience, genetic mutations in individuals can alter their experience of pain, if any at all (certain mutations yield individuals insensitive to pain). Despite its ubiquity, we do not have a complete understanding of the onset and/or mechanisms of pain sensation. Pain sensation can be broadly classified into three types: (i) nociceptive, (ii) neuropathic, and (iii) inflammatory. Nociceptive pain arises due to a noxious external stimulus (e.g., upon touching a hot object). Neuropathic pain (which is felt as a side-effect of the aforementioned chemotherapy agents) is the numbing and tingling sensation due to nerve damage. Inflammatory pain occurs due to damage to internal tissues. Pain in any form can be characterized in terms of electrical signaling by the pain-sensing neuron. Signal transmission regarding pain occurs through generation of an electrical signal called the action potential- a peak in neuron membrane potential. Excessive firing of action potentials by a pain-sensing neuron indicates pain of a specific form and intensity. In order to investigate this electrical signaling, a mathematical modeling approach was employed. The neuron membrane was assumed to be an electrical circuit and the potential across the membrane was modeled in terms of the sodium and potassium ions flowing across it via voltage-gated sodium and potassium channels, respectively. Generation of a single action potential followed by a resting state corresponds to a normal state, whereas periodic firing of action potentials (an oscillatory state) corresponds to pain of some form and intensity *in vitro*. Therefore, an investigation into the switch from a resting

state to an oscillatory state was proposed. A bifurcation theory approach (generally useful in exploring changes in qualitative behavior of a model) was used to explore possible bifurcations to explain this switch. Firstly, genetic mutations that can shift the pain sensation threshold in the pain-sensing neuron were explored. The detected bifurcation points were found to be sensitive to specific sodium channels model parameters, implying sodium channels sensitivity towards the pain sensation threshold. This was corroborated by experimental evidence in existing literature. Secondly, a theoretical analysis was performed to explore all possible bifurcations that can explain the dynamics of this pain-sensing neuron model. The mathematical modeling simulations revealed a mixture of small amplitude and large amplitude membrane potential oscillations (mixed-mode oscillations) for specific parameter values. The onset and disappearance of the oscillations were investigated. Model simulations further demonstrated that the mixed-mode oscillations solutions belonged to Farey sequences. Furthermore, regions of bistability- where stable steady state and periodic solutions coexisted- were explored. Additionally, chaotic behavior was observed for specific model parameters.

Finally, this thesis investigated the role of voltage-gated ion channels in inducing CIPN using the same mathematical model. Repetitive firing of action potentials in the absence of any external stimulus was used as an indicator of peripheral neuropathy. Bifurcation analysis revealed that specific sodium and potassium conductances can induce repetitive firing without any external stimulus. The findings were supplemented by recording the firing rate of a sensory neuron culture. Next, a chemotherapy agent - paclitaxel, was introduced in the model to investigate its potential effects on the firing behavior. It was seen that a medium dose of paclitaxel increased repetitive firing. This was supported by the firing rate recordings of the sensory neuron culture.

In summary, this thesis presents a prediction strategy for CIPN. Moreover, it presents a bifurcation theory-based framework that can be used to investigate pain sensation, in particular, genetic mutations related to pain sensation and chemotherapy-induced peripheral neuropathy. This framework can be used to find potential voltage-

gated ion channels that can be targeted to control the pain sensation threshold in individuals, and can be extended to investigate various degeneracies in CIPN mechanisms to find therapeutic cures for it.

1. INTRODUCTION

Currently, cancer is the second leading cause of mortality in the United States. It is estimated that there will be approximately 4,950 new cancer cases each day in the year 2020 [1]. Cancer is primarily treated using surgery, chemotherapy, radiation therapy, or a combination of these. While chemotherapy is one of the most common ways of treating cancer, it is like a double-edged sword. It can induce adverse side-effects such as fatigue, hair loss, constipation, among others, which can potentially impact the quality of life of these patients. This thesis focuses on one specific side-effect of multiple chemotherapy agents: peripheral neuropathy.

Chemotherapy-induced peripheral neuropathy (CIPN) is a painful, dose-limiting side effect of chemotherapy cancer treatment that affects more than 85% and 60% of patients during [2] the treatment and three months post chemotherapy treatment [3], respectively. Several chemotherapy agents, such as vinca alkaloids, taxane derivatives, platinum derivatives, epothilone, thalidomide, and bortezomib have been suggested to cause CIPN [4]. Each of these drugs induce CIPN as an undesired side effect. Patients administered with these drugs report enduring pin and needle paresthesias (i.e., tingling, numbness) in the peripheral nervous system (hands and feet) [5]. The onset of symptoms can range from one day to two years after treatment and can persist throughout the life, causing a significant decrease in the quality of life of cancer survivors [6, 7]. It impacts the domestic, work, and social life of patients [6]. On an emotional level, it has been shown to result in depression, frustration and a sense of loss of purpose among these patients [8]. To improve quality of life of cancer patients, it is imperative to find CIPN preventive agents. Since there is currently no FDA-approved treatment for CIPN, management of CIPN-induced pain includes many options such as antidepressants, anticonvulsants, anti-inflammatory, and opioid

therapies. However, the American Society of Clinical Oncology only recommends the antidepressant duloxetine which causes severe withdrawal symptoms when treatment is discontinued [9]. In addition to not being a viable long-term solution, these treatments focus on reducing the pain symptom of CIPN but not treating the neuropathy itself.

CIPN is difficult to manage because of lack of established strategies for predicting or treating it. Different patients experience CIPN with a different level of severity. While some patients do not experience any neuropathy, others experience severe neuropathy soon after the treatment starts. The complications increase further because multiple drugs are administered in combination to treat a specific type of cancer. As a result, the root cause of CIPN cannot be isolated and investigated many times. An added complication arises for patients with preexisting conditions that are related to the peripheral nervous system, such as diabetes, alcohol consumption, inherited neuropathy [10, 11]. In this thesis, an attempt is made to both predict CIPN in patients and investigate therapeutic cures for it. Below, both the areas will be addressed in more detail.

1.1 CIPN diagnosis and prediction

CIPN is diagnosed using multiple grading scales that are calculated based on clinical symptoms. These scales are Total Neuropathy Score (TNS), Eastern Clinical Oncology Group (ECOG) scale, National Cancer Information Center-Common Toxicity Criteria (NCIC-CTC) scale, and Ajani sensory scale. Scoring is based on the symptoms associated with peripheral neuropathy and the extent of spread. Details of these scales can be found in [12]. None of these scales have been established as being comprehensive. In case of severe CIPN, dose reduction, slower infusion rates, and increasing the interval between chemotherapy dose are potential remedies. Besides, neuroprotective agents can be explored, the details of which will be discussed in the next section.

While some potential clinical risk factors have been identified to contribute to CIPN, none of them are accurate predictors of CIPN severity [11, 13]. Cumulative dose, age, obesity, baseline neuropathy due to conditions such as diabetes, and race are some identified clinical risk factors [3, 11, 13]. In order to find accurate predictors, the focus has primarily been on genetic polymorphisms. It is hypothesized that genes related to drug pharmacokinetics and mechanisms related to electrophysiology of peripheral sensory neurons may be associated with CIPN severity [13]. Various genetic polymorphisms have been found to be associated with CIPN due to various antineoplastic agents, however, associations have either not been reproducible in subsequent studies or have not yet been validated in larger clinical studies [13]. Multiple hindrances are potentially responsible for the lack of predictors, all of which are mentioned in a review by Chan et al. [13]. These are: (i) lack of a uniform CIPN scoring system, (ii) not being able to find predictors separately for motor, sensory, and neuropathic pain as symptoms of CIPN, (iii) not including phenotypic variabilities, (iv) combination therapies, (v) sample size of studies, among others. In this thesis, an attempt is made to address one of these shortcomings, namely, not including phenotypic variabilities. A metabolomics study was performed to find potential metabolites that could accurately predict CIPN due to a chemotherapy agent: vincristine. More details on this study can be found in the next chapter.

1.2 CIPN mechanism

CIPN mechanism is complex and occurs due to a myriad of events such as alterations in calcium signaling, ion channels, axonal transport, and occurrence of oxidative stress and inflammation [4, 14]. It primarily occurs due to damage on and near the peripheral sensory neurons, or the nerve cells. These neurons are responsible for transmitting information regarding touch, temperature, pain, etc., through generation of electrical signals which are governed by various mechanisms. Apart from the damage on the peripheral neurons, these chemotherapy agents can also potentially

impact the spinal cord, the details of which are described in a review by Carozzi and coworkers [4]; this is beyond the scope of this thesis.

All these antineoplastic agents can lead to CIPN due to a poor blood nerve barrier. This allows these agents to travel to these neurons and impact them. Moreover, drug transporters are also involved in allowing these agents to attack these cells. Peripheral sensory neurons are called dorsal root ganglia (DRG) neurons. These are further subdivided based on their sizes into small, medium, and large DRG neurons. These are pseudounipolar with a cell body outside of the cell axon. These may or may not be myelinated, i.e., the axon may or may not be insulated by a myelin sheath. Figure 1.1 shows a myelinated DRG neuron. It consists of a cell body, a long axon which branches into dendrites and finally ends at synapses. These neurons are responsible for mechanosensation, thermosensation, nociception (sensing pain-causing dangerous stimuli), etc. They are long, starting from the periphery and ending at the spinal cord. Information regarding any form of sensation is transmitted in the form of electrical signals due to activation and inactivation of voltage-gated ion channels on its membrane. The details of the electrophysiology can be found in Chapter 3. Apart from the electrical signaling, other cellular mechanisms which are common across all the generic cells also occur. Neurons have a cell body; they have mitochondria which is responsible for generation of adenosine triphosphate (ATP), the energy molecule. Mitochondria are also responsible for apoptotic signaling pathways, regulation of intracellular Ca^{2+} and reactive oxygen species (ROS). A unique feature of these neurons is axonal transport. Due to the long length of these neurons, active transport of organelles from one end of the neuron to the other occurs via microtubules along the axon. These neurons are surrounded by glial cells, primarily Schwann cells, which can release pro-inflammatory cytokines and chemokines that can lead to neuroinflammation. Apart from voltage-gated ion channels, ATP-dependent pumps, transient receptor potential (TRP) channels, and various other ion channels are also present on the neuronal membrane. TRP channels are responsible for thermosensation and mechanosensation, the details of which can be found in a review by

Ramsey et al [15]. Different chemotherapy drugs lead to peripheral neuropathy via different mechanisms. Below, major neuropathy-causing agents and their potential mechanisms are summarized and tabulated in Table 1.1. Details of these mechanisms can be found in several review papers [4, 14]. Specific reviews can also be found for role of cytokines [16, 17], oxidative stress [18], mitochondrial dysfunction [19], and ion channels [20] in CIPN.

The first class of such chemotherapy agents are vinca alkaloids which include vincristine, vinblastine, vinorelbine, and vindesine. Vincristine leads to most severe side effects, and used to treat several cancers such as acute lymphoblastic leukemia. It acts as an antineoplastic drug by binding to the tubulins and blocking its polymerization into microtubules. This mechanism also impacts the peripheral neuron and impairs axonal transport, leading to axonal swelling and degeneration [21, 22]. Vincristine also alters Ca^{2+} homeostasis as a result of mitochondrial dysfunction [23–25]. Mitochondrial dysfunction also leads to oxidative stress and generation of ROS [26]. Furthermore, evidence suggests the involvement of MAP-kinases in vincristine-induced peripheral neuropathy [27]. It is suggested that other inflammatory pathways may also be involved [16, 28].

The second class of such agents are platinum-based, namely, oxaliplatin, cisplatin, and carboplatin. These are primarily used for solid tumors. They act on tumor cells by binding with nuclear DNA by forming platinum adducts, leading to cell apoptosis. Cisplatin and oxaliplatin also lead to oxidative stress as a result of mitochondrial dysfunction [29–35]. Mitochondrial dysfunction occurs through alteration of mitochondrial respiratory chain and induction of apoptotic mitochondrial pathway. Besides, they impact the transient potential receptors [36–39]. Transient potential receptors are involved in neurogenic inflammation [4]. These agents are also involved in elevation of pro-inflammatory cytokines [16, 40]. Oxaliplatin can also modulate the sodium and potassium ion channels [41–46], calcium homeostasis [25, 47], MAP-kinases [48], and protein-kinase C [49], and can elevate chemokines and their receptors [50–54].

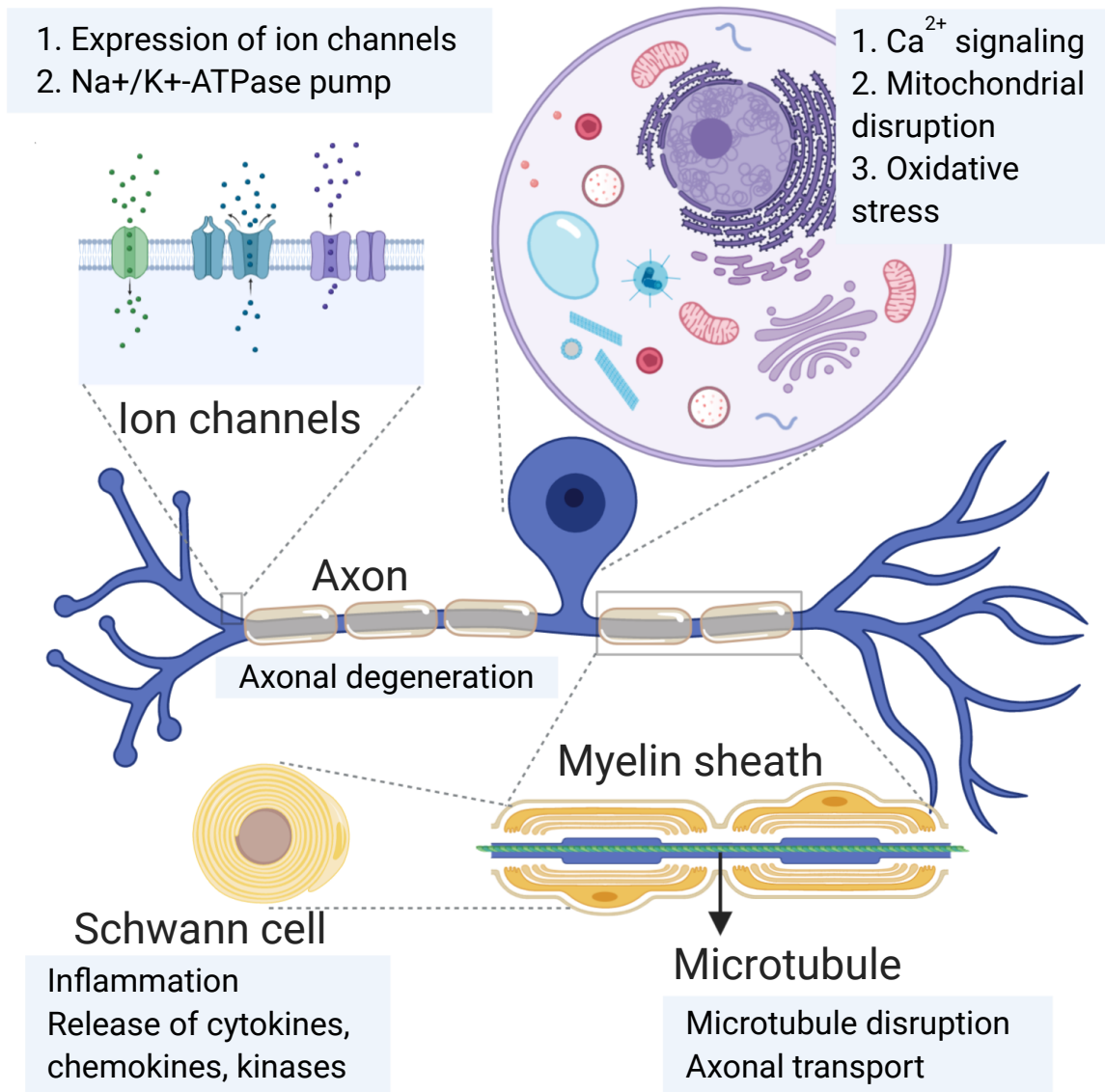


Figure 1.1.: Parts of a myelinated DRG neuron that can get impacted due to chemotherapy agents. (Figure developed using Biorender (<https://biorender.com/>))

Another type of antineoplastic agent is thalidomide, an immunomodulatory drug. It is used for the treatment of multiple myeloma [55]. It is conjectured that it may block the production of tumor necrosis factor alpha (TNF- α) and activation of nuclear factor kappaB (NF- κ B) to induce cell death [14, 56]. It also blocks tumor angiogenesis [57]. The mechanism of thalidomide-induced peripheral neuropathy is unclear. Potential mechanisms of thalidomide-induced peripheral neuropathy include its action on TNF- α and NF- κ B which can lead to neuronal cell death [58], and include the release of ROS [59].

The next class of agents is taxanes, which includes paclitaxel, docetaxel, and cabazitaxel. They are used for various cancers such as lung cancer, breast cancer, gastric cancer, bladder cancer, among others [60]. Their antineoplastic mechanism is via interference with microtubule depolymerization and repolymerization which leads to cell death. The highest CIPN incidence among these drugs is of paclitaxel. The action of microtubule disruption can also lead to peripheral neuropathy due to paclitaxel by impacting the axonal transport [61–63]. Paclitaxel can also result in mitochondrial dysfunction. It can alter mitochondrial Ca^{2+} homeostasis [64, 65], mitochondrial permeability [66–68], mitochondrial respiratory chain [69], and can lead to induction of apoptotic mitochondrial pathway [70]. This leads to oxidative stress and release of ROS [18, 71, 72]. Dysregulation of Ca^{2+} homeostasis can also lead to axon degeneration [73]. Paclitaxel can also induce release of pro-inflammatory cytokines [18, 71]. Moreover, it can regulate expression of various sodium [74, 75], potassium [74], calcium [76], and TRP [77–79] channels, which can impact the excitability behavior of peripheral sensory neurons.

Another class of agents is the protease inhibitor, named, bortezomib. It is used for treatment of multiple myeloma [80]. Bortezomib also leads to tubulin polymerization and microtubule stabilization that leads to cell death [81, 82]. This mechanism can also induce peripheral neuropathy [4]. It also leads to alteration of mitochondrial Ca^{2+} homeostasis [83] and mitochondrial respiratory chain [84] which can subsequently lead to production of ROS. Likewise, bortezomib can also induce oxidative stress and

release of ROS that can then damage the mitochondria [85]. Moreover, it is involved in inducing inflammation [82], increasing TRPV1 levels [86], and in impairing Na^+/K^+ -ATPase dependent pump [87].

1.3 Existing treatment strategies

There are two potential strategies for addressing CIPN: i) using neuroprotectant agents to prevent CIPN, ii) using therapeutic agents to treat established CIPN. Example neuroprotectants are calcium and magnesium infusions, vitamin E which is an anti-oxidant, glutamine, glutathione, however there is a lack of an established neuroprotectant for all the chemotherapy agents. Potential treatments for established CIPN include tricyclic antidepressants, gabapentin, and acetyl-L carnitine. Again, no effective treatments for established CIPN exist. More details on these neuroprotectant agents and potential treatments can be found in multiple review papers [88–90].

Existing treatment and neuroprotective strategies of CIPN are based on addressing a single event associated with peripheral neuropathy. For example, calcium and magnesium infusions can increase the concentration of extracellular calcium and thereby close sodium channels, reducing the hyperexcitability [91]. Antioxidants such as vitamin E can reduce the oxidative stress. Glutamine can up-regulate nerve growth factor mRNA [92]. However, a myriad of events such as alteration in calcium signaling, voltage-gated ion channels, axonal transport, and occurrence of oxidative stress and inflammation [4] have all been linked with CIPN. Moreover, they are interlinked in a complex fashion. For example, both voltage-gated ion channels and intracellular biochemical reactions play a role in dynamics of neuronal spiking and excitability. This complexity might explain the failure of potential preventive agents in clinical trials, since they target only one of these events. Even if one of the events is brought under control, CIPN can occur because of all other events. Hence, this thesis hypothesizes that *this system is degenerate*. Degeneracy implies that multiple pathways can lead to the same output [93]. Several biological processes are evidenced to be degenerate, including onset of neuropathic pain [94] and ion channel regulation in general [95]. To

Table 1.1.: A summary of potential mechanisms involved in CIPN due to the mentioned chemotherapy agents.

Chemotherapy agents	Mechanisms	Reference
Vincristine	Microtubule disruption	[21, 22]
	Ca ²⁺ homeostasis	[23–25]
	Oxidative stress	[26]
	Inflammation	[16, 27, 28]
Cisplatin	Oxidative stress	[29–35]
	Transient potential receptors	[36–39]
	Inflammation	[16, 40]
Oxaliplatin	Oxidative stress	[29–35]
	TRP	[36–39]
	Inflammation	[16, 40, 48–54]
	Ca ²⁺ homeostasis	[25, 47]
	Na ⁺ /K ⁺ ion channels	[41–46]
Thalidomide	Inflammation	[58]
	Oxidative stress	[59]
Paclitaxel	Microtubule disruption	[61–63]
	Ca ²⁺ homeostasis	[64, 65]
	Oxidative stress	[18, 71, 72]
	Inflammation	[18, 71]
	Sodium, potassium, calcium, TRP channels	[74, 74–79]
Bortezomib	Microtubule disruption	[81, 82]
	Ca ²⁺ homeostasis	[83]
	Oxidative stress	[84, 85]
	Inflammation	[82]
	TRP	[86]
	Na ⁺ /K ⁺ -ATPase dependent pump	[87]

investigate degeneracy more effectively, it is imperative to investigate all the events together. While it is difficult to control multiple events in an experimental setting, it is reasonable to do so using a mathematical model. A mathematical model provides the freedom to combine events and to observe how the system behavior changes upon any external perturbation. Furthermore, using a mathematical model, one can predict multiple possible ways of reversing neuropathy. All the events (such as axonal transport, action potential generation, intracellular biochemical reactions) can be investigated independently or together using mathematical models. At the same time, experimental validation of the results obtained from mathematical models is needed for practical application. Hence, a collaboration across multiple disciplines is necessary. This thesis focuses on exploring degeneracies in the electrophysiology of a pain-sensing neuron by investigating a mathematical model representing dynamics of a pain-sensing neuron and by supplementing the work with experimental support from collaborators. A pain-sensing neuron is a nerve cell that can detect signals that are interpreted as neuropathy. Further details regarding electrophysiology and an introduction to the working of this neuron can be found in Chapter 3. The work on exploring degeneracies in electrophysiology can be found in Chapter 5. A discussion of possible interactions in CIPN mechanisms can be found in chapter 7.

Peripheral Neuropathy is one form of pain sensation. In order to understand CIPN mechanism, it will be helpful to understand general pain sensation mechanism. Moreover, cancer itself causes pain due to the tumor. Thus, this thesis also develops an approach that can be used to explore pain sensation of any form. Below is an introduction to pain sensation and the pathway.

1.4 Pain sensation

Pain can be of three types: (i) nociceptive, (ii) neuropathic, and (iii) inflammatory. Nociceptive pain is the pain arising due to a noxious (potentially harmful) stimulus, such as touching an extremely hot or cold object. Neuropathic pain arises due to any nerve related injury, which may lead to hypersensitivity, tingling, or a burning

sensation. This is the form of pain that was investigated in the previous chapter. Inflammatory pain arises due to release of inflammatory molecules (e.g. $\text{TNF}\alpha$) as a result of internal tissue damage. Any form of sensation occurs through transmission of information across neurons in the nervous system, starting from the peripheral nervous system, reaching the central nervous system, and then transmitting back to the peripheral nervous system. Sensation is detected at the periphery by the sensory neurons, which is first converted to a chemical signal and subsequently to an electrical signal. The electrical signal is then transmitted to the spinal cord. In the case of a noxious stimulus, sensation is detected at the skin by the endings of specialized neurons. These specialized neurons are called nociceptive neurons, or nociceptors, which have receptors that can detect such a noxious stimulus, first proposed by Sherrington more than 100 years ago [96]. A nociceptor can detect noxious stimuli due to temperature, harmful chemicals such as acid, and extreme mechanical pressure. At the spinal cord, it is connected to another neuron to transmit the signal to the brain. There are a series of neuronal connections from the spinal cord to the brain. From the spinal cord, it first reaches the thalamus which relays the signal to the sensory cortex and thence to the motor cortex. From the motor cortex, the signal is sent back to the thalamus, then to the spinal cord and it finally reaches the targeted muscle cells through the motor neurons. The motor neurons control how the muscle cells will react to the noxious stimulus. If an individual touches something noxious, for example, a burning object, the following series of events will occur. The hot temperature sensation by the nociceptive neurons results in a signal to the brain and then back to the muscles at which point the individual feels a burning sensation and releases contact with the burning object. This pain sensation pathway is shown in Figure 1.2. There are primarily two processes involved in pain: sensation and perception. The nerve endings at the skin sense a noxious stimulus and eventually transmit the signal to the brain. The brain decodes and perceives the stimulus as painful and accordingly generates a response to be sent back to the motor neurons.

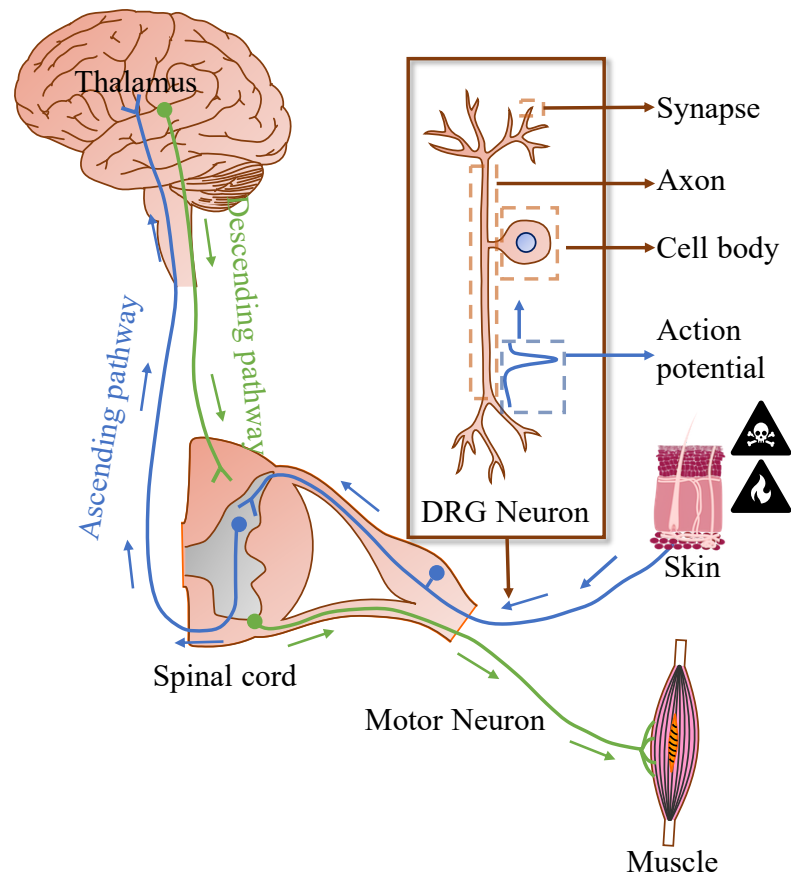


Figure 1.2.: The pain sensation pathway starts from a noxious stimulus being detected by a small DRG neuron (nociceptor) at the skin. The input leads to the generation of action potentials which are then transmitted to the spinal cord. From the spinal cord, the input is further transmitted to the thalamus via the ascending pathway. The response is transmitted back to the spinal cord via the descending pathway. It is finally transmitted to the muscle cells via the motor neuron. The muscle cells respond in concordance with the signal. The DRG neuron consists of a cell body, an axon across which the action potential is transmitted, and ends at the synapse which transmits information from one neuron to the other.

Throughout this paper, we focus on sensation, rather than perception. Details on the pain pathway can be found in multiple review papers [97–101].

Most small dorsal root ganglia (DRG) neurons are nociceptors [102], shown in Figure 1.2. In this work, the focus is only on small DRG neurons. Specific alterations or injury in this neuron can lead to change in the nociceptive pain threshold (gain or loss of pain sensation), neuropathic pain, inflammatory pain, or a combination of these. These neurons consist of a cell body, an axon, and synapses at the branch endings, as described earlier. Furthermore, all DRG neurons are pseudo-unipolar, which means that they have two axons branching out from the main cell body, one reaching the periphery and the other reaching the central nervous system. Unlike other DRG neurons, small DRG neurons are primarily unmyelinated. This implies that their speed of conduction is slower.

There is ongoing research on developing drugs that can control the pain sensation threshold. Currently, it is unclear how pain sensation threshold can be controlled and how this threshold varies among individuals, specifically among those with genetic mutations related to pain sensation. This thesis presents a specific framework that can be used to explore how pain sensation threshold can vary. This framework consists of analyzing mathematical modeling of a neuron's electrophysiology by using bifurcation theory. The mathematical model explains the electrophysiology of the membrane of a small dorsal root ganglia (DRG) which is a pain-sensing neuron present in the peripheral nervous system. Electrical firing by this neuron carries information that is transmitted across from one neuron to the next. Repetitive electrical firing corresponds to pain of some form and intensity. Details of neuron firing can be found in Chapter 3. In this thesis, bifurcation theory is used to find the bifurcation points that can be indicative of repetitive firing. Furthermore, sensitivity of these bifurcation points is investigated to analyze their role in controlling the pain sensation threshold.

1.5 Objectives

This thesis focuses both on chemotherapy-induced peripheral neuropathy and generic pain sensation. The objective of this thesis is to expand the understanding

of CIPN and pain sensation, and to provide approaches to investigate them further. This is done by accomplishing the following specific aims.

Specific Aim 1: Find metabolites that can predict vincristine-induced peripheral neuropathy accurately in order to aid in dosage decision making for pediatric acute lymphoblastic leukemia patients. In this work, metabolomics approach was used to find potential metabolites that can accurately predict CIPN susceptibility at various time points during the treatment. This work is primarily based on machine learning and is described in Chapter 2.

Specific Aim 2: Present a bifurcation theory-based approach that can be used to investigate potential parameters that can control the pain sensation threshold. This work is described in Chapter 3, where an introduction to neuronal electrophysiology, working of a pain-sensing neuron, a mathematical model representing a pain-sensing neuron, and how bifurcation theory can be used to find potential model parameters that can shift the bifurcation points and can therefore be indicative of mutations related to pain sensation, are described. This and the subsequent two chapters are based on mathematical modeling and bifurcation theory.

Specific Aim 3: Provide a deeper investigation of the dynamics of the mathematical model representing a pain-sensing neuron. In this work, various solution regimes and patterns of the dynamics were identified. Role of a specific sodium channel was also elaborated. This work is described in chapter 4.

Specific Aim 4: Investigate the electrophysiology of a pain-sensing neuron and how they can be used to find potential therapeutic measures for treating CIPN. In this work, role of various voltage-gated ion channels in regulating the excitability of this neuron are explored. A chemotherapy agent paclitaxel is also introduced in the model and analyzed. The results are supplemented by recording firing rate of DRG neuron culture. This work is described in chapter 5.

In chapter 6, interactions in CIPN mechanisms are elucidated. In chapter 7, all the previous chapters are summarized and in chapter 8, future work are enlisted.

2. A METABOLOMICS APPROACH FOR EARLY PREDICTION OF VINCRISTINE-INDUCED PERIPHERAL NEUROPATHY

This work has been submitted to Scientific Reports and is currently under review

Vincristine is a core chemotherapeutic drug administered to pediatric acute lymphoblastic leukemia patients. Despite its efficacy in treating leukemia, it can lead to severe peripheral neuropathy in a subgroup of the patients. Peripheral neuropathy is a debilitating and painful side-effect that can severely impact an individual's quality of life. Currently, there are no established predictors of peripheral neuropathy incidence during the early stage of chemotherapeutic treatment. As a result, patients who are not susceptible to peripheral neuropathy may receive sub-therapeutic treatment due to an empirical upper cap on the dose, while others may experience severe neuropathy at the same dose. Contrary to previous genomics based approaches, in this chapter, a metabolomics approach is employed to identify small sets of metabolites that can be used to predict a patient's susceptibility to peripheral neuropathy at different time points during the treatment. Using those identified metabolites, a novel strategy is developed to predict peripheral neuropathy and subsequently adjust the vincristine dose accordingly. In accordance with this novel strategy, a free user-friendly tool, *VIPNp*, is created for physicians to easily implement the prediction strategy. The results showed that focusing on metabolites, which encompasses both genotypic and phenotypic variations, can enable early prediction of peripheral neuropathy in pediatric leukemia patients.

2.1 Introduction

Acute lymphoblastic leukemia (ALL) is the most common cancer among children, accounting for approximately 26% of all pediatric cancers in the USA [103]. Although

the 5-year survival rate of pediatric leukemia patients is as high as 86%, the side-effects of the treatment can severely impact the quality of life of survivors [104]. In particular, vincristine, a core chemotherapeutic drug administered as part of the ALL therapy that has been in use for more than 50 years, has a dose-limiting toxicity: peripheral neuropathy. Vincristine-induced peripheral neuropathy (VIPN) is characterized primarily by numbness, tingling, and a painful sensation felt in the hands and feet, muscle weakness, and constipation due to its effect on the sensory, motor, and autonomic nerves [105–107]. In some instances, VIPN can be prolonged and may last even after discontinuation of the treatment, impairing patients' motor skills [108–111] which results in limitation of their daily life activities for many years after completion of therapy [112]. While VIPN is severe in a subpopulation of patients, another subpopulation experiences negligible neuropathy. Currently, there are neither established ways of predicting susceptibility to VIPN in patients, nor ways to treat it effectively, resulting in a suboptimal management for both the cohorts. Predicting VIPN susceptibility in patients will enable better dosage decision making tools for physicians and in turn may improve the quality of life of these patients.

Several researchers have studied the association between genomics and VIPN incidence; however, the majority of the results have been controversial. Most of the studied differences are based on race, CYP3A5, ABC transporter, and, more recently, CEP72 expression. While some studies have reported a significant association between race and VIPN incidence [113–116], others could not confirm those results [107,117]. CYP3A5 metabolizes vincristine and some studies have reported a significant association between CYP3A5 expression and VIPN [115,118,119]; however, one study could not establish such an association [120]. Similarly, there is evidence for association between the ABCB1 transporter and VIPN [121,122]; and there also exists evidence to the contrary [120]. Additional details on the associations and non-associations found between VIPN and other variables is addressed by Velde et al. [106] and Mora et al. [105]. Correlations between pharmacokinetics or other patient-specific co-variables and VIPN have also been evasive due to a large variability in the available interpa-

tient and inpatient data, making interpretation of these pharmacokinetic studies difficult [123–127]. Recently, significant correlation was discovered of a SNP in the promoter region of the CEP72 gene with VIPN, during the maintenance phase of the treatment. CEP72 expression was associated with VIPN in human neurons derived from human induced pluripotent stem cells, as well [114]. While some studies have been able to reproduce this finding during the late phase of the treatment [128,129], this association was not found in the earlier phase of therapy [130,131]. The literature clearly shows that an established predictor for the early stage of the treatment is still lacking.

In this chapter, a detour from the previous genomics and pharmacokinetics related studies is taken and a novel approach using metabolomics is employed to predict VIPN at an earlier stage of the treatment. The need to go beyond genomics has been raised before [132], and, specifically, the role of metabolomics in predicting drug response has garnered more attention [133,134] in recent years. The recent interest in pairing metabolomics and drug response is a result of phenotypic variations that can be captured at the downstream metabolite level. These phenotypic variations arise due to differences in environment, lifestyle, stochasticity in biochemical reactions, etc., and may be as important as, if not more important than, the upstream genomics to predict drug response [132]. Information transfer for expression of a disease outcome takes place at various stages, starting from transcription of a gene to mRNA, then translation to a protein, and, finally, to the synthesis of metabolites. Variations at any stage may induce a different response to any drug. Because of this, drug response of a homogeneous population of patients with a similar genome may vary. Moreover, variations at the genetic level may not get transferred to the downstream metabolite level because of the robustness of the metabolic pathways. Therefore, a metabolomics approach is employed to find metabolites that can accurately predict VIPN in a cohort of pediatric patients who underwent ALL treatment, with vincristine as the core chemotherapy drug. Small sets of metabolites were determined that can accurately predict VIPN at different stages of the treatment and they were subsequently used

to develop a strategy to identify patients that are highly susceptible to VIPN. Using this strategy, a free user-friendly tool was developed, *VIPN_p* [135,136], for physicians to apply these models for prediction of VIPN susceptibility at different stages of a patient’s chemotherapy treatment.

2.2 Results

In this section, the workflow and the results are elaborated upon. The neuropathy data obtained was categorized from physician evaluations of VIPN severity experienced by patients. Then, hierarchical clustering was performed to differentiate between metabolite profiles measured at both early and late time points of the treatment process. Based on their metabolite profiles measured at different time points, a small subset of biomarker metabolites was found which was used to build a predictive model of VIPN susceptibility. The molecular structure of some of the biomarkers were identified and then pathway analysis was performed.

2.2.1 Pediatric ALL patient data description

A total of 36 patients’ data was collected. These were pediatric patients treated with AALL0932 protocol for B-ALL enrolled in a study from 2010 to 2014 (see Methods for details). Vincristine was part of the core chemotherapeutic treatment. All subjects were phenotyped for peripheral neuropathy using the Total Neuropathy Score Pediatric Vincristine (TNS[©]-PV) [137]. Twenty-four of the 36 patients (67%) were phenotyped as patients experiencing high neuropathy (HN), while the remaining 12 patients (33%) were classified as patients experiencing low neuropathy (LN) after the treatment completion. Patient demographics are described in Table 2.1. Non-fasting blood samples for these patients were collected prior to administration of drugs at three time points of the treatment: during the induction phase (day 8 and day 29) and the consolidation phase (around 6 months).

Patients were assessed regularly using the TNS[⊙]-PV scoring scheme throughout the 2-3 years of treatment. A score less than 3 was considered of low intensity and a score greater than 8 was considered of high intensity. A patient was classified as LN if the TNS[⊙]-PV intensity remained low throughout the entire duration of treatment, regardless of the drug amount. A patient was classified as HN if the TNS[⊙]-PV intensity was high at any time point during the treatment. This classification scheme matched the course of treatment for patients experiencing severe neuropathy. A patient who presents a score of 8 or higher at least once indicates susceptibility for severe neuropathy. The degree of neuropathy may improve during later phases of treatment when the drug is given less frequently or after dose modifications have been made for severe VIPN. However, these adjustments do not make a patient less susceptible to neuropathy in the future; if a patient was susceptible to high neuropathy even once, we classified the patient as HN. As a result of this classification system, patients who never had a TNS[⊙]-PV greater than 8 but had a TNS[⊙]-PV greater than 3 at some point (medium intensity) were not considered for the purposes of this study. This classification, as well as, threshold scores of 3 and 8 TNS[⊙]-PV were delineated to ensure a clear demarcation between patients who were susceptible to severe neuropathy and those who experienced negligible neuropathy.

Figure 2.1 shows how the neuropathy score changed during the course of the treatment time points considered and how it compared to the overall neuropathy susceptibility of a patient. At day 8, most of the patients had a low TNS[⊙]-PV intensity (TNS[⊙]-PV less than 3) while the incidence of high neuropathy (TNS[⊙]-PV greater than 8) increased with time. However, one patient had low TNS[⊙]-PV at day 8, high TNS[⊙]-PV at day 29, and low again at the month 6 time point. Figure 2.1 shows that by 6 months, 17 out of 24 HN (TNS[⊙]-PV greater than 8 at least once during the treatment) patients had already experienced high neuropathy, indicating a need for dosage adjustment earlier in the treatment process. Consequently, this data shows it is imperative to find biomarkers that enable the prediction of overall neuropathy susceptibility during the early stage of the treatment. The focus of this

Table 2.1.: Patient characteristics were defined according to gender, age, and body mass index (BMI). For the day 8 treatment time point, 8 overall low neuropathy (LN) samples were available, while for day 29 and month 6 time points, 12 LN samples were available. 24 overall high neuropathy (HN) samples were available at all the three time points. Age and BMI correspond to that during the start of the treatment. Here, "HN" implies that the patient had a Total Neuropathy Score Pediatric Vincristine (TNS_{PV}) greater than 8 at least once, and "LN" implies that the patient had a TNS_{PV} less than 3 throughout the treatment. SD: standard deviation.

	Day 8		Day 29 and Month 6	
	HN	LN	HN	LN
Total	24	8	24	12
Females/Males	11/13	4/4	11/13	5/7
Age, in years (Mean, SD)	9.6,4.8	4.3,2.4	9.6,4.8	4.4,2.6
BMI, in Kg/m ² (Mean, SD)	24.4,12.4	14.5,2.6	24.4,12.4	15.1,2.8

study is on finding metabolites that can differentiate between HN and LN during these time points.

2.2.2 Longitudinal versus independent analysis of metabolite profiles

Following the collection of patient blood samples, metabolite profiling was performed using liquid chromatography with tandem mass spectrometry (LC-MS/MS) (refer to Methods for description). Then, metabolite profile across the three time points were analyzed, initially using hierarchical clustering. The hierarchical clustering dendrogram showed that the profiles clustered according to the time points, as shown in Figure 2.2. Each branch in the figure corresponds to a sample. Since the samples were clearly demarcated according to the time points, it implies that the metabolite profiles were distinctly expressed at the three time points. Following the hierarchical clustering, an algorithm to develop a longitudinal support vector classifier

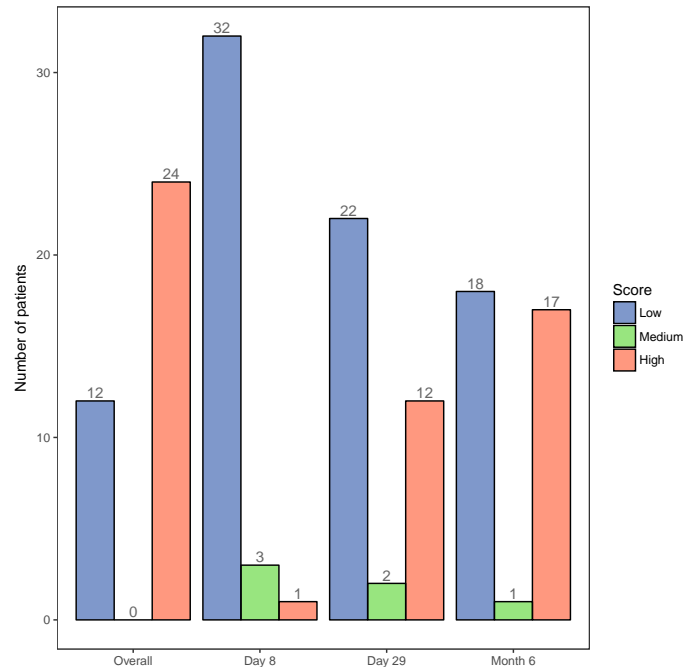


Figure 2.1.: A bar plot showing distribution of the neuropathy score of patients over time. A TNS \odot -PV less than 3 corresponds to low, a score between 3 and 8 corresponds to medium, and a score above 8 corresponds to high. The first group shows the overall susceptibility of patients to neuropathy (LN versus HN). The next three groups show the TNS \odot -PV intensity at that particular time point. Since patients with an overall medium TNS \odot -PV intensity were not considered in this study, the number of such patients is zero in the first group. Some HN patients had medium TNS \odot -PV intensity (TNS \odot -PV greater than 3 but lesser than 8) at some points during the treatment, as seen in the next three groups.

(SVC) [138] model was used to further confirm the distinct expression of metabolites at the three time points. The algorithm was used to estimate a parameter β according to the following equation:

$$Y = f(\tilde{\mathbf{X}}_{t_1} + \beta\tilde{\mathbf{X}}_{t_2}), \quad (2.1)$$

where, t_1 and t_2 are two time points, Y is the neuropathy response, and $\tilde{\mathbf{X}}$ is the metabolite expression matrix. This algorithm was used to estimate β by minimizing

the error between the predicted and actual response. For different combinations of the time points, β was approximately zero, regardless of the initial guess, implying that no identical set of metabolites can accurately predict neuropathy at different time points. Based on these two results, it was hypothesized that different metabolites should be predictive of neuropathy at the different time points; the profiles were analyzed separately as discussed in the next section.

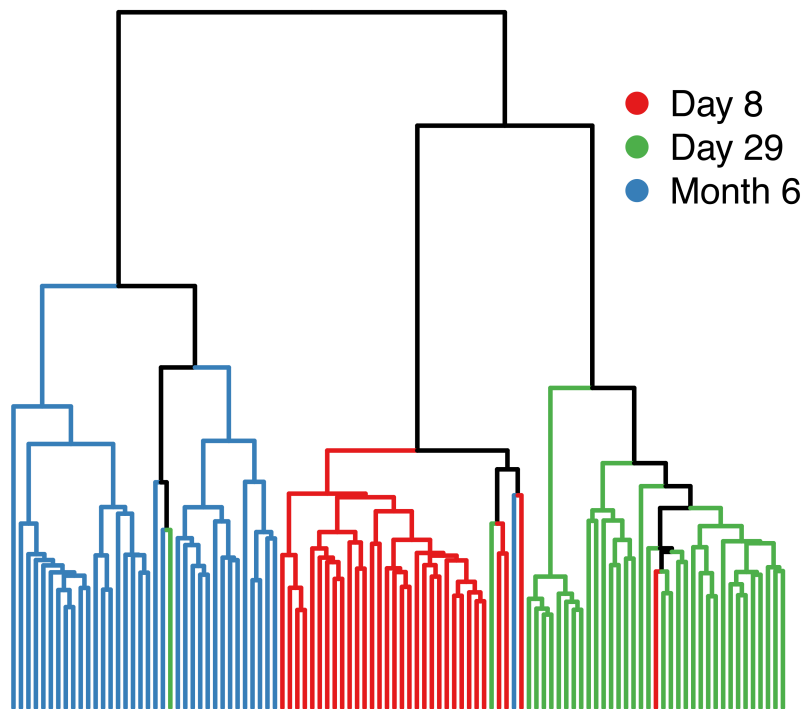


Figure 2.2.: A dendrogram created based on the Euclidean distance shows that the metabolite profiles are clustered according to their corresponding time points. Day 8 and day 29 metabolite profiles belong to the same primary branch and are consequently closer to each other.

2.2.3 Metabolite selection and model building

In order to find a small set of metabolites that can accurately predict overall susceptibility to neuropathy, recursive feature elimination (RFE) along with cross

validation was used to develop a linear SVC model. Since hierarchical clustering and longitudinal SVC modeling (described in the previous section) indicated that the metabolite profiles are distinctly expressed across the three time points, RFE was applied separately on each of the time point-specific metabolite profile matrix. The matrix of features included metabolite expression and vincristine concentration at the three time points: 5 metabolites at day 8, 46 metabolites at day 29, and 42 metabolites at the month 6 time point were chosen, with an area under the receiver operating characteristics curve (AUROC) of 0.97, 0.95, and 0.96, respectively. The vincristine concentration was not one of the selected features at any time point. As shown in Table 2.2A, these selected metabolites performed well at predicting neuropathy at all the three time points, with an average AUROC greater than 0.90 and standard deviation of AUROC less than 0.1.

RFE was also performed to find metabolites that can predict time point-specific neuropathy (i.e., high or low intensity of TNS \odot -PV) in patients (Table 2.2B). Since only 1 patient had high TNS \odot -PV during day 8, analysis was not performed on that data set. From the day 29 metabolite profile data, only 2 metabolites were chosen that could predict TNS \odot -PV intensity at that point, with an AUROC of 0.83 (lower accuracy than that obtained from the previous analysis shown in Table 2.2A). From the month 6 data, a small set of metabolites could not be selected; 1955 metabolites were chosen (Table 2.2B) with a lower accuracy (AUROC 0.81) as compared to the previous case (Table 2.2A). This implies that the metabolites are more effective in classifying patients based on the overall VIPN susceptibility, rather than VIPN intensity at the specific time points.

After selecting the small set of metabolites, that can classify between HN and LN, using RFE, integration of their chromatogram peaks at the corresponding retention times was investigated to ensure that they were correctly integrated and were not chosen because of any potential error in integration. In order to rigorously validate the selected metabolites as biomarkers, integration of peaks at the retention times was manually reviewed of every selected metabolite, for every sample, and at all the

Table 2.2.: Metrics obtained by performing RFE on the data sets at the three time points. A: The set of metabolites found that can accurately predict overall neuropathy susceptibility (HN versus LN) at these time points before manual integration of the chromatogram peaks. B: The set of metabolites found that can accurately predict TNS[©]-PV intensity of either high or low at that specific time point. C: The set of metabolites that can accurately predict overall neuropathy susceptibility at the time points after manual integration of peaks. AUROC: Area Under Receiver Operating Characteristics Curve, AUROCSD: standard deviations for AUROC. See Supplementary Table S1 for sensitivity and specificity corresponding to each of these.

	Time point	Predictors	AUROC	AUROCSD
A	Day 8	5	0.968	0.048
	Day 29	46	0.946	0.060
	Month 6	42	0.963	0.043
B	Day 29	2	0.831	0.120
	Month 6	1955	0.812	0.086
C	Day 8	6	0.938	0.047
	Day 29	48	0.861	0.122
	Month 6	45	0.923	0.069

time points. Agilent ProFinder software was used for this purpose. The peaks were found by matching the m/z and retention time from the metabolite profile matrix to the data loaded in ProFinder and then each of the peaks were manually visualized. If any integration was not precise, that peak was re-integrated. This resulted in a polished metabolite profile matrix.

RFE was repeated with this polished metabolite profile matrix to find metabolites that can classify between HN and LN. Using this polished data, 6 metabolites were selected at day 8, 48 metabolites at day 29, and 45 metabolites at month 6 time point, with AUROC of 0.94, 0.86, and 0.92, respectively. Table 2.2C shows the metrics obtained from the model fitting. In this case, the day 8 and month 6 metabo-

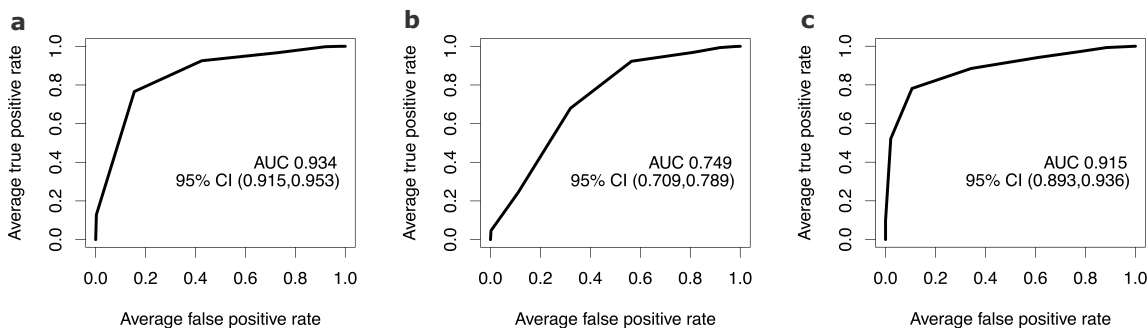


Figure 2.3.: ROC plots for the final trained models at the three time points. a: Day 8, b: Day 29, c: Month 6. AUC: Area Under Curve. CI: Confidence Interval.

lites performed better than those from the day 29 data, based on the AUROC and corresponding standard deviation.

To obtain the final list of correctly integrated and predictive metabolites, metabolites that were selected both from the polished (2.2C) and the unpolished data (2.2A) using RFE on each of them were chosen. Further, the metabolites whose peaks looked erroneous and were difficult to properly integrate were discarded. This refined procedure provided a final list of 2, 14, and 21 metabolites from day 8, day 29, and month 6 data, respectively. Repeated cross validation was performed again to train an SVC model using these final set of metabolites. Repeated cross validation was performed to estimate the predictability of the model and to find the optimal tuning parameter (the “cost” parameter) for the SVC model. The average cross validation AUROC was 0.93, 0.75, and 0.91 for day 8, day 29, and month 6 data, respectively. The average ROC’s for the trained models are shown in Figure 2.3.

After training the model corresponding to each time point using repeated cross validation, an optimal probability threshold was chosen to classify patients based on the output from the SVC model. To find the optimal probability threshold, the cross validation trained models’ accuracy was evaluated upon varying the threshold value. Evaluation of an appropriate threshold is needed since our data is unbalanced; keeping a threshold of 0.5 will lead to a bias towards HN. Supplementary Figure A.1 (shown

in Appendix A) shows sensitivity, specificity, Youden’s J statistic, and distance from best possible cutoff (i.e. sensitivity and specificity equal to 1) for the day 8, day 29, and month 6 trained models, where the models were built with the optimal tuning parameters obtained from cross validation. The threshold was chosen based on the minimum of distance from the best possible cutoff which led to thresholds of 0.7, 0.65, and 0.7 for the three respective time points. Finally, the cross validated trained models’ performance was evaluated based on this newly determined threshold. Model performance was based on a confusion matrix (provided in Table A.3 in Appendix A) and metrics calculated as shown in Table 2.3. The metrics shown in Table 2.3 show the ability of the models to make predictions when trained using a subset of the data. Only reported cross validation accuracy metrics has been reported test data set to assess the performance of the final trained model was not available. Finally, the model was trained using the whole data set and the optimal tuning parameters, which can be used to test new patient data.

Multiple metrics were used to determine the accuracy and validity of the predictive models. First, the p value of the one sided test for an accuracy greater than the No Information Rate is less than 0.05 for all the three time point models. This implies that the models predict better than simply random guessing. However, with accuracy as a metric, day 8 and month 6 data outperform. The balanced accuracy ((sensitivity + specificity)/2) is higher for day 8 and 6 month data as well, indicating that the model for day 8 and month 6 data seems to be more reliable in predicting overall VIPN susceptibility. A user-friendly interface, named *VIPNp*, was developed to use the trained models for day 8 and month 6 time points, freely available at GitHub [136] and the Shinyapps server [135].

2.2.4 Metabolite structure identification

After obtaining the final list of 2, 14, and 21 metabolites at day 8, day 29, and month 6, respectively, identification of the molecular structure of these metabolites was performed based on their mass-to-charge ratio (m/z), retention times, and tandem

Table 2.3.: Cross validation accuracy metrics for the models with optimal tuning using the final selected metabolites. These metrics were calculated after choosing the probability thresholds for each of the time points. Cost = 4, 0.25, 0.25 for day 8, day 29, and month 6 models, respectively.

Model Metric	Day 8	Day 29	Month 6
Accuracy	0.842	0.753	0.815
95% CI	(0.812, 0.870)	(0.720, 0.784)	(0.785, 0.843)
No Information Rate (NIR)	0.750	0.667	0.667
P-Value [Accuracy > NIR]	1.07e-08	3.14e-07	< 2.20e-16
Kappa	0.6093	0.448	0.625
McNemar's Test P-Value	3.41e-4	0.600	< 2.20e-16
Sensitivity	0.856	0.806	0.754
Specificity	0.800	0.646	0.938
Positive Predictive Value	0.928	0.820	0.960
Negative Predictive Value	0.650	0.625	0.656
Prevalence	0.750	0.667	0.667
Detection Rate	0.642	0.538	0.503
Detection Prevalence	0.692	0.656	0.524
Balanced Accuracy	0.828	0.726	0.846

mass spectrometry (MS/MS) spectra. MS/MS spectra was available for only a subset of the final list: 1 metabolite from the day 8 list, 5 metabolites from the day 29 list, and 8 metabolites from the month 6 list. MS/MS spectra was compared to the METLIN [139] database and the Human Metabolome Database (HMDB) [140]. No match was found for the day 8 metabolite; for day 29, one metabolite matched with Adenosine 5'-monophosphate (AMP) for all the collision energies; for month 6 data, one metabolite matched with L-pipecolic acid for one of the collision energies. In order to confirm the identity of these metabolites, MS/MS of commercially sourced AMP and pipecolic acid standards was performed to determine the retention times.

The retention times of the external compounds matched with that from the patient data (1 min of commercially sourced pipecolic acid versus 0.802 min as identified from the data, 1.4 min versus 1.77 min for AMP) confirming the identity of these two metabolites.

The LC-MS CEU Mass Mediator (CMM) search tool [141,142] was used with m/z value, adduct, and retention time inputs in the HMDB database to identify remaining metabolites. The most reasonable options were shortlisted. For example, if one of the searches was a metabolite that could only be found due to consumption of alcohol, it was discarded as a potential option since our focus in this study is on pediatric patients. Except for 1,7-Dimethylguanosine and Phenylalanylproline, all other potentially identified metabolites were at least previously detected in blood, according to HMDB. Using these approaches, 4 and 9 metabolites in the day 29 and month 6 lists, respectively were identified. Tables 2.4 and 2.5 define the identified metabolites from the day 29 and month 6 lists (Supplementary Tables A.4, A.5, and A.6 contain the complete list of metabolites, their mass, retention time, and adduct information, shown in Appendix A).

Table 2.4.: Identified metabolites that can accurately predict neuropathy susceptibility at the day 29 time point.

HMDB ID	Name	KEGG ID
HMDB0003357	N-Acetylornithine	C00437
HMDB0000757	Glycogen	C00182
HMDB0000045	Adenosine monophosphate	C00020
HMDB0001341	Adenosine diphosphate	C00008

2.2.5 Pathway analysis

In order to investigate the relevance of the chosen and identified metabolites, the pathway analysis tool in Metaboanalyst 4.0 [143,144] was used. The hypergeometric

Table 2.5.: Identified metabolites that can accurately predict neuropathy susceptibility at the month 6 time point.

HMDB ID	Name	KEGG ID
HMDB0000716	L-Pipecolic acid	C00408
HMDB0013464	SM(d18:0/16:1(9Z))	C00550
HMDB0000670	Homo-L-arginine	C01924
HMDB0001961	1,7-Dimethylguanosine	
HMDB0010383	LysoPC(16:1(9Z))	C04230
HMDB0003337	Oxidized glutathione	C00127
HMDB0011170	gamma-Glutamylisoleucine	
HMDB0001855	5-Hydroxytryptophol	
HMDB0011177	Phenylalanylproline	

test for over representation analysis and the relative-betweenness centrality for pathway topology analysis were selected.

For day 29, two metabolites (Adenosine diphosphate, Adenosine monophosphate) were identified to be part of purine metabolism, and one metabolite (N-Acetyloronithine) was identified to be part of the arginine biosynthesis (details in Supplementary Table A.7 in Appendix A). Since there were very limited metabolites to perform pathway analysis and only one or two of them belonged to a specific pathway which originally consisted of several metabolites, none of the metabolite to pathway associations were statistically significant after adjustment of the p values required to account for multiple testing. Furthermore, no evidence was found for the role of these pathways in chemotherapy-induced peripheral neuropathy in the existing literature.

For the set of month 6 metabolites, SM(d18:0/16:1(9Z)), Oxidized glutathione, LysoPC(18:1(9Z)), and Pipecolic acid were identified to be part of the sphingolipid metabolism, glutathione metabolism, glycerophospholipid metabolism, and lysine degradation, respectively (details in Supplementary Table A.8 in Appendix A). Again,

none of the pathway and metabolite associations were statistically significant after adjustment of the p values to account for multiple testing. However, evidence was found for the role of sphingolipid metabolism in chemotherapy-induced peripheral neuropathy [145–147]. Moreover, glutathione is a popular antioxidant tested as a therapeutic for chemotherapy-induced peripheral neuropathy, with various related studies mentioned in a review by Starobova and Vetter [148]. There is also evidence for the involvement of glycerophospholipid metabolism [149] which indicates that these metabolites may be biologically relevant to VIPN.

2.3 Discussion

Peripheral neuropathy is a painful and debilitating side-effect of vincristine, a common chemotherapeutic drug used for treatment of pediatric ALL patients, as well as, many other pediatric and adult cancers. Currently, there is no established way of predicting VIPN during the initial stage of the treatment. Identification of specific biomarkers will aid in adjusting the vincristine dose according to susceptibility of patients to VIPN in order to improve their quality of life. Even though all previous omics related studies have focused on genomics, it is imperative to include phenotypic variabilities to find VIPN predictors given their known impact on drug response. In this study, the role of metabolites in predicting susceptibility of ALL pediatric patients to VIPN was investigated.

Metabolite profiling of ALL patients was performed for three time points during the treatment: day 8, day 29, and month 6. First, it was found that the metabolite profiles were distinctly expressed at the three time points, as shown by hierarchical clustering (Figure 2.2) and longitudinal SVC modeling, indicating that the overall metabolite profile varied as a direct response to the treatment. Second, preliminary analysis using RFE resulted in sets of 5, 46, and 42 metabolites that accurately predicted overall VIPN susceptibility. Since the vincristine concentration was not one of the selected features from RFE, it was concluded that regardless of the vincristine concentration at the time points, a small set of metabolites can accurately predict

overall neuropathy susceptibility in these patients at these time points. Third, chromatogram peaks of these selected metabolites were manually integrated and RFE was performed again with the polished matrix. Subsequently, the metabolites that overlapped from the analysis with unpolished and polished data were chosen. Then, final sets of 2, 14, and 21 metabolites were found that could predict overall VIPN susceptibility at day 8, day 29, and month 6, respectively.

Metabolites could not predict time point-specific TNS \odot -PV intensity as accurately as overall susceptibility to VIPN (LN versus HN). This further strengthened the hypothesis that specific downstream metabolites can be potential biomarkers of overall neuropathy susceptibility due to treatment with vincristine. Furthermore, the final models built with the chosen metabolites were more accurate in predicting neuropathy at day 8 and month 6 as compared to the model built for the day 29 data (Table 2.3), implying that the developed predictive models can be used to evaluate VIPN susceptibility at the day 8 and month 6 time points during the treatment.

Based on the final developed models at the day 8 and month 6 time points, a framework is presented for predicting a patient's overall VIPN susceptibility during ALL treatment (Figure 2.4). On day 8 of the treatment, blood samples can be collected for metabolite profiling, specifically to obtain expression of the 2 chosen metabolites. The expression of these metabolites can be used to predict overall neuropathy susceptibility from the trained model. If the output of the model is a probability greater than the threshold value of 0.7, the physician may need to lower the vincristine dose as that sample might correspond to an HN patient. A follow up evaluation can be performed after 6 months by obtaining expression of the 21 chosen metabolites (Supplementary Table S5). If the output from the two trained models is consistently a probability greater than 0.7, the physician could consider lowering the vincristine dose. This framework can aid in vincristine dose decision making for the physicians. The user-friendly tool, *VIPN_p* [135,136], can be used to execute this strategy.

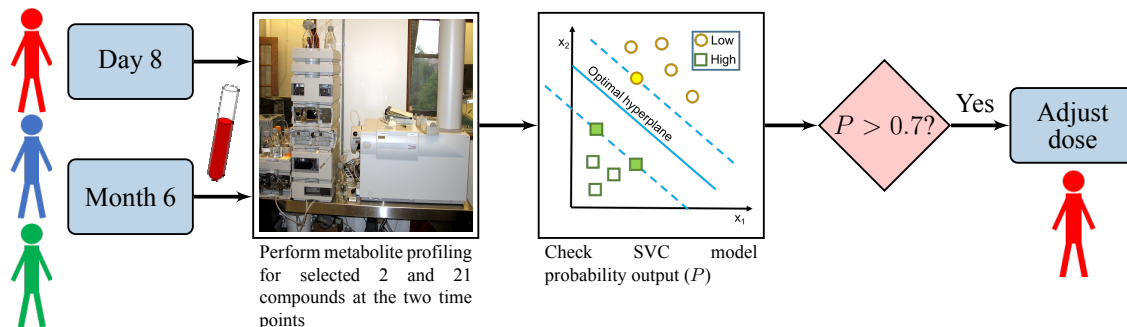


Figure 2.4.: A workflow showing a potential vincristine dose decision making strategy based on the trained SVC models. Blood samples of patients can be collected at day 8 and month 6 time points of the treatment. Samples can then be analyzed using mass spectrometry for metabolite profiling of the selected 2 and 21 metabolites at the day 8 and month 6 time points, respectively. The metabolite profile data can then be used to predict overall neuropathy susceptibility from the trained SVC models. If the model output probability is greater than a threshold value of 0.7, the patient might be susceptible to overall high neuropathy (HN). This strategy enables identification of patients susceptible to HN. The vincristine dose for HN patients may require adjustment.

In the foregoing suggested strategy, a significant caveat is that these models can only classify patients as susceptible to HN or LN. Some patients might be susceptible to “medium” VIPN (TNS \odot -PV greater than 3 but lesser than 8) during the treatment. Such cases have not been included here, implying that the models have limited predictability and that they should be used with caution. As a result, it is only suggested that if the output of the model is greater than 0.7 at both day 8 and month 6 predictions, then there may be a need to adjust vincristine dose, since such patients are most likely classified as HN.

Even though a list of metabolites using RFE (Supplementary Tables A.4, A.5, and A.6 in Appendix A) was finalized, all of them could not be identified. This greatly reduced the capability to find the biological relevance of these chosen metabolites.

MS/MS spectra could not be found for all of them, which may be a result of their presence in smaller quantities. Even after obtaining the MS/MS spectra, matches from existing databases could not be found for most of these metabolites. As a result, only the available m/z value, retention time, and adduct information for the remaining unidentified metabolites was used, which does not ensure that the metabolites were identified correctly. For a thorough identification, MS/MS spectra is needed for all of the chosen metabolites and subsequently the retention times of those compounds need to be validated using authentic standards. Since only a few metabolites could be identified and consequently used for pathway analysis, none of the associations between the metabolites and their pathways found were statistically significant. Even though some of the identified metabolites for the month 6 data belonged to pathways that are relevant to chemotherapy-induced peripheral neuropathy, their biological relevance could not be established with certainty.

The peak integration of chromatograms also needs to be interpreted with caution. It was observed that some peaks may not be integrated correctly or may simply be difficult to integrate for only a few metabolites. This has two implications: 1) The chosen metabolites may be predictive of neuropathy because they were improperly integrated. This possibility was eliminated by manually integrating and repeating RFE with a polished metabolite profile matrix. 2) Some potential biomarker metabolites might not have been chosen because of poor integration. It is not feasible to manually inspect every peak for every sample given that there were approximately 2000 metabolites and 104 samples (including all the time points), leaving a possibility that all potential predictors might not have been identified. Regardless, the current metabolites found at day 8 and month 6 are certainly potential predictors since they accurately predict VIPN susceptibility.

It should also be noted that the metabolite profile matrix is defined as high dimensional—with several metabolites and very few samples. This leaves a possibility that, despite using feature selection machine learning algorithms, some potential metabolites may have been overlooked. Moreover, the patient dataset does not have

balanced samples; having an equal number of high and low neuropathy patients will allow for a more accurate model. There is also lack of a test set to validate the model. It is critical to perform this study with more samples and additional datasets in order to test and validate the model. *VIPNp* [135, 136] can be used to test the trained models on new datasets in the future. There is also a need to include "medium" neuropathy patients to accurately predict multiple outcomes of the treatment. Since this is the first metabolomics based pilot study for VIPN, focus was only on HN and LN patients to explore the potential of this approach in predicting VIPN susceptibility. Lastly, it is assumed that these plasma samples are accurate representations of the metabolite profiles during the treatment. It needs to be noted that these samples were kept frozen in the biobank. For a more accurate analysis, newer samples need to be collected.

Another approach that can be taken is to perform a univariate analysis, keeping the patient characteristics as control variable. This analysis was performed for the data at every time point, keeping covariates age, gender, and BMI as control. 9 metabolites were found significant after p-value adjustment for multiple testing for day 8 data. Interestingly, 2 of them were the ones which were also identified as potential biomarkers for the day 8 data. However, none of the metabolites were significant for day 29 and month 6 data. See the Appendix A for details on the univariate analysis performed.

Despite these limitations, this preliminary study has shown that ALL treatment can alter the metabolite profiles, and a few selected metabolites can accurately predict the overall VIPN susceptibility. A strategy has also been provided (Figure 2.4) to adjust the vincristine dose based on VIPN susceptibility at two time points: day 8 and month 6. This work shows that metabolomics can aid in predicting VIPN susceptibility during the early stage of treatment. Although it must be admitted that the prediction of high and low neuropathy could have had a stronger statistical backing with a larger cohort of patients, it is contended that the numbers in this study were not so unreasonably small as to challenge this major conclusion. Based on an

exhaustive literature review, all previous studies have only focused on genomics and pharmacokinetics in the prediction of chemotherapy-induced peripheral neuropathy with the exception of one proteomics study [150]. This pilot study is the first of its kind focused on metabolomics to predict VIPN. In order for this methodology to be more effective, there is a need for a balanced and large number of fasting samples, accurate integration of chromatogram peaks, MS/MS spectra for all the chosen metabolites, and a more exhaustive database to identify these metabolites.

Peripheral neuropathy is not just limited to vincristine but is a dose-limiting toxicity of several other chemotherapy drugs (paclitaxel, taxane, and cisplatin), as well. A problem of this scale requires expertise and continued collaboration of individuals across multiple disciplines. An integrative approach involving better quantitation of all the omics data, large patient cohorts, careful phenotyping of patient data, and state of the art machine learning and statistical techniques is necessary in order to find a robust prediction of VIPN and any other chemotherapy-induced peripheral neuropathy, even before the start of the treatment.

The subsequent chapters of this thesis are focused on understanding pain sensation and the dynamics of a pain-sensing neuron, and the mechanism of chemotherapy-induced peripheral neuropathy.

2.4 Methods

2.4.1 ALL patient data collection [151]

Children with newly diagnosed precursor B-cell ALL were recruited from four academic medical centers: Indiana University School of Medicine/Riley Hospital for Children, the University of Michigan Comprehensive Cancer Center/Mott Childrens Hospital, Vanderbilt University Medical Center/Monroe Carell Jr. Childrens Hospital, and George Washington University/Childrens National Medical Center. Participants were between the ages of 1 and 18 at the time of diagnosis and received vincristine according to a Childrens Oncology Group (COG) treatment trial for acute

lymphoblastic leukemia. The standard vincristine dosage received was 1.5 mg/m² (capped at 2-mg maximum dose). Toxicity-based dose modifications were defined according to the specific COG protocol guiding the individual child's leukemia treatment. Patients were excluded if they had any of the following criteria: baseline peripheral neuropathy score greater than grade 1 per the NCI CTCAE©version 4.0; currently receiving erythropoietin, itraconazole, or vitamin supplement greater than 100% of the recommended daily allowance; Downs syndrome; pregnancy; or a history of co-existing serious illness that would limit neurological assessments. The protocol was reviewed and approved by the Institutional Review Boards at all four participating centers. All the methods were performed in accordance with the relevant guidelines and regulations. Informed consent was obtained from a parent and/or legal guardian for study participation.

2.4.2 Metabolomics sample preparation and extraction

Protein removal and sample extraction were performed by adding 200 μ L methanol to 100 μ L of plasma. Solutions were sonicated for 2 minutes, chilled at -20 °C for 1 hour, and centrifuged at 16,000 \times g for 8 minutes. The supernatants were transferred to separate vials and evaporated to dryness in a vacuum concentrator. The dried fractions were reconstituted in 75 μ L of diluent composed of 95% water and 5% acetonitrile, containing 0.1% formic acid. Solutions were sonicated for 5 minutes, centrifuged at 16,000 \times g for 8 minutes, and the supernatants were transferred to plastic HPLC total recovery autosampler vials.

2.4.3 HPLC-MS analysis of metabolomics samples [152]

Separations were performed on an Agilent 1290 system (Palo Alto, CA), with a mobile phase flow rate of 0.45 mL/min. The metabolites were assayed using a Waters HSS T3 UPLC column (1.8 μ m, 2.1 x 100 mm), where the mobile phase A and B were 0.1% formic acid in ddH₂O and acetonitrile, respectively. Initial conditions were

100:0 A:B, held for 1 minute, followed by a linear gradient to 70:30 at 16 min, then 5:95 at 21 min. Column re-equilibration was performed by returning to 100:0 A:B at 22 minutes and holding until 27 minutes. The mass analysis was obtained using an Agilent 6545 Q-TOF mass spectrometer with electrospray ionization (ESI) capillary voltage +3.2 kV, nitrogen gas temperature 325 °C, drying gas flow rate 8.0 L/min, nebulizer gas pressure 30 psig, fragmentor voltage 130 V, skimmer 45 V, and OCT RF 750 V. Mass data from m/z 70-1000 scans were collected at 5 Hz using Agilent MassHunter Acquisition software (v. B.06). Mass accuracy was improved by infusing Agilent Reference Mass Correction Solution (G1969-85001). To assist with compound identification, MS/MS was performed in a Data-dependent Acquisition mode. Five precursors per cycle were obtained using fixed collision energies of 10, 20, and 40 eV.

Peak deconvolution, integration, and alignment was performed using Agilent ProFinder (v. B.06). Peak annotations were performed using the METLIN (www.metlin.scripps.edu) and HMDB (www.hmdb.ca) metabolite databases, with a mass error of less than 15 ppm.

2.4.4 Vincristine quantitation [153]

Sample preparation 100 μ L plasma was pipetted to a microcentrifuge tube. Protein precipitation was performed by adding 200 μ L cold methanol. The mixture was vortexed for 2 minutes, chilled at -20 °C for 1 hour, and then centrifuged at 13,000 g for 8 minutes. Supernatant was transferred to a fresh microcentrifuge tube and vacuum concentrated to dryness. Reconstituted in 75 μ L of diluent (95% water and 5% acetonitrile, with 0.1% formic acid), sonicated for 5 minutes, centrifuged at 13,000 rpm for 8 minutes, and supernatant was transferred to HPLC vials.

HPLC/MS-MS analysis Vincristine plasma levels were quantitated by HPLC/MS-MS. Separation was performed on an Agilent Rapid Res 1200 HPLC system using an Agilent Zorbax XDB-C18 (2.1 \times 50 mm, 3.5 μ m) column. Mobile phase A was water with 0.1% formic acid and mobile phase B was acetonitrile with 0.1% formic acid.

Initial conditions were 95:5 A:B, held for 0.5 minute, followed by a linear gradient to 0:100 at 8 min, and held until 10 min. Column re-equilibration was performed by returning to 95:5 A:B at 11 minutes and held until 15 minutes. Column flow rate was 0.3 mL/min. Retention time for vincristine was 5.9 minutes.

Analytes were quantified by MS/MS utilizing an Agilent 6460 triple quadrupole mass spectrometer with electrospray ionization (ESI). Quantitation was based on Multiple Reaction Monitoring (MRM). ESI positive mode was used with a transition of 825.2 to 807.7 (quantifier) and 825.2 to 765.3 (qualifier), with a collision energy (CE) of 45 and 40 V, respectively. A fragmentor energy of 135 V and a dwell time of 80 ms was used. Source parameters were as follows: nitrogen gas temperature = 330 °C and flow rate = 10 L/min, nebulizer pressure = 35 psi, sheath gas temperature = 250 °C, sheath gas flow rate = 7 L/min, and capillary potential = 3.5 kV. All the data were collected and analyzed with Agilent MassHunter B.03 software. Quantitation was based on a 6 point standard curve, with concentration range from 0.1 to 500 ng/mL, by spiking vincristine into unmedicated human plasma (Sigma). Standard curves were fit to a quadratic function, with a 1/x curve fit weighting. Correlation coefficients > 0.99 were obtained.

2.4.5 Metabolite profiling data analysis

Data analysis was performed in R [154]. First, metabolites that were not present in at least 75% of the patients in at least one group were discarded. Subsequently, missing data imputation was performed using a modified k-nearest neighbours (KNN) imputation as specified in [155]. Impute package in R was used to perform the KNN imputation [156]. Hierarchical clustering was performed using hclust, with ward.D2 as the method and Euclidean distance as the metric. For metabolite selection, recursive feature elimination (RFE) along with repeated 5-fold cross validation support vector classifier was used. Repetition was done 20 times. This was further iterated 100 times and the model was chosen based on highest AUROC and lowest specificity standard deviation. For recursive feature elimination, all sizes of number of predic-

tors between 1 to 50 were allowed. Caret [157] package from R was used for this. The method specified in caret for this algorithm is svmLinear2, from the package e1071 [158]. Tunelength was kept as 1 and hence the cost parameter was fixed to 0.25. SVM with linear kernel was chosen because more tuned parameters would be needed for nonlinear kernels. Since our dataset had few samples, that may have lead to overfitting. Final model fitting results specified in Table 2.2 were based on resampling from bootstrapping 25 times, using the selected number of predictors. This was the default model fitting mode in caret while performing RFE.

For model training after finalizing the set of metabolites, 5-fold repeated cross validation was used, repeated 20 times. The metric for accuracy was kept as AUROC. Here, tuneLength was kept as 10. Cost function of the SVM model was tuned using this. After model training, for deciding the probability threshold, thresholds between 0.5 and 1 were explored. The one corresponding to minimum distance from perfect sensitivity and specificity (i.e. both of them equal to 1) was chosen. Subsequently, confusion matrix and its metrics were generated using caret package's confusion matrix generator.

Please see Appendix A for extra details of the work presented in this chapter.

3. USING BIFURCATION THEORY FOR EXPLORING PAIN

This work is published in Industrial & Engineering Chemistry Research [159]

Pain is a common sensation which inescapably arises due to injuries, as well as, various diseases and disorders. However, for the same intensity of disturbance arising due to the foregoing causes, the threshold for pain sensation and perception varies among individuals. Here, a computational approach using bifurcation theory is presented to understand how the pain sensation threshold varies and how it can be controlled, the threshold being quantified by the electrical activity of a pain-sensing neuron. To this end, the bifurcations arising from a mathematical model representing the dynamics of this neuron are explored. The findings in this chapter indicate that the bifurcation points are sensitive to specific model parameters. This demonstrates that the pain sensation threshold can change as shown in experimental studies found in literature. Further investigation using this bifurcation approach coupled with experimental studies can facilitate rigorous understanding of pain response mechanism and provide strategies to control the pain sensation threshold.

3.1 Introduction

Nonlinear dynamics has been an integral element of the methodology of process control. Traditionally, nonlinear dynamics and bifurcation theory have had many practical applications in chemical engineering involving dynamics and stability in chemically reacting systems [160], in particular, dynamics and control of polymerization reactions [161] including multiple steady states and oscillatory behavior, pattern formation on catalytic surfaces [162], multiple steady states in nonreactive [163, 164] and reactive distillation processes [165], nonlinear oscillations in population balance systems including continuous crystallization [166, 167] and fluidized bed gran-

ulation [168–170], electrochemical processes including fuel cell systems [171], and bioreactors [172–174], among others. A model based analysis aims at understanding particular nonlinear phenomena, and it often builds the basis to design and control the processes so that they behave in a desired way. A constructive approach for the latter has been proposed by Marquardt and Mönnigmann [175]. In the last few decades, however, the implications of nonlinear phenomena have expanded to even areas of translational significance with a potential for impact on health sciences. In this regard, as a reflection of this development, an example is cited here, Christini et al. [176] who deliberated on the role of nonlinear dynamics in cardiac arrhythmia control. Likewise, the field of neuronal dynamics has been under active study through the noted Hodgkin-Huxley equations [177], which were developed more than 60 years ago. The objective in this chapter is to address this latter area in a direction that has high therapeutic significance for alleviating pain which invariably accompanies any form of injury and of various diseases. As pain is the body's mechanism of protection from external danger, it must be regarded as inevitable. However, the threshold for pain can vary across individuals. In this work, how this threshold can be controlled using bifurcation theory is investigated.

The domain of pain and its level of intensity are inherently subjective in nature. The subjectivity of pain is in regard to its perception by a given individual; however, its reality is dependent on an objective external perturbation. This chapter views pain as the consequence of a certain type of response by a neuron to an electrical perturbation for which there is much support in the literature [178]. The electrical perturbation is the result of an external stimulus, e.g. touch, which can excite the neuron. The response to the electrical perturbation is known to be governed by several electrical and biochemical factors. The Hodgkin-Huxley equations account for many of the electrical factors. These equations have the means to understand the generation of electrical signal in a neuron which is called an action potential. The temporal pattern of action potentials carries information that is ultimately transmitted to the brain, where it can be perceived as pain. The voltage-gated ion channels located

in a neuron cell membrane play a significant role in the generation of these action potentials. This work will examine the role of specific sodium and potassium voltage-gated ion channels as potential contributors to the generation of pain. The aim of this chapter is to promote the general exploration of pain using bifurcation theory by providing its application to a relatively simple scenario for pain mechanism.

Through this approach, one can identify parameters that can alter the pain sensation threshold. The results of this approach can be used to aid in designing experiments and subsequently exploring therapeutic strategies to control the threshold. In this chapter, the following are addressed: i) biological mechanism of pain sensation, ii) mathematical model representing dynamics of a pain-sensing neuron, iii) bifurcation analysis of the model equations, iv) identification of sensitive parameters in setting pain sensation threshold, and v) discussion of results with implications for a cure. This chapter is intended for engineers new to computational neuroscience, the details of which can be found in books by Izhikevich, Keener, Dayan, Jaeger, Ermentrout, Schutter and Johnston [179–185].

3.2 The Neuroscience of Pain Sensation

Neuron signal transmission occurs when it becomes excitable due to an adequate electrical perturbation and consequently generates action potentials. An action potential is a brief peak in potential dynamics observed across a neuronal membrane. The temporal pattern (consisting of frequency and duration) and source of action potential generation determine the message being transmitted. A schematic of an action potential is shown in Figure 3.1. Action potential transmission occurs within a neuron across the length of the axon and subsequently in between two neurons via their synapses. The action potential is generated due to opening and closing of voltage-gated ion channels on a neuronal membrane. The neuronal membrane consists of a lipid bilayer, and the voltage-gated ion channels are transmembrane proteins with pores that are selectively permeable to specific ions (e.g. sodium, potassium, calcium, or chloride). These ions have their respective equilibrium potentials. Sodium has a

positive while potassium has a negative equilibrium potential. The resting membrane potential of a neuron is negative. These channels are shown in Figure 3.2.

When an external stimulus is applied, sodium channels get activated and open up. This leads to a flux of sodium ions across the membrane into the neuron, raising the membrane potential towards the positive equilibrium potential of sodium. This inflow continues until it reaches a threshold which corresponds to a peak in the action potential. While reaching the peak, sodium channels start to inactivate by closing while potassium channels activate and open. Activation of potassium channels lead to an inflow of potassium ions, lowering the membrane potential towards the negative equilibrium potential of potassium. Subsequently, most of the channels close, reaching a steady state and bringing the membrane potential back to the resting membrane potential. These series of events correspond to the generation of one action potential. The timing associated with opening or closing of these channels is a function of time constants of activation and inactivation. Sodium activation has a smaller time constant and as a result activates first. Sodium inactivation and potassium activation have relatively larger time constants resulting in a time lag. This interplay of fast and slow dynamics leads to the generation of an action potential.

A stimulus can either be an interim, pulse-like disturbance in which case the membrane potential will return to the same rest point, as shown in Figure 3.1. Or, it can be a permanent disturbance in which case the membrane potential will return to a new rest point which is discussed in the next section. In both the cases, action potentials are only fired if the stimulus exceeds a threshold value.

Hodgkin and Huxley were the first researchers to develop a mathematical model describing action potential generation via interplay of one sodium and one potassium channel. They developed this model for a squid giant axon. Since then, Hodgkin-Huxley type models have been developed for several other neurons, incorporating multiple channels. In this chapter, focus is on a Hodgkin-Huxley type model representing dynamics of a pain-sensing neuron.

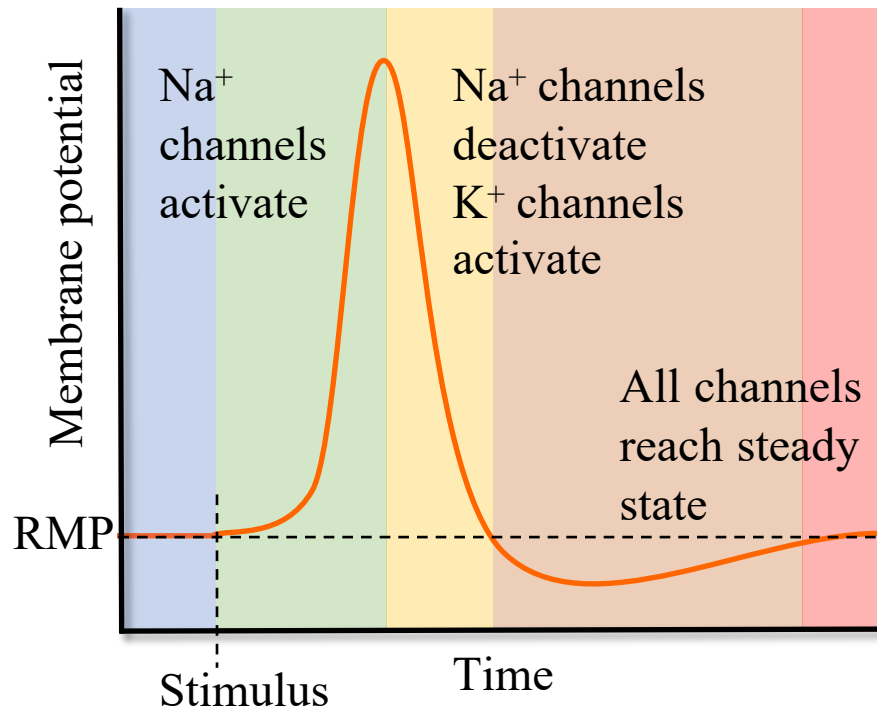


Figure 3.1.: A schematic of an action potential. When a stimulus is applied, an action potential is generated due to activation of sodium channels leading to the rise in membrane potential. Following this rise, sodium channels inactivate and potassium channels activate, leading to a decrease in the potential. Finally, all channels attain steady states and the membrane reverts back to the resting membrane potential (RMP).

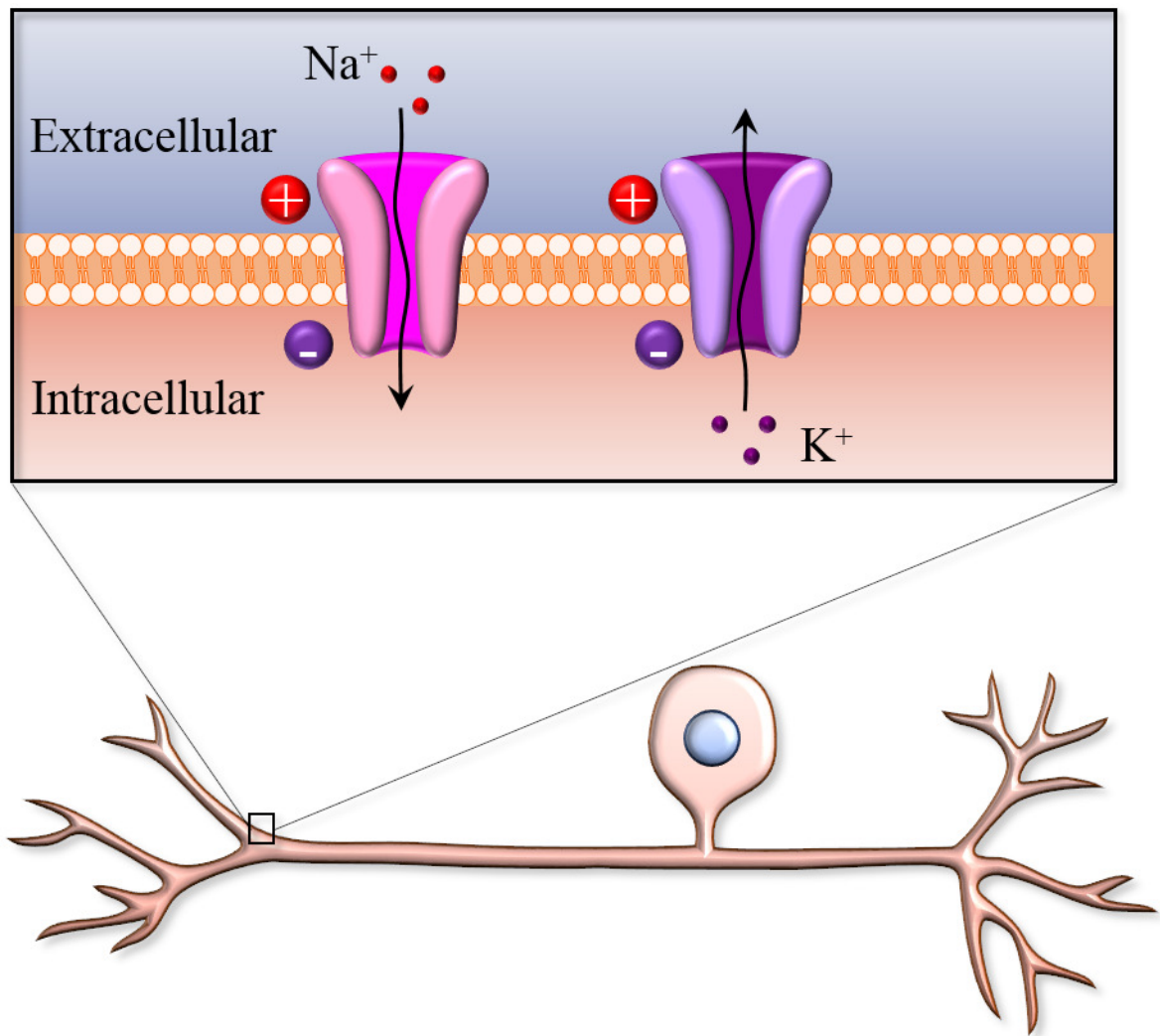


Figure 3.2.: A schematic of a neuronal membrane. The membrane consists of a lipid bilayer. The voltage-gated sodium and potassium channels are transmembrane pores. The extracellular concentration of sodium is greater, leading to an inflow of sodium ions when the channel opens. The intracellular concentration of potassium is greater, leading to an outflow of potassium ions when the channel opens.

3.3 Mathematical Model of a Pain-Sensing Neuron

Here, a model representing dynamics of a small DRG neuron is described. As previously mentioned, the model equations are of Hodgkin-Huxley type. There are multiple types of ion channels present in the human nervous system. For every ion type, a variation of channel subtypes exist, each having different kinetic properties. For this model, two sodium channels: $\text{Na}_v1.7$ and $\text{Na}_v1.8$, and two potassium channels: delayed-rectifier potassium channel (K channel) and A-type transient potassium channel (KA channel), are included. $\text{Na}_v1.7$ and $\text{Na}_v1.8$ are simply two types of sodium channels with different kinetic properties, but both consist of fast activating and slow inactivating gating variables. The K channel is a Hodgkin-Huxley type potassium channel with only one activating gate variable which is activated later than the sodium channels. The KA channel has both activating and inactivating gating variables, similar to sodium channels. Further, a non-gated leak channel is included, as was done for the original Hodgkin-Huxley models. These specific channels were chosen since they are most prominent in a small DRG neuron membrane, and, therefore, models consisting only of these channels have been developed and analyzed previously [186, 187].

The aforementioned components of the neuronal membrane can be represented as an electrical circuit, as shown in Figure 3.3. The membrane is assumed to have a specific capacitance c ($= C/A$, C being the membrane capacitance and A the membrane surface area) with some potential V ($= V_{in} - V_{out}$) across it. Traditionally, the extracellular potential is assigned as zero which then defines the intracellular resting potential as negative. $I_{ext}(t)$, where t is time, is the external stimulus current. The direction of this current is opposite to the direction of current due to the ion channels. As shown in the figure, the sodium and potassium channels have variable conductance, while the leak channel has a constant conductance, implying it is non-gated. The equilibrium potential of the leak channel is negative as well, in order to bring the membrane potential back to the negative resting membrane potential. The

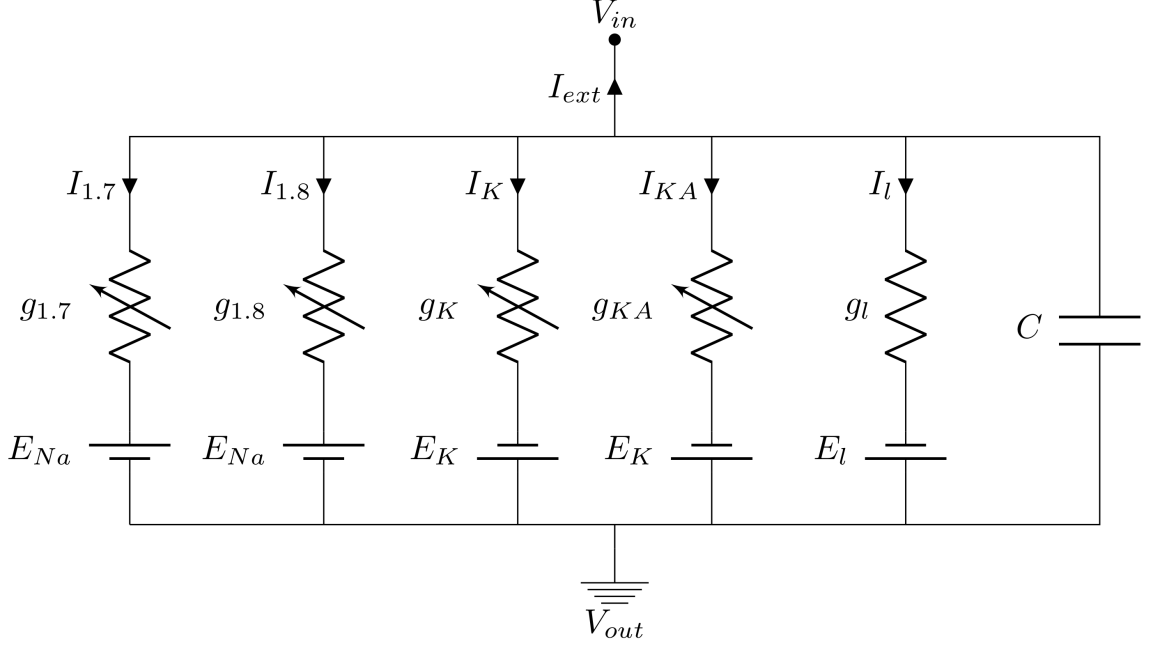


Figure 3.3.: Circuit diagram representing neuron membrane. V_{in} : intracellular potential; V_{out} : extracellular potential; $I_{1.7}, I_{1.8}, I_K, I_{KA}, I_l$: current due to $\text{Na}_v1.7$, $\text{Na}_v1.8$, delayed rectifier potassium, A-type transient potassium and leak channels respectively; I_{ext} : external stimulus current; $g_{1.7}, g_{1.8}, g_K, g_{KA}, g_l$: conductance of $\text{Na}_v1.7$, $\text{Na}_v1.8$, delayed rectifier potassium, A-type transient potassium and leak channels respectively; E_{Na}, E_K, E_l : equilibrium sodium, potassium and leak potentials respectively, C : membrane capacitance.

variable conductance are functions of the membrane potential, described by Hodgkin-Huxley type equations.

Using Kirchhoff's law, the equation for potential dynamics can be written as the following:

$$c \frac{dV}{dt} = \frac{I_{ext}(t)}{A} - (i_{1.7} + i_{1.8} + i_K + i_{KA} + i_l) \quad (3.1)$$

The individual specific ionic currents are defined as following:

1. $i_{1.7} = \bar{g}_{1.7} m_{1.7}^3 h_{1.7} s_{1.7} (V - E_{Na})$
2. $i_{1.8} = \bar{g}_{1.8} m_{1.8} h_{1.8} (V - E_{Na})$

3. $i_K = \bar{g}_K n_K (V - E_K)$
4. $i_{KA} = \bar{g}_{KA} n_{KA} h_{KA} (V - E_K)$
5. $i_l = \bar{g}_l (V - E_l)$

Here, $\bar{g}_{1.7}$, $\bar{g}_{1.8}$, \bar{g}_K , \bar{g}_{KA} , \bar{g}_l are the maximal specific conductance, taken as constants. The gating variables $m_{1.7}$, $h_{1.7}$, $s_{1.7}$, $m_{1.8}$, $h_{1.8}$, n_K , n_{KA} , h_{KA} lie between 0 and 1, and are functions of V . E_{Na} , E_K and E_l are ion equilibrium potentials. The final equation for membrane potential is the following:

$$\begin{aligned} c \frac{dV}{dt} = \frac{I_{ext}(t)}{A} - & (\bar{g}_{1.7} m_{1.7}^3 h_{1.7} s_{1.7} (V - E_{Na}) + \bar{g}_{1.8} m_{1.8} h_{1.8} (V - E_{Na}) \\ & + \bar{g}_K n_K (V - E_K) + \bar{g}_{KA} n_{KA} h_{KA} (V - E_K) \\ & + \bar{g}_l (V - E_l)) \end{aligned}$$

The gating variables correspond to fractions of ion channels that are open. Suppose x is a gating variable, where $x = m_{1.7}$, $h_{1.7}$, $s_{1.7}$, $m_{1.8}$, $h_{1.8}$, n_K , n_{KA} , h_{KA} . Then, the equation for x is written as:

$$\frac{dx}{dt} = \alpha_x(V)(1 - x) - \beta_x(V)x, \quad (3.2)$$

where, $\alpha_x(V)$ is the rate of opening of gate x and $\beta_x(V)$ is the rate of closing. On rearranging this equation, the following equation is obtained:

$$\frac{dx}{dt} = \frac{x_\infty(V) - x}{\tau_x(V)}, \quad (3.3)$$

where, $x_\infty(V) = \frac{\alpha_x(V)}{\alpha_x(V) + \beta_x(V)}$ and $\tau_x(V) = \frac{1}{\alpha_x(V) + \beta_x(V)}$. $\tau_x(V)$ is the potential-dependent time constant. Typically, $\alpha_x(V)$ and $\beta_x(V)$ are assumed to be of the following form:

$$k_1 + \frac{k_2}{1 + \exp\left(\frac{V + k_3}{k_4}\right)}, \quad (3.4)$$

where, for each x , the corresponding k_1 to k_4 are constants. In total, this model consists of 9 ordinary differential equations.

When $I_{ext} = 0$, the resting membrane potential of this system will be the following, by setting all the derivatives to zero:

$$\frac{(\bar{g}_{1.7}m_{1.7\infty}^3 h_{1.7\infty} s_{1.7\infty} + \bar{g}_{1.8}m_{1.8\infty} h_{1.8\infty})E_{Na} + (\bar{g}_K n_{K\infty} + \bar{g}_{KA} n_{KA\infty} h_{KA\infty})E_K + \bar{g}_l E_l}{\bar{g}_{1.7}m_{1.7\infty}^3 h_{1.7\infty} s_{1.7\infty} + \bar{g}_{1.8}m_{1.8\infty} h_{1.8\infty} + \bar{g}_K n_{K\infty} + \bar{g}_{KA} n_{KA\infty} h_{KA\infty} + \bar{g}_l} \quad (3.5)$$

Leak current kinetics, area, membrane capacitance, and equilibrium potential values for a small DRG neuron were extracted from [187]. Maximal specific conductances \bar{g}_K and \bar{g}_{KA} were estimated to ensure that their corresponding currents were 6 nA and 1 nA at 0 mV when the cell is initially depolarized to -120 mV, and $\bar{g}_{1.7}$ was set to 18 mS/cm², based on [187]. $\bar{g}_{1.8}$ was set to 7 mS/cm², which led to the generation of one action potential (current threshold) at 100 pA when the neuron is at the resting membrane potential (RMP), which is determined by simulating the model for $I_{ext} = 0$ pA. The current threshold of 100 pA was chosen based on approximate values from previous experiments and simulations [186, 188]. The parameter values of this model and the equations can be found in appendix B. These parameter values result in an RMP of -66.48 mV which belongs to the physiological range of RMP recorded in small DRG neurons in [189], and the resulting action potential amplitude (approximately 120 mV) is comparable to that reported in [190]. Typically, channel kinetics (values of k_1, k_2, k_3, k_4) are obtained from voltage-clamp experiments. In these experiments, the potential across a neuron is fixed and then it is stepped to a different value, and the corresponding current pattern evolution is observed. This data is fit to the model equations to determine the constants. k_1 corresponds to offset, k_2 to amplitude, k_3 to $V_{1/2}$ (voltage for half-maximal activation) and k_4 to slope in the variable versus voltage plot. The details of voltage-clamp experiments and subsequent parameter estimation are not described here here, but the seminal paper by Hodgkin and Huxley for details on how the original equations were obtained [177], and the book by Johnston and Wu for more details on the neurophysiology [185] are recommended. Throughout this thesis, the units of potential are mV, specific capacitance mS/cm², current pA, and time ms.

$m_{1.7}$ and $m_{1.8}$ are fast activation variables of sodium, $h_{1.7}$ and $h_{1.8}$ are slow inactivation variables of sodium, and $s_{1.7}$ is ultra-slow inactivation of sodium 1.7 channel. n_K and n_{KA} are activation variables of potassium channels and h_{KA} is inactivation variable of KA channel. The gating variables n_K and n_{KA} are slower than those of sodium channels, which ensures the descent after the peak in the action potential. This is discussed below by comparing Figure 3.4C-F and by evaluating approximate time scale of evolution of these variables in the supplementary document.

Upon simulating the system with a constant external current source of 100 pA (starting from $t = 0$ ms), an action potential is generated, shown in Figure 3.4A. The initial conditions here correspond to those for $I_{ext} = 0$. At around 5 ms, membrane potential begins to shoot up drastically. At this time, as shown in Figure 3.4B, the state variables $m_{1.7}$ and $m_{1.8}$ begin to increase. Simultaneously, $h_{1.7}$ and $h_{1.8}$ start decreasing and remain low in the region between around 7-12 ms, corresponding to the relatively flat region in the descent of the action potential. During the descent, both n_K and n_{KA} increase, corresponding to opening of potassium channels. The temporal pattern of h_{KA} is similar to $h_{1.7}$ and $h_{1.8}$. $s_{1.7}$ remains relatively constant in this time frame. Eventually, these state variables reach steady state values, and the updated resting membrane potential, for a given external input (in the form of a step function), is the following:

$$\frac{I_{ext}/A + (\bar{g}_{1.7}m_{1.7\infty}^3 h_{1.7\infty} s_{1.7\infty} + \bar{g}_{1.8}m_{1.8\infty} h_{1.8\infty})E_{Na} + (\bar{g}_K n_{K\infty} + \bar{g}_{KA} n_{KA\infty} h_{KA\infty})E_K + \bar{g}_l E_l}{\bar{g}_{1.7}m_{1.7\infty}^3 h_{1.7\infty} s_{1.7\infty} + \bar{g}_{1.8}m_{1.8\infty} h_{1.8\infty} + \bar{g}_K n_{K\infty} + \bar{g}_{KA} n_{KA\infty} h_{KA\infty} + \bar{g}_l} \quad (3.6)$$

The temporal pattern of the potential-dependent time constants are shown in Figure 3.4C-F. $m_{1.7}$ and $m_{1.8}$ have relatively smaller time constants, implying faster kinetics as seen in Figure 3.4B, ensuring activation of sodium channels first. The remaining time constants for n_{KA} , h_{KA} , $h_{1.7}$, $h_{1.8}$ are larger, implying slow activation of the KA channel and slower inactivation of KA and both the sodium channels. The K channel inactivates even slower, as seen in Figure 3.4F by the magnitude of its time constant. $s_{1.7}$ is the slowest with time constant larger than all other variables,

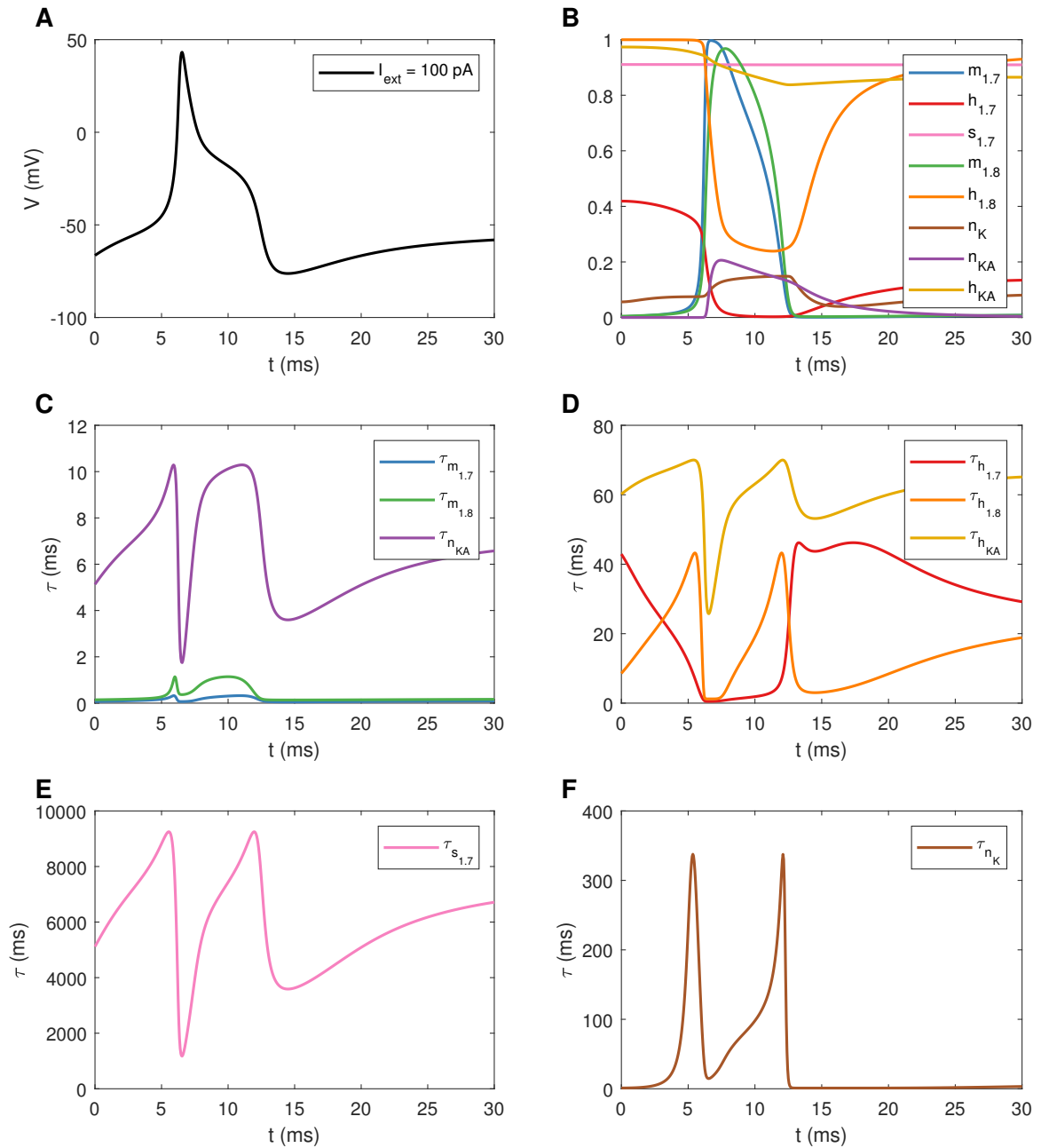


Figure 3.4.: A: Action potential generated due to a constant external current $I_{ext} = 100$ pA, B: Dynamics of activation and inactivation state variables, C-F: Dynamics of potential-dependent time constants for the state variables.

leading to ultra-slow inactivation of $Na_v1.7$ channel. Therefore, $s_{1.7}$ remains relatively constant as shown in Figure 3.4B.

Periodic firing of action potentials by this neuron is associated with pain of some degree. Moreover, pain increases with the frequency of firing [191, 192]. In order to understand the onset of periodic firing (indicating the onset of pain), bifurcation theory is applied to this model, using I_{ext} , E_{Na} , and E_K as the primary bifurcation parameters. In this section, some dynamic simulations are demonstrated to show how the system dynamics vary upon changing these parameters. First, I_{ext} was varied, assuming it to be a time-independent step function. As shown in Figure 3.5A, for a small value of I_{ext} , one action potential is produced after which the system approaches a steady state. Upon increasing I_{ext} , the system displayed various types of mixed-mode oscillations (MMOs) consisting of small amplitude oscillations around the lowest unstable steady state solution (see Figure 3.8) and full-blown action potentials, as shown in Figure 3.5B. For specific values of I_{ext} , more complicated attractors were observed which will not be investigated here. They are investigated in the next chapter. Upon further increasing I_{ext} , the system displayed periodic firing of action potentials (Figure 3.5C), indicative of pain of higher intensity as compared to that in Figure 3.5B. In general, dynamical simulations suggest that the average frequency of the large amplitude oscillations is increasing with I_{ext} (corresponding to increase in pain intensity). The bottom sub-figures show phase portraits with three state variables: V , n_K and h_{KA} . For Figure 3.5A, since there are no oscillations, a closed curve is not formed in the phase portrait. The phase portrait in Figure 3.5B consists of a closed curve with extra smaller loops to take into account the small amplitude oscillations. The phase portrait in Figure 3.5C is a single closed curve corresponding to the large amplitude oscillations of action potentials.

Similar dynamical patterns are observed upon varying E_{Na} and E_K . For smaller values of E_{Na} , a single action potential is generated, as shown in Figure 3.6A. Increasing E_{Na} leads to MMO and then periodic firing, as shown in Figure 3.6B and Figure 3.6C respectively. A similar pattern is observed in the case of E_K , as shown in Figure 3.7. The phase portraits look similar as well.

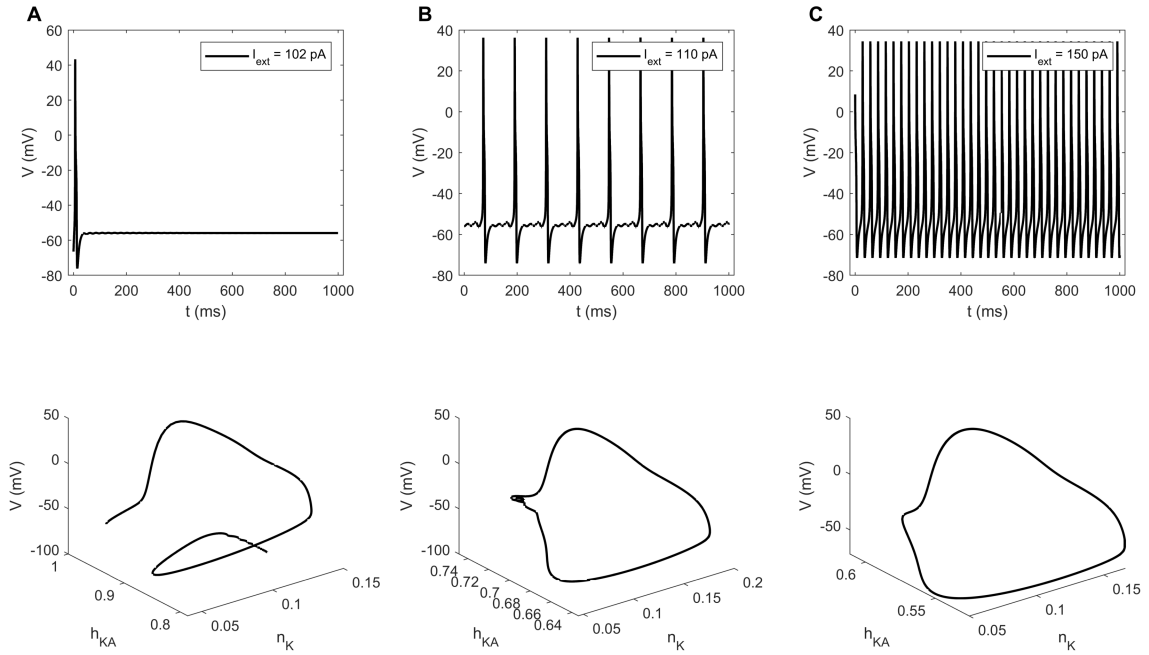


Figure 3.5.: Dynamic simulations for A: $I_{ext} = 102$ pA, B: $I_{ext} = 110$ pA, C: $I_{ext} = 150$ pA

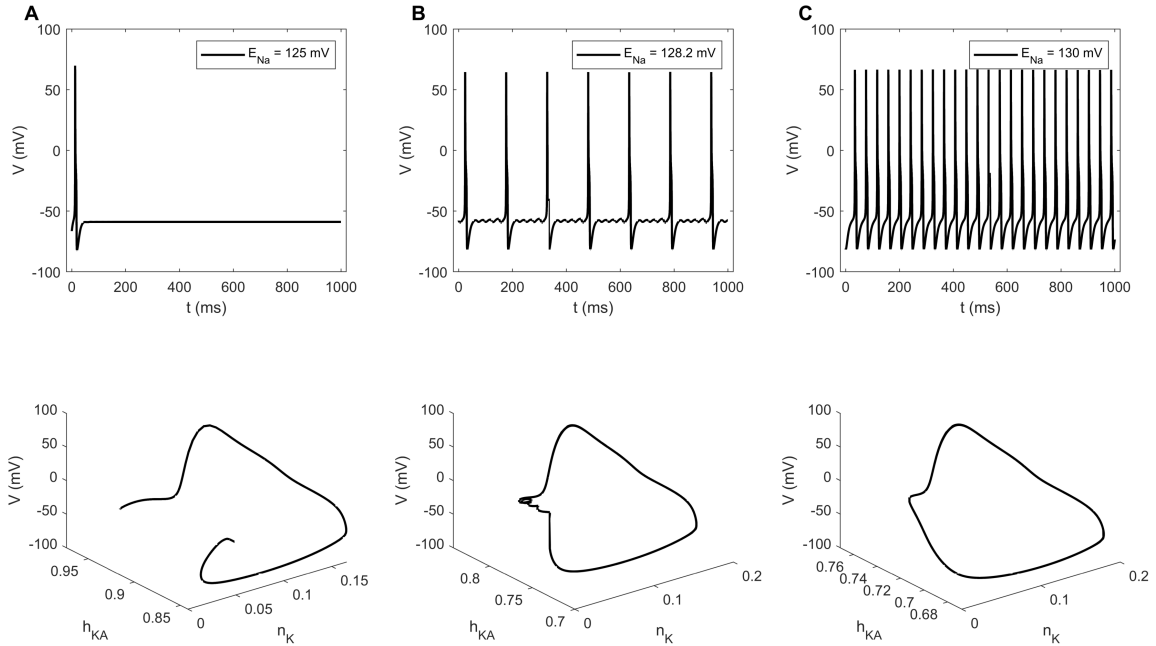


Figure 3.6.: Dynamic simulations for A: $E_{Na} = 125$ mV, B: $E_{Na} = 128.2$ mV, C: $E_{Na} = 130$ mV

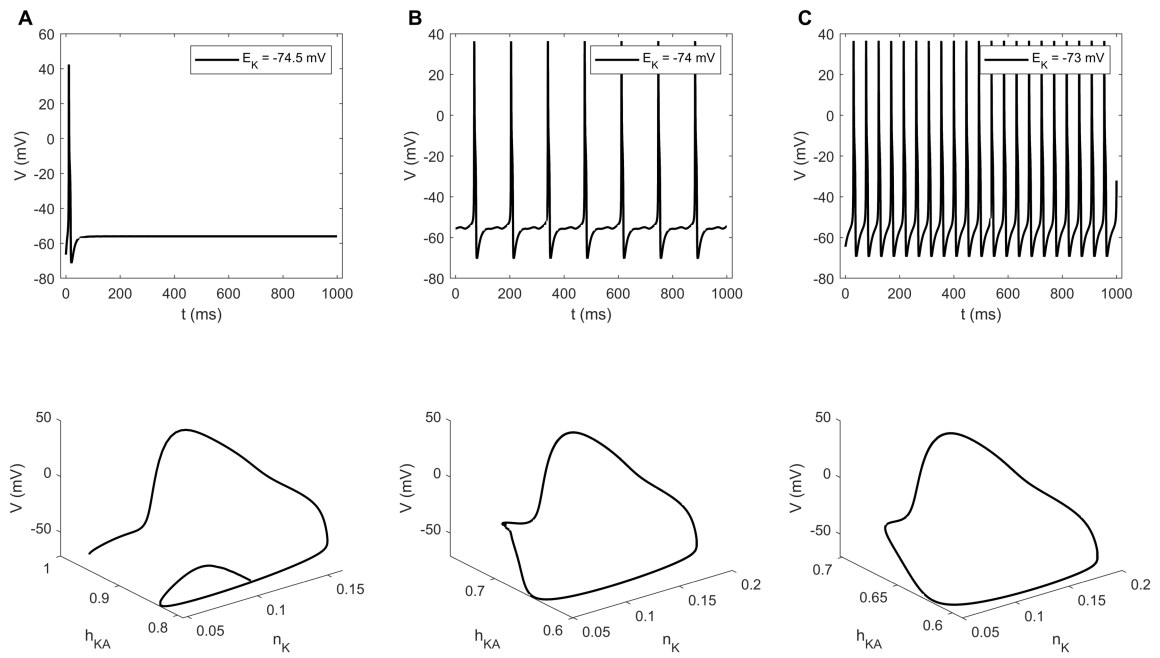


Figure 3.7.: Dynamic simulations for A: $E_K = -74.5$ mV, B: $E_K = -74$ mV, C: $E_K = -73$ mV

3.4 Influence of external current I_{ext}

First, a one-parameter continuation of solutions was performed with I_{ext} as the primary bifurcation parameter, using XPPAUT [193]. I_{ext} is assumed to be time independent. The partial bifurcation diagram is shown in Figure 3.8. First, a continuation of steady state solutions was done starting from a stable steady state at the left of Figure 3.8. The red branch of stable steady state solutions loses its stability at a subcritical Hopf bifurcation point (HB in Figure 3.8 at around $I_{ext} = 103$ pA) and undergoes subsequent hysteresis with two limit points (LP in Figure 3.8) leading to a multiplicity of unstable steady state solutions in between (in black). At the HB point, a branch of stable steady states coalesces with a branch of unstable period solutions (in blue), with the blue branch undergoing a cyclic limit point (CLP in Figure 3.8) at its turning point. Starting at the HB point, the blue periodic branch has two unstable directions, and beyond the CLP, it has either one or three unstable directions due to one real characteristic value passing through zero. At the end of this branch, the period increases massively. It is, therefore, conjectured that this branch ends in a period-infinity solution.

Furthermore, there is a branch of stable large amplitude oscillations indicated by the green circles in Figure 3.8, which corresponds to the periodic firing of action potentials as illustrated in Figure 3.5C. The branch of large amplitude oscillations becomes unstable at a CLP (Figure 3.8 at around $I_{ext} = 117$ pA) and ends shortly after a period-infinity solution. Between the HB point and this CLP, MMOs (Figure 3.5B) are observed as well as more complicated patterns of behavior associated with these types of MMOs. Bifurcations and solution branches corresponding to the MMOs region are currently under investigation and are, therefore, not shown in Figure 3.8.

In this chapter, the focus is on how these detected bifurcation points are helpful in understanding the pain sensation. The bifurcation points separate the “no-pain” (stable steady state) region from the “painful” (oscillation of action potentials) region, where the intensity of pain increases upon increasing I_{ext} since it is determined by the

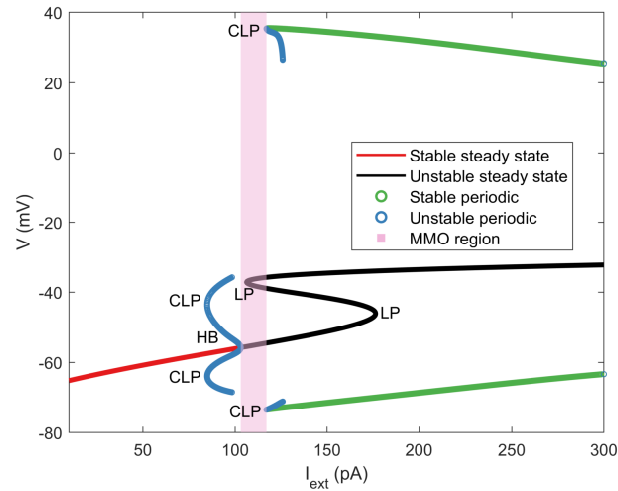


Figure 3.8.: Partial bifurcation diagram with I_{ext} as the bifurcation parameter. HB: Subcritical Hopf bifurcation point (at $I_{ext} = 102.99$ pA), LP: Limit point, CLP: Cyclic limit point (at $I_{ext} = 116.98$ pA for the stable periodic branch).

frequency of firing of action potentials. Hence, understanding how these bifurcation points can shift can indicate how the pain threshold changes, due to factors such as external injury or genetic mutations. In order to explore this, focus is on the following bifurcation points: HB point, LP on the unstable steady state branch, and CLP of the stable periodic branch. Two-parameter continuations of these points was performed to demonstrate how they shift on changing specific model parameters, possibly shifting the pain sensation threshold.

Further, the focus is on finding specific kinetic parameters in sodium channels that can shift the bifurcation points. This is because several mutations in sodium channels have been found to be associated with loss or gain of pain sensation [194–196]. Most of the previous work in this field is based on experiments and computational modeling. There is limited literature on use of bifurcation theory to understand the role of pain sensation [94, 197, 198]. Here, an approach using bifurcation theory is presented to examine some of these mutations.

3.4.1 Na_v1.7 Channel Mutations

Na_v1.7 is a widely studied channel and a myriad of mutations in Na_v1.7 have been found to be associated with gain or loss of pain sensation [199]. Gain of pain sensation implies that the pain sensation threshold is relatively lower, while individuals with loss of pain sensation might not feel any pain even after severe injury. Such a mutation was identified in specific individuals who had never experienced pain [200]. The gain of pain sensation case is associated with discomfort even without being in a dangerous scenario. The loss of pain sensation is associated with multiple severe injuries with little to no reaction. In both cases, the pain sensation threshold no longer meets the physiological requirements. In order to understand how the pain threshold can change due to mutations in Na_v1.7, specific parameters in the activation variable $m_{1.7}$ are varied. The kinetics of $m_{1.7}$ is described by $\alpha_{m_{1.7}}(V)$ and $\beta_{m_{1.7}}(V)$, which are written in the form of Eq. (3.4). To investigate mutation in kinetics of $m_{1.7}$, k_3 was varied by introducing a dummy variable v_0 , first in the equation for $\alpha_{m_{1.7}}(V)$, such that it becomes:

$$k_1 + \frac{k_2}{1 + \exp\left(\frac{V + k_3 + v_0}{k_4}\right)}, \quad (3.7)$$

Then, a two-parameter continuation of bifurcation points is performed with v_0 and I_{ext} , shown in Figure 3.9A. Similarly, mutation in $\beta_{m_{1.7}}(V)$ kinetics is investigated, by introducing the dummy variable exclusively in its kinetics. Again, two-parameter continuation is performed with v_0 and I_{ext} , shown in Figure 3.9B. For both the cases, it can be seen that the bifurcation points shift to the left upon increasing v_0 . This leads to a lower bifurcation point, implying the neuron will start periodic firing of action potentials with a lesser stimulus. This would lead to a decrease in the threshold for pain sensation.

Increasing v_0 shifts the steady state activation variable ($m_{1.7\infty}^3$) versus potential plot to the left, as shown in Figure 3.10. Figure 3.10 is a plot of activation variable versus potential during the ascent of the action potential. Association between the leftward shift of the steady state activation variable and the gain of pain sensation has

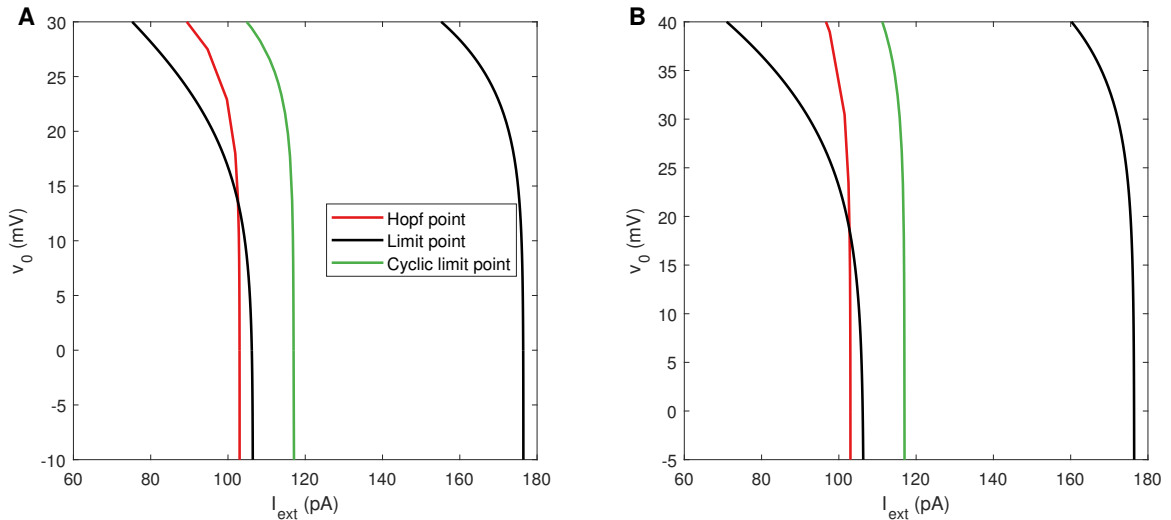


Figure 3.9.: Two parameter continuation for v_0 in A: $\alpha_{m_{1.7}}(V)$ and B: $\beta_{m_{1.7}}(V)$. The plot shows how the bifurcation points vary upon changing v_0 . An approximately 300% increase or more in k_3 of $\alpha_{m_{1.7}}(V)$ and a 28% increase or more in k_3 of $\beta_{m_{1.7}}(V)$ shifts the bifurcation points.

been seen in several experiments, where mutations in $\text{Na}_v1.7$ such as I848T, L858H, F1449V, F216S, A863P, N395K, G856R, and L858F led to chronic pain associated with a burning sensation in individuals [186, 201–206]. Thus, these results are in concordance with existing experimental findings. Focus was only on k_3 instead of k_1 , k_2 , and k_4 because k_3 corresponds to $V_{1/2}$; varying k_3 would shift the activation versus voltage curve in the horizontal direction. A leftward shift in the horizontal direction of this plot has been associated with gain of pain sensation mutations.

3.4.2 $\text{Na}_v1.8$ Channel Mutations

$\text{Na}_v1.8$ channel has also been associated with alterations in pain sensation [207]. However, it is not as well studied as $\text{Na}_v1.7$. $\text{Na}_v1.8$ is associated primarily with inflammatory pain. Here, similarly, dummy variable v_0 was introduced one by one in both $\alpha_{m_{1.8}}(V)$ and $\beta_{m_{1.8}}(V)$. As shown in Figure 3.11, the bifurcation points shift to the left, indicative of a decrease in pain sensation threshold. Furthermore, for lower

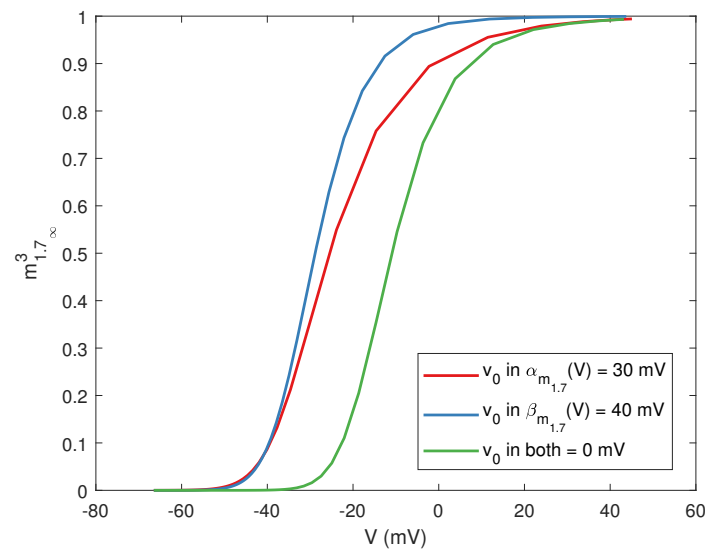


Figure 3.10.: There is a shift in $m_{1.7, \infty}^3$ as a result of an increase in v_0 .

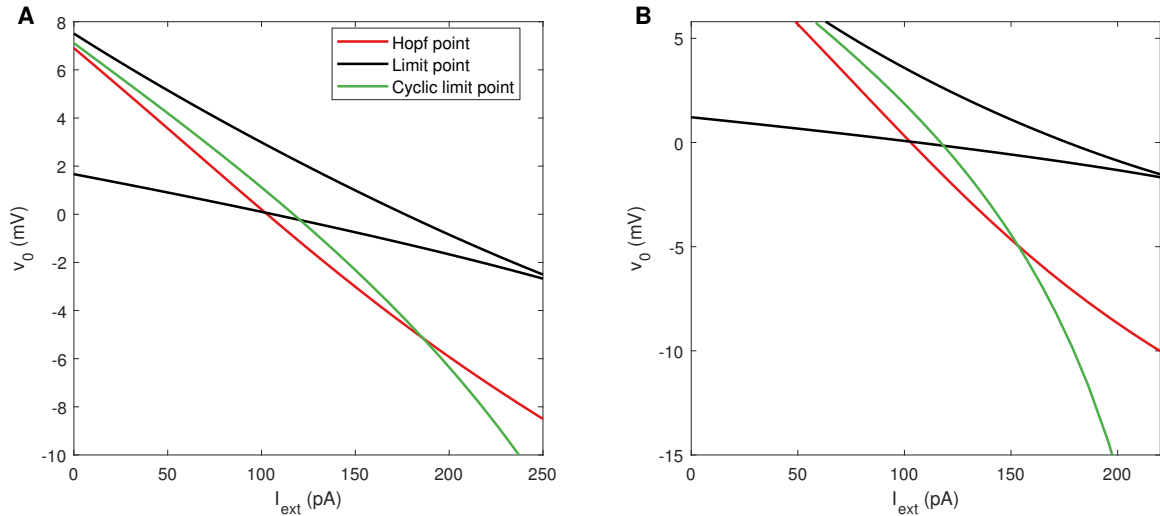


Figure 3.11.: Two parameter continuation for v_0 in A: $\alpha_{m_{1.8}}(V)$ and B: $\beta_{m_{1.8}}(V)$. The plot shows how the bifurcation points vary upon changing v_0 . An approximately 170% increase or more in k_3 of $\alpha_{m_{1.8}}(V)$ and a 4% increase or more in k_3 of $\beta_{m_{1.8}}(V)$ shifts the bifurcation points.

values of v_0 , the CLP is to the left of the HB point (see Figure 3.11), which indicates bistability.

Similar to the $\text{Na}_v1.7$ analysis, a leftward shift in the plot of steady state activation variable $m_{1.8\infty}$ versus membrane potential can be seen in Figure 3.12. Again, such a shift has been reported in literature, corresponding to gain of sensation mutations such as A1304T and I1706V in $\text{Na}_v1.8$, associated with painful neuropathy in individuals [208, 209].

The above channel mutation analyses demonstrated the use of bifurcation theory. In particular, two-parameter continuation of bifurcation points identified specific parameters that can shift the bifurcation points and impact the excitability of this neuron.

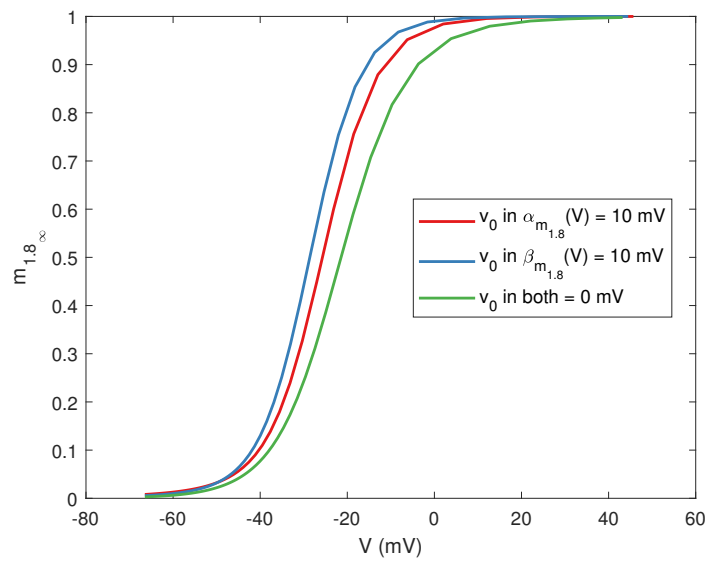


Figure 3.12.: There is a shift in $m_{1.8\infty}$ as a result of an increase in v_0 .

3.5 Influence of Ion Equilibrium Potentials at $I_{ext} = 0$

In this section, the results with E_{Na} and E_K as the bifurcation parameters and keeping $I_{ext} = 0$ are presented. These equilibrium potentials are functions of intracellular and extracellular ionic concentrations [180,183]. A nerve injury can change the ion concentration, subsequently impacting the equilibrium ion potential. A computational study on the nerve injury has been done with Hodgkin-Huxley type equations [198], where alterations in ion concentrations changed the excitability of the neuron. Here, how sodium and potassium equilibrium ion potentials can potentially alter the pain sensation threshold is demonstrated, using bifurcation theory.

The partial bifurcation diagrams are shown in Figure 3.13. The structures are similar to the previous bifurcation diagram in Figure 3.8. The diagram consists of a HB with unstable periodic solutions arising from it. There are two LP's leading to hysteresis in the unstable steady state solution branch. The unstable periodic solution branch emanating from the HB point ends at an unstable steady state branch, with a turning point (CLP) in between. This end point represents a homoclinic orbit, which is a specific type of periodic solution with infinite period. Another CLP separates unstable and stable periodic solutions. MMOs are observed between the HB point and this CLP. In both the cases, an increase in the equilibrium potential leads to generation of periodic firing even without any external stimulus. This is called spontaneous firing, and is indicative of neuropathic pain. In case of neuropathic pain, one may experience a tingling and burning sensation even without any external stimulus. Experimental or computational analysis of equilibrium ion potentials and their relation to pain has not been performed before, although this has been studied theoretically for nerve injury which can lead to pain [198]. The above results suggest a direct link between equilibrium sodium and potassium potential and the periodic firing threshold of a pain-sensing neuron. Further computational and experimental investigation of these results can provide strategies for alleviating neuropathic pain.

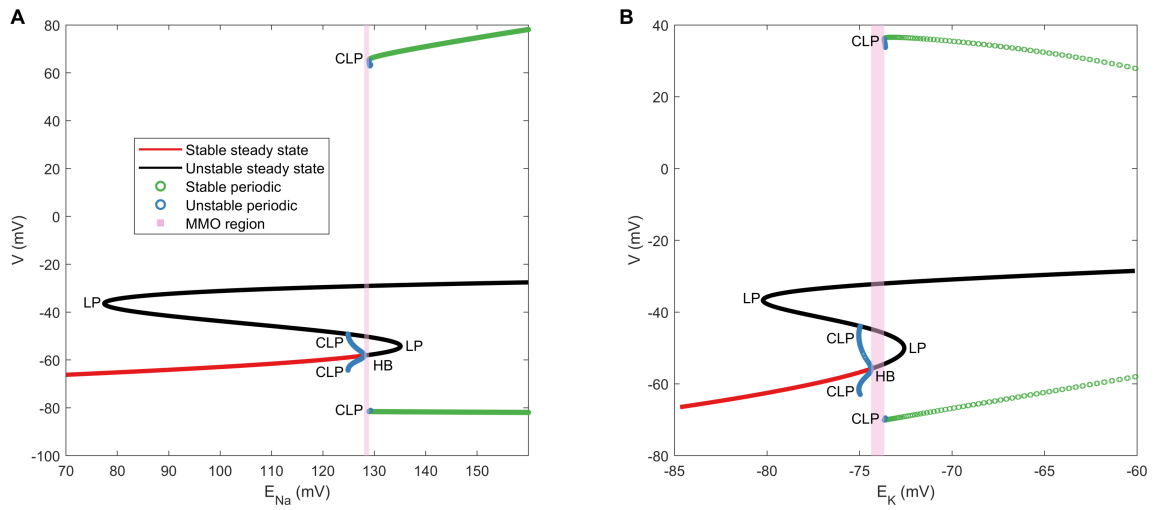


Figure 3.13.: Bifurcation diagram with A: E_{Na} (HB at $E_{Na} = 128.04$ mV and CLP of stable periodic branch at $E_{Na} = 128.96$ mV) and B: E_K (HB at $E_K = -74.37$ mV and CLP of stable periodic branch at $E_K = -73.66$ mV) as primary bifurcation parameters. HB: Subcritical Hopf bifurcation point, CLP: Cyclic limit point

3.6 Discussions

Pain is an unavoidable aspect of the average human experience. Any form of injury can lead to localized pain. This is the body's mechanism to begin healing the injured area. However, the pain threshold varies among individuals. The same intensity of a noxious stimulus may not be painful for one individual but may be extremely painful for another. In this chapter, a computational approach to understand pain sensation and to detect possible parameters that can shift the pain sensation threshold, is presented. To this end, bifurcation theory was used to understand the bifurcations arising in a mathematical model representative of a small DRG neuron's (pain-sensing neuron) dynamics. The bifurcations of this model can establish the boundary between the sensation of pain and no pain; a stable steady state solution is indicative of no pain, while a periodic solution indicates pain. The frequency of the large amplitude periodic firing further captures the degree of pain. Using this theory, potential mutation points were identified in sodium channels that can alter the pain sensation threshold. Evidence in literature was found for $\text{Na}_v1.7$ and $\text{Na}_v1.8$ mutations which were associated with conditions such as chronic pain associated with a burning sensation. It was also found that an increase in sodium or potassium equilibrium ion potential can lead to spontaneous firing, an indicator of neuropathic pain. Identifying such sensitive parameters can aid in developing therapeutic drugs that can control the pain sensation threshold.

This bifurcation analysis has some limitations based on its assumptions. The model used for this study is relatively simple from a physiological point of view. Several other ion channels in addition to the four channels addressed in this paper are present in a small DRG neuron as well. For example, $\text{Na}_v1.9$, also plays a role in the pain sensation [194–196] and is present in small DRG neurons but was not included in this model. Furthermore, neuron activity is not only a function of electrochemical reactions but also of biochemical reactions that occur within a neuron and at the synapse, where biochemicals in the form of neurotransmitters participate in synaptic

transmission. Additionally, a mutation can also occur at the central nervous system instead of the periphery. In this case, analyzing the synaptic ending can become essential. Since these neurons are relatively long compared to any other cell, starting from the periphery and reaching the spinal cord, organelles are actively transported from one end of the axon to the other. This is called axonal transport. This transport can also get disrupted due to any injury, genetic disorder, or disease, which may lead to neuropathic pain [210]. Lastly, biochemical processes such as release of cytokines and other inflammatory molecules are also involved in generation of inflammatory pain. All the aforementioned mechanisms are potential areas that can benefit from computational modeling and bifurcation theory to find sensitive parameters that impact the pain sensation threshold.

Much variability has been observed in electrical recordings of small DRG neurons [188, 189, 211]. Some of these neurons display MMOs, while others do not. Therefore, eventually there is a need for an ensemble of parameter values in order to capture such variations. This model is representative of a specific sub-type of small DRG neurons and is robust in the sense that the dynamical patterns are conserved even after increasing all the maximal conductances proportionately. Recording of currents due to each ion channel along with the structure of the action potential for various small DRG neurons will enable building a more accurate model. This can be achieved using voltage-clamp experiments.

The two parameter approach presented here was useful in identifying potential alterations that can occur in the fast activation of $\text{Na}_v1.7$ and $\text{Na}_v1.8$ and can shift the bifurcation points, consequently impacting the pain sensation threshold, which have been observed experimentally in the literature. This approach's limitation is in the number of parameters that can be varied simultaneously. Most numerical tools are designed for one and two parameter continuations corresponding to codimension 0 or 1 bifurcation points. For the continuation of higher codimensions, see Krasnyk et al. [212] and references therein.

This work demonstrates the use of bifurcation theory in understanding the variation associated with pain: a vital physiological phenomenon. It was identified that alterations in specific model parameters can shift the bifurcation points, which can consequently impact the excitability of a pain-sensing neuron. A thorough analysis using the foregoing approach outlined in this chapter corroborated with experimental studies can advance the understanding of the mechanism of pain sensation.

The next chapter focuses on a detailed investigation of the dynamics of this model. In particular, MMOs are elaborated upon.

3.7 Supplementary Information

XPPAUT [193] was used for numerical integration and bifurcation analysis, MATCONT [213] for performing two-parameter continuation of bifurcation points, and MATLAB [214] for generating the plots. The XPPAUT and MATLAB codes are publicly available on ModelDB (<http://modeldb.yale.edu/264591>). Biological figures in this chapter and chapter 1 were developed using Motifolio (<https://www.motifolio.com/>) and somersault18:24 (<https://www.somersault1824.com/>).

4. COMPUTATIONAL ANALYSIS OF A 9D MODEL FOR A SMALL DRG NEURON

This work has been submitted to Journal of Computational Neuroscience and is currently under review.

In this chapter, focus on the same model as the one in the previous chapter. This chapter delves deeper into the bifurcations that can explain the dynamics of this neuron. The dynamics of this model strongly depends on the maximal conductances of the voltage-gated ion channels and the external current, which can be adjusted experimentally. It is shown that the neuron dynamics are most sensitive to the $\text{Na}_v1.8$ channel maximal conductance ($\bar{g}_{1.8}$). Numerical bifurcation analysis shows that depending on $\bar{g}_{1.8}$ and the external current, different parameter regions can be identified with stable steady states, periodic firing of action potentials, mixed-mode oscillations (MMOs), and bistability between stable steady states and stable periodic firing of action potentials. This chapter illustrates and discusses the transitions between these different regimes. Further, the behavior of MMOs are analyzed. As the external current is decreased, MMOs appear after a cyclic limit point, as shown in the previous chapter. Within this region, bifurcation analysis shows a sequence of isolated periodic solution branches with one large action potential and a number of small amplitude peaks per period. For decreasing external current, the number of small amplitude peaks is increasing and the distance between the large amplitude action potentials is growing, finally tending to infinity and thereby leading to a stable steady state. A closer inspection reveals more complex concatenated MMOs in between these periodic MMOs branches, forming Farey sequences. Lastly, small solution windows with aperiodic oscillations are also found, which seem to be chaotic. The dynamical patterns found here as a function of different parameters contain information of translational

importance as their relation to pain sensation and its intensity is a potential source of insight into controlling pain.

4.1 Introduction

Neurons display a variety of rich dynamics such as repetitive firing of action potentials, bursting, mixed-mode oscillations, and bistability. The diversity of dynamics displayed by a multitude of neurons has led several researchers to bifurcation theory to understand the transition from one dynamical pattern to the other for more than 40 years [179, 215–217]. Starting with the analysis of low dimensional models such as Hodgkin-Huxley and Fitzhugh-Nagumo equations, it has recently been used for higher dimensional models such as a 14D model of a pyramidal cell [218], as well. In this chapter, we employ numerical bifurcation analysis to understand the dynamics of a 9D model of a small dorsal root ganglion (DRG) neuron.

Small DRG neurons are primary nociceptors, i.e., they are responsible for sensing pain [96], as described in the previous chapter. From a theoretical point of view, pain corresponds to repetitive firing of action potentials [191, 192]. To understand how pain can be controlled, it is therefore essential to determine how the transition to periodic firing of action potentials depends on the physiological parameters and how these parameters can be manipulated in a suitable way.

While limited numerical [186, 187, 219] and extensive experimental [211, 220–222] studies have been executed for this type of neuron, a detailed bifurcation analysis has not been undertaken so far. The importance of using bifurcation theory to understand pain is emphasized in the works of [197] and [94] where 2D and 3D models of an afferent sensory neuron were analyzed with regard to neuropathic pain and, subsequently, bifurcation theory aided in finding parametric regions of pain and no-pain. Previous work on a model of a small DRG neuron [159] (explained in the previous chapter) also illustrates the utility of bifurcation theory for understanding pain. In that chapter, genetic mutations in sodium channels that are associated with pain sensation were also investigated.

In this chapter, the aforementioned theory is used extensively to find the bifurcations explaining the excitability patterns of this model. Both one-parameter and two-parameter continuation of model solutions is performed, with external current as the primary bifurcation parameter and maximal conductance of one of the voltage-gated ion channels as the secondary parameter. Here, different solution regimes are found, consisting of stable steady states, periodic firing of action potentials, and mixed-mode oscillations (MMOs). The latter are periodic or aperiodic oscillatory solutions consisting of small amplitude (subthreshold) and large amplitude (action potential) peaks. They have been recorded in DRG neuron cultures before [188, 211]. Besides, they have been observed in many other chemical and neuronal systems [223, 224], and are therefore of broader interest. We elaborate on the mechanisms of onset and disappearance of MMOs, and compare them to other extensively analyzed MMO-generating systems.

This chapter is organized as follows. In Sec. 4.2, the model is described and various patterns of behaviour are shown using dynamic simulation for selected parameter values. Sec. 4.3 identifies different parameter regions corresponding to the different patterns of behavior using one- and two-parameter continuation with external current as the primary bifurcation parameter and maximal conductance of the $\text{Na}_v1.8$ sodium channels as the secondary bifurcation parameter. To account for model uncertainties, sensitivity with respect to the other model parameters are also studied afterwards using two-parameter continuation of critical boundaries. In Sec. 4.4, the focus is on MMOs. Periodic continuation is used to calculate a sequence of periodic solution branches with one large amplitude action potential and various numbers of small amplitude subthreshold peaks per period. Further, dynamic simulations illustrate the existence of more complex concatenated periodic and aperiodic MMOs. Lastly, Sec. 4.5 discusses and concludes the results, providing remarks on problems that still need to be addressed.

4.2 Model description and first simulation results

In this chapter, we focus on a single compartment minimal conductance model as mentioned in the previous chapter. Following [187], the model accounts for currents due to two sodium channels: $\text{Na}_v1.7$ ($I_{1.7}$) and $\text{Na}_v1.8$ ($I_{1.8}$), two potassium channels: a delayed rectifier (I_K) and an A-type transient (I_{KA}) channel, and a leak channel (I_l). These are the primary ion channels found on the membrane of a small DRG neuron. The equation for membrane voltage dynamics are written in the following Hodgkin-Huxley [177] type of form. Refer to the previous chapter and appendix for details of this model.

In a first step, selected dynamic simulations are presented of the above equations to illustrate some characteristic patterns of behavior, to be analyzed in more detail in the remainder. Results are shown in Figure 4.1. Initial condition for all simulations was the stable steady state for $I_{ext} = 0$ pA.

In the first row of Fig. 4.1 the maximum conductance of the $\text{Na}_v1.8$ channel equals 7 mS/cm² and the value of the external current is increased from 100 pA in the left diagram, to 106 pA in the middle, to 120 pA in the right diagram. In the left diagram, for the lowest value of I_{ext} , a stable steady state is attained after the firing of an action potential, whereas periodic firing of large amplitude action potentials is observed for the highest value of I_{ext} in the right diagram. For values of I_{ext} in between, there is a region where mixed mode oscillations (MMOs) are observed as illustrated in the middle diagram. There, after some initial transient, a periodic regime is attained with one large amplitude action potential and eight small amplitude subthreshold peaks per period.

A different situation is seen in the second row of Figure 4.1 with some representative simulations. There, the maximum conductance of the $\text{Na}_v1.8$ channel is equal to 4.5 mS/cm². Again the values of the external current are increasing from the left to the right. The qualitative behavior in the left and the right diagrams, for the lowest and the highest value of I_{ext} , is similar to the behavior shown in the corresponding

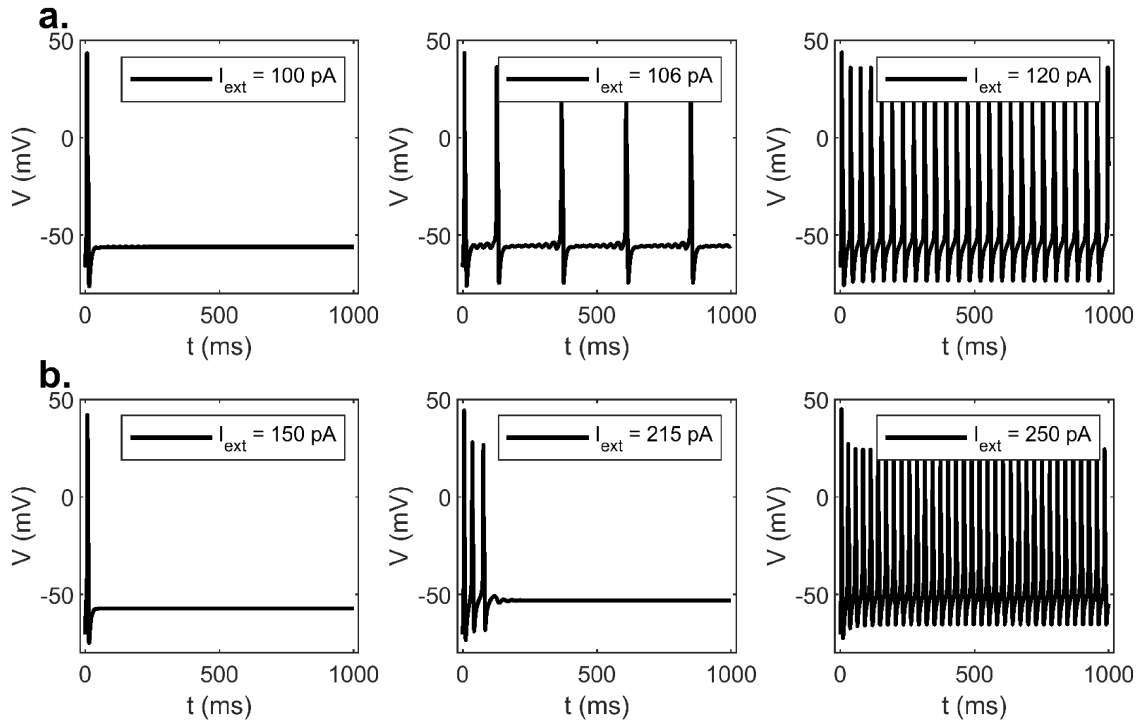


Figure 4.1.: Dynamic simulations of action potentials. For higher values of $\bar{g}_{1,8}$, MMOs are observed. a.: Dynamic simulations for $\bar{g}_{1,8}$ at 7 mS/cm^2 , and $I_{ext} = 100, 106, 120$ pA. b.: Dynamic simulations for $\bar{g}_{1,8}$ at 4.5 mS/cm^2 , and $I_{ext} = 115, 215, 230$ pA. No MMOs are observed in this case.

diagrams of Figure 4.1a. However, in contrast to Figure 4.1a, no MMOs are found in the intermediate range of I_{ext} . This is illustrated in the middle diagram for one specific value of I_{ext} of 215 pA, where the cell potential decays to a stable steady state after firing of three action potentials. It will be shown in more detail in the next section that MMOs do not exist for any value of the intermediate range for $\bar{g}_{1.8}$ equal to 4.5 mS/cm².

Both of the cases shown in Figure 4.1 have been observed in DRG culture recordings. See [189] for recordings resembling Figure 4.1b, and [211] and [188] for recordings displaying MMOs as in Figure 4.1a.

4.3 Numerical bifurcation analysis

In order to explain the transitions between different dynamical patterns observed in this model, one-parameter and two-parameter continuation of solutions are performed, with I_{ext} as the primary bifurcation parameter, and $\bar{g}_{1.8}$ as the secondary bifurcation parameter. First, one-parameter continuations of steady state and periodic solutions upon varying the primary bifurcation parameter I_{ext} are performed. Results are shown in Figure 4.2 for four different values of $\bar{g}_{1.8}$. The first diagram in Figure 4.2a is for a value of 4.5 mS/cm² corresponding to the scenario in Figure 4.1b, whereas the third diagram in Figure 4.2c is for a value of 7 mS/cm² corresponding to the scenario in Figure 4.1a. Two additional scenarios for values of 5 and 8 mS/cm² are shown in Figures 4.2b and 4.2d.

In all the four diagrams of Figure 4.2, a branch of stable steady states is obtained for low values of I_{ext} starting from the left boundary of the corresponding diagram. It is indicated by the red solid line and correspond to the behavior shown in the left diagrams of Figures 4.1a, b. The stable steady states become unstable at a subcritical Hopf bifurcation point (HB), from where a branch of unstable periodic solutions emerges indicated by the blue circles in Figure 4.2.

Furthermore, in all the four diagrams of Figure 4.2, a branch of stable periodic solutions is observed for high values of I_{ext} at the right boundary of the corresponding

diagrams. It is indicated by the green filled circles and correspond to periodic firing of action potentials as shown in the right diagrams of Figures 4.1a, b. In all the four cases, these branches of stable periodic solutions lose their stability at a cyclic limit point (CLP_3), giving rise to a branch of unstable periodic solutions.

Qualitative differences in the four diagrams of Figure 4.2 occur with respect to the unstable periodic branches indicated by the blue circles. In the first two diagrams, the unstable periodic solution branches are connected and show two more cyclic limit points (CLP_1 and CLP_2); after the third cyclic limit point (CLP_3), they turn into the stable periodic solution branch with periodic firing of action potentials as described above. In contrast to this, in the last two diagrams, the unstable periodic solution branches are disconnected and CLP_2 disappears. At the end points of these branches, the period of the unstable periodic solutions is increasing rapidly during continuation with XPPAUT and MATCONT, indicating the presence of a period infinity solution at the end points.

Another difference occurs with respect to the unstable steady state branches indicated by the dashed lines in Figure 4.2. They display hysteresis with two limit points (LP_1 and LP_2) in Figure 4.2c, one of which (LP_2) has moved out of the positive range for I_{ext} in Figure 4.2d.

Further, it is seen that the I_{ext} value of the bifurcation points varies significantly between the four diagrams of Figure 4.2, indicating a high sensitivity to $\bar{g}_{1.8}$. For the increasing values of $\bar{g}_{1.8}$ from Figure 4.2a to 4.2d, the bifurcation points are shifted to lower values of I_{ext} . Besides the absolute I_{ext} value, it is found that the relative position of the HB point and the CLP_3 point is of major importance for the qualitative differences reported in Figure 4.1. In Figure 4.2a, the I_{ext} value of HB is higher than that of CLP_3 , leading to an overlap between stable steady state and stable periodic solutions indicated by the orange region of Figure 4.2a. An increase of I_{ext} will lead to the periodic firing of action potentials when the HB point is crossed as shown in the scenario in Figure 4.1b. A transition back to stable steady states will occur at the value of the CLP_3 point if I_{ext} is decreased again afterwards. Between the CLP_3

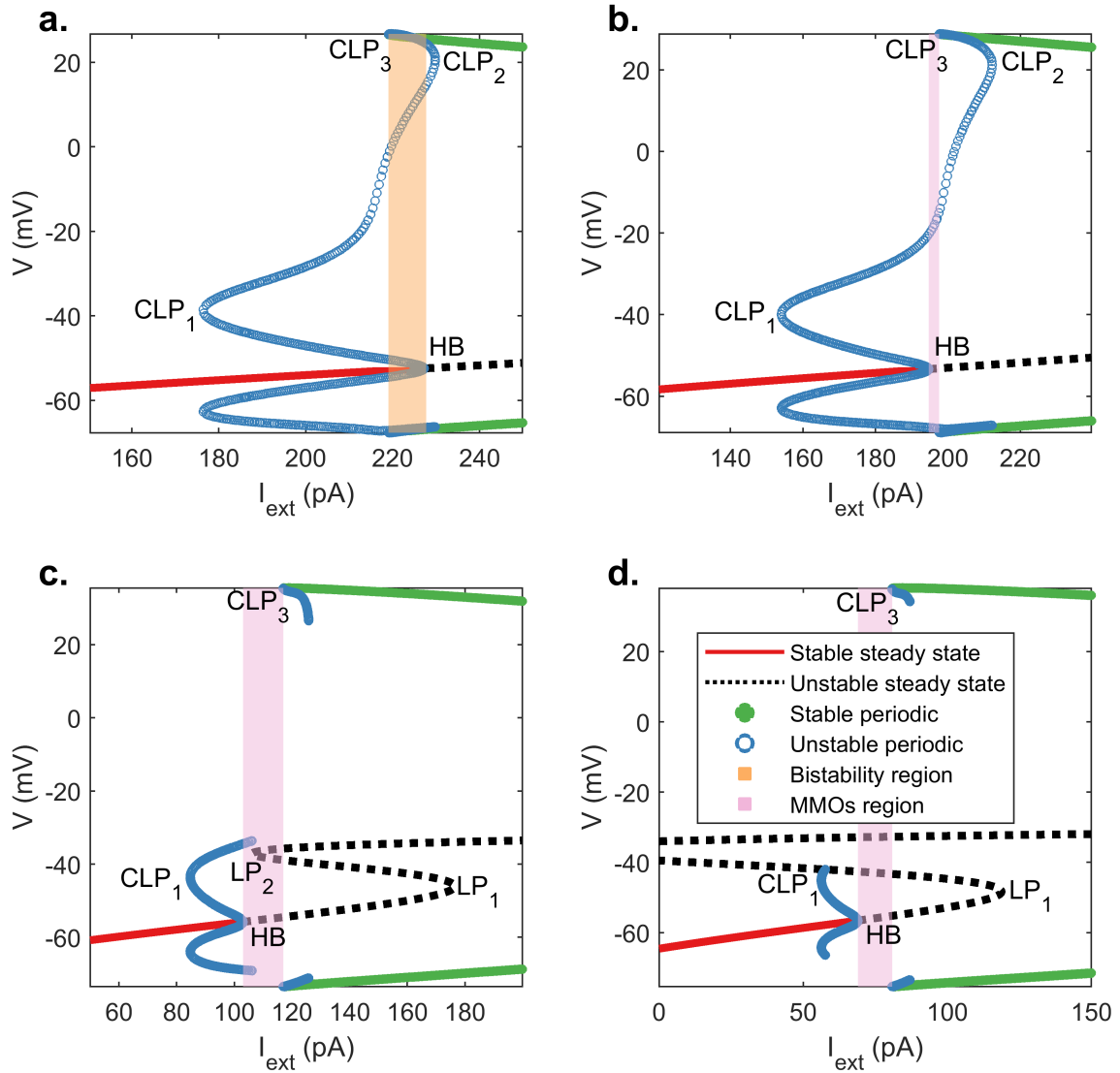


Figure 4.2.: Bifurcation diagrams for $\bar{g}_{1.8} = 4.5, 5, 7$ and 8 mS/cm^2 for diagrams a, b, c and d, respectively. For lower values of $\bar{g}_{1.8}$ in diagram (a), MMOs are not observed, and there is a region of bistability between steady state and periodic firing of action potentials, as shown by the orange shaded region. This bistability is not present in diagrams b, c, d. Instead, MMOs are observed in these diagrams in the purple shaded region. MMOs solution branches will be discussed separately in section 3 and are not included in this figure. Note that the unstable blue periodic branch in diagram c ends before the LP_2 point which is not evident from the figure because of the thickness of the branches. HB: Hopf bifurcation point, CLP: Cyclic limit point, LP: limit point

and the HB point in Figure 4.2a, the system is bistable, i.e., the initial conditions regulate whether a stable periodic or a stable steady state solution is attained.

The situation is fundamentally different in Figures 4.2c and 4.2d. Here, the I_{ext} value of the HB point is lower than the value of the CLP_3 point, leading to a situation where no stable attracting solutions are shown in the purple shaded region of these diagrams. This is the region where various types of stable periodic and aperiodic MMOs exist. The MMOs solution branches are missing in Figure 4.2 and will be discussed in the next section. Further, it will be shown that in these cases, the CLP_3 point provides a strict upper limit of the MMOs region, whereas the lower limit is not determined by the HB point but by a value close by where the time between subsequent large amplitude action potentials of the MMOs tends to infinity.

To map out the regions in the I_{ext} and $\bar{g}_{1.8}$ parameter space with different patterns of behavior, a two-parameter continuation of the relevant critical points HB, CLP_3 , LP_1 , and LP_2 is performed. The results are shown in Figure 4.3. As mentioned above, the upper boundary of the MMOs region is the curve of the CLP_3 points, whereas the lower boundary is a solution where the time between subsequent action potentials tends to infinity close to the HB curve. These boundaries are seen best in Figure 4.3b. A direct calculation and continuation of the lower boundary is substantially challenging and was not done. Instead, the lower boundary of the MMOs region is determined by point-wise dynamic simulation over a prolonged time period. In summary, it is found that the transition from the stable steady state region (“no pain”) to the repetitive firing of action potentials (“pain”) differs depending on the value of $\bar{g}_{1.8}$. For high values of $\bar{g}_{1.8}$, MMOs occur. As it will be shown in the next section, the frequency of action potentials in this region is increasing step by step as the stimulus I_{ext} is increased. In contrast to this, for values of $\bar{g}_{1.8}$ below the intersection of the HB and the CLP_3 curve, there is the orange bistable region with a ‘hard’ onset of the periodic firing of action potentials with high frequency.

This analysis suggests that the small DRG neuron dynamics depend strongly on the expression of $Na_v1.8$. For lower expression of $Na_v1.8$, it may not display

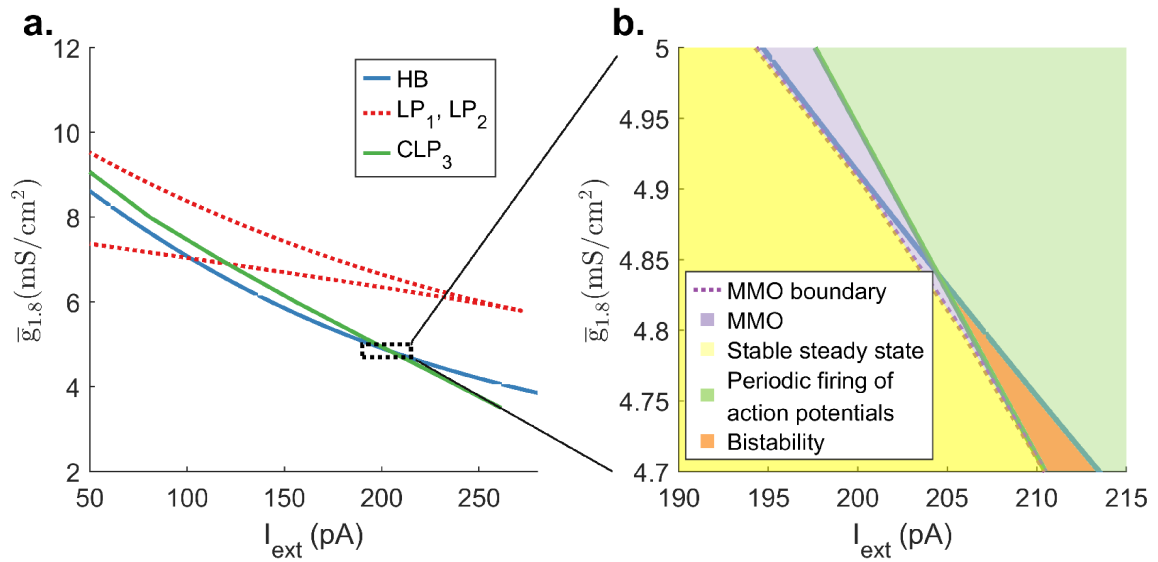


Figure 4.3.: Two parameter plot with $\bar{g}_{1.8}$ as the secondary continuation parameter. a.: Variation over a large interval of $\bar{g}_{1.8}$. b.: Zoomed in version of a. near the intersection of the HB point and the CLP₃ point.

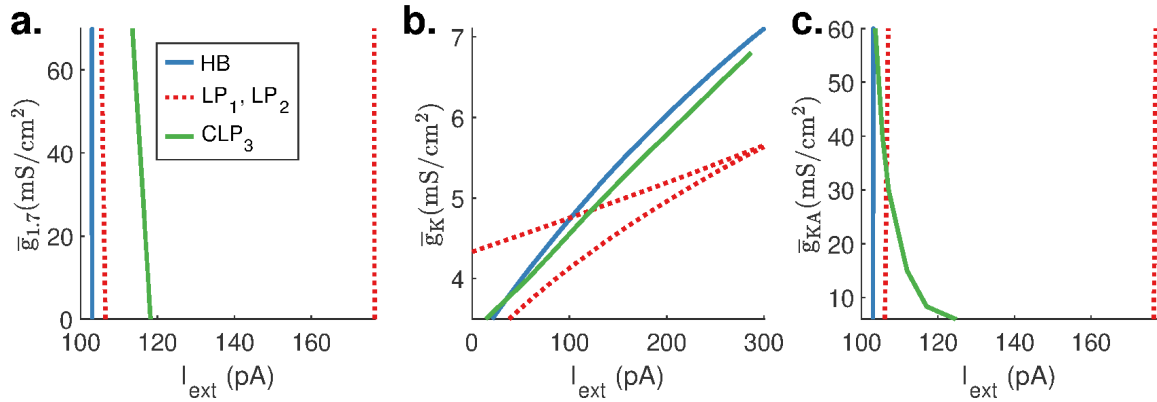


Figure 4.4.: Two parameter plot with the following secondary continuation parameters: a.: $\bar{g}_{1.7}$, b.: \bar{g}_K and c.: \bar{g}_{KA} .

subthreshold oscillations. This can explain the variability in DRG culture recordings reported in [188, 189, 211].

The influence of the other maximal conductances \bar{g}_i ($i = 1.7, K, KA$) is also investigated using two-parameter continuations of the critical bifurcation points with I_{ext} as the primary bifurcation parameter and the corresponding maximal conductance as the secondary bifurcation parameter. Results are shown in Fig. 4.4. As seen in Figure 4.4a and Figure 4.4c, $\bar{g}_{1.7}$ and \bar{g}_{KA} have negligible effect on the HB and the LP points. The CLP₃ point is sensitive only to lower values of \bar{g}_{KA} . All the bifurcation points are sensitive to \bar{g}_K , as seen in Figure 4.4b. Here, the CLP₃, HB, and LP points vary substantially from 0 to 300 pA in a small range of \bar{g}_K .

4.4 Mixed-mode oscillations

In this section, the focus is on the periodic and aperiodic MMOs solutions already mentioned in the previous sections. For the characterization of periodic MMOs solutions, the nomenclature introduced, for example, in [225] is applied. Basic MMOs patterns consist of L large amplitude peaks (action potentials) followed by S small amplitude (subthreshold) peaks per period, termed as L^S patterns in this notation. In particular, L is equal to one in the remainder of this section. More complex patterns

arise due to the concatenation of different basic patterns, for example, a pattern of the form $L_1^{S_1}L_2^{S_2}$ can occur between the basic patterns $L_1^{S_1}$ and $L_2^{S_2}$. It consists of L_1 action potentials, followed by S_1 subthreshold peaks, followed by L_2 action potentials, followed by S_2 subthreshold peaks in each period.

Some characteristic basic patterns of MMOs are shown in Figure 4.5 for different values of I_{ext} . In the remainder of this section, the default parameter values from Table B.1 and B.2 and the value of $\bar{g}_{1,8}$ is equal to 7 mS/cm² corresponding to Figure 4.2c. According to this figure and our previous results, MMOs are expected in the range of I_{ext} of roughly 103 to 117 pA. More precise values will be given in the course of this discussion. According to the nomenclature mentioned above, the patterns in Figure 4.5 can be characterized as 1^6 for $I_{ext} = 107$ pA, 1^3 for $I_{ext} = 110$ pA, and 1^1 for $I_{ext} = 114$ pA. In this series, the number of small subthreshold peaks is decreasing with increasing external current, and the distance between the action potentials is decreasing with increasing external current.

For the dynamic simulation of MMOs, it is important to note that the system has multiple time scales. The $s_{1,7}$ variable is by far the slowest variable. Therefore, all the dynamic simulations in this section are performed with a startup phase of 100,000 ms to achieve the desired asymptotic behavior of all variables. The time window shown, for example, in Figure 4.5, starts after this startup phase of 100,000 ms.

To add more details to the picture presented in Figure 4.5, a one-parameter continuation of the basic MMOs patterns illustrated in Figure 4.5 is performed. Results are shown in Figure 4.6. The maximum amplitude of these periodic solutions is almost constant and therefore not compelling; instead of the amplitude, the period of different solutions is used for graphical representation of the results.

Figure 4.6 shows a sequence of isolated periodic solution branches, with one action potential per period. The number of small amplitude peaks between the action potentials and the period increases from the right to the left in the direction of decreasing external current. The right most branch with label 1^0 corresponds to the periodic firing of action potentials without any small amplitude peaks in between, as

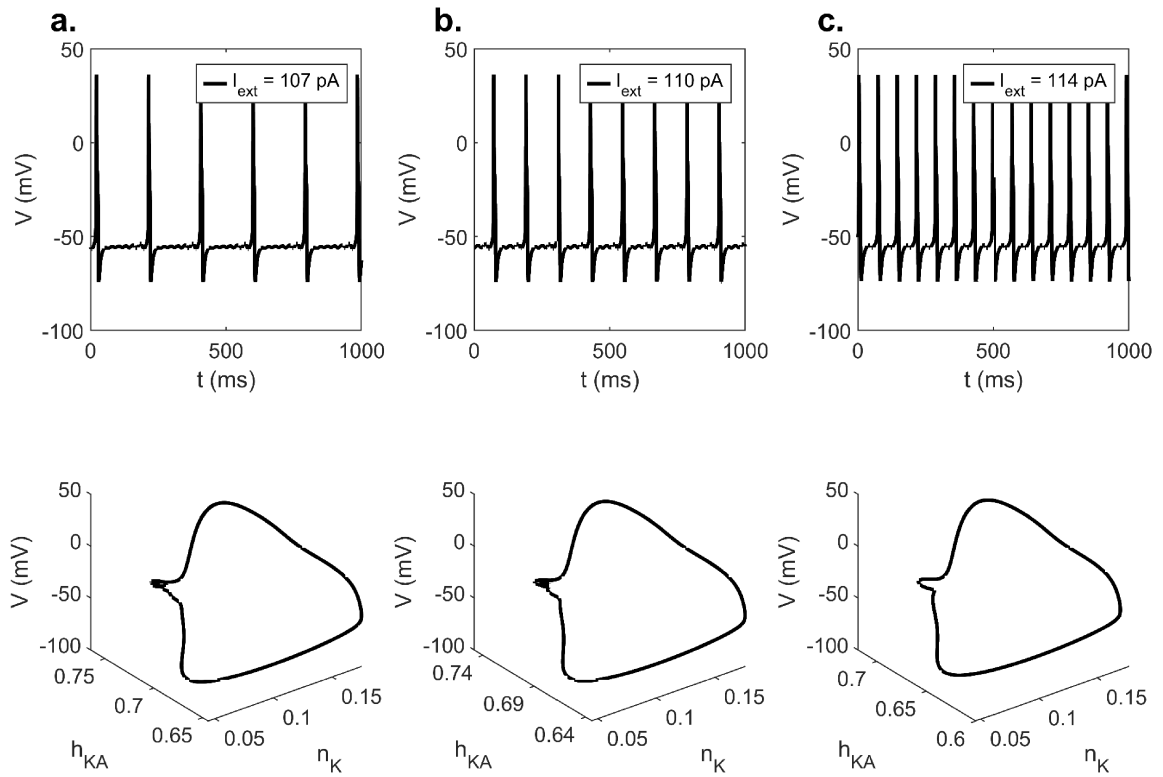


Figure 4.5.: Basic MMOs solutions of the type: a.: 1^6 , b.: 1^3 , and c.: 1^1 for selected values of I_{ext} . Upper row: temporal evolution of membrane voltage, lower row: orbits in the V , h_{ka} , n_K phase space.

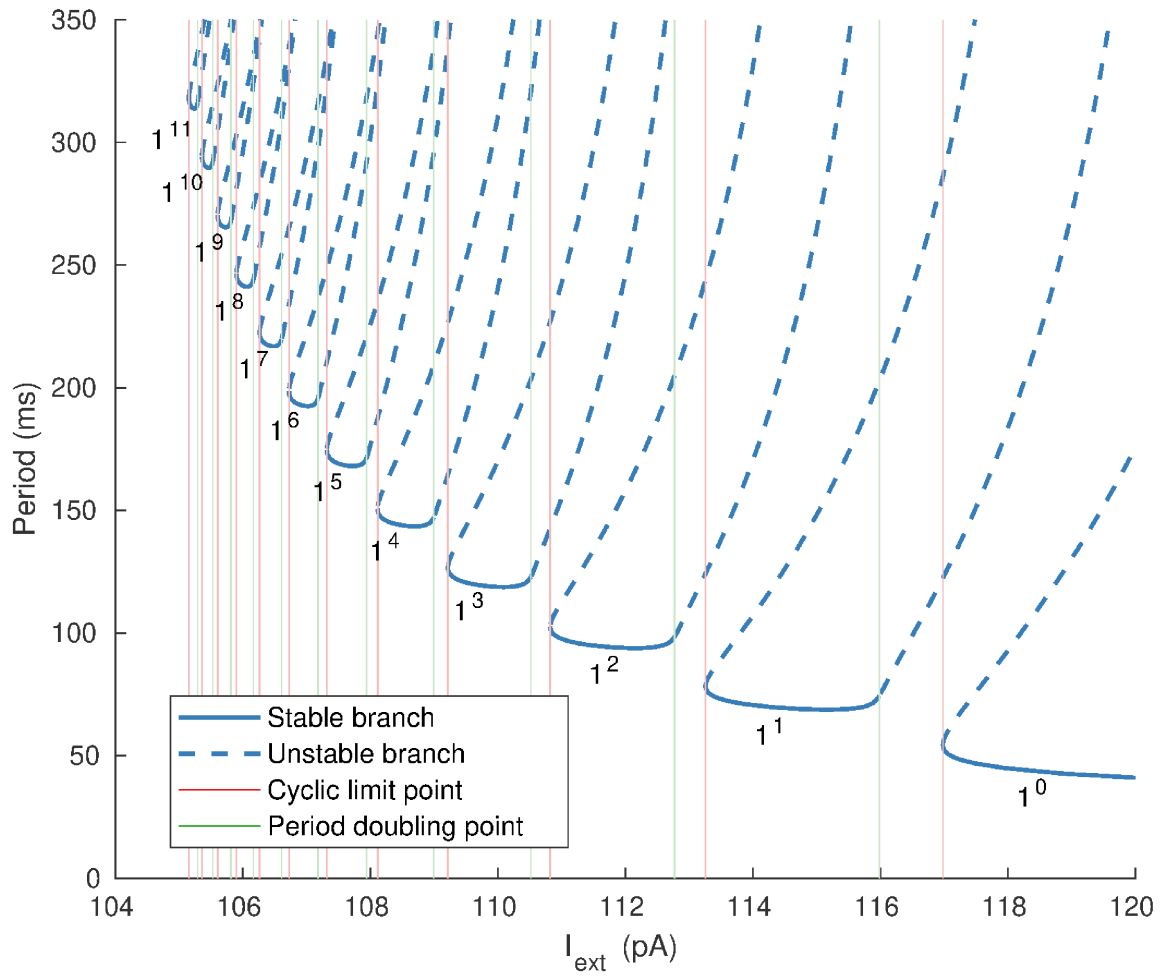


Figure 4.6.: Basic periodic solution branches with one action potential per period in the range of I_{ext} from 105 to 120 pA. Solid lines: stable periodic solutions, dashed line: unstable periodic solutions.

Table 4.1.: Values of I_{ext} at the cyclic limit points (CLP) and the period doubling bifurcation points (PD) in Fig. 4.6.

Solution type	CLP (pA)	PD (pA)
1^{11}	105.1554	105.2914
1^{10}	105.3609	105.5277
1^9	105.6055	105.8133
1^8	105.9013	106.1649
1^7	106.2657	106.6072
1^6	106.7246	107.1787
1^5	107.3185	107.9409
1^4	108.1125	108.9962
1^3	109.2164	110.5166
1^2	110.8213	112.7732
1^1	113.2577	115.9832
1^0	116.9811	

illustrated in the right diagram of Figure 4.1a. This periodic solution branch becomes unstable at a cyclic limit point at $I_{ext} = 116.9811$ pA, which corresponds to the CLP₃ point in Figure 4.2c. On every other branch in Figure 4.6, the corresponding periodic solution becomes unstable at a cyclic limit point on the left and at a period doubling bifurcation point on the right. The values of I_{ext} at the cyclic limit points are indicated by the red lines and the values at the period doubling bifurcation points by the green lines in Figure 4.6. These values are also listed in Table 4.1.

Solutions below 105 pA are not shown in this figure. Below 105 pA, the distance between the large amplitude action potentials becomes larger and larger as we increase I_{ext} and finally tends to infinity close to the subcritical Hopf bifurcation point, for which I_{ext} equals 102.9935 pA. Accordingly, the number of subthreshold peaks becomes larger and larger and their amplitude smaller and smaller as the critical

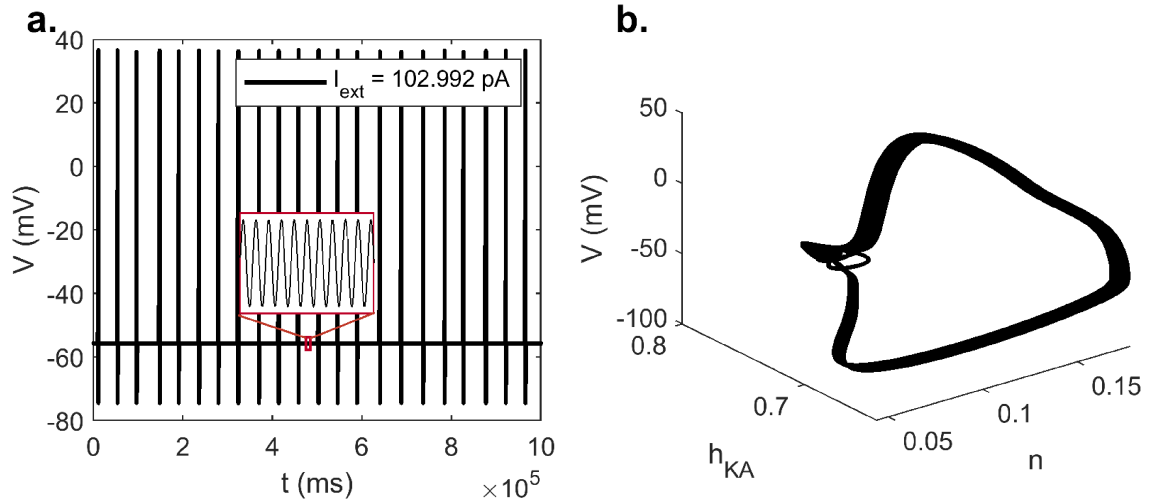


Figure 4.7.: a.: MMOs for $I_{ext} = 102.992$ pA below the Hopf bifurcation point at $I_{ext} = 102.9935$ pA. b.: Representation of the solution in the V, h_{KA}, n_K phase diagram.

point is approached. As an example, dynamic simulations are shown for a value of $I_{ext} = 102.992$ pA which is slightly below the subcritical Hopf bifurcation point, shown in Figure 4.7. The distance between two action potentials is roughly 40,000 ms. However, as shown in the phase diagram in Figure 4.7b, the orbit is a narrow band and does not seem to be strictly periodic. For I_{ext} slightly below this value, MMOs finally vanish and a stable steady state is obtained.

Concatenated periodic solutions are found in the gaps of the basic periodic patterns in Figure 4.6 between the period doubling points and the cyclic limit points of the subsequent solution branches on the right. Further, the dynamic behavior in these regions is studied for selected values of I_{ext} using dynamic simulations. Again, it is crucial to account for the long transient phase introduced by the very slow $s_{1.7}$ variable as described above. Some characteristic patterns of behavior in the range of 112.9 to 113.2 pA are shown in Figure 4.8. According to the aforementioned nomenclature, the solution in Figure 4.8a can be characterized as a concatenation between the basic 1^2 pattern on the left of this value and the basic 1^1 on the right of this value in Figure 4.6, leading to a $1^2 1^1$ solution with two action potentials per period. Accord-

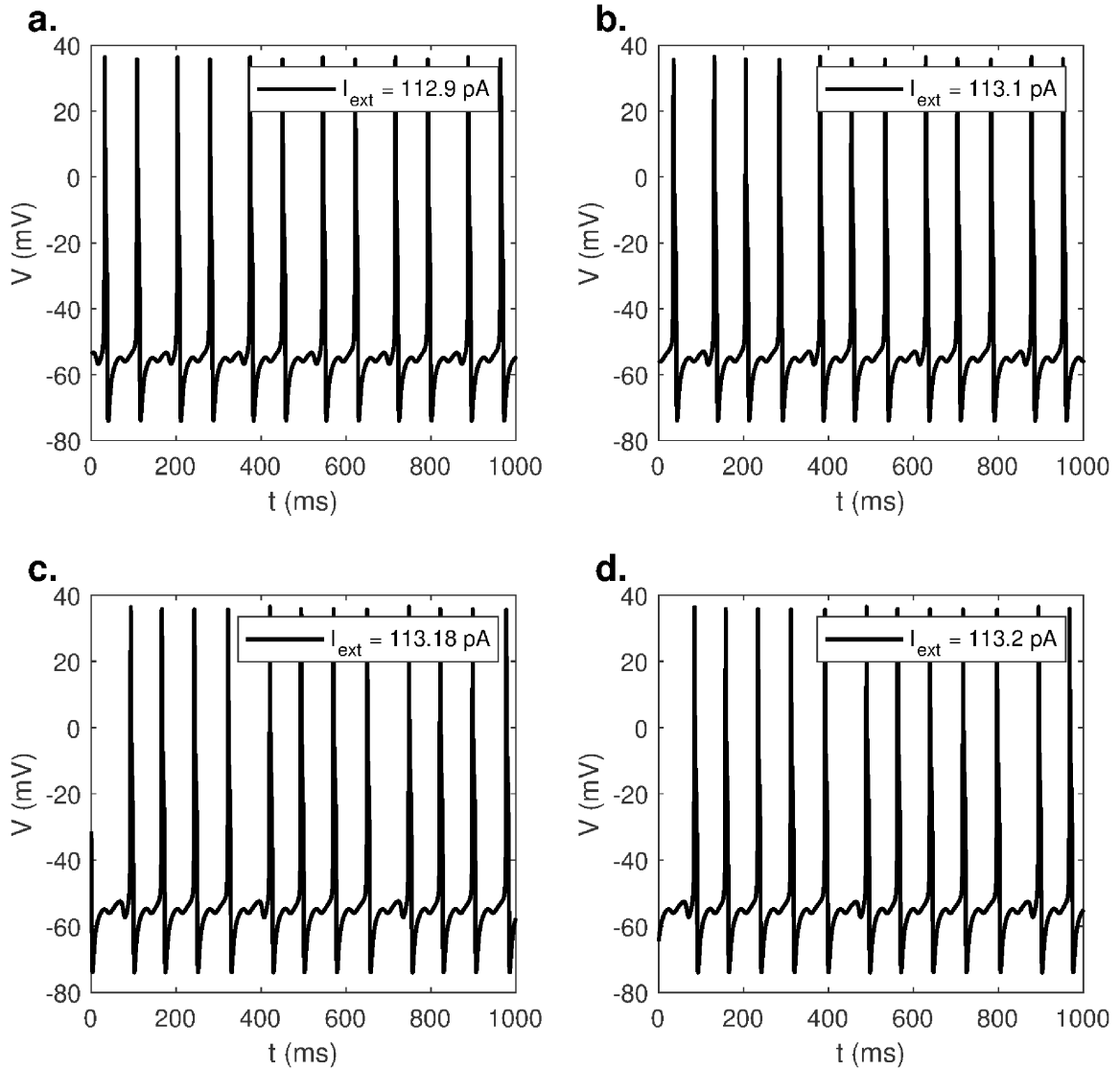


Figure 4.8.: A sequence of concatenated periodic solutions. a.: $1^2 1^1$ at $I_{ext} = 112.9$ pA, b.: $1^2 (1^1)^2$ at $I_{ext} = 113.1$ pA, c.: $1^2 (1^1)^3$ at $I_{ext} = 113.18$ pA, d.: $1^2 (1^1)^4$ at $I_{ext} = 113.2$ pA.

ingly, Figure 4.8b demonstrates a $1^2 (1^1)^2$ pattern with 3 action potentials per period, Figure 4.8c a $1^2 (1^1)^3$ pattern with 4 action potentials per period, and Figure 4.8d a $1^2 (1^1)^4$ pattern with 5 action potentials per period.

Subsequently, the MMOs solutions which were found for selected values of I_{ext} are ordered in a tree like structure in Figure 4.9 containing basic and concatenated

MMOs patterns as described above. The corresponding values of I_{ext} in pA are given in parentheses. The solutions highlighted in yellow correspond to those shown in Figure 4.8. It is worth noting that the solution tree is not complete, since only selected values of I_{ext} have been considered. For example, it is expected that between the solution $1^6(1^5)^2$ at $I_{ext} = 107.27$ pA and the solution $1^6(1^5)^4$ at $I_{ext} = 107.3$ pA, another solution of the form $1^6(1^5)^3$ can be found for some suitable value of I_{ext} , so that the solutions form a regular so-called Farey sequence [225]. Furthermore, it is expected that even higher order concatenated solutions can be found for some suitable values of I_{ext} .

Close to the cyclic limit point at $I_{ext} = 116.9811$ pA in Figure 4.6 corresponding to CLP_3 in Figure 4.2c before the MMOs disappear, the solution consists of one small amplitude peak and multiple large amplitude peaks. If n is the number of large amplitude peaks, this can be written as a concatenation of one 1^1 solution and $(n - 1)$ 1^0 solutions as $1^1(1^0)^{n-1}$. Selected solutions for this region are shown in Figure 4.10. The number of large amplitude action potentials per period is increasing in this sequence from the left to the right.

The solution tree in Figure 4.10 is also not complete. For example, it is expected that one can also find solutions of the form $1^1(1^0)^{12}$ and $1^1(1^0)^{13}$ between $1^1(1^0)^{11}$ and $1^1(1^0)^{14}$ for some suitable value of I_{ext} in between.

For an additional characterization of periodic MMOs, we introduce a firing number F . Following [225], F is defined as the number of small amplitude subthreshold peaks per total number of peaks in a period. For a basic L^S pattern, F is given by:

$$F = \frac{S}{L + S}. \quad (4.1)$$

Accordingly, $1 - F$ is the firing rate of action potentials per period, which is even more interesting from the physiological point of view.

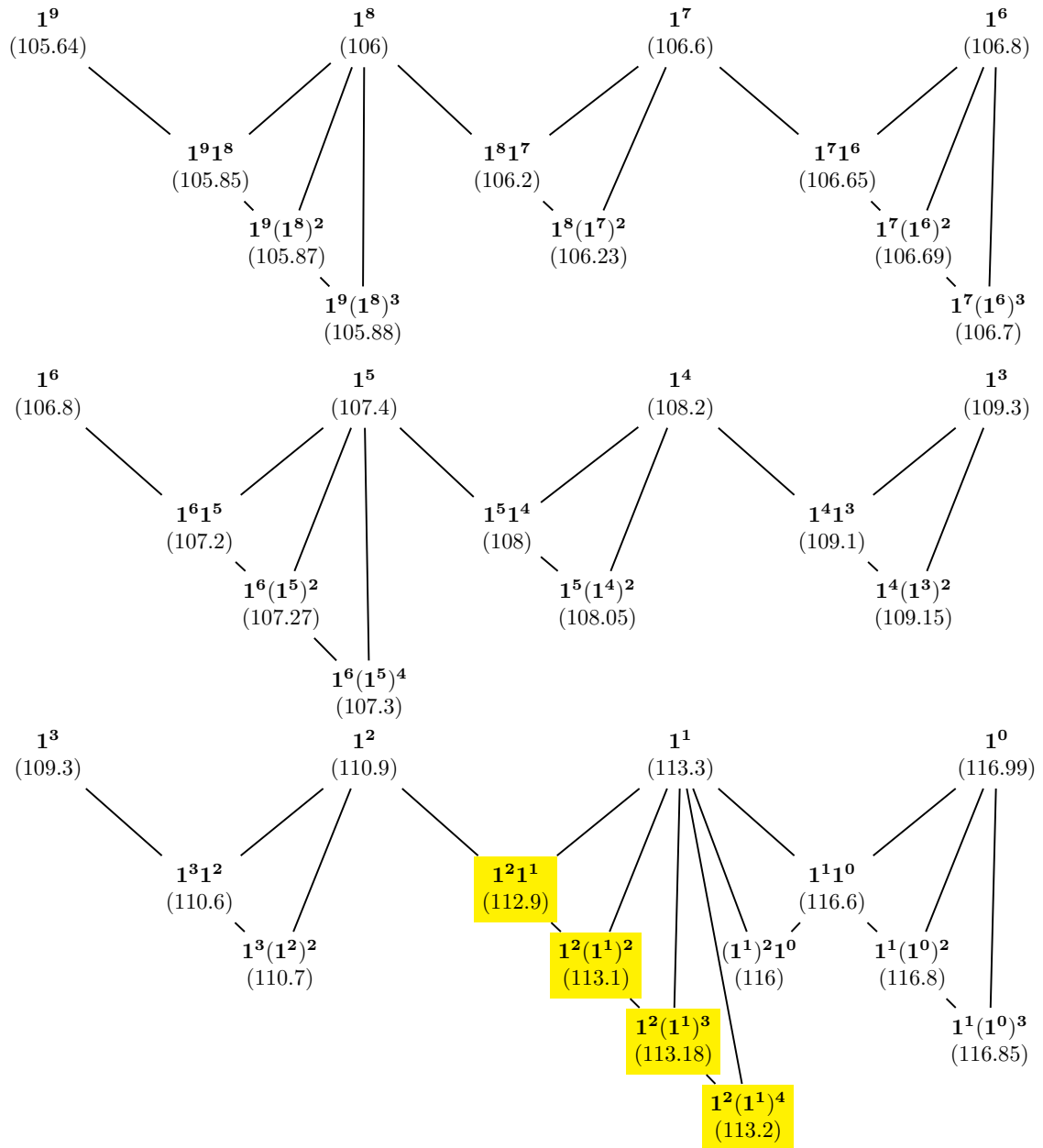


Figure 4.9.: Tree of selected periodic MMOs solutions. Numbers in parentheses are values of I_{ext} in pA corresponding to the solution on top of it. Solutions highlighted in yellow are shown in Figure 4.8.

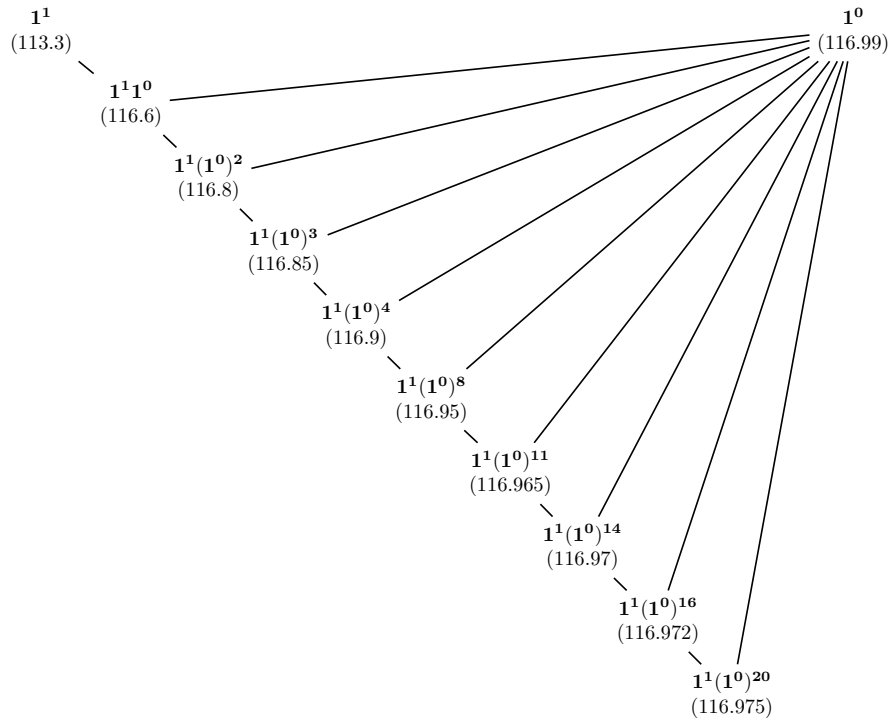


Figure 4.10.: Selected periodic MMOs patterns observed below but close to the cyclic limit point CLP_3 in Figure 4.2c before small amplitude oscillations disappear. Numbers in parentheses are the corresponding values of I_{ext} in pA, corresponding to the solution on top of it.

Table 4.2.: An illustration of MMOs solution sequences satisfying the Farey arithmetic.

MMOs solution	Firing number	$p_1q_2 - p_2q_1$
1^{11}	$\frac{11}{12}$	
$1^{11}1^{10}$	$\frac{11}{12} \oplus \frac{10}{11} = \frac{21}{23}$	1
$1^{11}(1^{10})^2$	$\frac{21}{23} \oplus \frac{10}{11} = \frac{31}{34}$	1
$1^{11}(1^{10})^3$	$\frac{31}{34} \oplus \frac{10}{11} = \frac{41}{45}$	1
1^{10}	$\frac{10}{11}$	1

The firing number of concatenated MMOs solutions can be calculated using the Farey arithmetic [226]. According to this arithmetic, the Farey sum \oplus of two rational numbers p_1/q_1 and p_2/q_2 is defined as:

$$\frac{p_1}{q_1} \oplus \frac{p_2}{q_2} = \frac{p_1 + p_2}{q_1 + q_2}. \quad (4.2)$$

Using this definition, the firing number F of a concatenated solution $L_1^{S_1}L_2^{S_2}$ is, for example, obtained from the following:

$$F = F_1 \oplus F_2 = \frac{S_1 + S_2}{L_1 + S_1 + L_2 + S_2}. \quad (4.3)$$

Furthermore, for the firing numbers of two adjacent solutions in a regular Farey sequence p_1/q_1 and p_2/q_2 , the following condition holds:

$$|p_1q_2 - p_2q_1| = 1. \quad (4.4)$$

An illustration of the Farey arithmetic for specific MMOs solutions sequence is shown in Table 4.2.

Finally, aperiodic MMOs are also found in the gaps between the stable solution branches in Figure 4.6 for values of I_{ext} slightly above the period doubling points. This is illustrated in Figure 4.11 by two simulations. The diagrams on the left demonstrate the dynamic behavior after the startup phase at $I_{ext} = 108.9$ pA, below the period doubling point at $I_{ext} = 108.9962$ pA, with a stable periodic 1^4 MMOs solution.

The diagrams on the right demonstrate a second solution at $I_{ext} = 109$ pA after the startup phase, slightly above the period doubling point. The aperiodic, seemingly chaotic behavior, is not so obvious from the voltage dynamics; however, irregularity is seen in the dynamics of the $s_{1.7}$ variable. In Figure 4.11c, $s_{1.7}$ forms a thick straight band over a long time period, implying that no variation is seen in the $s_{1.7}$ oscillations. However, in Figure 4.11d, irregularity in $s_{1.7}$ is found over this long time period and no repeating patterns are observed.

4.5 Discussion

In this work, an attempt is made to understand the dynamics of a 9D model representative of a small DRG neuron. Small DRG neurons are primary nociceptors and can sense pain. Any damage to them due to injuries, diseases, or genetic disorders, can lead to conditions such as loss or gain of nociceptive pain sensation, and neuropathic or inflammatory pain. A bifurcation analysis of this model can aid in understanding the transition of this system from steady state to mixed-mode oscillations, and finally to full blown periodic firing of action potentials, where oscillations of any frequency indicate pain of a specific form and intensity [191, 192].

The model displays rich dynamics, which is investigated by studying the bifurcations numerically using the external applied current as the primary bifurcation parameter and the maximal conductances \bar{g}_i ($i = 1.7, 1.7, K, KA$) of the sodium and potassium channels as secondary parameters. It is shown that, in particular, $\bar{g}_{1.8}$ and \bar{g}_K are the most sensitive maximal conductances. A detailed analysis for $\bar{g}_{1.8}$ as the secondary parameter is provided. It is shown that there is a hard onset of periodic firing of action potentials due to hysteresis between stable steady state and periodic firing of action potentials for low values of $\bar{g}_{1.8}$. This pattern of behavior can also be found in the original Hodgkin-Huxley equations (see, for example, [217]). For high values of $\bar{g}_{1.8}$, the frequency of firing of action potentials is increasing step by step as we pass through a region of MMOs where the distance between the action potentials is getting smaller and smaller as the number of subthreshold peaks between the action

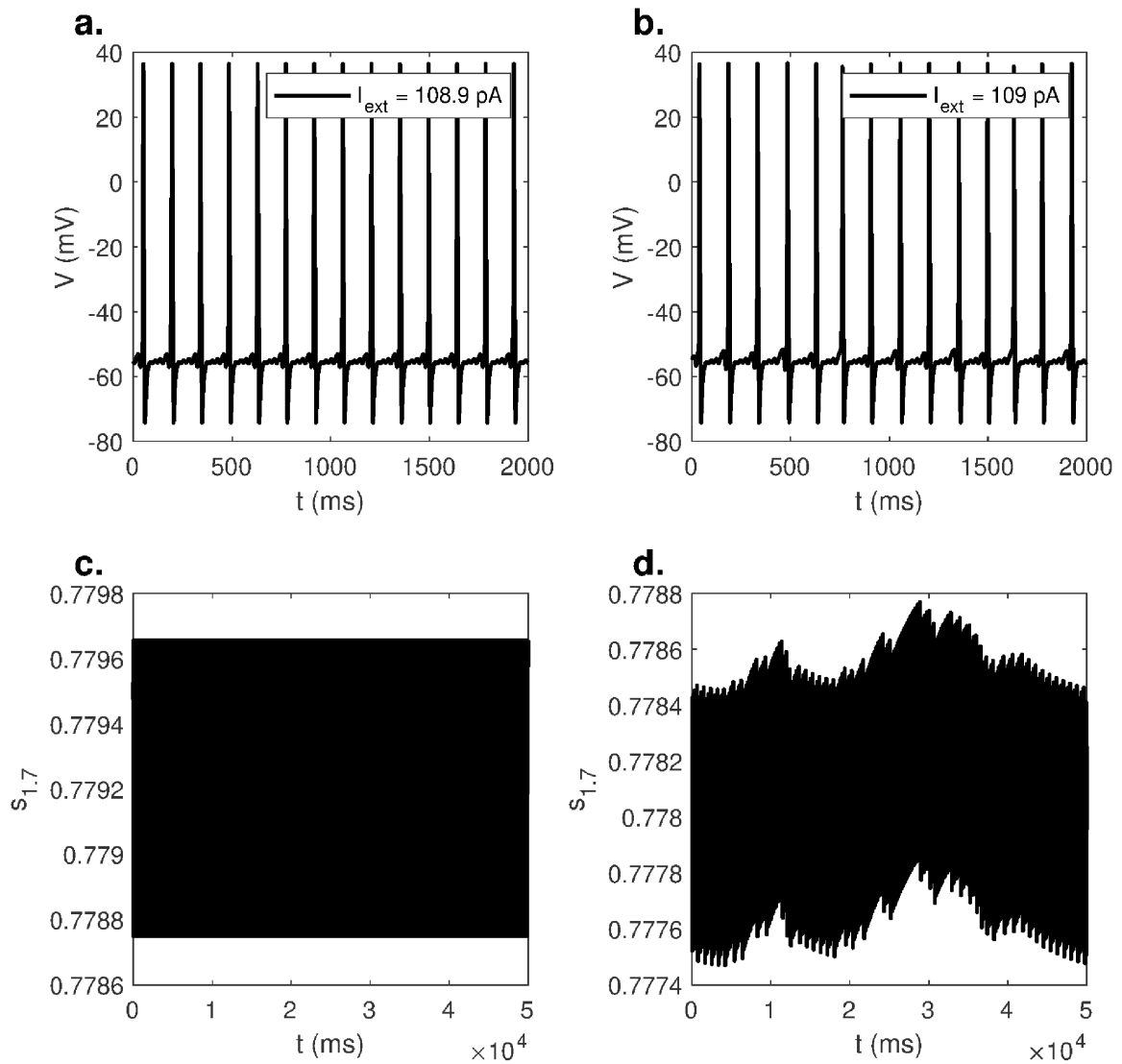


Figure 4.11.: Simulations before and after the period doubling bifurcation at $I_{ext} = 108.9962$ pA. Left column: $I_{ext} = 108.9$ pA, right column: $I_{ext} = 109$ pA. After the period doubling bifurcation, the system exhibits chaotic-like behavior which is evident in the dynamics of $s_{1,7}$.

potentials is reduced step by step until they finally vanish. Although the region of MMOs is rather narrow in terms of I_{ext} for the parameter values considered in this chapter, it represents a second, and a fundamentally different path to pain.

Using selected dynamic simulations, it is conjectured that the periodic MMOs build Farey sequences. Such Farey sequences have also been observed for various other systems displaying MMOs (see [225, 227–230] for examples); however, they have not been widely studied for neuron models (see [231] for an example). Given the diversity and abundance of neuron models that can generate MMOs [223], it will be interesting to explore the existence of Farey sequences in other neuron models as well.

Besides periodic, aperiodic MMOs were also found for very small ranges of I_{ext} . It is conjectured that these aperiodic MMOs solutions are chaotic. Further investigations are required to validate this hypothesis. From a mechanistic point of view, it would be interesting to record such chaotic behavior in DRG cultures and find its implications on pain sensation.

From the mathematical point of view, the 9D model used in this study is rather complex and prohibits further analytical insight as demonstrated for example in [232] for a lower dimensional problem. To gain further theoretical insight it would therefore be desirable to reduce the present model to a lower dimensional problem showing similar patterns of behavior.

From the physiological point of view, the model used in this study is still relatively simple. Towards a more realistic description of small DRG neurons, additional ion channels should be taken into account such as $Na_v1.9$, inward rectifier potassium, and calcium channels. Furthermore, this neuron is long and therefore spatially distributed. A more elaborate model needs to be considered in order to perform a further detailed bifurcation analysis and to capture other dynamical behaviours such as bursting [211]. Moreover, in order to build a more realistic model, experimental validation of the observed dynamical patterns along with the current due to each of the ion channels needs to be done, using patch clamp experiments. Lastly, there is vast heterogeneity in

the characteristics of action potentials observed in small DRG neuron cultures. While some of these neurons spontaneously fire (repetitive firing at $I_{ext} = 0$ pA), others do not [190]. This indicates that simply fixing maximal conductances as constants will not suffice, and there is a need to analyze an ensemble of possible parameter values to capture the heterogeneity observed in electrical recordings. These points have been raised in the previous chapter as well.

Mathematical understanding of the sensing of pain is necessarily an evolving process of manipulating model scale to suitably match the minimum physiological details associated with pain. Each step in this process involves comparing predictions with experimental observations and identifying how parameters connected with various ion channels relate to pain. Thus both model elaboration and reduction are potential future areas of interest, and can enable a rigorous investigation of possible dynamics that can be displayed by this system. This can further shape our understanding of pain sensation and how it can be controlled.

5. A MATHEMATICAL INVESTIGATION OF CHEMOTHERAPY-INDUCED PERIPHERAL NEUROPATHY

This work has been submitted to elife and is currently under review. It is jointly first-authored with Muriel Eaton.

Chemotherapy-induced peripheral neuropathy (CIPN) is a prevalent, painful side effect which arises due to a number of chemotherapy agents. CIPN can have a prolonged effect on quality of life. occasionally, chemotherapy treatment is reduced or stopped altogether because of the severe pain. Currently, there are no FDA-approved treatments for CIPN due to its complex pathogenesis in multiple pathways involving a variety of channels, specifically, voltage-gated ion channels. An indicator of neuropathic pain in an *in vitro* setting is hyperexcitability in dorsal root ganglia (DRG) peripheral sensory neurons. This study employs bifurcation theory to investigate the role of voltage-gated ion channels in inducing hyperexcitability as a consequence of spontaneous firing, due to the common chemotherapy agent paclitaxel. The mathematical investigation here suggests that sodium channel $\text{Na}_v1.8$ and delayed rectifier potassium channel conductances are most critical for hyperexcitability. Introducing paclitaxel into the model, the bifurcation analysis predicts that hyperexcitability is extreme for a medium dose of paclitaxel, which is validated by multi-electrode array recordings. The findings are supplemented using multi-electrode array experiments that reveal that $\text{Na}_v1.8$ blocker A-803467 and delayed rectifier potassium enhancer L-alpha-phosphatidyl-D-myo-inositol 4,5-diphosphate, dioctanoyl (PIP_2) have a protective effect on firing rate in DRG when administered separately together with paclitaxel.

5.1 Introduction

In this study, the focus is on the chemotherapy agent paclitaxel (brand name Taxol). Paclitaxel is a microtubule-binding cancer agent used for several solid tumor cancers such as breast, ovarian, and lung. The conjecture concerning the paclitaxel-induced CIPN (PIP) mechanism is that it reduces axonal transport of mRNA which can lead to axonal degeneration, alters expression of membrane ion channels, and induces inflammation and oxidative stress [4]. Several agents have been tested in clinical trials, but their ability to prevent PIP is still unclear [233]. The hypothesis of this thesis is that, even if one of the effects is brought under control, CIPN can still occur because of degeneracies, i.e., multiple pathways can lead to the same output [93]. Several biological processes are evidenced to be degenerate, including the onset of neuropathic pain [94]. While it is difficult to control and examine multiple events in an experimental setting, it is reasonable to do so by using a mathematical model to investigate degeneracies more effectively by providing the possibility to combine effects and to observe how the system behavior changes upon any external influences. In this study, the role of voltage-gated ion channels and paclitaxel are analyzed using mathematical modeling and bifurcation theory, and the results are supplemented *in vitro*. In particular, degeneracy in neuronal electrophysiology is explored by investigating the role of voltage-gated ion channels in inducing hyperexcitability via spontaneous firing. The hypothesis is that multiple ion channels can lead to hyperexcitability and therefore all of them should be taken into account.

Neurons in both the peripheral and central nervous system (PNS and CNS, respectively) are involved in the pain sensing and relay pathway. Although there is some role of the CNS in CIPN, treatments targeting CNS-based pain pathways have not been sufficient to reduce CIPN [234, 235]. Mainly, CIPN has been studied in the dorsal root ganglia (DRG) peripheral sensory neuron model. Since DRG are pseudo-unipolar, they can relay to other neurons in both the central and peripheral nervous system, thus allowing the different subpopulations of DRG to respond to different

nociceptive stimuli including mechanical, thermal, and chemical [191]. Specifically, a nociceptive pain response can be identified through hyperexcitability, through increased spontaneous firing in voltage-gated sodium channels $\text{Na}_v1.6-1.9$ [236] and potassium channels [237]. DRG are more susceptible to chemotherapy agents than the central nervous system neurons because DRG do not have an extensive neurovascular barrier to limit drug entry [17, 238]. Thus, DRG is chosen to be the model system for this study. In particular, the focus is on the mathematical model of a small DRG neuron, and the results are validated on a DRG neuron culture.

5.2 Results

5.2.1 Model description

The mathematical model is same as the one used in the previous two chapters. It consists of the two sodium channels: $\text{Na}_v1.7$ and $\text{Na}_v1.8$; and two potassium channels: delayed rectifier (KDR) and A-type transient (KA); and one leak channel. Note that the delayed rectifier was denoted as K in the previous two chapters and is denoted as KDR in this chapter. The main equation for membrane voltage is written as:

$$C \frac{dV}{dt} = \frac{I_{ext}}{A} - (i_{1.7} + i_{1.8} + i_{KDR} + i_{KA} + i_l), \quad (5.1)$$

where, I_{ext} is the external applied current, $i_{1.7}$, $i_{1.8}$, i_{KDR} , i_{KA} , i_l are specific ionic currents due to $\text{Na}_v1.7$, $\text{Na}_v1.8$, delayed rectified potassium, A-type transient potassium, and leak channels. C is the specific membrane capacitance, A is the area, V the membrane voltage, and t is time. These ionic currents are written as following:

$$i_{1.7} = \bar{g}_{1.7} m_{1.7}^3 h_{1.7} s_{1.7} (V - E_{Na}), \quad (5.2)$$

$$i_{1.8} = \bar{g}_{1.8} m_{1.8} h_{1.8} (V - E_{Na}), \quad (5.3)$$

$$i_{KDR} = \bar{g}_{KDR} n_{KDR} (V - E_K), \quad (5.4)$$

$$i_{KA} = \bar{g}_{KA} n_{KA} h_{KA} (V - E_K), \quad (5.5)$$

$$i_l = \bar{g}_l (V - E_l), \quad (5.6)$$

where, \bar{g}_i ($i = 1.7, 1.8, KDR, KA, l$) are maximal conductances and are constants. E_{Na} , E_K , and E_l are equilibrium ion potentials. All the activation and inactivation gating variables x ($x = m_{1.7}, h_{1.7}, s_{1.7}, m_{1.8}, h_{1.8}, n_{KDR}, n_{KA}, h_{KA}$) are written in the following in Hodgkin-Huxley form [239]:

$$\frac{dx}{dt} = \frac{x_\infty - x}{\tau_x}. \quad (5.7)$$

The expressions of x_∞ and τ_x , and the parameter values are specified in the appendix B. All the equation forms have been extracted from literature [187].

An indicator of peripheral neuropathy is spontaneous firing: repetitive firing of action potentials for $I_{ext} = 0$. In this work, the parameters that can lead to spontaneous firing and can be potentially impacted by paclitaxel are explored. The maximal ion conductances are varied to explore whether they can induce spontaneous firing since current literature indicates that paclitaxel can manipulate the expression of voltage-gated ion channels [74]. A bifurcation analysis of this model with I_{ext} as the bifurcation parameter can be found elsewhere [159].

First, dynamic simulations for different parameter values were performed. The initial conditions correspond to the stable steady state solution obtained for the parameter values mentioned in Table 5.2. Figure 5.1 demonstrates how the voltage dynamics vary upon increasing $\bar{g}_{1.8}$. For a low value of $\bar{g}_{1.8}$, only a single action potential is observed and the system settles down to a steady state, shown in Figure 5.1A. For a higher value of $\bar{g}_{1.8}$, mixed-mode oscillations (MMOs) are observed, shown in Figure 5.1B. MMOs consist of both small amplitude (subthreshold) and large amplitude (action potential) oscillations. For a higher value, continuous firing of action potentials is observed, shown in Figure 5.1C. In the next section, the focus is on the switch from steady state to continuous firing by treating different channel conductances as bifurcation parameters. Mixed-mode oscillations were investigated in the previous chapter.

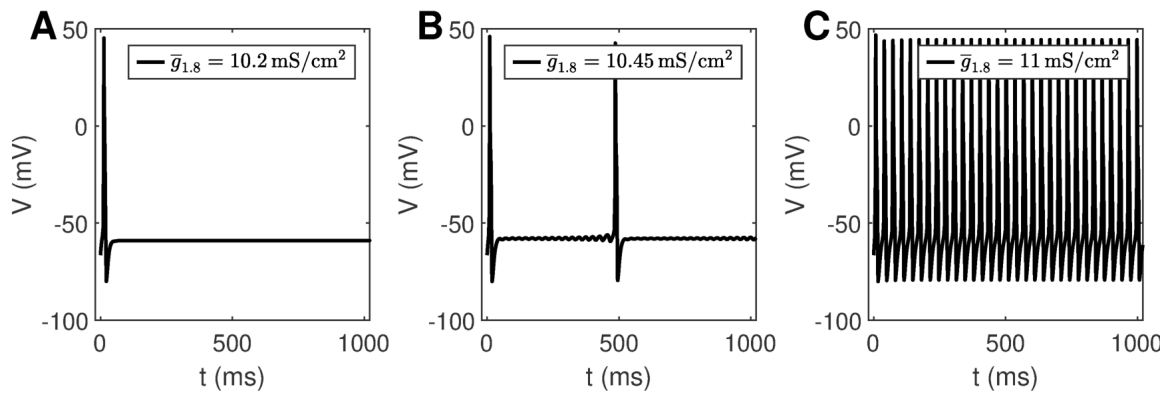


Figure 5.1.: Dynamic simulations obtained by varying $\bar{g}_{1.8}$. A: One action potential followed by a steady state is observed for $\bar{g}_{1.8} = 10.2 \text{ mS/cm}^2$, B: MMOs are observed for $\bar{g}_{1.8} = 10.45 \text{ mS/cm}^2$, and C: Continuous firing of action potentials is observed for $\bar{g}_{1.8} = 11 \text{ mS/cm}^2$

5.2.2 Bifurcation analysis

XPPAUT is used to perform preliminary bifurcation analysis, and confirmation of results is done using MATCONT. Parameter settings for XPPAUT and MATCONT are mentioned in the methods section. As mentioned before, bifurcation diagrams are generated by setting the maximal conductance as the bifurcation parameter, one by one, for each voltage-gated ion channel involved in this model ($\text{Na}_v1.7$, $\text{Na}_v1.7$, KDR, and KA).

5.2.2.1 One-parameter continuation

Firstly, a one-parameter continuation is performed to find bifurcation points which could separate steady state from MMOs, and MMOs from continuous firing of action potentials. A partial bifurcation diagram is shown in Figure 5.2. As seen in Figure 5.2A and D, no bifurcation points are generated upon varying $\bar{g}_{1.7}$ and \bar{g}_{KA} . A single red line, representing stable steady state solutions, is observed. On the contrary, bifurcation points are observed in Figure 5.2B and C. In Figure 5.2B, a subcritical Hopf bifurcation point (HB) is detected upon increasing $\bar{g}_{1.8}$. Beyond this point, steady state solutions become unstable, shown by the black branch. Two turning points/limit points (LP_1 , LP_2) are also detected on the black branch of unstable steady state solutions. Since the Hopf bifurcation point is subcritical, unstable periodic solutions emanate from it, as shown by the blue branch. This branch first turns at a cyclic limit point (CLP_1) and then meets the unstable steady state branch, indicating a homoclinic orbit. This turning is not obvious from the figure, however, it can be observed upon zooming into the branch. Upon moving in the backward direction starting from a large value of $\bar{g}_{1.8}$ resulting in stable periodic solutions, a stable periodic solution branch is generated, indicated in green, finally leading to a cyclic limit point (CLP_2) beyond which the periodic solutions become unstable, indicated in blue. This unstable periodic branch abruptly ends due to the period of the branch increasing substantially, indicating that it may tend towards a period-infinity

solution, as shown in Figure 5.2E. The stable periodic solution branch indicates the spontaneous firing parameter regime. The frequency of spontaneous firing increase with $\bar{g}_{1.8}$, as shown in Figure 5.2E. MMOs are found in some region between the Hopf bifurcation point (HB) and the cyclic limit point (CLP₂), shown by the shaded pink region. A detailed discussion for a similar situation can be found in the previous chapter.

A similar, although horizontally flipped, bifurcation diagram is generated with \bar{g}_{KDR} as the bifurcation parameter, shown in Figure 5.2C. Upon decreasing \bar{g}_{KDR} , a subcritical Hopf bifurcation point (HB) is detected with unstable periodic solutions emanating from it. These unstable periodic solutions also intersect the unstable steady state branch, indicating a homoclinic orbit. Similarly to Figure 5.2B, a stable periodic solution branch (indicated by green circles) is detected as well which becomes unstable after a cyclic limit point (CLP₂). As shown in Figure 5.2F, the unstable periodic solution again seems to tend towards a period-infinity solution. Moreover, the frequency of spontaneous firing decreases with increase in \bar{g}_{KDR} .

These bifurcation diagrams indicate that manipulating $\bar{g}_{1.8}$ or \bar{g}_{KDR} can induce spontaneous firing, while manipulating $\bar{g}_{1.7}$ or \bar{g}_{KA} will not decrease hyperexcitability. Therefore, to reverse hyperexcitability, Na_v1.8 and KDR channels should be targeted. These channels were targeted in case of paclitaxel-induced hyperexcitability, in a DRG culture, the results of which are described in the Experimental validation results section.

5.2.2.2 Two-parameter continuation

Two-parameter continuation was also performed in order to explore the combinational effects of these conductances. To this end, the changes in the detected bifurcation points upon changing another maximal conductance are observed. In particular, continuation of HB, LP₁, LP₂, and CLP₂ was performed. These results are shown in Figure 5.3.

As seen in Fig 5.3A and 5.3B, $\bar{g}_{1.7}$ and \bar{g}_{KA} do not impact the bifurcation points substantially even in combination with $\bar{g}_{1.8}$. Decrease in \bar{g}_{KA} can shift the cyclic limit point of $\bar{g}_{1.8}$ to the right, as seen in Fig 5.3B, which implies that the MMOs regime will become wider. In both the cases, the bifurcation points vary within a narrow range of $\bar{g}_{1.8}$. Similarly, Fig 5.3C and 5.3D show that $\bar{g}_{1.7}$ and \bar{g}_{KA} do not impact the bifurcation points substantially even in combination with \bar{g}_{KDR} . In these two cases, increase in $\bar{g}_{1.7}$ and \bar{g}_{KDR} can lead to a region of bistability where stable steady state and continuous firing of action potentials solutions coexist. However, the bifurcation points only vary within a narrow range of \bar{g}_{KDR} . Upon varying $\bar{g}_{1.8}$ and \bar{g}_{KDR} together, the bifurcation points vary linearly, as shown in Fig 5.3E. This indicates that decreasing $\bar{g}_{1.8}$ and increasing \bar{g}_{KDR} can eliminate spontaneous firing.

Figure 5.2.: A-D: Bifurcation diagrams obtained by keeping A: $\bar{g}_{1.7}$, B: $\bar{g}_{1.8}$, C: \bar{g}_{KDR} , and D: \bar{g}_{KA} as the bifurcation parameters. E-F: Frequency versus maximal conductance obtained in the periodic firing regime with E: $\bar{g}_{1.8}$ and F: \bar{g}_{KDR} as the bifurcation parameters. The frequency of firing increases with $\bar{g}_{1.8}$ and decreases with \bar{g}_{KDR} . The frequency of unstable periodic solutions tends towards zero, implying that the unstable branch is ending in a period-infinity solution.

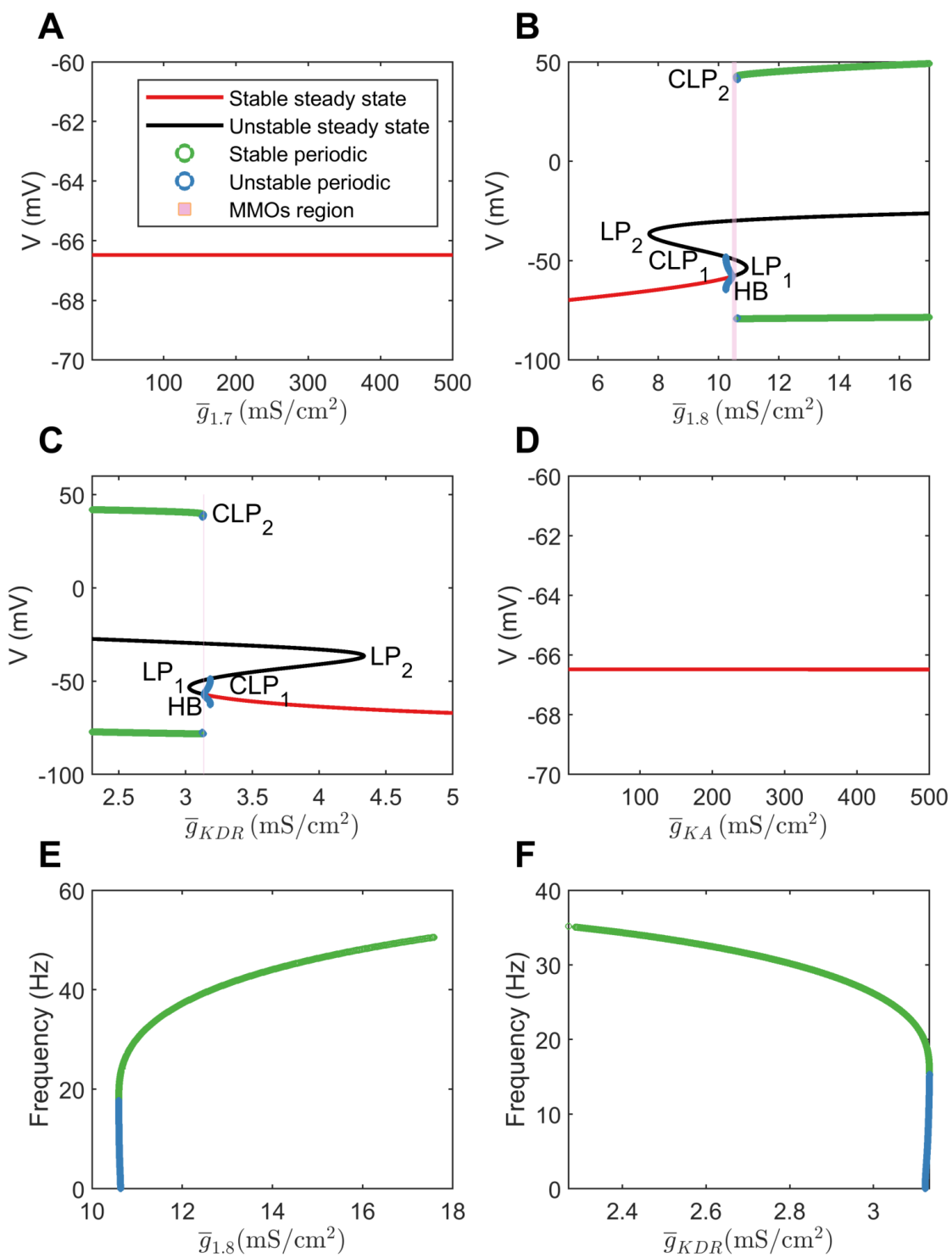


Figure 5.2.: (Caption described in previous page.)

5.2.3 Effect of Paclitaxel

Current literature suggests that paclitaxel can impact gene expression of various voltage-gated ion channels [20, 74]. However, it is not known whether the impact is direct or indirect. Evidence suggests that paclitaxel impacts inflammatory cytokines, which can subsequently manipulate the ion channels [20]. For example, these inflammatory signals can increase sodium current [16]. Moreover, a sigmoidal dose-dependent relation is observed between paclitaxel and macrophage IL-12, as seen in Fig 3 in [240]. Based on these evidences, a Hill's kinetics type relation between paclitaxel and ion channel maximal conductances is assumed in this work. Hill's kinetics are widely used to model dose-response curves. It is assumed that the conductances will vary as a function of paclitaxel dosage. Moreover, it is assumed that paclitaxel will lead to an increase in maximal conductance of both the sodium channels, while it would lead to a decrease in maximal conductance of both the potassium channels since these cases would lead to spontaneous firing. Therefore, the following relationships are considered:

$$\bar{g}_{1.7,new} = \bar{g}_{1.7} + (\bar{G}_{Na,max} - \bar{g}_{1.7}) \frac{[P]^{h_n}}{[P]^{h_n} + k_{0.5}^{h_n}} \quad (5.8)$$

$$\bar{g}_{1.8,new} = \bar{g}_{1.8} + (\bar{G}_{Na,max} - \bar{g}_{1.8}) \frac{[P]^{h_n}}{[P]^{h_n} + k_{0.5}^{h_n}} \quad (5.9)$$

$$\bar{g}_{KDR,new} = \bar{g}_{KDR} + (\bar{G}_{K,min} - \bar{g}_{KDR}) \frac{[P]^{h_n}}{[P]^{h_n} + k_{0.5}^{h_n}} \quad (5.10)$$

$$\bar{g}_{KA,new} = \bar{g}_{KA} + (\bar{G}_{K,min} - \bar{g}_{KA}) \frac{[P]^{h_n}}{[P]^{h_n} + k_{0.5}^{h_n}} \quad (5.11)$$

where, h_n is Hill's coefficient, $[P]$ is the paclitaxel concentration (in nM), $k_{0.5}$ is the half maximal effective concentration, $\bar{g}_{i,old}$ ($i = 1.7, 1.8, KDR, KA$) is the original maximal conductance value, $\bar{g}_{i,new}$ is the updated maximal conductance value from the above equation. $\bar{G}_{Na,max}$ and $\bar{G}_{K,min}$ stand for the upper or the lower limit of the maximal conductances.

Figure 5.3.: Two parameter continuations performed for the Hopf bifurcation point HB, limit points LP_1 and LP_2 , and cyclic limit point CLP_2 . A: Continuation plot for $\bar{g}_{1.7}$ versus $\bar{g}_{1.8}$ show that the bifurcation points generated by keeping $\bar{g}_{1.8}$ as the bifurcation parameter do not shift upon varying $\bar{g}_{1.7}$. B: HB and LP's of $\bar{g}_{1.8}$ bifurcation diagram do not shift upon varying \bar{g}_{KA} . CLP_2 shift rightwards upon decreasing \bar{g}_{KA} . This implies that the MMOs region will be wider in this case. C: Bifurcation points of \bar{g}_{KDR} do not shift upon varying $\bar{g}_{1.7}$. D: HP and LP's of \bar{g}_{KDR} do not shift upon varying \bar{g}_{KA} . CLP_2 shifts leftwards upon decreasing \bar{g}_{KA} . This implies that the MMOs region will become narrower in this case. E: A linear combinational effect is seen between $\bar{g}_{1.8}$ and \bar{g}_{KDR} . Note that the thin gap between stable steady state and continuous firing regimes is the MMOs region.

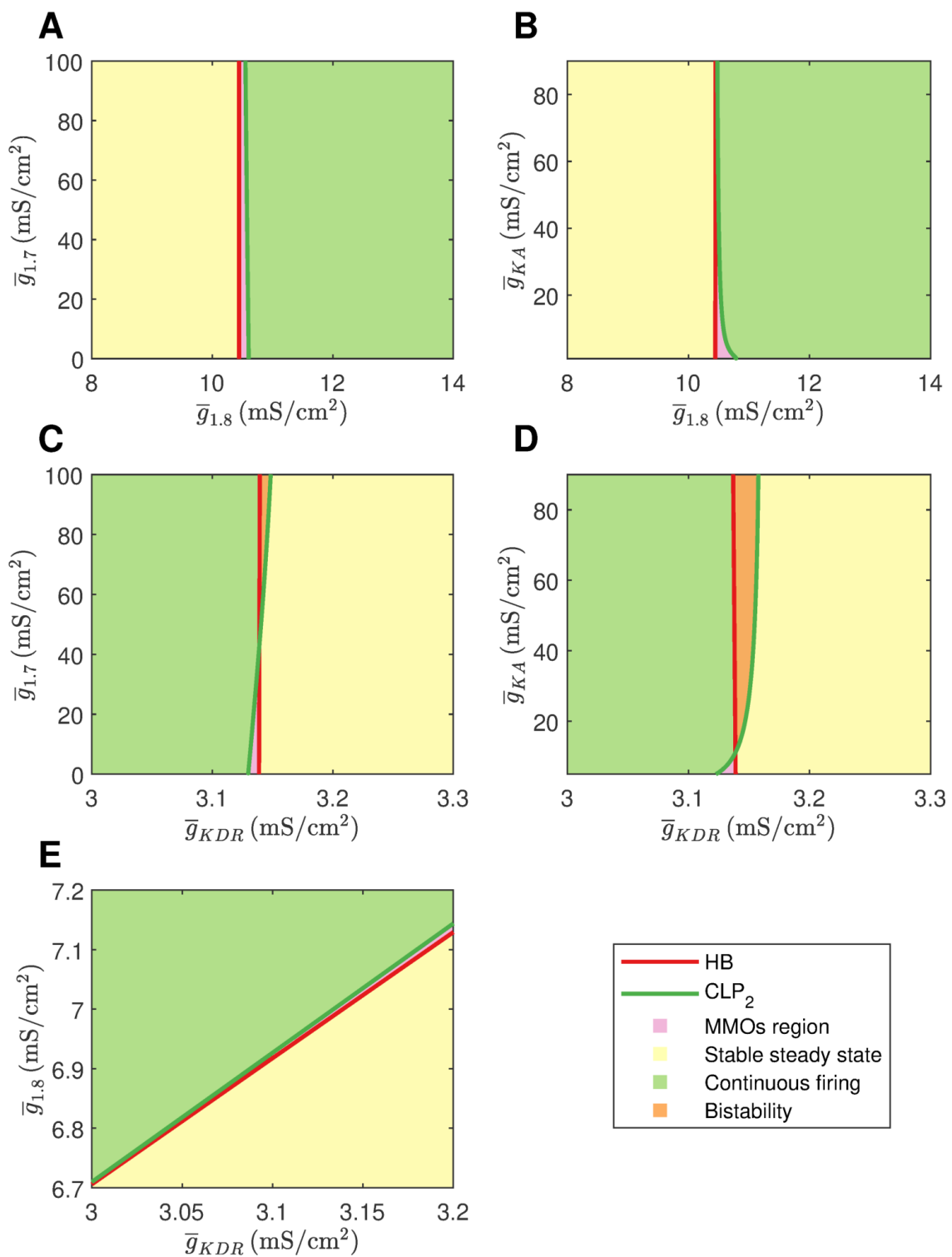


Figure 5.3.: (Caption described in previous page.)

Depending on \bar{G}_j ($j = Na, max, K, min$) and h_n , the relationship between [P] and $\bar{g}_{i,new}$ ($i = 1.7, 1.8, KDR, KA$) will vary, as shown in Supplementary figure S1 FigA, S1 FigB, and S1 FigC. Increasing or decreasing \bar{G}_j increases or decreases the maximal conductance parameter ($\bar{g}_{i,new}$) range covered upon varying [P]. Large h_n creates sigmoidal curves. Decreasing h_n makes the curve seem exponential. The values of \bar{G}_j and h_n are assumed. See supplementary figure S2 Fig for a sensitivity analysis of these parameters with respect to the bifurcation points.

Following this, numerical bifurcation analysis with paclitaxel concentration [P] as the bifurcation parameter was performed. A partial bifurcation diagram is shown in Figure 5.4A. Figure 5.4A shows that upon stable steady state solution continuation, a subcritical Hopf bifurcation point (HB_1) is found beyond which the solutions become unstable. Unstable periodic solutions emanate from this Hopf bifurcation point. Upon continuation of the unstable steady state solution branch in black, a supercritical Hopf bifurcation point (HB_2) is found, beyond which the steady state solutions become stable again. Stable periodic solutions (indicated in green) emanate from this point. The paclitaxel-interval between these two Hopf bifurcation points constitutes the spontaneous firing regime. The subinterval where the periodic and the steady state branch are unstable (between PD and CLP_4) corresponds to the MMOs regime. MMOs of this model have been studied in some detail in the previous chapter. A detailed investigation of the MMOs shown in Figure 5.4A was beyond the scope of this work. Stable periodic solutions with a small amplitude arise from the supercritical Hopf bifurcation point which turn unstable after a cyclic limit point (CLP_4). The unstable periodic solutions finally become stable after a subcritical period doubling bifurcation point (PD) when going in the direction of decreasing [P]. The stable periodic solutions become unstable again after a cyclic limit point (CLP_2).

The frequency of firing in the first stable periodic solutions regime (between CLP_2 and PD) is shown in Figure 5.4B. It is shown that upon increasing paclitaxel concentration, frequency of firing first increases, and then decreases after reaching a

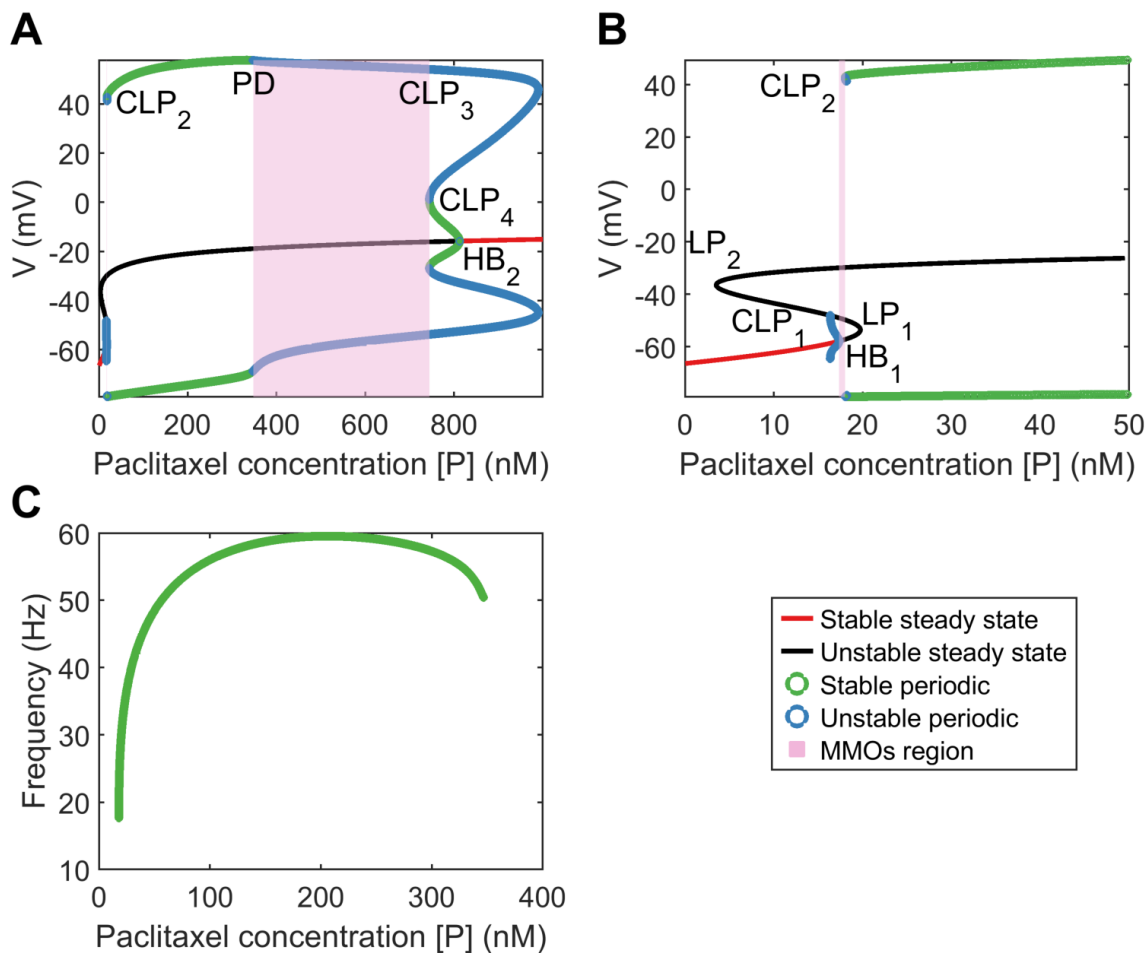


Figure 5.4.: A: Bifurcation diagram obtained by treating paclitaxel concentration as the bifurcation parameter. B: A zoomed in version of the bifurcation diagram in A. HB_1 : subcritical Hopf bifurcation point, HB_2 : supercritical Hopf bifurcation point, LP_1 and LP_2 : limit points, CLP_1 , CLP_2 , CLP_3 , and CLP_4 : cyclic limit points, PD: periodic doubling bifurcation point. C: Frequency plot for the stable periodic firing region. Frequency first increases and then decreases upon increasing paclitaxel concentration. Left and right end points of this curve refer to CLP_2 and PD, respectively.

maximum firing rate. Beyond the PD point, the frequency of firing decreases further since the solutions are of MMOs type.

5.2.4 Experimental validation results

A high-throughput way to continuously record neuronal firing patterns is to use multielectrode array (also referred to as microelectrode array, MEA). This system is capable of recording of extracellular voltage potentials with millisecond temporal resolution of neurons in cultures grown on a 768 array of electrodes up to 96 well format, which makes it high-throughput.

To validate the mathematical modeling of the effect of paclitaxel dose on hyperexcitability, the firing for different doses of paclitaxel was measured. Low doses (10 nM) and high doses (1 μ M) of 24-hour paclitaxel administration caused lower firing than 250 nM paclitaxel as expected (Fig 5.5A). Thus, 250 nM was decided as the dose of paclitaxel for the subsequent experiments. Na_v1.8 blocker A-803467 and KDR enhancer L-alpha-phosphatidyl-D-myo-inositol 4,5-diphosphate, dioctanoyl (PIP₂) when administered separately together with paclitaxel reduces the number of spontaneous firing neurons (Table 5.1) and firing rate (Fig 5.5B). Similarly, the representative heat maps of firing frequency reveals the same trend qualitatively (Fig 5.5C). However, when A-803467 and PIP₂ are administered simultaneously together with paclitaxel, it causes a significant increase in mean firing rate compared to the media control. Specifically, the mean firing rate fold change from baseline is 1.16 ± 0.07 for media control and increases to 1.50 ± 0.10 for paclitaxel ($p < 0.0001$ compared to media). Na_v1.8 blocker A-803467 decreases the firing rate to 1.28 ± 0.07 ($p = 0.0449$ compared to paclitaxel). Similarly, KDR enhancer PIP₂ reduced paclitaxel-induced hyperexcitability to 1.28 ± 0.09 ($p < 0.0001$ compared to paclitaxel). These results match the prediction from the bifurcation analysis that blocking Na_v1.8 and enhancing KDR will protect against paclitaxel-induced hyperexcitability. However, when Na_v1.8 blocker A-803467 and KDR enhancer PIP₂ are administered in combination, the mean firing fold change from baseline is 1.56 ± 0.09 ($p < 0.0001$ compared to media control).

Table 5.1.: Spontaneous neurons. Pax: Paclitaxel, Na_v1.8-: Na_v1.8 blocker, KDR+: KDR enhancer

Treatment	Paclitaxel (nM)	Fold change	Percent change
Media	None	0.94	-3.64 %
Pax	250	1.42	21.09%
Na _v 1.8-	250	1.27	11.83%
KDR+	250	1.28	5.64%
Na _v 1.8- and KDR+	250	2.53	50.49%

5.3 Discussions

CIPN is a debilitating experience for cancer patients with no current established methods of preventing or treating it due to minimal understanding of its pathophysiology [5]. In this work, a novel mathematical approach is applied using bifurcation theory to understand the role of sodium and potassium ion channels in CIPN. To this end, a mathematical model representative of a small DRG neuron is analyzed. Maximal conductances were kept as bifurcation parameters to identify those that can induce spontaneous firing (an indicator of peripheral neuropathy). Furthermore, MEA experiments were used to support the findings.

Using bifurcation theory, it is found that, increasing $\bar{g}_{1.8}$ and decreasing \bar{g}_{KDR} can induce spontaneous firing (see Fig 5.2). The effect may be aggravated in combination, as seen from the two parameter plot in Fig 5.3E. These results indicate that a Na_v1.8 blocker should reduce spontaneous firing which supports the role of Na_v1.8 in contributing to the increased excitability in peripheral neuropathy [241, 242]. The significance of blocking Na_v1.8 in PIPN was also observed in our MEA experiment in that Na_v1.8 blocker A-803467 had a neuroprotective effect on paclitaxel-induced hyperexcitability when administered together in DRG neuron culture (Fig 5.5). Similarly, KDR was indicated in the model and MEA finding to be involved with hyperexcitability which is supported by literature [237]. Although these results are for

Figure 5.5.: Multielectrode array (MEA) firing summary shows amelioration of hyperexcitability after treatment of A-803467 ($\text{Na}_v1.8$ blocker) and PIP_2 (KDR enhancer). All parameters are reported as fold change (treatment over baseline of culture before treatment). A) Mean firing rate for different dosages of paclitaxel. B) Mean firing rate reveals a significant increase in paclitaxel firing from media control ($p < 0.0001$), a decrease from paclitaxel when A-803467 and PIP_2 are administered separately ($p = 0.0449$ and $p < 0.0001$, respectively), but a significant increase from media when administered together ($p < 0.0001$). C) Heatmap of representative MEA recordings with firing frequency of each active electrode colorcoded: warm colors (red, orange, yellow) represent high firing frequency (white=10Hz); cool colors (green, blue) represent low firing frequency (black=0Hz). Each circle represents a spontaneous firing neuron within the 8 X 8 electrode array. Top row is baseline at time 0 before treatment is added. Bottom row is 24 hours after treatment was added. Asterisks denote statistical significance from Mann-Whitney U test (* $P < 0.05$, ** $P < 0.01$, *** $P < 0.001$)

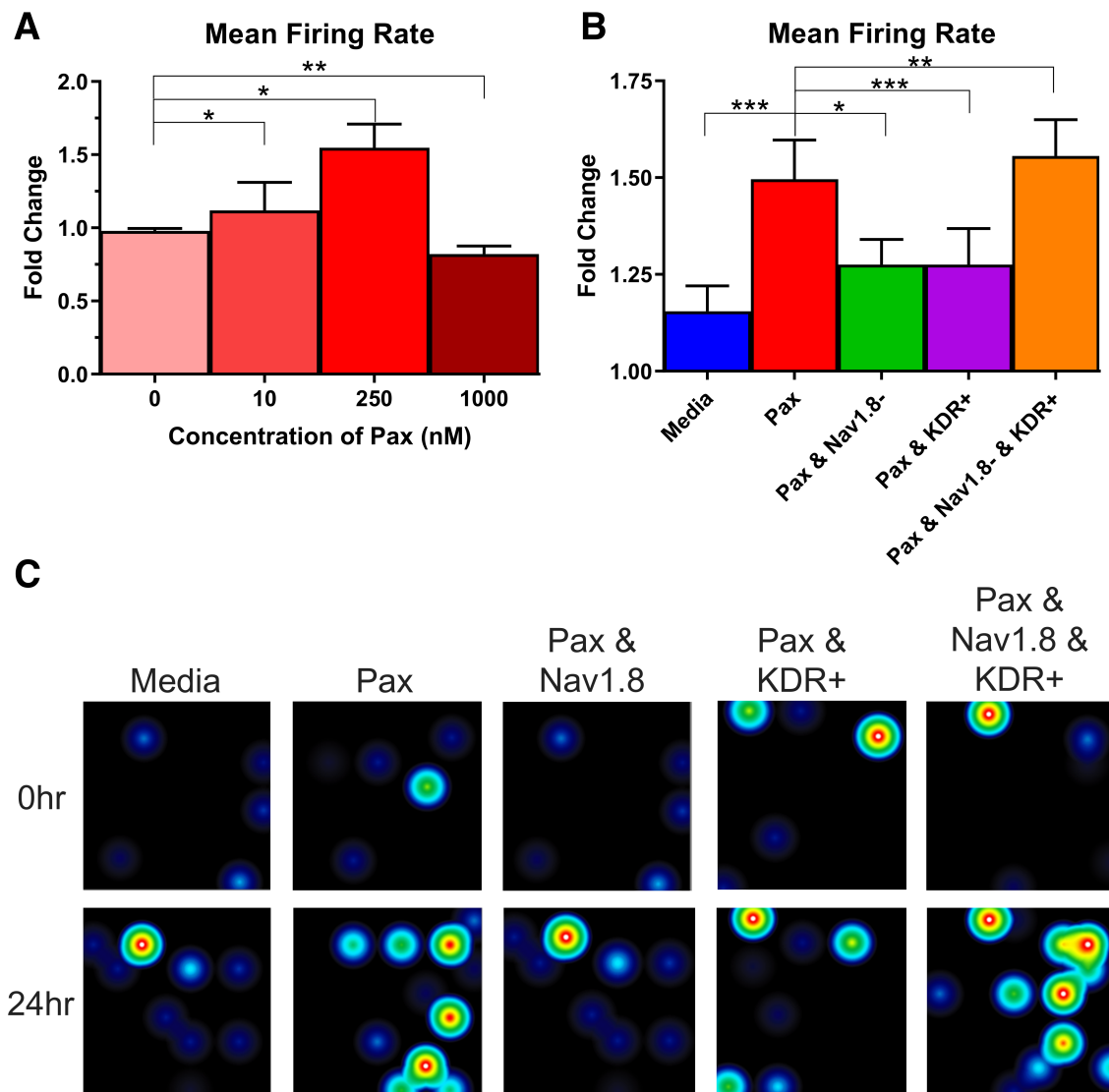


Figure 5.5.: (Caption described in previous page.)

specific dosages of A-803467 and PIP₂ to observe the change in excitability, this electrophysiology data support the trends found in the bifurcation analysis. Depending on the amount of A-803467 and PIP₂, hyperexcitability should change. Interestingly, Na_v1.8 and KDR channels were found to be sensitive even with I_{ext} as the primary bifurcation parameter [243] as mentioned in previous Chapter 4. It will be of interest to investigate their protective effects on CIPN due to other chemotherapy agents such as vincristine and oxaliplatin, as well.

A Hill's type kinetics is assumed for the effect of paclitaxel on the ion channels. Based on this, a partial bifurcation diagram is generated, treating paclitaxel concentration as the bifurcation parameter. This bifurcation diagram indicates that spontaneous firing should arise for a mid-range of paclitaxel dosage. Moreover, firing rate should first increase and then decrease, seen from the frequency diagram in Fig 5.4C. A similar trend is seen in the MEA recordings, shown in Fig 5.5A. Firing rate is larger for the middle values of paclitaxel concentration in the range considered here. The frequency diagram (Fig 5.4C) may not reflect the actual reason for this trend. It may be that the cells died at a higher concentration, or they may not fire because of manipulation of the ion channels as shown by a mathematical relationship with paclitaxel. Further investigation is required to establish with certainty the reason behind this observation.

The parameters for the relationship between paclitaxel and ion channel maximal conductances are also assumed (see Table 5.2). In the supplementary figure S2 Fig, it is shown how the behavior of the model varies upon changing these parameters. Upon varying h_n , $\overline{G}_{Na,max}$, or $\overline{G}_{K,min}$, the qualitative behavior of the diagram does not change for the range of parameters considered here; stable steady states, MMOs, and continuous firing regimes are observed. Assuming that Hill's kinetics is a reasonable relationship between paclitaxel and ion channel conductance, defined upper and lower limits of how much the conductances can vary may exist. These parameters can be estimated by recording currents due to each of these ion channels for different doses of paclitaxel, using patch-clamping experiments. Lastly, the value of $k_{0.5}$ used in

this mathematical model (500 nM) is different from the paclitaxel dose amount used for the MEA experiment (250 nM). This is because the value was estimated from literature which was based on the IC₅₀ value for iPSC-derived human neurons and clinical data based on paclitaxel's toxicity on cancer cells [244,245]. However, as seen in 5.4C, maximum spontaneous firing is observed around 200 nM. Since the only intention is to perform a qualitative comparison between the bifurcation diagram (Fig 5.4A) and MEA paclitaxel dose trend (Fig 5.5A), the value of $k_{0.5}$ assumed is not important. A different value of $k_{0.5}$ will shift the complete bifurcation diagram, however, the qualitative structure of the diagram will remain the same.

The mathematical model that is considered here is a minimal model representing dynamics of one type of peripheral neurons: small DRG neurons (as mentioned in previous chapters). *In vivo*, many more ion channels such as inward rectifier potassium and calcium channels are present in this neuron, and they need to be added to the model in future studies. More detailed mathematical models have been developed previously and can be used for this purpose [246]. Paclitaxel can also induce cytosolic calcium oscillations [65], which can again be analyzed using bifurcation theory. Another factor to add in future models is the impairment of axonal transport that occurs due to paclitaxel and its effect on microtubules [247], which can be modeled using cable equations [248]. As mentioned previously, the effect of paclitaxel on ion channels may be indirect and due to other inflammatory cytokines [20]. In the future, this can also be included in the model. Lastly, this model consists of only small DRG neurons. However, paclitaxel impacts medium and large DRG neurons as well [74]. It will be of interest to evaluate models representing different subtypes of DRG neurons and investigate the role of voltage-gated ion channels specific to each of them. The experimental setup recorded firing of all DRG subtypes. The blocker and enhancer may have regulated ion channels in other DRG neurons as well. However, it can be said with certainty that Na_v1.8 blocker acted on small DRG neurons since it is only present in them. PIP₂ may have acted on other ion channels of other DRG subtypes.

Similarly, paclitaxel may have impacted the firing rate of all DRG subtypes. This will require further investigation in the future by recording DRG subtype-specific firing.

DRG neuron firing has been correlated with neuropathic pain *in vitro* [190,249], thus analyzing changes in firing patterns allows for a surrogate to study “pain in a dish”. Recent advances in neuroelectrophysiology technology have allowed for more temporal and spatial dynamic data collection on live cells. A non-invasive method was chosen here to measure the electrophysiological properties (spontaneous/non-evoked firing rate) of a network of neurons through microelectrode array (MEA) recording. Therefore, MEA was used to support our model outputs by recording the neuronal activity of the effect of paclitaxel on cultured DRG neurons, as shown in Fig 5.5. From the MEA recordings, molecule antagonism is observed that is not accounted for in the mathematical model. There was an increase in firing rate when the $\text{Na}_v1.8$ blocker and K enhancer were both administered together concurrently with paclitaxel. Various mechanisms could have led to this antagonism. Here, one possibility is stated. A-803467 acts on $\text{Na}_v1.8$ in the inactivation state [250]. However, the potassium enhancer PIP_2 is not specific to the delayed rectifier. It can potentially activate protein kinase C (PKC) [251], which can regulate $\text{K}_v3.4$ (an A-type potassium channel enriched in small DRG neurons [252]) and reduce the action potential duration [253]. This would lead to a reduction of the availability of $\text{Na}_v1.8$ in the inactivated state. Therefore, an increase in firing rate could be seen since one drug (PIP_2) can counteract the action of the other (A-803467). This is based on the guarded receptor [254] or the modulated receptor [255] hypotheses, and such an increase in firing, when such drugs are administered in combination, has been observed in case of arrhythmia [256]. Therefore, more factors seem to be involved, and this needs further investigation. As of now, any small DRG neuron delayed rectifier enhancers are not known. PIP_2 can also regulate inward rectifying potassium channels, transient receptor potential (TRP), and voltage-gated calcium channels [251]. It is, therefore, unclear if a reduction in spontaneous firing was indeed due to enhancement of the delayed rectifier. For an accurate validation of the bifurcation analysis, specific channel blockers and

Table 5.2.: Model parameter values

Parameter	Value	Units	Reference
$k_{0.5}$	500	nM	[244, 245]
h_n	1	Unitless	Assumed
$\bar{G}_{Na,max}$	100	mS/cm ²	Assumed
$\bar{G}_{K,min}$	0.1	mS/cm ²	Assumed

enhancers will be needed. Moreover, it is expected that adding more of A-803467 or PIP₂ should counteract this molecular antagonism.

The bifurcation analysis identified that Na_v1.8 and KDR are involved with the induction of spontaneous firing, associated with paclitaxel-induced hyperexcitability. This approach, along with patient-specific pharmacokinetics of paclitaxel, can be applied to the clinic by obtaining the patients electrophysiological profile using patch clamp or MEA and using those values as parameters in our model to determine the optimal dose of paclitaxel based on the individual, and for examining acute versus chronic onset of PIPN. Also, treatments can be designed to specifically block Na_v1.8 or enhance KDR conductance to reduce hyperexcitability caused by paclitaxel since the corresponding channels have been identified as the most relevant ones.

5.4 Materials and methods

5.4.1 Model parameter values

The model parameter values and the corresponding references are mentioned in Table 5.2. Remaining parameter values can be found in appendix B.

5.4.2 XPPAUT settings

All the bifurcation diagrams were primarily generated from XPPAUT [193]. Confirmation of the results were done using MATCONT [213]. Moreover, two parameter

continuation was performed using MATCONT. All the plots were generated using MATLAB [214].

NTST = 100, Method = Stiff, Tolerance = 1e-07, EPSL, EPSU, EPSS = 1e-07, ITMX, ITNW = 20, Dsmin = 1e-05, Dsmax = 0.05 (there may be a need to adjust Dsmax to 0.1). There may be a need to adjust Ds to 0.01. All other settings were same as default.

5.4.3 MATCONT settings

MaxCorrIters = 20, MaxTestIters = 20, FunTolerance = 1e-6, VarTolerance = 1e-6, TestTolerance = 1e-5, MaxStepsize = 0.01.

When keeping paclitaxel as the bifurcation parameter, following settings are changed from the above:

MaxStepsize = 0.001, InitStepsize = 0.0001, MinStepsize = 1e-7.

5.4.4 Reagents

200 nM A-803467 (Na_v1.8 inhibitor) and 100 μM L-alpha-phosphatidyl-D-myoinositol 4,5-diphosphate, dioctanoyl (PIP₂, KDR enhancer) were diluted in NbActiv4 recording media (BrainBits, Springfield, IL, USA). Complete saline solution (CSS) was made from 137 mM NaCl, 5.3 mM KCl, 1 mM MgCl₂-6H₂O, 25 mM sorbitol, 10 mM HEPES, and 3 mM CaCl₂ equilibrated to pH 7.2.

5.4.5 Primary Cell Culture

Dorsal root ganglia (DRG) was extracted from wild-type Sprague-Dawley rat pups 7-14 days old. Animals were maintained in the norovirus-negative facility of the Centrally Managed Animal Facilities at Purdue University. They were housed in at a constant temperature and humidity on a 12:12 light-dark cycle (lights on 0600-1800) with ad lib access to food and water according to as approved by the Purdue Animal Care and Use Committee and the Institutional Animal Care and Use Committee

(IACUC) and will be conducted in accordance with the National Institutes of Health Guide for the Care and Use of Laboratory Animals. Pups were placed on a paper towel on ice for two minutes before decapitation. The spinal cord was extracted and the DRG was dissected and placed in complete saline solution (CSS). Cells were prepared by centrifuging at $2.5 \times g$ for 30 seconds then adding 1.5 mg/mL of collagenase A in CSS with 0.05 mM EDTA. After rotating in the 37C incubator for 20 minutes, cells were spun at $2.5 \times g$ for 30 seconds. 1.5 mg/mL collagenase D and 30U papain in CSS were added then placed in the incubator rotator for 20 minutes. Cells were spun at $2.5 \times g$ for 3 minutes. DRG were triturated in 1 mL of 0.15% trypsin inhibitor and 0.15% bovine serum albumin (BSA) in Dulbeccos Modification of Eagles Medium (DMEM) medium with 10% fetal bovine serum (FBS) (Corning, Corning, NY, USA) then spun again at $2.5 \times g$ for three minutes before placing in a $40 \mu\text{M}$ filter before seeding on a coated plate. DRG from one pup was divided into six wells. Culture media was changed after two days to NbActiv4 recording media (BrainBits, Springfield, IL, USA). Four days after seeding, culture was recorded.

5.4.6 Micro/multielectrode Array (MEA)

Firing properties was recorded using a Maestro Pro (Axion BioSystems, Atlanta, GA, USA). Twelve well plates of 64 electrodes per well used for culture. Plates were coated the day of seeding by incubating with poly-d-lysine for two hours, washing with sterile milli-q water three times, then incubating with laminin for one hour. All recordings were at 37°C . The plate was recorded before treatment and 24 hours after treatment. Then $200 \mu\text{L}$ of $1.0 \mu\text{M}$ capsaicin was added and recorded for two minutes as a positive control. Analysis was performed using the manufacturers software, Axion BioSystems Integrated Studio (AxIS) and NeuroMetric Tool. An electrode ($n=1$) was considered active if there was more than two action potentials in the baseline, response to buffer, or response to capsaicin. Mean firing rate (Hz) was calculated for active electrodes. An electrode will be considered active ($n=1$) if it has >1 spikes per 200 seconds. Chili pepper compound capsaicin will be added into the system to trigger

a sensory response. Fold change of response to treatment was calculated based on baseline of the culture before treatment (treatment after 24 hours)/(cells at time zero before treatment). Recordings were compiled from different cultures extracted from different animals on different days.

5.4.7 Statistics

A Shapiro-Wilk test determined that the data was not normal so Krushal-Wallis and Mann-Whitney U test were used to determine statistical significance of treatment differences. Results are presented as mean \pm S.E.M. Effect size is Cohens D. P-value was set at $p \leq 0.05$ (*), $p \leq 0.01$ (**), and $p \leq 0.001$ (***). P-value is the probability that the means of two groups are either the same or different based on a threshold level of marginal significance ($p=0.05$). If $p < 0.05$, one can be 95% confident that the means are significantly different. GraphPad Prism 8.3.0 was used to determine statistical significance.

5.5 Supporting information

S1 Fig.

S2 Fig.

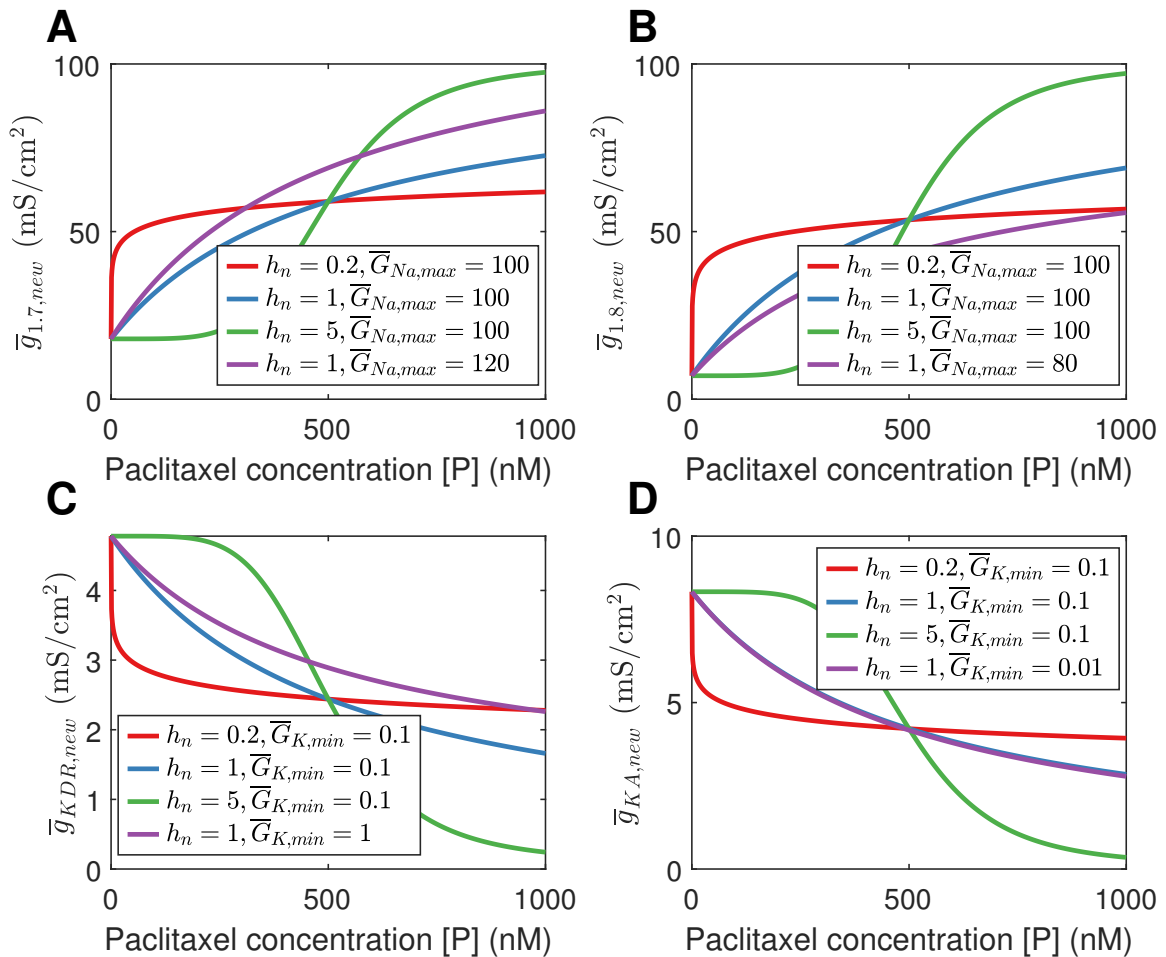


Figure 5.6.: Effect of paclitaxel on conductances and firing. A: Effect of paclitaxel on $\bar{g}_{1.7,new}$ upon varying h_n and $\bar{G}_{Na,max}$. Increasing $\bar{G}_{Na,max}$ will widen the parameter range of $\bar{g}_{1.7,new}$. Increasing h_n alters the curve to become more sigmoidal. B: Similar effect is seen with $\bar{g}_{1.8,new}$. Decreasing $\bar{G}_{Na,max}$ will reduce the parameter range of $\bar{g}_{1.8,new}$. C: Increasing paclitaxel concentration decreases $\bar{g}_{KDR,new}$. As before, increasing h_n makes the curve more sigmoidal. Decreasing $\bar{G}_{K,min}$ increases the parameter range. D: Similar effect is seen for $\bar{g}_{KA,new}$. Increasing $\bar{G}_{K,min}$ decreases the parameter range in this case. The blue curves correspond to the parameter values that were considered for bifurcation analysis. Note that the blue and purple curves are overlapping in in D, thus the blue curve is not visible.

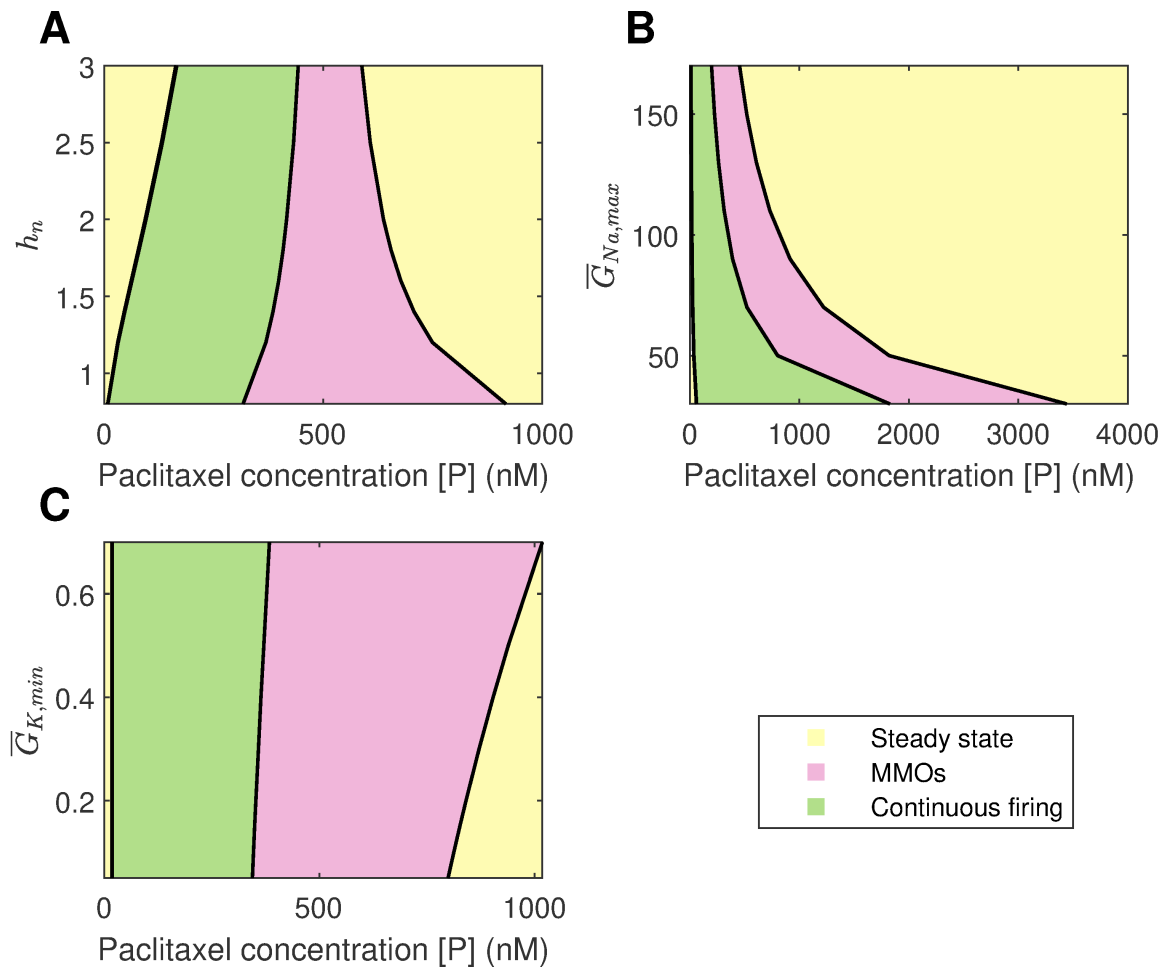


Figure 5.7.: **Regions of stable steady state, MMOs, and continuous firing upon varying h_n , $\bar{G}_{Na,max}$, and $\bar{G}_{K,min}$ with paclitaxel concentration $[P]$.** A: Continuation of Hill's coefficient h_n . Upon increasing h_n , the spontaneous firing regime becomes narrower. B: Continuation of $\bar{G}_{Na,max}$. Upon increasing $\bar{G}_{Na,max}$, the spontaneous firing regime becomes narrower. C: Continuation of $\bar{G}_{K,min}$. Upon increasing $\bar{G}_{K,min}$, the spontaneous firing regime becomes wider

6. EXPLORING INTERACTIONS IN CIPN MECHANISMS

Degeneracy, as mentioned before, is “*the ability of elements that are structurally different to perform the same function or yield the same output*” [93]. In case of CIPN, this would imply that multiple mechanisms/routes can lead to peripheral neuropathy. Indeed, multiple mechanisms are involved, as pointed out in chapter 1 and summarized in Table 1.1. It has been pointed out that oxidative stress [18], inflammation [16], mitochondrial dysfunction [19], ion channel modulation [20], are common mechanisms that can result in peripheral neuropathy. The aim of this chapter is to demonstrate how these mechanisms have been evidenced to be interlinked and how various pathways can lead to the same outcome, indicating towards degeneracy in CIPN mechanisms. It is pointed out here that since CIPN is degenerate, there is a need for a holistic approach to find therapeutic cures for it. In the previous chapter, degeneracy in the electrophysiology was explored. It was seen that modulating either $\text{Na}_v1.8$ or KDR can increase/decrease hyperexcitability. It is illustrated below that electrophysiology is interlinked to various biochemical reactions, thus increasing the complexity of the system. The intent of this chapter is not to point out to all possible mechanisms that are potentially interlinked, but illustration specific examples to incite research in this direction.

6.1 Calcium homeostasis

Various chemotherapy agents, in particular, the mitrotubule disrupting agents, also impact calcium homeostasis. Calcium has multiple roles to play in a cell, and in particular a neuronal cell. It is a second messenger, involved in energy metabolism, neurotransmission, among other functions. In case of neurons, apart from calcium signaling pathways, voltage-gated calcium channels and calcium-activated potassium

ion channels are also present. The dynamics of these channels are a function of calcium concentration, where the intracellular calcium concentration is in turn a function of calcium dynamics controlled by receptors such as inositol triphosphate (IP3R) and ryanodine (RyR) receptors. Additionally, calcium can control other ion channels as well [257]. Calcium can regulate voltage-gated sodium ion channels, possibly through calmodulin which is a sensor protein that is involved in calcium signaling [258]. Likewise, it can regulate voltage-gated calcium channels as well. Apart from modulating voltage-gated potassium ion channels via calmodulin, it can directly activate calcium-activated potassium channels, which activate as a direct consequence of calcium. See [257] for a review on the role of calcium in modulating ion channels. Likewise, ion channels can regulate calcium homeostasis as well, for example, by regulating the resting membrane potential [259]. The above evidences suggest that calcium and ion channel regulation are closely interlinked.

6.2 Oxidative stress

Oxidative stress commonly occurs due to mitochondrial disruption as a result of various chemotherapy drugs [18]. It is suggested that oxidative stress can regulate IP3Rs and RyRs activity, both of which can impact calcium signaling [260]. As described in the previous section, calcium signaling can in turn lead to ion channel modulation. Oxidative stress can both be the cause or the outcome of the damage. This is because ROS production can lead to a feedback loop leading to further damage of the mitochondria [85]. ROS can also induce inflammation by production of pro-inflammatory mediators [261]. Moreover, oxidative stress can also modulate ion channels either by directly impacting the channel proteins (e.g. oxidation of cysteine residues on the membrane) or indirectly by impacting the signaling pathways involved in channel regulation [262–264]. These evidences suggest that calcium regulation, oxidative stress, and ion channel modulation are interlinked.

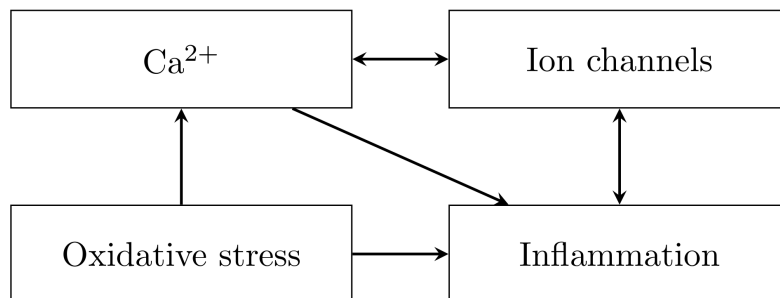


Figure 6.1.: Potential interactions between different CIPN-related mechanisms based on current literature.

6.3 Inflammation

Ion channels and transporters can regulate intracellular calcium concentration which can in turn regulate the immune response [265–267]. Immune response can trigger inflammatory response. As seen earlier, calcium concentration can also be regulated by altering calcium permeability of calcium channels or transporters such as voltage-gated calcium ion channels or the receptors such as IP3Rs and RyRs. Besides, specific ion channels and transporters can also regulate generation of ROS which can subsequently lead to regulation of the immune response [268,269]. On the other hand, immune cells can also regulate ion channels to release pro-inflammatory cytokine IL-1 β [270–272]. Additionally, multiple TRP channels can modulate inflammation [273–276]. They can also modulate intracellular calcium flux [274]. Alternatively, inflammatory molecules can increase sodium currents, thus modulating the ion channels as well [16]. These evidences suggest that calcium regulation, inflammation, and ion channel modulation are interlinked.

6.4 Axonal degeneration

Chemotherapy agents can also impact axonal transport by their interference with microtubules, as described in chapter 1. This can subsequently lead to axonal degeneration. Axonal degeneration in itself can be a result of multiple mechanisms. While

interference with microtubules can lead to axonal degeneration, other mechanisms can lead to this final outcome as well. Mitochondrial dysfunction, a common CIPN mechanism, can also lead to axonal degeneration. This is because a dysfunction can be a result of a change in the morphology such as swelling and vacuolation [68,84,277,278]. Furthermore, calcium dysregulation can activate caspase, subsequently leading to axonal degeneration [73]. See the review by Fukuda et al. [235] for potential mechanisms that can lead to chemotherapy-induced axonal degeneration. These evidences imply that axonal degeneration is a degenerate process since multiple pathways can lead to the same final outcome.

The above survey indicates that calcium signaling, ion channel modulation, oxidative stress, and inflammation are interlinked. A perturbation on any one of these can impact the other processes. Moreover, multiple pathways can lead to the same final outcome as seen in case of axonal degeneration. Thus, it is imperative to investigate CIPN in a holistic manner, taking such interactions into account. Mathematical modeling can be helpful in integrating such events. This is discussed in chapter 8 which is based on potential future work that can sprout out from this thesis.

7. CONCLUSIONS

This thesis focuses on chemotherapy-induced peripheral neuropathy and pain sensation. Chemotherapy-induced peripheral neuropathy is a dose-limiting toxicity that arises due to several chemotherapy agents such as vincristine, paclitaxel, cisplatin, among others. Peripheral neuropathy is a numbing and tingling sensation felt in the palm and feet. Its intensity, duration, and symptoms vary depending on various clinical factors, the individual, and the antineoplastic agent being used. Different individuals experience CIPN of varying intensity. It is of interest to predict CIPN severity to personalize the treatment for individual patients. Moreover, it is of interest to investigate potential mechanisms that can lead to CIPN to develop a therapeutic cure for it. Peripheral neuropathy is a form of pain. In this thesis, pain sensation mutations and dynamics of a pain-sensing neuron were also explored. Various pain sensation mutations can shift the pain sensation threshold, due to which certain individuals experience chronic pain, while others do not experience pain at all. Pain sensation mutations parameters that lead to a decrease in pain sensation threshold were identified.

Firstly, a metabolomics approach was undertaken to identify potential metabolite biomarkers that can predict vincristine-induced peripheral neuropathy. Vincristine is a common chemotherapy drug, used for several cancers including pediatric acute lymphoblastic leukemia (ALL). In this work, blood samples and neuropathy score of pediatric ALL patients were provided. Blood samples were used to perform metabolite profiling. The metabolite profiles were subsequently used to find metabolites that could accurately classify patients into high or low neuropathy, using recursive feature elimination on a support vector classifier model. Small sets of metabolites on day 8 and month 6 of the treatment were found. Predictive models were developed that

could be used in the future to classify patients into high or low neuropathy based on their metabolite profile. This work emphasized on the use of metabolomics to aid in developing personalized treatments for patients.

The second focus of this thesis was on analyzing the dynamics of a single pain-sensing neuron and exploring pain sensation and mechanism of chemotherapy-induced peripheral neuropathy. In particular, bifurcation theory was applied to analyze a mathematical model representing dynamics of a small DRG neuron, a pain-sensing neuron. An introduction to computational neuroscience and pain sensation was also provided. Thereafter, firstly, bifurcation theory was applied to explore how perturbations in the kinetics of specific sodium channels $\text{Na}_v1.7$ and $\text{Na}_v1.8$ can lead to a shift in bifurcation points of this model, implying a shift in the pain sensation threshold. Specific model parameters were found that could shift the bifurcation points leftwards, implying a decrease in the pain sensation threshold. This was corroborated by experimental observations which showed a similar shift in the model parameter that was associated with mutations in these sodium channels that lead to chronic burning pain. Thus, a framework was presented in this work that can be further used to explore other pain related mutations as well. Role of equilibrium sodium and potassium ion potentials were also elucidated. It was shown that increasing these potentials can lead to generation of bifurcation points without any external stimulus, implying that they may lead to neuropathic pain.

The dynamics of this model were further explored and a relatively theoretical approach was undertaken in Chapter 4. In particular, mixed-mode oscillations and role of $\text{Na}_v1.8$ channel maximal conductance were elaborated upon. It was shown that, MMOs were observed for only higher values of $\bar{g}_{1.8}$. Bifurcation analysis showed that for lower values of $\bar{g}_{1.8}$, bistability between stable steady state and periodic firing of action potentials was observed. MMOs solutions belonged to isolated branches, each ending on a cyclic limit point on the left and a period doubling bifurcation point on the right. Small windows of chaotic-like solutions were observed after every period doubling bifurcation point. Besides, these MMOs solutions followed a pattern where

a concatenated solution of two parent solutions could always be observed in between them. These solutions formed a Farey sequence, satisfying the Farey arithmetic. These are theoretical results and that need to be validated using patch-clamp or voltage-clamp experiments.

Lastly, this model was used and modified to explore the role of ion channels in inducing peripheral neuropathy, in particular, paclitaxel-induced peripheral neuropathy. Bifurcation theory was applied again, but by keeping the maximal conductances as bifurcation parameters. Moreover, external current was kept as zero since spontaneous firing was being analyzed. It was found that increasing $\bar{g}_{1.8}$ or decreasing \bar{g}_{KDR} can induce spontaneous firing, and in turn induce peripheral neuropathy. This implies that out of the four voltage-gated ion channels, there is a need to focus on these two channels to reduce hyperexcitability. This was supplemented by multi-electrode array recordings where it was shown that upon administering a $\text{Na}_v1.8$ blocker or a delayed rectifier potassium enhancer concurrently with paclitaxel, mean firing rate in a DRG culture reduced. Furthermore, paclitaxel was introduced in the model, assuming that it will impact maximal conductance of each of the ion channels, and then it treated as the bifurcation parameter. It was shown that spontaneous firing only occurred for a medium dose of paclitaxel. Moreover, firing frequency was highest in between. A similar result was seen in the multi-electrode array experiments, where the mean firing rate was maximum for a medium dose of paclitaxel. This work presents a novel framework that can be used to explore CIPN mechanisms by investigating the role of various voltage-gated ion channels in inducing hyperexcitability.

In Chapter 6, interactions in CIPN mechanisms were discussed, suggesting a need to integrate multiple mechanisms for a comprehensive investigation of CIPN. Various mechanisms are involved such as alteration of voltage-gated ion channels, dysregulation of calcium signaling, mitochondrial dysfunction, axonal transport impairment, release of inflammatory cytokines, oxidative stress. Every chemotherapy agent has varying pathophysiologies, however, there are common underlying mechanisms that are observed due to each of these agents. In this chapter, interaction between each

of these mechanisms was explored. It was shown how multiple mechanisms are interlinked, implying that CIPN occurs due to various interlinked events. This may explain the failure of clinical trials in treating CIPN since they are focused on only one of these mechanisms. It was argued that there is a need for a more comprehensive approach to find therapeutic cures for CIPN. Mathematical modeling and bifurcation theory can help in integrating these mechanisms and identifying the parameters that are sensitive to CIPN. A minimal version of this approach was shown in chapter 5 and this approach is discussed further in the next chapter.

8. FUTURE WORK

Potential future work for every specific project is mentioned in the corresponding chapters 2 to 5. Additionally, here, a mathematical modeling approach is proposed that can be used for a thorough investigation of interactions in CIPN mechanisms.

8.1 A comprehensive approach to investigate CIPN

As shown in chapter 6, multiple mechanisms are involved in CIPN that can be potentially interlinked, based on prior evidence. It was argued that mathematical modeling can aid in investigating multiple mechanisms together. For example, electrophysiology and calcium signaling can be integrated using a mathematical modeling approach. For this, voltage-gated calcium ion channels and calcium dependent potassium channels should be included in the electrophysiology part of the model. IP3Rs and RyRs mediated calcium signaling can then be integrated with the electrophysiology. This is linked because calcium and calcium-activated potassium currents will be a function of calcium concentration which is in turn controlled by the intracellular receptors. Sensitivity analysis as well as bifurcation analysis can be performed to find sensitive parameters that can be associated with peripheral neuropathy. Application of bifurcation theory has been shown in chapter 5. Sensitivity analysis of a model of IP3R induced calcium is also shown in appendix C. Many other mathematical models of calcium signaling exist [279–281] and can be explored. In appendix C, the parameters that were sensitive to calcium peak were explored. Both of these models can be integrated. Prior evidence suggests that acute paclitaxel exposure can induce cytosolic calcium oscillations [65]. Bifurcation theory can be used to explore model parameters that can induce such oscillations, as well. Paclitaxel also affects mitochondrial permeability, which leads to opening up of mitochondrial permeability transition

pore (mPTP). This then leads to mitochondrial depolarization, calcium release and vacuolated and swollen mitochondria [64, 68, 282, 283]. Since calcium flux also gets dysregulated because of the mitochondria, mitochondria can also be included in the model as a separate compartment. Previously, it has been reported that this may alter the calcium oscillations amplitude and lead to more complex dynamics such as chaos and bursting [284]. It will be of interest to explore how the dynamics vary upon introduction of mitochondria in the mathematical model discussed here. These results can be validated experimentally using calcium real time live imaging. Moreover, live dynamic mitochondrial membrane potential and ATP production can be recorded, which can be potentially used to validate mitochondrial calcium flux dynamics of our model and to monitor mitochondria's health. IP3R mediated calcium signaling is a common signaling mechanism observed even in non neuronal cells. It is being widely studied in the heart cells and the hepatocytes, where calcium oscillations are observed due to muscle cell contraction [285] and hormone stimulation [286, 287], respectively. This analysis can suggest potential bifurcation parameters, which are more widely applicable in the study of these systems.

In addition to integrating electrophysiology and calcium signaling, inflammatory cytokines can also be introduced in the model. Potentially, these cytokines may be impacting the ion channels and calcium signaling. To include these events in the model, a cybernetic modeling approach can be undertaken [288]. Application of cybernetic modeling in inflammation has been demonstrated in the past [289]. Next, oxidative stress can also be included. Various mathematical models of oxidative stress exist [290]. Axonal transport can also be integrated by converting these equations into partial differential equations and introducing cable equations [248]. Axonal transport impairment mathematical models exist [291] and can be used in this case.

Apart from simply extending the model, there is a need to validate the model at every step. This can be performed using voltage-clamp experiments and recording the action potentials. This will also require investigating each isolated mechanism separately before integrating. This is to ensure that the model is accurate before adding

more compartments. Moreover, the electrophysiology model considered here is not mechanistic; a potential future work is to develop a mechanism-based model. After validation of the model at every step, MEA experiments can be used to supplement model findings in a similar fashion as demonstrated in chapter 5.

In summary, the model complexity can be increased by introducing intracellular biochemical reactions, ion channels, compartments such as mitochondria, and axonal transport. From a physiological point of view, a model incorporating multiple mechanisms will be more realistic. Sensitivity analysis, bifurcation theory or high codimension bifurcation points continuation can then be performed to identify the important model parameters. These can then be targeted in experiments to confirm their sensitivity. The sensitive parameters can then be targeted to alleviate CIPN.

8.2 Developing personalized treatment strategy for cancer patients

It will also be of interest to investigate if CIPN mechanism and its onset in specific individuals are related. It is possible that specific drug transporters may be responsible for both the onset and the intensity of CIPN in specific individuals. Alternatively, CIPN pathogenesis may be associated with the primary action of the drugs on a particular cell. For example, in case of VIPN, a genetic polymorphism in CEP72 was an indicator of VIPN during the later stage of the treatment [114]. This gene encodes a centrosome involved in microtubule formation. Vincristine's primary action is microtubule disruption. This example indicates that the mechanism and its onset in only specific individuals may share a common root.

It will also be of interest to investigate pharmacokinetics of these agents. Furthermore, pharmacokinetics can be integrated with omics to develop a personalized treatment strategy for individual patients. An example of this idea is demonstrated in appendix E. Pharmacokinetic variables can be derived from the omics data to develop an individualized treatment profile. In appendix E, since the pharmacokinetics data was only available for initial time points, results were not conclusive. This work can be repeated with a more detailed dataset. Specific clinical parameters can also

be optimized for a more optimal treatment which can reduce chances of CIPN. In appendix D, a population balance approach was demonstrated which can be used to find an optimal infusion time for vincristine administration. It was shown that slower infusion times can kill more cancer cells. Apart from genomics, proteomics, and metabolomics, lipidomics can also be investigated to explore their potential role in drug metabolism in the liver. An example of lipidomics investigation on a different disease (non-alcoholic fatty liver disease) is demonstrated in appendix F. Ultimately, optimal treatment regime for individual patients derived from their profiles can improve treatment outcomes and their quality of lives. Thus, there is a need to combine neurophysiology, neuropharmacology, omics, and systems biology to thoroughly understand this dose-limiting toxicity of these chemotherapy agents and to develop therapeutic cures for it.

REFERENCES

- [1] Rebecca L. Siegel, Kimberly D. Miller, and Ahmedin Jemal. Cancer statistics, 2020. *CA: A Cancer Journal for Clinicians*, 70(1):7–30, 2020.
- [2] M. T. Fallon. Neuropathic pain in cancer. *BJA: British Journal of Anaesthesia*, 111(1):105–111, 07 2013.
- [3] Marta Seretny, Gillian L Currie, Emily S Sena, Sabrina Ramnarine, Robin Grant, Malcolm R MacLeod, Leslie A Colvin, and Marie Fallon. Incidence, prevalence, and predictors of chemotherapy-induced peripheral neuropathy: a systematic review and meta-analysis. *PAIN®*, 155(12):2461–2470, 2014.
- [4] VA Carozzi, A Canta, and A Chiorazzi. Chemotherapy-induced peripheral neuropathy: what do we know about mechanisms? *Neuroscience letters*, 596:90–107, 2015.
- [5] Susanna B. Park, David Goldstein, Arun V. Krishnan, Cindy S-Y Lin, Michael L. Friedlander, James Cassidy, Martin Koltzenburg, and Matthew C. Kiernan. Chemotherapy-induced peripheral neurotoxicity: A critical analysis. *CA: A Cancer Journal for Clinicians*, 63(6):419–437, 2013.
- [6] Rebecca M Speck, Angela DeMichele, John T Farrar, Sean Hennessy, Jun J Mao, Margaret G Stineman, and Frances K Barg. Scope of symptoms and self-management strategies for chemotherapy-induced peripheral neuropathy in breast cancer patients. *Supportive Care in Cancer*, 20(10):2433–2439, 2012.
- [7] Guido Cavaletti and Paola Marmiroli. Chemotherapy-induced peripheral neurotoxicity. *Nature Reviews Neurology*, 6(12):657, 2010.
- [8] Cindy Toftagen. Patient perceptions associated with chemotherapy-induced peripheral neuropathy. *Clinical journal of oncology nursing*, 14(3), 2010.
- [9] Dawn L Hershman, Christina Lacchetti, Robert H Dworkin, Ellen M Lavoie Smith, Jonathan Bleeker, Guido Cavaletti, Cynthia Chauhan, Patrick Gavin, Antoinette Lavino, Maryam B Lustberg, et al. Prevention and management of chemotherapy-induced peripheral neuropathy in survivors of adult cancers: American society of clinical oncology clinical practice guideline. *Journal of Clinical Oncology*, 32(18):1941–1967, 2014.
- [10] Frederick H. Hausheer, Richard L. Schilsky, Stacey Bain, Elmer J. Berghorn, and Frank Lieberman. Diagnosis, management, and evaluation of chemotherapy-induced peripheral neuropathy. *Seminars in Oncology*, 33(1):15–49, 2006. Toxicity of Chemotherapy—The Last Decade.

- [11] Alex Molassiotis, Hui Lin Cheng, Kwun To Leung, Yu Chung Li, Kam Hung Wong, Joseph Siu Kie Au, Raghav Sundar, Alexandre Chan, Terrence Rong De Ng, Lorna K. P. Suen, Choi Wan Chan, Janelle Yorke, and Violeta Lopez. Risk factors for chemotherapy-induced peripheral neuropathy in patients receiving taxane- and platinum-based chemotherapy. *Brain and Behavior*, 9(6):e01312, 2019.
- [12] Gerardo Gutiérrez-Gutiérrez, María Sereno, Ambrosio Miralles, Enrique Casado-Sáenz, and Eduardo Gutiérrez-Rivas. Chemotherapy-induced peripheral neuropathy: clinical features, diagnosis, prevention and treatment strategies. *Clinical and Translational Oncology*, 12(2):81–91, 2010.
- [13] Alexandre Chan, Daniel L Hertz, Manuel Morales, Elizabeth J Adams, Sharon Gordon, Chia Jie Tan, Nathan P Staff, Jayesh Kamath, Jeong Oh, Shivani Shinde, et al. Biological predictors of chemotherapy-induced peripheral neuropathy (cipn): Mascc neurological complications working group overview. *Supportive Care in Cancer*, pages 1–9, 2019.
- [14] Renata Zajackowska, Magdalena Kocot-Kepska, Wojciech Leppert, Anna Wrzosek, Joanna Mika, and Jerzy Wordliczek. Mechanisms of chemotherapy-induced peripheral neuropathy. *International journal of molecular sciences*, 20(6):1451, 2019.
- [15] I. Scott Ramsey, Markus Delling, and David E. Clapham. An introduction to trp channels. *Annual Review of Physiology*, 68(1):619–647, 2006. PMID: 16460286.
- [16] Xiao-Min Wang, Tanya J Lehky, Joanna M Brell, and Susan G Dorsey. Discovering cytokines as targets for chemotherapy-induced painful peripheral neuropathy. *Cytokine*, 59(1):3–9, 2012.
- [17] Justin G. Lees, Preet G.S. Makker, Ryan S. Tonkin, Munawwar Abdulla, Susanna B. Park, David Goldstein, and Gila Moalem-Taylor. Immune-mediated processes implicated in chemotherapy-induced peripheral neuropathy. *European Journal of Cancer*, 73:22 – 29, 2017.
- [18] Aparna Areti, Veera Ganesh Yerra, VGM Naidu, and Ashutosh Kumar. Oxidative stress and nerve damage: role in chemotherapy induced peripheral neuropathy. *Redox biology*, 2:289–295, 2014.
- [19] Annalisa Canta, Eleonora Pozzi, and Valentina Alda Carozzi. Mitochondrial dysfunction in chemotherapy-induced peripheral neuropathy (cipn). *Toxics*, 3(2):198–223, 2015.
- [20] Kelly A Aromolaran and Peter A Goldstein. Ion channels and neuronal hyperexcitability in chemotherapy-induced peripheral neuropathy: Cause and effect? *Molecular pain*, 13:1744806917714693, 2017.
- [21] Kimberly D. Tanner, David B. Reichling, and Jon D. Levine. Nociceptor hyperresponsiveness during vincristine-induced painful peripheral neuropathy in the rat. *Journal of Neuroscience*, 18(16):6480–6491, 1998.
- [22] Kimberly D. Tanner, Jon D. Levine, and Kimberly S. Topp. Microtubule disorientation and axonal swelling in unmyelinated sensory axons during vincristine-induced painful neuropathy in rat. *Journal of Comparative Neurology*, 395(4):481–492, 1998.

- [23] Tari Chantal, Fournier Nancy, Briand Claudette, Ducet Gaston, and Crevat Aime. Action of vinca alkaloids on calcium movements through mitochondrial membrane. *Pharmacological Research Communications*, 18(6):519 – 528, 1986.
- [24] Mayte Montero, Maria Teresa Alonso, Estela Carnicero, Inmaculada Cuchillo-Ibáñez, Almudena Albillos, Antonio G García, Javier García-Sancho, and Javier Alvarez. Chromaffin-cell stimulation triggers fast millimolar mitochondrial Ca^{2+} transients that modulate secretion. *Nature cell biology*, 2(2):57–61, 2000.
- [25] Chiang Siau and Gary J Bennett. Dysregulation of cellular calcium homeostasis in chemotherapy-evoked painful peripheral neuropathy. *Anesthesia and analgesia*, 102(5):1485, 2006.
- [26] Chao-Hung Wang, Subodh Verma, I-Chang Hsieh, Yeung-Jen Chen, Li-Tang Kuo, Ning-I Yang, Shin-Yi Wang, Mei-Yun Wu, Chia-Ming Hsu, Chi-Wen Cheng, and Wen-Jin Cherng. Enalapril increases ischemia-induced endothelial progenitor cell mobilization through manipulation of the cd26 system. *Journal of Molecular and Cellular Cardiology*, 41(1):34 – 43, 2006.
- [27] Amteshwar Singh Jaggi and Nirmal Singh. Analgesic potential of intrathecal farnesyl thiosalicylic acid and gw 5074 in vincristine-induced neuropathic pain in rats. *Food and Chemical Toxicology*, 50(5):1295 – 1301, 2012.
- [28] Annemiek Broyl, Sophie L Corthals, Joost LM Jongen, Bronno van der Holt, Rowan Kuiper, Yvonne de Knecht, Mark van Duin, Laila el Jarari, Uta Bertsch, Henk M Lokhorst, Brian G Durie, Hartmut Goldschmidt, and Pieter Sonneveld. Mechanisms of peripheral neuropathy associated with bortezomib and vincristine in patients with newly diagnosed multiple myeloma: a prospective analysis of data from the hovan-65/gmmg-hd4 trial. *The Lancet Oncology*, 11(11):1057 – 1065, 2010.
- [29] Jewel L Podratz, Andrew M Knight, Lauren E Ta, Nathan P Staff, Jennifer M Gass, Konstantin Genelin, Alexander Schlattau, Liselle Lathroum, and Anthony J Windebank. Cisplatin induced mitochondrial dna damage in dorsal root ganglion neurons. *Neurobiology of disease*, 41(3):661–668, 2011.
- [30] Yang Yang, Lan Luo, Xueting Cai, Yuan Fang, Jiaqi Wang, Gang Chen, Jie Yang, Qian Zhou, Xiaoyan Sun, Xiaolan Cheng, Huaijiang Yan, Wuguang Lu, Chungping Hu, and Peng Cao. Nrf2 inhibits oxaliplatin-induced peripheral neuropathy via protection of mitochondrial function. *Free Radical Biology and Medicine*, 120:13 – 24, 2018.
- [31] Rachel M. McQuade, Vanesa Stojanovska, Joel C. Bornstein, and Kulmira Nurgali. Parp inhibition in platinum-based chemotherapy: Chemopotential and neuroprotection. *Pharmacological Research*, 137:104 – 113, 2018.
- [32] Elizabeth K. Joseph, Xiaojie Chen, Oliver Bogen, and Jon D. Levine. Oxaliplatin acts on $ib4$ -positive nociceptors to induce an oxidative stress-dependent acute painful peripheral neuropathy. *The Journal of Pain*, 9(5):463 – 472, 2008.
- [33] Lorenzo Di Cesare Mannelli, Matteo Zanardelli, Paola Failli, and Carla Ghelardini. Oxaliplatin-induced neuropathy: Oxidative stress as pathological mechanism. protective effect of silibinin. *The Journal of Pain*, 13(3):276 – 284, 2012.

- [34] L. Di Cesare Mannelli, M. Zanardelli, P. Failli, and C. Ghelardini. Oxaliplatin-induced oxidative stress in nervous system-derived cellular models: Could it correlate with in vivo neuropathy? *Free Radical Biology and Medicine*, 61:143–150, 2013.
- [35] Mohammad Waseem, Pooja Kaushik, Heena Tabassum, and Suhel Parvez. Role of mitochondrial mechanism in chemotherapy-induced peripheral neuropathy. *Current drug metabolism*, 19(1):47–54, 2018.
- [36] Lauren E Ta, Allan J Bieber, Susan M Carlton, Charles L Loprinzi, Philip A Low, and Anthony J Windebank. Transient receptor potential vanilloid 1 is essential for cisplatin-induced heat hyperalgesia in mice. *Molecular Pain*, 6:1744–8069–6–15, 2010. PMID: 20205720.
- [37] Peter Horvath, Judith Szilvassy, Jozsef Nemeth, Barna Peitl, Maria Szilasi, and Zoltan Szilvassy. Decreased sensory neuropeptide release in isolated bronchi of rats with cisplatin-induced neuropathy. *European Journal of Pharmacology*, 507(1):247–252, 2005.
- [38] Uma Anand, William R Otto, and Praveen Anand. Sensitization of capsaicin and icilin responses in oxaliplatin treated adult rat drg neurons. *Molecular pain*, 6(1):82, 2010.
- [39] Punam Gauchan, Tsugunobu Andoh, Atsushi Kato, and Yasushi Kuraishi. Involvement of increased expression of transient receptor potential melastatin 8 in oxaliplatin-induced cold allodynia in mice. *Neuroscience Letters*, 458(2):93–95, 2009.
- [40] Dongsheng Xu, Hui Zhao, Han Gao, Huiling Zhao, Dandan Liu, and Jing Li. Participation of pro-inflammatory cytokines in neuropathic pain evoked by chemotherapeutic oxaliplatin via central gabaergic pathway. *Molecular pain*, 14:1744806918783535, 2018.
- [41] Helmuth Adelsberger, Stefan Quasthoff, Julian Grosskreutz, Alexandra Lepier, Florian Eckel, and Christian Lersch. The chemotherapeutic oxaliplatin alters voltage-gated na⁺ channel kinetics on rat sensory neurons. *European Journal of Pharmacology*, 406(1):25–32, 2000.
- [42] Nobuaki Egashira, Shingo Hirakawa, Takehiro Kawashiri, Takahisa Yano, Hiroaki Ikesue, and Ryozi Oishi. Mexiletine reverses oxaliplatin-induced neuropathic pain in rats. *Journal of pharmacological sciences*, 112(4):473–476, 2010.
- [43] Richard G Webster, Keith L Brain, Richard H Wilson, Jean L Grem, and Angela Vincent. Oxaliplatin induces hyperexcitability at motor and autonomic neuromuscular junctions through effects on voltage-gated sodium channels. *British Journal of Pharmacology*, 146(7):1027–1039, 2005.
- [44] Andreas A. Argyriou, Guido Cavaletti, Anna Antonacopoulou, Armando A. Genazzani, Chiara Briani, Jordi Bruna, Salvatore Terrazzino, Roser Velasco, Paola Alberti, Marta Campagnolo, Sara Lonardi, Diego Cortinovis, Marina Cazzaniga, Cristina Santos, Aikaterini Psaromyalou, Aikaterini Angelopoulou, and Haralabos P. Kalofonos. Voltage-gated sodium channel polymorphisms play a pivotal role in the development of oxaliplatin-induced peripheral neurotoxicity: Results from a prospective multicenter study. *Cancer*, 119(19):3570–3577, 2013.

- [45] Juliette Descoeur, Vanessa Pereira, Anne Pizzoccaro, Amaury Francois, Bing Ling, Violette Maffre, Brigitte Couette, Jrme Busserolles, Christine Courteix, Jacques Noel, Michel Lazdunski, Alain Eschalier, Nicolas Authier, and Emmanuel Bourinet. Oxaliplatin-induced cold hypersensitivity is due to remodelling of ion channel expression in nociceptors. *EMBO Molecular Medicine*, 3(5):266–278, 2011.
- [46] Ruth Sittl, Richard W. Carr, Johannes Fleckenstein, and Peter Grafe. Enhancement of axonal potassium conductance reduces nerve hyperexcitability in an in vitro model of oxaliplatin-induced acute neuropathy. *NeuroToxicology*, 31(6):694 – 700, 2010.
- [47] Christin Schulze, Margit McGowan, Sven-Eric Jordt, and Barbara E. Ehrlich. Prolonged oxaliplatin exposure alters intracellular calcium signaling: A new mechanism to explain oxaliplatin-associated peripheral neuropathy. *Clinical Colorectal Cancer*, 10(2):126 – 133, 2011.
- [48] Arianna Scuteri, Alessia Galimberti, Maddalena Ravasi, Silvia Pasini, Elisabetta Donzelli, Guido Cavaletti, and Giovanni Tredici. Ngf protects dorsal root ganglion neurons from oxaliplatin by modulating jnk/sapk and erk1/2. *Neuroscience Letters*, 486(3):141 – 145, 2010.
- [49] M. Norcini, E. Vivoli, N. Galeotti, E. Bianchi, A. Bartolini, and C. Ghelardini. Supraspinal role of protein kinase c in oxaliplatin-induced neuropathy in rat. *PAIN*, 146(1):141 – 147, 2009.
- [50] Ye-song Wang, Yuan-yuan Li, Wei Cui, Li-bin Li, Zhao-cai Zhang, Bao-ping Tian, and Gen-sheng Zhang. Melatonin attenuates pain hypersensitivity and decreases astrocyte-mediated spinal neuroinflammation in a rat model of oxaliplatin-induced pain. *Inflammation*, 40(6):2052–2061, 2017.
- [51] Amina M Illias, Andrea C Gist, Haijun Zhang, Alyssa K Kosturakis, and Patrick M Dougherty. Chemokine ccl2 and its receptor ccr2 in the dorsal root ganglion contribute to oxaliplatin-induced mechanical hypersensitivity. *Pain*, 159(7):1308, 2018.
- [52] Yong-Yong Li, He Li, Ze-Long Liu, Qiong Li, Hua-Wen Qiu, Li-Jin Zeng, Wen Yang, Xiang-Zhong Zhang, and Zhen-Yu Li. Activation of stat3-mediated cxcl12 up-regulation in the dorsal root ganglion contributes to oxaliplatin-induced chronic pain. *Molecular pain*, 13:1744806917747425, 2017.
- [53] Zhen-Zhen Huang, Dai Li, Han-Dong Ou-Yang, Cui-Cui Liu, Xian-Guo Liu, Chao Ma, Jia-You Wei, Yong Liu, and Wen-Jun Xin. Cerebrospinal fluid oxaliplatin contributes to the acute pain induced by systemic administration of oxaliplatin. *Anesthesiology: The Journal of the American Society of Anesthesiologists*, 124(5):1109–1121, 2016.
- [54] Jing Wang, Xin-Sheng Zhang, Rong Tao, Jie Zhang, Lin Liu, Ying-Hai Jiang, Song-He Ma, Lin-Xia Song, and Ling-Jie Xia. Upregulation of cx3cl1 mediated by nf- κ b activation in dorsal root ganglion contributes to peripheral sensitization and chronic pain induced by oxaliplatin administration. *Molecular pain*, 13:1744806917726256, 2017.
- [55] P Richardson, T Hideshima, and K Anderson. Thalidomide in multiple myeloma. *Biomedicine & Pharmacotherapy*, 56(3):115 – 128, 2002.

- [56] Paul Fernyhough, Darrell R Smith, Jason Schapansky, Randy Van Der Ploeg, Natalie J Gardiner, Christopher W Tweed, Andreas Kontos, Lyle Freeman, Tertia D Purves-Tyson, and Gordon W Glazner. Activation of nuclear factor- κ b via endogenous tumor necrosis factor α regulates survival of axotomized adult sensory neurons. *Journal of Neuroscience*, 25(7):1682–1690, 2005.
- [57] Bilal Mohty, Jean El-Cheikh, Ibrahim Yakoub-Agha, Philippe Moreau, Jean-Luc Harousseau, and Mohamad Mohty. Peripheral neuropathy and new treatments for multiple myeloma: background and practical recommendations. *haematologica*, 95(2):311–319, 2010.
- [58] Jayne A Keifer, Denis C Guttridge, Brian P Ashburner, and Albert S Baldwin. Inhibition of nf- κ b activity by thalidomide through suppression of ikb kinase activity. *Journal of Biological Chemistry*, 276(25):22382–22387, 2001.
- [59] Tasaduq H. Wani, Anindita Chakrabarty, Norio Shibata, Hiroshi Yamazaki, F. Peter Guengerich, and Goutam Chowdhury. The dihydroxy metabolite of the teratogen thalidomide causes oxidative dna damage. *Chemical Research in Toxicology*, 30(8):1622–1628, 2017. PMID: 28745489.
- [60] Jean A Yared and Katherine HR Tkaczuk. Update on taxane development: new analogs and new formulations. *Drug design, development and therapy*, 6:371, 2012.
- [61] Or A Shemesh and Micha E Spira. Paclitaxel induces axonal microtubules polar reconfiguration and impaired organelle transport: implications for the pathogenesis of paclitaxel-induced polyneuropathy. *Acta neuropathologica*, 119(2):235–248, 2010.
- [62] Nichole E. LaPointe, Gerardo Morfini, Scott T. Brady, Stuart C. Feinstein, Leslie Wilson, and Mary Ann Jordan. Effects of eribulin, vincristine, paclitaxel and ixabepilone on fast axonal transport and kinesin-1 driven microtubule gliding: Implications for chemotherapy-induced peripheral neuropathy. *NeuroToxicology*, 37:231 – 239, 2013.
- [63] Brian G. Bober and Sameer B. Shah. Paclitaxel alters sensory nerve biomechanical properties. *Journal of Biomechanics*, 48(13):3559 – 3567, 2015.
- [64] Jackie F Kidd, Mary F Pilkington, Michael J Schell, Kevin E Fogarty, Jeremy N Skepper, Colin W Taylor, and Peter Thorn. Paclitaxel affects cytosolic calcium signals by opening the mitochondrial permeability transition pore. *Journal of Biological Chemistry*, 277(8):6504–6510, 2002.
- [65] Wolfgang Boehmerle, Ute Splittgerber, Michael B Lazarus, Kathleen M McKenzie, David G Johnston, David J Austin, and Barbara E Ehrlich. Paclitaxel induces calcium oscillations via an inositol 1, 4, 5-trisphosphate receptor and neuronal calcium sensor 1-dependent mechanism. *Proceedings of the National Academy of Sciences*, 103(48):18356–18361, 2006.
- [66] Nicolas André, Diane Braguer, Gaël Brasseur, Anthony Gonçalves, Danielle Lemesle-Meunier, Stéphanie Guise, Mary Ann Jordan, and Claudette Briand. Paclitaxel induces release of cytochrome c from mitochondria isolated from human neuroblastoma cells. *Cancer research*, 60(19):5349–5353, 2000.

- [67] Manon Carré, Nicolas André, Gérard Carles, Hélène Borghi, Laetitia Brichese, Claudette Briand, and Diane Braguer. Tubulin is an inherent component of mitochondrial membranes that interacts with the voltage-dependent anion channel. *Journal of Biological Chemistry*, 277(37):33664–33669, 2002.
- [68] Sarah J.L. Flatters and Gary J. Bennett. Studies of peripheral sensory nerves in paclitaxel-induced painful peripheral neuropathy: Evidence for mitochondrial dysfunction. *Pain*, 122(3):245 – 257, 2006.
- [69] Huaïen Zheng, Wen Hua Xiao, and Gary J. Bennett. Functional deficits in peripheral nerve mitochondria in rats with paclitaxel- and oxaliplatin-evoked painful peripheral neuropathy. *Experimental Neurology*, 232(2):154 – 161, 2011.
- [70] Diane J Rodi, Robert W Janes, Hitesh J Sanganee, Robert A Holton, B.A Wallace, and Lee Makowski. Screening of a library of phage-displayed peptides identifies human bcl-2 as a taxol-binding protein. Edited by i. a. wilson. *Journal of Molecular Biology*, 285(1):197 – 203, 1999.
- [71] Timothy Doyle, Zhoumou Chen, Carolina Muscoli, Leesa Bryant, Emanuela Esposito, Salvatore Cuzzocrea, Concetta Dagostino, Jan Ryerse, Smita Rausaria, Andrew Kamadulski, et al. Targeting the overproduction of peroxynitrite for the prevention and reversal of paclitaxel-induced neuropathic pain. *Journal of Neuroscience*, 32(18):6149–6160, 2012.
- [72] Natalie A. Duggett, Lisa A. Griffiths, Olivia E. McKenna, Vittorio de Santis, Nutchua Yongsanguanchai, Esther B. Mokeri, and Sarah J.L. Flatters. Oxidative stress in the development, maintenance and resolution of paclitaxel-induced painful neuropathy. *Neuroscience*, 333:13 – 26, 2016.
- [73] Sarah E Pease-Raissi, Maria F Pazyra-Murphy, Yihang Li, Franziska Wachter, Yusuke Fukuda, Sara J Fenstermacher, Lauren A Barclay, Gregory H Bird, Loren D Walensky, and Rosalind A Segal. Paclitaxel Reduces Axonal Bclw to Initiate IP3R1-Dependent Axon Degeneration. *Neuron*, 96(2):373–386, 2017.
- [74] Haijun Zhang and Patrick M. Dougherty. Enhanced Excitability of Primary Sensory Neurons and Altered Gene Expression of Neuronal Ion Channels in Dorsal Root Ganglion in Paclitaxel-induced Peripheral Neuropathy. *Anesthesiology*, 120(6):1463–1475, 2014.
- [75] Yan Li, Robert Y North, Laurence D Rhines, Claudio Esteves Tatsui, Ganesh Rao, Denaya D Edwards, Ryan M Cassidy, Daniel S Harrison, Caj A Johansson, Hongmei Zhang, et al. Drg voltage-gated sodium channel 1.7 is upregulated in paclitaxel-induced neuropathy in rats and in humans with neuropathic pain. *Journal of Neuroscience*, 38(5):1124–1136, 2018.
- [76] Yan Li, Claudio Esteves Tatsui, Laurence D Rhines, Robert Y North, Daniel S Harrison, Ryan M Cassidy, Caj A Johansson, Alyssa K Kosturakis, Denaya D Edwards, Hongmei Zhang, and Patrick M Dougherty. Dorsal root ganglion neurons become hyperexcitable and increase expression of voltage-gated T-type calcium channels (Cav3. 2) in paclitaxel-induced peripheral neuropathy. *Pain*, 158(3):417, 2017.
- [77] Y. Chen, C. Yang, and Z.J. Wang. Proteinase-activated receptor 2 sensitizes transient receptor potential vanilloid 1, transient receptor potential vanilloid

- 4, and transient receptor potential ankyrin 1 in paclitaxel-induced neuropathic pain. *Neuroscience*, 193:440 – 451, 2011.
- [78] Serena Materazzi, Camilla Fusi, Silvia Benemei, Pamela Pedretti, Riccardo Patacchini, Bernd Nilius, Jean Prenen, Christophe Creminon, Pierangelo Geppetti, and Romina Nassini. Trpa1 and trpv4 mediate paclitaxel-induced peripheral neuropathy in mice via a glutathione-sensitive mechanism. *Pflügers Archiv-European Journal of Physiology*, 463(4):561–569, 2012.
- [79] Tomomi Hara, Terumasa Chiba, Kenji Abe, Akiko Makabe, Souichi Ikeno, Kazuyoshi Kawakami, Iku Utsunomiya, Toshihiro Hama, and Kyoji Taguchi. Effect of paclitaxel on transient receptor potential vanilloid 1 in rat dorsal root ganglion. *PAIN®*, 154(6):882–889, 2013.
- [80] Mohammad A Shahshahan, Maureen N Beckley, and Ali R Jazirehi. Potential usage of proteasome inhibitor bortezomib (velcade, ps-341) in the treatment of metastatic melanoma: basic and clinical aspects. *American journal of cancer research*, 1(7):913, 2011.
- [81] Marianne S Poruchynsky, Dan L Sackett, Robert W Robey, Yvona Ward, Christina Annunziata, and Tito Fojo. Proteasome inhibitors increase tubulin polymerization and stabilization in tissue culture cells: a possible mechanism contributing to peripheral neuropathy and cellular toxicity following proteasome inhibition. *Cell Cycle*, 7(7):940–949, 2008.
- [82] Cristina Meregalli, Alessia Chiorazzi, Valentina A Carozzi, Annalisa Canta, Barbara Sala, Matteo Colombo, Norberto Oggioni, Cecilia Ceresa, Dana Foudah, Federica La Russa, et al. Evaluation of tubulin polymerization and chronic inhibition of proteasome as cytotoxicity mechanisms in bortezomib-induced peripheral neuropathy. *Cell Cycle*, 13(4):612–621, 2014.
- [83] Terry H Landowski, Christina J Megli, Kevin D Nullmeyer, Ronald M Lynch, and Robert T Dorr. Mitochondrial-mediated dysregulation of ca²⁺ is a critical determinant of velcade (ps-341/bortezomib) cytotoxicity in myeloma cell lines. *Cancer research*, 65(9):3828–3836, 2005.
- [84] H. Zheng, W.H. Xiao, and G.J. Bennett. Mitotoxicity and bortezomib-induced chronic painful peripheral neuropathy. *Experimental Neurology*, 238(2):225 – 234, 2012.
- [85] Luena Papa and Patricia Rockwell. Persistent mitochondrial dysfunction and oxidative stress hinder neuronal cell recovery from reversible proteasome inhibition. *Apoptosis*, 13(4):588–599, 2008.
- [86] Marina Quartu, VALENTINA A Carozzi, SG Dorsey, MARIA PINA Serra, LAURA Poddighe, CRISTINA Picci, MARIANNA Boi, TIZIANA Melis, M Del Fiacco, CRISTINA Meregalli, et al. Bortezomib treatment produces nocifensive behavior and changes in the expression of trpv1, cgrp, and substance p in the rat drg, spinal cord, and sciatic nerve. *BioMed research international*, 2014, 2014.
- [87] Saiko Nasu, Sonoko Misawa, Chiaki Nakaseko, Kazumoto Shibuya, Sagiri Isole, Yukari Sekiguchi, Satsuki Mitsuma, Shigeki Ohmori, Yuta Iwai, Minako Beppu, Naomi Shimizu, Chikako Ohwada, Yusuke Takeda, Yumi Fujimaki, and Satoshi

- Kuwabara. Bortezomib-induced neuropathy: Axonal membrane depolarization precedes development of neuropathy. *Clinical Neurophysiology*, 125(2):381 – 387, 2014.
- [88] Sherry Wolf, Debra Barton, Lisa Kottschade, Axel Grothey, and Charles Loprinzi. Chemotherapy-induced peripheral neuropathy: Prevention and treatment strategies. *European Journal of Cancer*, 44(11):1507 – 1515, 2008.
- [89] N.C. Miltenburg and W. Boogerd. Chemotherapy-induced neuropathy: A comprehensive survey. *Cancer Treatment Reviews*, 40(7):872 – 882, 2014.
- [90] Jennifer Piccolo and Jill M. Kolesar. Prevention and treatment of chemotherapy-induced peripheral neuropathy. *American Journal of Health-System Pharmacy*, 71(1):19–25, 01 2014.
- [91] C. M. Armstrong and Gabriel Cota. Calcium block of na^+ channels and its effect on closing rate. *Proceedings of the National Academy of Sciences*, 96(7):4154–4157, 1999.
- [92] BJ Gwag, FM Sessler, V Robine, and JE Springer. Endogenous glutamate levels regulate nerve growth factor mrna expression in the rat dentate gyrus. *Molecules and cells*, 7(3):425–430, 1997.
- [93] Gerald M. Edelman and Joseph A. Gally. Degeneracy and complexity in biological systems. *Proceedings of the National Academy of Sciences*, 98(24):13763–13768, 2001.
- [94] Stéphanie Ratté, Yi Zhu, Kwan Yeop Lee, and Steven A Prescott. Criticality and degeneracy in injury-induced changes in primary afferent excitability and the implications for neuropathic pain. *Elife*, 3, 2014.
- [95] Timothy OLeary. Homeostasis, failure of homeostasis and degenerate ion channel regulation. *Current Opinion in Physiology*, 2:129 – 138, 2018. Ion Channels.
- [96] Charles S Sherrington. Qualitative difference of spinal reflex corresponding with qualitative difference of cutaneous stimulus. *The Journal of physiology*, 30(1):39, 1903.
- [97] David Julius and Allan I Basbaum. Molecular mechanisms of nociception. *Nature*, 413(6852):203, 2001.
- [98] Joachim Scholz and Clifford J Woolf. Can we conquer pain? *Nature neuroscience*, 5(11s):1062, 2002.
- [99] Allan I Basbaum, Diana M Bautista, Grégory Scherrer, and David Julius. Cellular and molecular mechanisms of pain. *Cell*, 139(2):267–284, 2009.
- [100] Lynne U. Sneddon. Comparative physiology of nociception and pain. *Physiology*, 33(1):63–73, 2018. PMID: 29212893.
- [101] Mun Fei Yam, Yean Chun Loh, Chu Shan Tan, Siti Khadijah Adam, Nizar Abdul Manan, and Rusliza Basir. General pathways of pain sensation and the major neurotransmitters involved in pain regulation. *International Journal of Molecular Sciences*, 19(8), 2018.

- [102] E.R. Kandel, J.H. Schwartz, T.M. Jessell, S.A. Siegelbaum, and A.J. Hudspeth. *Principles of Neural Science, Fifth Edition*. McGraw-Hill Education, 2012.
- [103] Elizabeth Ward, Carol DeSantis, Anthony Robbins, Betsy Kohler, and Ahmedin Jemal. Childhood and adolescent cancer statistics, 2014. *CA: a cancer journal for clinicians*, 64(2):83–103, 2014.
- [104] American Cancer Society, Cancer Facts & Figures 2018. <https://www.cancer.org/research/cancer-facts-statistics/all-cancer-facts-figures/cancer-facts-figures-2018.html>. Accessed: 04-08-2019.
- [105] Erika Mora, Ellen M Lavoie Smith, Clare Donohoe, and Daniel L Hertz. Vincristine-induced peripheral neuropathy in pediatric cancer patients. *American journal of cancer research*, 6(11):2416, 2016.
- [106] Mirjam E. van de Velde, Gertjan L. Kaspers, Floor C.H. Abbink, Abraham J. Wilhelm, Johannes C.F. Ket, and Marleen H. van den Berg. Vincristine-induced peripheral neuropathy in children with cancer: A systematic review. *Critical reviews in oncology/hematology*, 114:114–130, 2017.
- [107] Ellen M Lavoie Smith, Lang Li, ChienWei Chiang, Karin Thomas, Raymond J Hutchinson, Elizabeth M Wells, Richard H Ho, Jodi Skiles, Arindom Chakraborty, Celia M Bridges, et al. Patterns and severity of vincristine-induced peripheral neuropathy in children with acute lymphoblastic leukemia. *Journal of the Peripheral Nervous System*, 20(1):37–46, 2015.
- [108] Satu S Lehtinen, Usko E Huuskonen, Arja H Harila-Saari, Uolevi Tolonen, Leena K Vainionpää, and B Marjatta Lanning. Motor nervous system impairment persists in long-term survivors of childhood acute lymphoblastic leukemia. *Cancer: Interdisciplinary International Journal of the American Cancer Society*, 94(9):2466–2473, 2002.
- [109] Kirsten K Ness, Melissa M Hudson, Ching-Hon Pui, Daniel M Green, Kevin R Krull, Tseng T Huang, Leslie L Robison, and E Brannon Morris. Neuro-muscular impairments in adult survivors of childhood acute lymphoblastic leukemia: associations with physical performance and chemotherapy doses. *Cancer*, 118(3):828–838, 2012.
- [110] Heleen A Reinders-Messelink, Marina M Schoemaker, Marjorie Hofte, Ludwig NH Göeken, Annet Kingma, Meta M van den Briel, and Willem A Kamps. Fine motor and handwriting problems after treatment for childhood acute lymphoblastic leukemia. *Medical and Pediatric Oncology*, 27(6):551–555, 1996.
- [111] Cinzia R De Luca, Maria McCarthy, Jane Galvin, Jessica L Green, Alexandra Murphy, Sarah Knight, and Jacqueline Williams. Gross and fine motor skills in children treated for acute lymphoblastic leukaemia. *Developmental neurorehabilitation*, 16(3):180–187, 2013.
- [112] Kirsten K Ness, Ann C Mertens, Melissa M Hudson, Melanie M Wall, Wendy M Leisenring, Kevin C Oeffinger, Charles A Sklar, Leslie L Robison, and James G Gurney. Limitations on physical performance and daily activities among long-term survivors of childhood cancer. *Annals of internal medicine*, 143(9):639–647, 2005.

- [113] Doralina L. Anghelescu, Lane G. Faughnan, Sima Jeha, Mary V. Relling, Pamela S. Hinds, John T. Sandlund, Cheng Cheng, Deqing Pei, Gisele Hankins, Jennifer L. Pauley, and Ching-Hon Pui. Neuropathic pain during treatment for childhood acute lymphoblastic leukemia. *Pediatric Blood & Cancer*, 57(7):1147–1153, 2011.
- [114] Barthelemy Diouf, Kristine R Crews, Glen Lew, Deqing Pei, Cheng Cheng, Ju Bao, Jie J Zheng, Wenjian Yang, Yiping Fan, Heather E Wheeler, et al. Association of an inherited genetic variant with vincristine-related peripheral neuropathy in children with acute lymphoblastic leukemia. *Jama*, 313(8):815–823, 2015.
- [115] Shinji Kishi, Cheng Cheng, Deborah French, Deqing Pei, Soma Das, Edwin H. Cook, Nobuko Hijiya, Carmelo Rizzari, Gary L. Rosner, Tony Frudakis, Ching-Hon Pui, William E. Evans, and Mary V. Relling. Ancestry and pharmacogenetics of antileukemic drug toxicity. *Blood*, 109(10):4151–4157, 2007.
- [116] Jamie L Renbarger, Kevin C McCammack, Caroline E Rouse, and Stephen D Hall. Effect of race on vincristine-associated neurotoxicity in pediatric acute lymphoblastic leukemia patients. *Pediatric blood & cancer*, 50(4):769–771, 2008.
- [117] Andrew S Moore, Ross Norris, Gareth Price, Thu Nguyen, Ming Ni, Rani George, Karin van Breda, John Duley, Bruce Charles, and Ross Pinkerton. Vincristine pharmacodynamics and pharmacogenetics in children with cancer: A limited-sampling, population modelling approach. *Journal of Paediatrics and Child Health*, 47(12):875–882, 2011.
- [118] Richard Aplenc, Wendy Glatfelter, Peggy Han, Eric Rappaport, Mei La, Avital Cnaan, M Anne Blackwood, Beverly Lange, and Timothy Rebbeck. CYP3A genotypes and treatment response in paediatric acute lymphoblastic leukaemia. *British journal of haematology*, 122(2):240–244, 2003.
- [119] Akinbode Egbelakin, Michael J. Ferguson, Emily A. MacGill, Amalia S. Lehmann, Ariel R. Toplez, Sara K. Quinney, Lang Li, Kevin C. McCammack, Stephen D. Hall, and Jamie L. Renbarger. Increased risk of vincristine neurotoxicity associated with low CYP3A5 expression genotype in children with acute lymphoblastic leukemia. *Pediatric Blood & Cancer*, 56(3):361–367, 2011.
- [120] Romain Guilhaumou, Caroline Solas, Veronique Bourgarel-Rey, Sylvie Quaranta, Angelique Rome, Nicolas Simon, Bruno Lacarelle, and Nicolas Andre. Impact of plasma and intracellular exposure and CYP3A4, CYP3A5, and ABCB1 genetic polymorphisms on vincristine-induced neurotoxicity. *Cancer chemotherapy and pharmacology*, 68(6):1633–1638, 2011.
- [121] Francesco Ceppi, Chlo Langlois-Pelletier, Vincent Gagn, Julie Rousseau, Claire Ciolino, Samanta De Lorenzo, Kojok M Kevin, Diana Cijov, Stephen E Sallan, Lewis B Silverman, Donna Neuberg, Jeffery L Kutok, Daniel Sinnett, Caroline Laverdure, and Maja Krajinovic. Polymorphisms of the vincristine pathway and response to treatment in children with childhood acute lymphoblastic leukemia. *Pharmacogenomics*, 15(8):1105–1116, 2014. PMID: 25084203.
- [122] Elixabet Lopez-Lopez, Angela Gutierrez-Camino, Itziar Astigarraga, Aurora Navajas, Aizpea Echebarria-Barona, Purificacion Garcia-Miguel, Nagore Garcia de Andoin, Carmen Lobo, Isabel Guerra-Merino, Idoia Martin-Guerrero,

- and Africa Garcia-Orad. Vincristine pharmacokinetics pathway and neurotoxicity during early phases of treatment in pediatric acute lymphoblastic leukemia. *Pharmacogenomics*, 17(7):731–741, 2016. PMID: 27180762.
- [123] Ellis Groninger, Tiny Meeuwsen-de Boer, Pauline Koopmans, Donald Uges, Wim Sluiter, Anjo Veerman, Willem Kamps, and Siebold de Graaf. Pharmacokinetics of vincristine monotherapy in childhood acute lymphoblastic leukemia. *Pediatric Research*, 52(1):113, 2002.
- [124] William R Crom, Siebold SN de Graaf, Timothy Synold, Donald RA Uges, Henk Bloemhof, Gaston Rivera, Michael L Christensen, Hazem Mahmoud, and William E Evans. Pharmacokinetics of vincristine in children and adolescents with acute lymphocytic leukemia. *The Journal of pediatrics*, 125(4):642–649, 1994.
- [125] CEM Gidding, GJ Meeuwsen-de Boer, P Koopmans, DRA Uges, WA Kamps, and SSN De Graaf. Vincristine pharmacokinetics after repetitive dosing in children. *Cancer chemotherapy and pharmacology*, 44(3):203–209, 1999.
- [126] HW Van den Berg, ZR Desai, R Wilson, G Kennedy, JM Bridges, and RG Shanks. The pharmacokinetics of vincristine in man. *Cancer chemotherapy and pharmacology*, 8(2):215–219, 1982.
- [127] CEM Gidding, SJ Kellie, WA Kamps, and SSN De Graaf. Vincristine revisited. *Critical reviews in oncology/hematology*, 29(3):267–287, 1999.
- [128] W Stock, B Diouf, KR Crews, D Pei, C Cheng, K Laumann, SJ Mandrekar, S Luger, A Advani, RM Stone, RA Larson, and WE Evans. An Inherited Genetic Variant in CEP72 Promoter Predisposes to Vincristine-Induced Peripheral Neuropathy in Adults With Acute Lymphoblastic Leukemia. *Clinical Pharmacology & Therapeutics*, 101(3):391–395, 2017.
- [129] Galen E.B. Wright, Ursula Amstutz, Britt I. Drgemller, Joanne Shih, Shahrar R. Rassekh, Michael R. Hayden, Bruce C. Carleton, Colin J.D. Ross, and The Canadian Pharmacogenomics Network for Drug Safety Consortium. Pharmacogenomics of Vincristine-Induced Peripheral Neuropathy Implicates Pharmacokinetic and Inherited Neuropathy Genes. *Clinical Pharmacology & Therapeutics*, 105(2):402–410, 2019.
- [130] Angela Gutierrez-Camino, Idoia Martin-Guerrero, Elixabet Lopez-Lopez, Aizpea Echebarria-Barona, Iñaki Zabalza, Irune Ruiz, Isabel Guerra-Merino, and Africa Garcia-Orad. Lack of association of the CEP72 rs924607 TT genotype with vincristine-related peripheral neuropathy during the early phase of pediatric acute lymphoblastic leukemia treatment in a Spanish population. *Pharmacogenetics and genomics*, 26(2):100–102, 2016.
- [131] Barthelemy Diouf and William E. Evans. Pharmacogenomics of Vincristine-Induced Peripheral Neuropathy: Progress Continues. *Clinical Pharmacology & Therapeutics*, 105(2):315–317, 2019.
- [132] D Jayachandran, Usha Ramkrishna, Jodi Skiles, Jamie Renbarger, and Doraiswami Ramkrishna. Revitalizing personalized medicine: respecting biomolecular complexities beyond gene expression. *CPT: pharmacometrics & systems pharmacology*, 3(4):1–11, 2014.

- [133] R Kaddurah-Daouk, R Weinshilboum, and on behalf of the Pharmacometabolomics Research Network. Metabolomic Signatures for Drug Response Phenotypes: Pharmacometabolomics Enables Precision Medicine. *Clinical Pharmacology & Therapeutics*, 98(1):71–75, 2015.
- [134] Bingbing Li, Xuyun He, Wei Jia, and Houkai Li. Novel Applications of Metabolomics in Personalized Medicine: A Mini-Review. *Molecules*, 22(7), 2017.
- [135] VIPNp. https://parulv1.shinyapps.io/vipnp_shiny/.
- [136] VIPNp. <https://github.com/parulv1/VIPNp>.
- [137] Ellen M Lavoie Smith, Lang Li, Raymond J Hutchinson, Richard Ho, W Bryan Burnette, Elizabeth Wells, Ms Celia Bridges, and Jamie Renbarger. Measuring vincristine-induced peripheral neuropathy in children with acute lymphoblastic leukemia. *Cancer nursing*, 36(5):E49, 2013.
- [138] Shuo Chen and F DuBois Bowman. A novel support vector classifier for longitudinal high-dimensional data and its application to neuroimaging data. *Statistical Analysis and Data Mining: The ASA Data Science Journal*, 4(6):604–611, 2011.
- [139] Colin A Smith, Grace O’Maille, Elizabeth J Want, Chuan Qin, Sunia A Trauger, Theodore R Brandon, Darlene E Custodio, Ruben Abagyan, and Gary Siuzdak. METLIN: a metabolite mass spectral database. *Therapeutic drug monitoring*, 27(6):747–751, 2005.
- [140] David S Wishart, Yannick Djoumbou Feunang, Ana Marcu, An Chi Guo, Kevin Liang, Rosa Viquez-Fresno, Tanvir Sajed, Daniel Johnson, Carin Li, Naama Karu, Zinat Sayeeda, Elvis Lo, Nazanin Assempour, Mark Berjanskii, Sandeep Singhal, David Arndt, Yonjie Liang, Hasan Badran, Jason Grant, Arnau Serracayuela, Yifeng Liu, Rupa Mandal, Vanessa Neveu, Allison Pon, Craig Knox, Michael Wilson, Claudine Manach, and Augustin Scalbert. HMDB 4.0: the human metabolome database for 2018. *Nucleic Acids Research*, 46(D1):D608–D617, 11 2017.
- [141] Alberto Gil de la Fuente, Joanna Godzien, Mariano Fernández López, Francisco J Rupérez, Coral Barbas, and Abraham Otero. Knowledge-based metabolite annotation tool: CEU Mass Mediator. *Journal of pharmaceutical and biomedical analysis*, 154:138–149, 2018.
- [142] Alberto Gil-de-la Fuente, Joanna Godzien, Sergio Saugar, Rodrigo Garcia-Carmona, Hasan Badran, David S Wishart, Coral Barbas, and Abraham Otero. CEU Mass Mediator 3.0: a metabolite annotation tool. *Journal of proteome research*, 18(2):797–802, 2018.
- [143] Jasmine Chong and Jianguo Xia. MetaboAnalystR: an R package for flexible and reproducible analysis of metabolomics data. *Bioinformatics*, 34(24):4313–4314, 2018.
- [144] Jasmine Chong, Othman Soufan, Carin Li, Iurie Caraus, Shuzhao Li, Guillaume Bourque, David S Wishart, and Jianguo Xia. MetaboAnalyst 4.0: towards more transparent and integrative metabolomics analysis. *Nucleic acids research*, 46(W1):W486–W494, 2018.

- [145] Kali Janes, Joshua W Little, Chao Li, Leesa Bryant, Collin Chen, Zhoumou Chen, Krzysztof Kamocki, Timothy Doyle, Ashley Snider, Emanuela Esposito, et al. The development and maintenance of paclitaxel-induced neuropathic pain require activation of the sphingosine 1-phosphate receptor subtype 1. *Journal of Biological Chemistry*, 289(30):21082–21097, 2014.
- [146] Rita Kramer, Jacek Bielawski, Emily Kistner-Griffin, Alaa Othman, Irina Alecu, Daniela Ernst, Drew Kornhauser, Thorsten Hornemann, and Stefka Spassieva. Neurotoxic 1-deoxysphingolipids and paclitaxel-induced peripheral neuropathy. *The FASEB Journal*, 29(11):4461–4472, 2015.
- [147] Katherine Stockstill, Timothy M Doyle, Xisheng Yan, Zhoumou Chen, Kali Janes, Joshua W Little, Kathryn Braden, Filomena Lauro, Luigino Antonio Gi-ancotti, Caron Mitsue Harada, et al. Dysregulation of sphingolipid metabolism contributes to bortezomib-induced neuropathic pain. *Journal of Experimental Medicine*, 215(5):1301–1313, 2018.
- [148] Hana Starobova and Irina Vetter. Pathophysiology of chemotherapy-induced peripheral neuropathy. *Frontiers in molecular neuroscience*, 10:174, 2017.
- [149] Fei-ze Wu, Wen-juan Xu, Bo Deng, Si-da Liu, Chao Deng, Meng-yu Wu, Yu Gao, and Li-qun Jia. Wen-Luo-Tong Decoction Attenuates Paclitaxel-Induced Peripheral Neuropathy by Regulating Linoleic Acid and Glycerophospholipid Metabolism Pathways. *Frontiers in pharmacology*, 9, 2018.
- [150] Emily I. Chen, Katherine D. Crew, Meghna Trivedi, Danielle Awad, Mathew Maurer, Kevin Kalinsky, Antonius Koller, Purvi Patel, Jenny Kim Kim, and Dawn L. Hershman. Identifying Predictors of Taxane-Induced Peripheral Neuropathy Using Mass Spectrometry-Based Proteomics Technology. *PLOS ONE*, 10(12):1–15, 12 2016.
- [151] Lang Li, Tammy Sajdyk, Ellen M. L. Smith, Chien Wei Chang, Claire Li, Richard H. Ho, Raymond Hutchinson, Elizabeth Wells, Jodi L. Skiles, Naomi Winick, Paul L. Martin, and Jamie L. Renbarger. Genetic variants associated with vincristine-induced peripheral neuropathy in two populations of children with acute lymphoblastic leukemia. *Clinical Pharmacology & Therapeutics*, 105(6):1421–1428, 2019.
- [152] Sherleen Xue-Fu Adamson, Ruoxing Wang, Wenzhuo Wu, Bruce Cooper, and Jonathan Shannahan. Metabolomic insights of macrophage responses to graphene nanoplatelets: Role of scavenger receptor cd36. *PLOS ONE*, 13(11):1–30, 11 2018.
- [153] Fen Yang, Hongyun Wang, Ming Liu, Pei Hu, and Ji Jiang. Determination of free and total vincristine in human plasma after intravenous administration of vincristine sulfate liposome injection using ultra-high performance liquid chromatography tandem mass spectrometry. *Journal of Chromatography A*, 1275:61 – 69, 2013.
- [154] R Core Team. *R: A Language and Environment for Statistical Computing*. R Foundation for Statistical Computing, Vienna, Austria, 2017.
- [155] Emily Grace Armitage, Joanna Godzien, Vanesa Alonso-Herranz, Ángeles López-González, and Coral Barbas. Missing value imputation strategies for metabolomics data. *Electrophoresis*, 36(24):3050–3060, 2015.

- [156] Trevor Hastie, Robert Tibshirani, Balasubramanian Narasimhan, and Gilbert Chu. *impute: Imputation for microarray data*, 2017. R package version 1.50.1.
- [157] Max Kuhn. Contributions from Jed Wing, Steve Weston, Andre Williams, Chris Keefer, Allan Engelhardt, Tony Cooper, Zachary Mayer, Brenton Kenkel, the R Core Team, Michael Benesty, Reynald Lescarbeau, Andrew Ziem, Luca Scrucca, Yuan Tang, Can Candan, and Tyler Hunt. *caret: Classification and Regression Training*. R package version 6.0-78.
- [158] David Meyer, Evgenia Dimitriadou, Kurt Hornik, Andreas Weingessel, and Friedrich Leisch. *e1071: Misc Functions of the Department of Statistics, Probability Theory Group (Formerly: E1071), TU Wien*, 2017. R package version 1.6-8.
- [159] Parul Verma, Achim Kienle, Dietrich Flockerzi, and Doraiswami Ramkrishna. Using bifurcation theory for exploring pain. *Industrial & Engineering Chemistry Research*, 59(6):2524–2535, 2020.
- [160] L. F. Razon and R. A. Schmitz. Multiplicities and instabilities in chemically reacting systems - a review. *Chem. Eng. Sci.*, 42:1005–1047, 1987.
- [161] W. H. Ray and C. M. Villa. Nonlinear dynamics found in polymerization processes - a review. *Chem. Eng. Sci.*, 55:275–290, 2000.
- [162] G. Ertl. Reactions at surfaces: From atoms to complexity (nobel lecture). *Angewandte Chemie - International Edition*, 47:3524–3535, 2008.
- [163] E. W. Jacobsen and S. Skogestad. Multiple steady states in ideal two-product distillation. *AIChE J.*, 37:499–511, 1991.
- [164] Nikolaos Bekiaris, George A. Meski, Christian M. Radu, and Manfred Morari. Multiple steady states in homogeneous azeotropic distillation. *Ind. Eng. Chem. Res.*, 32:2023–2038, 1993.
- [165] K. D. Mohl, A. Kienle, E. D. Gilles, P. Rapmund, K. Sundmacher, and U. Hoffmann. Steady-state multiplicities in reactive distillation columns for the production of fuel ethers mtbe and tame via reactive distillation – theoretical and experimental results. *Chem. Eng. Sci.*, 54:1029–1043, 1999.
- [166] A. D. Randolph and M. A. Larson. *Theory of Particulate Processes*. Academic Press, New York, 1988.
- [167] A. Gerstlauer, C. Gahn, H. Zhou, M. Rauls, and M. Schreiber. Application of population balances in the chemical industry - Current status and future needs. *Chem. Eng. Sci.*, 61:205–217, 2006.
- [168] R. Radichkov, T. Müller, A. Kienle, S. Heinrich, M. Peglow, and L. Mörl. A numerical bifurcation analysis of fluidized bed spray granulation with external classification. *Chem. Eng. Proc.*, 45:826–837, 2006.
- [169] M. Schmidt, C. Rieck, A. Bück, and E. Tsotsas. Experimental investigation of process stability of continuous spray fluidized bed layering granulation with external product separation. *Chem. Eng. Sci.*, 137:466–475, 2015.

- [170] C. Neugebauer, E. Diez, A. Bück, S. Palis, S. Heinrich, and A. Kienle. Dynamics and control of continuous fluidized bed layering granulation with screen-mill-cycle. *Powder Technol.*, 354:765–778, 2019.
- [171] R. Hanke-Rauschenbach, M. Mangold, and K. Sundmacher. Nonlinear dynamics of fuel cells: A review. *Rev. Chem. Eng.*, 27:23–52, 2011.
- [172] Abhijit Namjoshi, Achim Kienle, and Doraiswami Ramkrishna. Steady-state multiplicity in bioreactors: bifurcation analysis of cybernetic models. *Chemical Engineering Science*, 58(3):793 – 800, 2003. 17th International Symposium of Chemical Reaction Engineering (IS CRE 17).
- [173] Jin Il Kim, Hyun-Seob Song, Sunil R. Sunkara, Arvind Lali, and Doraiswami Ramkrishna. Exacting predictions by cybernetic model confirmed experimentally: Steady state multiplicity in the chemostat. *Biotechnology Progress*, 28(5):1160–1166, 2012.
- [174] Hyun-Seob Song and Doraiswami Ramkrishna. Complex nonlinear behavior in metabolic processes: Global bifurcation analysis of escherichia coli growth on multiple substrates. *Processes*, 1(3):263–278, 2013.
- [175] W. Marquardt and M. Mönnigmann. Constructive nonlinear dynamics in process systems engineering. *Computers Chem. Eng.*, 29:1265–1275, 2005.
- [176] David J Christini, Kenneth M Stein, Steven M Markowitz, Suneet Mittal, DJ Slotwiner, and BB Lerman. The role of nonlinear dynamics in cardiac arrhythmia control. *Heart Disease*, 1(4):190–200, 1999.
- [177] A. L. Hodgkin and A. F. Huxley. A quantitative description of membrane current and its application to conduction and excitation in nerve. *The Journal of Physiology*, 117(4):500–544, 1952.
- [178] Jin Mo Chung and Kyungsoon Chung. Importance of hyperexcitability of drg neurons in neuropathic pain. *Pain Practice*, 2(2):87–97, 2002.
- [179] Eugene M Izhikevich. *Dynamical systems in neuroscience*. MIT press, 2007.
- [180] James P Keener and James Sneyd. *Mathematical physiology*, volume 1. Springer, 1998.
- [181] Peter Dayan, Laurence F Abbott, and L Abbott. Theoretical neuroscience: computational and mathematical modeling of neural systems. 2001.
- [182] Dieter Jaeger and Ranu Jung. *Encyclopedia of computational neuroscience*. Springer Publishing Company, Incorporated, 2015.
- [183] G Bard Ermentrout and David H Terman. *Mathematical foundations of neuroscience*, volume 35. Springer Science & Business Media, 2010.
- [184] Erik De Schutter. *Computational modeling methods for neuroscientists*. The MIT Press, 2009.
- [185] Daniel Johnston and Samuel Miao-Sin Wu. *Foundations of cellular neurophysiology*. MIT press, 1994.

- [186] Patrick L Sheets, James O Jackson, Stephen G Waxman, Sulayman D Dib-Hajj, and Theodore R Cummins. A Nav1.7 channel mutation associated with hereditary erythromelalgia contributes to neuronal hyperexcitability and displays reduced lidocaine sensitivity. *The Journal of physiology*, 581(3):1019–1031, 2007.
- [187] Jin-Sung Choi and Stephen G Waxman. Physiological interactions between Nav1.7 and Nav1.8 sodium channels: a computer simulation study. *Journal of neurophysiology*, 106(6):3173–3184, 2011.
- [188] Qin Zheng, Dong Fang, Jie Cai, You Wan, Ji-Sheng Han, and Guo-Gang Xing. Enhanced excitability of small dorsal root ganglion neurons in rats with bone cancer pain. *Molecular pain*, 8(1):24, 2012.
- [189] Jianying Huang, Malgorzata A Mis, Brian Tanaka, Talia Adi, Mark Estacion, Shujun Liu, Suellen Walker, Sulayman D Dib-Hajj, and Stephen G Waxman. Atypical changes in DRG neuron excitability and complex pain phenotype associated with a Nav1.7 mutation that massively hyperpolarizes activation. *Scientific reports*, 8(1):1811, 2018.
- [190] Yang Yang, Jianying Huang, Malgorzata A. Mis, Mark Estacion, Lawrence Macala, Palak Shah, Betsy R. Schulman, Daniel B. Horton, Sulayman D. Dib-Hajj, and Stephen G. Waxman. Nav1.7-A1632G mutation from a family with inherited erythromelalgia: Enhanced firing of dorsal root ganglia neurons evoked by thermal stimuli. *Journal of Neuroscience*, 36(28):7511–7522, 2016.
- [191] Adrienne E. Dubin and Ardem Patapoutian. Nociceptors: the sensors of the pain pathway. *The Journal of Clinical Investigation*, 120(11):3760–3772, 11 2010.
- [192] Laiche Djouhri, Stella Koutsikou, Xin Fang, Simon McMullan, and Sally N. Lawson. Spontaneous pain, both neuropathic and inflammatory, is related to frequency of spontaneous firing in intact c-fiber nociceptors. *Journal of Neuroscience*, 26(4):1281–1292, 2006.
- [193] Bard Ermentrout. *Simulating, analyzing, and animating dynamical systems: a guide to XPPAUT for researchers and students*, volume 14. Siam, 2002.
- [194] David L. Bennett, Alex J. Clark, Jianying Huang, Stephen G. Waxman, and Sulayman D. Dib-Hajj. The role of voltage-gated sodium channels in pain signaling. *Physiological Reviews*, 99(2):1079–1151, 2019. PMID: 30672368.
- [195] Edward C Emery, Ana Paula Luiz, and John N Wood. Nav1.7 and other voltage-gated sodium channels as drug targets for pain relief. *Expert Opinion on Therapeutic Targets*, 20(8):975–983, 2016. PMID: 26941184.
- [196] Theodore R. Cummins, Patrick L. Sheets, and Stephen G. Waxman. The roles of sodium channels in nociception: Implications for mechanisms of pain. *PAIN*, 131(3):243 – 257, 2007.
- [197] Young-Ah Rho and Steven A. Prescott. Identification of molecular pathologies sufficient to cause neuropathic excitability in primary somatosensory afferents using dynamical systems theory. *PLOS Computational Biology*, 8(5):1–14, 05 2012.

- [198] Na Yu, Catherine E. Morris, Bla Jos, and Andr Longtin. Spontaneous excitation patterns computed for axons with injury-like impairments of sodium channels and na/k pumps. *PLOS Computational Biology*, 8(9):1–20, 09 2012.
- [199] Sulayman D Dib-Hajj, Yang Yang, Joel A Black, and Stephen G Waxman. The Na_v 1.7 sodium channel: from molecule to man. *Nature Reviews Neuroscience*, 14(1):49, 2013.
- [200] James J Cox, Frank Reimann, Adeline K Nicholas, Gemma Thornton, Emma Roberts, Kelly Springell, Gulshan Karbani, Hussain Jafri, Jovaria Mannan, Yasmin Raashid, Lihadh Al-Gazali, Henan Hamamy, Enza Maria Valente, Shaun Gorman, Richard Williams, Duncan P McHale, John N Wood, Fiona M Gribble, and C Geoffrey Woods. An scn9a channelopathy causes congenital inability to experience pain. *Nature*, 444(7121):894, 2006.
- [201] Theodore R. Cummins, Sulayman D. Dib-Hajj, and Stephen G. Waxman. Electrophysiological properties of mutant na_v1.7 sodium channels in a painful inherited neuropathy. *Journal of Neuroscience*, 24(38):8232–8236, 2004.
- [202] S. D. Dib-Hajj, A. M. Rush, T. R. Cummins, F. M. Hisama, S. Novella, L. Tyrrell, L. Marshall, and S. G. Waxman. Gain-of-function mutation in Na_v1.7 in familial erythromelalgia induces bursting of sensory neurons. *Brain*, 128(8):1847–1854, 06 2005.
- [203] Jin-Sung Choi, Sulayman D. Dib-Hajj, and Stephen G. Waxman. Inherited erythromelalgia. *Neurology*, 67(9):1563–1567, 2006.
- [204] T. Patrick Harty, Sulayman D. Dib-Hajj, Lynda Tyrrell, Rachael Blackman, Fuki M. Hisama, John B. Rose, and Stephen G. Waxman. Na_v1.7 mutant a863p in erythromelalgia: Effects of altered activation and steady-state inactivation on excitability of nociceptive dorsal root ganglion neurons. *Journal of Neuroscience*, 26(48):12566–12575, 2006.
- [205] Chongyang Han, Anthony M. Rush, Sulayman D. Dib-Hajj, Song Li, Zhe Xu, Yun Wang, Lynda Tyrrell, Xiaoliang Wang, Yong Yang, and Stephen G. Waxman. Sporadic onset of erythromelalgia: A gain-of-function mutation in na_v1.7. *Annals of Neurology*, 59(3):553–558, 2006.
- [206] Brian S Tanaka, Phuong T Nguyen, Eray Yihui Zhou, Yong Yang, Vladimir Yarov-Yarovoy, Sulayman D Dib-Hajj, and Stephen G Waxman. Gain-of-function mutation of a voltage-gated sodium channel na_v1.7 associated with peripheral pain and impaired limb development. *Journal of Biological Chemistry*, 292(22):9262–9272, 2017.
- [207] Chongyang Han, Jianying Huang, and Stephen G. Waxman. Sodium channel na_v1.8. *Neurology*, 86(5):473–483, 2016.
- [208] Catharina G. Faber, Giuseppe Lauria, Ingemar S. J. Merkies, Xiaoyang Cheng, Chongyang Han, Hye-Sook Ahn, Anna-Karin Persson, Janneke G. J. Hoeijmakers, Monique M. Gerrits, Tiziana Pierro, Raffaella Lombardi, Dimos Kapetis, Sulayman D. Dib-Hajj, and Stephen G. Waxman. Gain-of-function na_v1.8 mutations in painful neuropathy. *Proceedings of the National Academy of Sciences*, 109(47):19444–19449, 2012.

- [209] Jianying Huang, Yang Yang, Peng Zhao, Monique M. Gerrits, Janneke G.J. Hoeijmakers, Kim Bekelaar, Ingemar S.J. Merkies, Catharina G. Faber, Sulayman D. Dib-Hajj, and Stephen G. Waxman. Small-fiber neuropathy $\text{nav}1.8$ mutation shifts activation to hyperpolarized potentials and increases excitability of dorsal root ganglion neurons. *Journal of Neuroscience*, 33(35):14087–14097, 2013.
- [210] Robert Prior, Lawrence Van Helleputte, Veronick Benoy, and Ludo Van den Bosch. Defective axonal transport: a common pathological mechanism in inherited and acquired peripheral neuropathies. *Neurobiology of disease*, 105:300–320, 2017.
- [211] Ron Amir, Martin Michaelis, and Marshall Devor. Membrane potential oscillations in dorsal root ganglion neurons: Role in normal electrogenesis and neuropathic pain. *Journal of Neuroscience*, 19(19):8589–8596, 1999.
- [212] Mykhaylo Krasnyk, Martin Ginkel, Michael Mangold, and A Kienle. Numerical analysis of higher order singularities in chemical process models. *Computers & chemical engineering*, 31(9):1100–1110, 2007.
- [213] A. Dhooge, W. Govaerts, Yu. A. Kuznetsov, H. G.E. Meijer, and B. Sautois. New features of the software MatCont for bifurcation analysis of dynamical systems. *Mathematical and Computer Modelling of Dynamical Systems*, 14(2):147–175, 2008.
- [214] The Mathworks, Inc., Natick, Massachusetts. *MATLAB version 9.5.0.944444 (R2018b)*, 2018.
- [215] William C Troy. The bifurcation of periodic solutions in the Hodgkin-Huxley equations. *Quarterly of Applied Mathematics*, 36(1):73–83, 1978.
- [216] Brian Hassard. Bifurcation of periodic solutions of the hodgkin-huxley model for the squid giant axon. *Journal of Theoretical Biology*, 71(3):401–420, 1978.
- [217] John Rinzel. Numerical calculation of stable and unstable periodic solutions to the Hodgkin-Huxley equations. *Mathematical Biosciences*, 49:27–59, 1980.
- [218] Huiwen Ju, Alexander B. Neiman, and Andrey L. Shilnikov. Bottom-up approach to torus bifurcation in neuron models. *Chaos: An Interdisciplinary Journal of Nonlinear Science*, 28(10):106317, 2018.
- [219] Danielle Sundt, Nikita Gamper, and David B. Jaffe. Spike propagation through the dorsal root ganglia in an unmyelinated sensory neuron: a modeling study. *Journal of Neurophysiology*, 114(6):3140–3153, 2015. PMID: 26334005.
- [220] Anthony M. Rush, Theodore R. Cummins, and Stephen G. Waxman. Multiple sodium channels and their roles in electrogenesis within dorsal root ganglion neurons. *The Journal of Physiology*, 579(1):1–14, 2007.
- [221] Elliot S. Krames. The Role of the Dorsal Root Ganglion in the Development of Neuropathic Pain. *Pain Medicine*, 15(10):1669–1685, 10 2014.
- [222] Temugin Berta, Yawar Qadri, Ping-Heng Tan, and Ru-Rong Ji. Targeting dorsal root ganglia and primary sensory neurons for the treatment of chronic pain. *Expert opinion on therapeutic targets*, 21(7):695–703, 2017.

- [223] Morten Brøns, Tasso J. Kaper, and Horacio G. Rotstein. Introduction to focus issue: Mixed mode oscillations: Experiment, computation, and analysis. *Chaos: An Interdisciplinary Journal of Nonlinear Science*, 18(1):015101, 2008.
- [224] Mathieu Desroches, John Guckenheimer, Bernd Krauskopf, Christian Kuehn, Hinke M Osinga, and Martin Wechselberger. Mixed-mode oscillations with multiple time scales. *Siam Review*, 54(2):211–288, 2012.
- [225] J. Maseko and Harry L. Swinney. Complex periodic oscillations and Farey arithmetic in the BelousovZhabotinskii reaction. *The Journal of Chemical Physics*, 85(11):6430–6441, 1986.
- [226] Godfrey Harold Hardy, Edward Maitland Wright, et al. *An introduction to the theory of numbers*. Oxford university press, 1979.
- [227] F. N. Albahadily, John Ringland, and Mark Schell. Mixedmode oscillations in an electrochemical system. I. A Farey sequence which does not occur on a torus. *The Journal of Chemical Physics*, 90(2):813–821, 1989.
- [228] T Hauck and FW Schneider. Chaos in a Farey sequence through period doubling in the peroxidase-oxidase reaction. *The Journal of Physical Chemistry*, 98(8):2072–2077, 1994.
- [229] Andrzej L. Kawczynski and Peter E. Strizhak. Period adding and broken Farey tree sequence of bifurcations for mixed-mode oscillations and chaos in the simplest three-variable nonlinear system. *The Journal of Chemical Physics*, 112(14):6122–6130, 2000.
- [230] Wieslaw Marszalek. Circuits with oscillatory hierarchical Farey sequences and fractal properties. *Circuits, Systems, and Signal Processing*, 31(4):1279–1296, Aug 2012.
- [231] Martin Krupa, Nikola Popovi, Nancy Kopell, and Horacio G. Rotstein. Mixed-mode oscillations in a three time-scale model for the dopaminergic neuron. *Chaos: An Interdisciplinary Journal of Nonlinear Science*, 18(1):015106, 2008.
- [232] Jonathan Rubin and Martin Wechselberger. Giant squid-hidden canard: The 3d geometry of the Hodgkin–Huxley model. *Biological Cybernetics*, 97(1):5–32, Jul 2007.
- [233] Andreas A Argyriou, Martin Koltzenburg, Panagiotis Polychronopoulos, Spiridon Papapetropoulos, and Haralabos P Kalofonos. Peripheral nerve damage associated with administration of taxanes in patients with cancer. *Critical reviews in oncology/hematology*, 66(3):218–228, 2008.
- [234] Sang Hui Chu, Young Joo Lee, Eon Sook Lee, Yimin Geng, Xin Shelley Wang, and Charles S. Cleeland. Current use of drugs affecting the central nervous system for chemotherapy-induced peripheral neuropathy in cancer patients: a systematic review. *Supportive Care in Cancer*, 23(2):513–524, Feb 2015.
- [235] Yusuke Fukuda, Yihang Li, and Rosalind A. Segal. A mechanistic understanding of axon degeneration in chemotherapy-induced peripheral neuropathy. *Frontiers in Neuroscience*, 11:481, 2017.

- [236] Jun-Yang Lou, Fernanda Laezza, Benjamin R. Gerber, Maolei Xiao, Kathryn A. Yamada, Hali Hartmann, Ann Marie Craig, Jeanne M. Nerbonne, and David M. Ornitz. Fibroblast growth factor 14 is an intracellular modulator of voltage-gated sodium channels. *The Journal of Physiology*, 569(1):179–193, 2005.
- [237] Xiaona Du and Nikita Gamper. Potassium channels in peripheral pain pathways: expression, function and therapeutic potential. *Current neuropharmacology*, 11(6):621–640, 2013.
- [238] Lital Livni, Justin G Lees, Mallory E Barkl-Luke, David Goldstein, and Gila Moalem-Taylor. Dorsal root ganglion explants derived from chemotherapy-treated mice have reduced neurite outgrowth in culture. *Neuroscience letters*, 694:14–19, 2019.
- [239] Alan L Hodgkin and Andrew F Huxley. A quantitative description of membrane current and its application to conduction and excitation in nerve. *The Journal of physiology*, 117(4):500–544, 1952.
- [240] David W. Mullins, Carol J. Burger, and Klaus D. Elgert. Paclitaxel enhances macrophage il-12 production in tumor-bearing hosts through nitric oxide. *The Journal of Immunology*, 162(11):6811–6818, 1999.
- [241] Yucheng Xiao, Cindy Barbosa, Zifan Pei, Wenrui Xie, Judith A. Strong, Jun-Ming Zhang, and Theodore R. Cummins. Increased Resurgent Sodium Currents in Nav1.8 Contribute to Nociceptive Sensory Neuron Hyperexcitability Associated with Peripheral Neuropathies. *Journal of Neuroscience*, 39(8):1539–1550, 2019.
- [242] Xiao-Long Zhang, Xian-Ying Cao, Ren-Chun Lai, Man-Xiu Xie, and Wei-An Zeng. Puerarin relieves paclitaxel-induced neuropathic pain: The role of nav1.8 β 1 subunit of sensory neurons. *Frontiers in Pharmacology*, 9:1510, 2019.
- [243] Parul Verma, Achim Kienle, Dietrich Flockerzi, and Doraiswami Ramkrishna. Computational analysis of a 9D model for a small DRG neuron, 2020.
- [244] Eric K. Rowinsky, Micheal Jiroutek, Philip Bonomi, David Johnson, and Sharyn D. Baker. Paclitaxel steady-state plasma concentration as a determinant of disease outcome and toxicity in lung cancer patients treated with paclitaxel and cisplatin. *Clinical Cancer Research*, 5(4):767–774, 1999.
- [245] Payal Rana, Gregory Luerman, Dietmar Hess, Elizabeth Rubitski, Karissa Adkins, and Christopher Soms. Utilization of ipsc-derived human neurons for high-throughput drug-induced peripheral neuropathy screening. *Toxicology in Vitro*, 45:111 – 118, 2017.
- [246] Darshan Mandge and Rohit Manchanda. A biophysically detailed computational model of urinary bladder small drg neuron soma. *PLOS Computational Biology*, 14(7):1–51, 07 2018.
- [247] Gabriella Nicolini, Marianna Monfrini, and Arianna Scuteri. Axonal transport impairment in chemotherapy-induced peripheral neuropathy. *Toxics*, 3(3):322–341, 2015.
- [248] William R. Holmes. *Cable Equation*, pages 1–13. Springer New York, New York, NY, 2013.

- [249] Yang Yang, Talia Adi, Philip R Effraim, Lubin Chen, Sulayman D Dib-Hajj, and Stephen G Waxman. Reverse pharmacogenomics: carbamazepine normalizes activation and attenuates thermal hyperexcitability of sensory neurons due to nav1.7 mutation i234t. *British Journal of Pharmacology*, 175(12):2261–2271, 2018.
- [250] Michael F. Jarvis, Prisca Honore, Char-Chang Shieh, Mark Chapman, Shailen Joshi, Xu-Feng Zhang, Michael Kort, William Carroll, Brian Marron, Robert Atkinson, James Thomas, Dong Liu, Michael Krambis, Yi Liu, Steve McGaraughty, Katharine Chu, Rosemarie Roeloffs, Chengmin Zhong, Joseph P. Mikusa, Gricelda Hernandez, Donna Gauvin, Carrie Wade, Chang Zhu, Madhavi Pai, Marc Scanio, Lei Shi, Irene Drizin, Robert Gregg, Mark Matulenko, Ahmed Hakeem, Michael Gross, Matthew Johnson, Kennan Marsh, P. Kay Wagoner, James P. Sullivan, Connie R. Faltynek, and Douglas S. Krafte. A-803467, a potent and selective nav1.8 sodium channel blocker, attenuates neuropathic and inflammatory pain in the rat. *Proceedings of the National Academy of Sciences*, 104(20):8520–8525, 2007.
- [251] Martin Kruse, Gerald RV Hammond, and Bertil Hille. Regulation of voltage-gated potassium channels by pi (4, 5) p2. *The Journal of general physiology*, 140(2):189–205, 2012.
- [252] Benjamin M Zemel, David M Ritter, Manuel Covarrubias, and Tanziyah Muqeem. A-type kv channels in dorsal root ganglion neurons: diversity, function, and dysfunction. *Frontiers in molecular neuroscience*, 11:253, 2018.
- [253] David M. Ritter, Cojen Ho, Michael E. OLeary, and Manuel Covarrubias. Modulation of kv3.4 channel n-type inactivation by protein kinase c shapes the action potential in dorsal root ganglion neurons. *The Journal of Physiology*, 590(1):145–161, 2012.
- [254] C.F. Starmer, A.O. Grant, and H.C. Strauss. Mechanisms of use-dependent block of sodium channels in excitable membranes by local anesthetics. *Biophysical Journal*, 46(1):15 – 27, 1984.
- [255] Luc M. Hondeghem and Bertram G. Katzung. Time- and voltage-dependent interactions of antiarrhythmic drugs with cardiac sodium channels. *Biochimica et Biophysica Acta (BBA) - Reviews on Biomembranes*, 472(3):373 – 398, 1977.
- [256] Quan Yang, Roberto Padrini, Sergio Bova, Donatella Piovan, and Gianna Magnolfi. Electrocardiographic interactions between pinacidil, a potassium channel opener and class i antiarrhythmic agents in guinea-pig isolated perfused heart. *British Journal of Pharmacology*, 114(8):1745–1749, 1995.
- [257] Vikas N Shah, Benjamin Chagot, and Walter J Chazin. Calcium-dependent regulation of ion channels. *Calcium binding proteins*, 1(4):203, 2006.
- [258] Elzbieta Rebas, Tomasz Boczek, Antoni Kowalski, Kinga Kumirowska, Malwina Lisek, and Ludmia Zyliska. [the role of calmodulin in calcium-dependent signalling in excitable cells]. *Postepy biochemii*, 58(4):393402, 2012.
- [259] Tanimasa Bose, Artur Ciešlar-Pobuda, and Emilia Wiechec. Role of ion channels in regulating ca²⁺ homeostasis during the interplay between immune and cancer cells. *Cell death & disease*, 6(2):e1648–e1648, 2015.

- [260] Kirill Kiselyov and Shmuel Muallem. Ros and intracellular ion channels. *Cell Calcium*, 60(2):108–114, 2016.
- [261] Ariel C Bulua, Anna Simon, Ravikanth Maddipati, Martin Pelletier, Heiyoung Park, Kye-Young Kim, Michael N Sack, Daniel L Kastner, and Richard M Siegel. Mitochondrial reactive oxygen species promote production of proinflammatory cytokines and are elevated in tnfr1-associated periodic syndrome (traps). *Journal of Experimental Medicine*, 208(3):519–533, 2011.
- [262] Lucio Annunziato, Anna Pannaccione, Mauro Cataldi, Agnese Secondo, Pasqualina Castaldo, Gianfranco Di Renzo, and Maurizio Tagliabatella. Modulation of ion channels by reactive oxygen and nitrogen species: a pathophysiological role in brain aging? *Neurobiology of Aging*, 23(5):819 – 834, 2002. Brain Aging: Identifying the Brakes and Accelerators.
- [263] Yanping Liu and David D Gutterman. Oxidative stress and potassium channel function. *Clinical and experimental pharmacology and physiology*, 29(4):305–311, 2002.
- [264] Ana Ramírez, Alma Yolanda Vázquez-Sánchez, Natalia Carrión-Robalino, and Javier Camacho. Ion channels and oxidative stress as a potential link for the diagnosis or treatment of liver diseases. *Oxidative medicine and cellular longevity*, 2016, 2016.
- [265] Valentin Schatz, Patrick Neubert, Agnes Schröder, Katrina Binger, Matthias Gebhard, Dominik N Müller, Friedrich C Luft, Jens Titze, and Jonathan Jantsch. Elementary immunology: Na⁺ as a regulator of immunity. *Pediatric Nephrology*, 32(2):201–210, 2017.
- [266] Regina A. Clemens and Clifford A. Lowell. Store-operated calcium signaling in neutrophils. *Journal of Leukocyte Biology*, 98(4):497–502, 2015.
- [267] Gregory R Tintinger, Helen C Steel, Annette J Theron, and Ronald Anderson. Pharmacological control of neutrophil-mediated inflammation: strategies targeting calcium handling by activated polymorphonuclear leukocytes. *Drug design, development and therapy*, 2:95, 2008.
- [268] Melania Capasso, Mandeep K Bhamrah, Tom Henley, Robert S Boyd, Claudia Langlais, Kelvin Cain, David Dinsdale, Karen Pulford, Mahmood Khan, Boris Musset, et al. Hvcn1 modulates bcr signal strength via regulation of bcr-dependent generation of reactive oxygen species. *Nature immunology*, 11(3):265, 2010.
- [269] Anke Di, Xiao-Pei Gao, Feng Qian, Takeshi Kawamura, Jin Han, Claudie Hecquet, D Ye Richard, Stephen M Vogel, and Asrar B Malik. The redox-sensitive cation channel trpm2 modulates phagocyte ros production and inflammation. *Nature immunology*, 13(1):29, 2012.
- [270] Francesco Di Virgilio, Diego Dal Ben, Alba Clara Sarti, Anna Lisa Giuliani, and Simonetta Falzoni. The p2x7 receptor in infection and inflammation. *Immunity*, 47(1):15 – 31, 2017.
- [271] Gloria Lopez-Castejon and David Brough. Understanding the mechanism of il-1 β secretion. *Cytokine & growth factor reviews*, 22(4):189–195, 2011.

- [272] Bénédicte F Py, Mingzhi Jin, Bimal N Desai, Anirudh Penumaka, Hong Zhu, Maike Kober, Alexander Dietrich, Marta M Lipinski, Thomas Henry, David E Clapham, et al. Caspase-11 controls interleukin-1 β release through degradation of trpc1. *Cell reports*, 6(6):1122–1128, 2014.
- [273] A Parenti, F De Logu, P Geppetti, and S Benemei. What is the evidence for the role of trp channels in inflammatory and immune cells? *British journal of pharmacology*, 173(6):953–969, 2016.
- [274] Bernd Nilius and Grzegorz Owsianik. The transient receptor potential family of ion channels. *Genome biology*, 12(3):218, 2011.
- [275] Marc Freichel, Julia Almering, and Volodymyr Tsvilovskyy. The role of trp proteins in mast cells. *Frontiers in immunology*, 3:150, 2012.
- [276] Giuseppe A Ramirez, Lavinia A Coletto, Clara Sciorati, Enrica P Bozzolo, Paolo Manunta, Patrizia Rovere-Querini, and Angelo A Manfredi. Ion channels and transporters in inflammation: special focus on trp channels and trpc6. *Cells*, 7(7):70, 2018.
- [277] W.H. Xiao, H. Zheng, and G.J. Bennett. Characterization of oxaliplatin-induced chronic painful peripheral neuropathy in the rat and comparison with the neuropathy induced by paclitaxel. *Neuroscience*, 203:194 – 206, 2012.
- [278] Ilja Bobylev, Abhijeet R Joshi, Mohammed Barham, Wolfram F Neiss, and Helmar C Lehmann. Depletion of mitofusin-2 causes mitochondrial damage in cisplatin-induced neuropathy. *Molecular neurobiology*, 55(2):1227–1235, 2018.
- [279] Genevieve Dupont and Albert Goldbeter. One-pool model for Ca²⁺ oscillations involving Ca²⁺ and inositol 1, 4, 5-trisphosphate as co-agonists for Ca²⁺ release. *Cell calcium*, 14(4):311–322, 1993.
- [280] Yue-Xian Li and John Rinzel. Equations for InsP₃ receptor-mediated [Ca²⁺]_i oscillations derived from a detailed kinetic model: a hodgkin-huxley like formalism. *Journal of theoretical Biology*, 166(4):461–473, 1994.
- [281] Marko Marhl, Stefan Schuster, Milan Brumen, and Reinhart Heinrich. Modelling the interrelations between calcium oscillations and ER membrane potential oscillations. *Biophysical chemistry*, 63(2-3):221–239, 1997.
- [282] Sergej L Mironov, Maxim V Ivannikov, and Mattias Johansson. [ca²⁺]_i signaling between mitochondria and endoplasmic reticulum in neurons is regulated by microtubules from mitochondrial permeability transition pore to ca²⁺-induced ca²⁺ release. *Journal of Biological Chemistry*, 280(1):715–721, 2005.
- [283] Paolo Bernardi, Alexandra Krauskopf, Emy Basso, Valeria Petronilli, Elizabeth Blalchy-Dyson, Fabio Di Lisa, and Michael A Forte. The mitochondrial permeability transition from in vitro artifact to disease target. *The FEBS journal*, 273(10):2077–2099, 2006.
- [284] Stefan Schuster, Marko Marhl, and Thomas Höfer. Modelling of simple and complex calcium oscillations: From single-cell responses to intercellular signalling. *European Journal of Biochemistry*, 269(5):1333–1355, 2002.

- [285] K. Morita, K. Koketsu, and K. Kuba. Oscillation of $[Ca^{2+}]_i$ -linked K^+ conductance in bullfrog sympathetic ganglion cell is sensitive to intracellular anions. *Nature*, 283:204 EP –, 01 1980.
- [286] Niall M. Woods, K. S. Roy Cuthbertson, and Peter H. Cobbold. Repetitive transient rises in cytoplasmic free calcium in hormone-stimulated hepatocytes. *Nature*, 319:600 EP –, 02 1986.
- [287] Niall M. Woods, K.S.Roy Cuthbertson, and Peter H. Cobbold. Agonist-induced oscillations in cytoplasmic free calcium concentration in single rat hepatocytes. *Cell Calcium*, 8(1):79 – 100, 1987.
- [288] Doraiswami Ramkrishna and Hyun-Seob Song. *Cybernetic Modeling for Bioreaction Engineering*. Cambridge University Press, 2018.
- [289] Lina Aboulmouna, Shakti Gupta, Mano R Maurya, Frank T DeVilbiss, Shankar Subramaniam, and Doraiswami Ramkrishna. A cybernetic approach to modeling lipid metabolism in mammalian cells. *Processes*, 6(8):126, 2018.
- [290] Mahendra Kavdia. Mathematical and computational models of oxidative and nitrosative stress. *Critical Reviews in Biomedical Engineering*, 39(5), 2011.
- [291] Chuan Xue and Gregory Jameson. *Recent Mathematical Models of Axonal Transport*, pages 265–285. Springer International Publishing, Cham, 2017.
- [292] JH Schild, JW Clark, M Hay, D Mendelowitz, MC Andresen, and DL Kunze. A- and C-type rat nodose sensory neurons: model interpretations of dynamic discharge characteristics. *Journal of Neurophysiology*, 71(6):2338–2358, 1994.
- [293] Guido Cavaletti, Paola Alberti, Barbara Frigeni, Marialuisa Piatti, and Emanuela Susani. Chemotherapy-induced neuropathy. *Current treatment options in neurology*, 13(2):180–190, 2011.
- [294] Amteshwar Singh Jaggi and Nirmal Singh. Mechanisms in cancer-chemotherapeutic drugs-induced peripheral neuropathy. *Toxicology*, 291(1-3):1–9, 2012.
- [295] Jason Yao, Anna Pilko, and Roy Wollman. Distinct cellular states determine calcium signaling response. *Molecular systems biology*, 12(12):894, 2016.
- [296] William E Hart, Jean-Paul Watson, and David L Woodruff. Pyomo: modeling and solving mathematical programs in python. *Mathematical Programming Computation*, 3(3):219–260, 2011.
- [297] William E. Hart, Carl D. Laird, Jean-Paul Watson, David L. Woodruff, Gabriel A. Hackebeil, Bethany L. Nicholson, and John D. Sirola. *Pyomo-optimization modeling in python*, volume 67. Springer Science & Business Media, second edition, 2017.
- [298] Andreas Wächter and Lorenz T Biegler. On the implementation of an interior-point filter line-search algorithm for large-scale nonlinear programming. *Mathematical programming*, 106(1):25–57, 2006.

- [299] G Lemon, WG Gibson, and MR Bennett. Metabotropic receptor activation, desensitization and sequestration: modelling calcium and inositol 1, 4, 5-trisphosphate dynamics following receptor activation. *Journal of Theoretical Biology*, 223(1):93–111, 2003.
- [300] R H Himes, R N Kersey, I Heller-Bettinger, and F E Samson. Action of the vinca alkaloids vincristine, vinblastine, and desacetyl vinblastine amide on microtubules in vitro. *Cancer Res*, 36(10):3798–802, Oct 1976.
- [301] H O Klein. Cell kinetic alterations in normal and neoplastic cell populations in vitro and in vivo following vincristine: a reply to Dr Camplejohn’s review article. *Cell Tissue Kinet*, 13(4):425–34, Jul 1980.
- [302] K Lu, H Y Yap, and T L Loo. Clinical pharmacokinetics of vinblastine by continuous intravenous infusion. *Cancer Res*, 43(3):1405–8, Mar 1983.
- [303] M A Jordan, R H Himes, and L Wilson. Comparison of the effects of vinblastine, vincristine, vindesine, and vinepidine on microtubule dynamics and cell proliferation in vitro. *Cancer Res*, 45(6):2741–7, Jun 1985.
- [304] J A Donoso, K M Haskins, and R H Himes. Effect of microtubule-associated proteins on the interaction of vincristine with microtubules and tubulin. *Cancer Res*, 39(5):1604–10, May 1979.
- [305] P George, L J Journey, and M N Goldstein. Effect of vincristine on the fine structure of HeLa cells during mitosis. *J Natl Cancer Inst*, 35(2):355–75, Aug 1965.
- [306] R J Owellen, C A Hartke, R M Dickerson, and F O Hains. Inhibition of tubulin-microtubule polymerization by drugs of the vinca alkaloid class. *Cancer Res*, 36(4):1499–502, Apr 1976.
- [307] R H Himes. Interactions of the catharanthus (vinca) alkaloids with tubulin and microtubules. *Pharmacol Ther*, 51(2):257–67, 1991.
- [308] H Madoc-Jones and F Mauro. Interphase action of vinblastine and vincristine: differences in their lethal action through the mitotic cycle of cultured mammalian cells. *J Cell Physiol*, 72(3):185–96, Dec 1968.
- [309] M A Jordan, D Thrower, and L Wilson. Mechanism of inhibition of cell proliferation by vinca alkaloids. *Cancer Res*, 51(8):2212–22, Apr 1991.
- [310] Anisha Kothari, Walter N Hittelman, and Timothy C Chambers. Cell cycle-dependent mechanisms underlie vincristine-induced death of primary acute lymphoblastic leukemia cells. *Cancer research*, 76(12):3553–3561, 2016.
- [311] Karen E Gascoigne and Stephen S Taylor. How do anti-mitotic drugs kill cancer cells? *Journal of cell science*, 122(15):2579–2585, 2009.
- [312] Doraiswami Ramkrishna. *Population balances: Theory and applications to particulate systems in engineering*. Elsevier, 2000.
- [313] E Sherer, RE Hannemann, A Rundell, and D Ramkrishna. Analysis of resonance chemotherapy in leukemia treatment via multi-staged population balance models. *Journal of theoretical biology*, 240(4):648–661, 2006.

- [314] Shea N Gardner. Modeling multi-drug chemotherapy: tailoring treatment to individuals. *Journal of theoretical biology*, 214(2):181–207, 2002.
- [315] Ellis Groninger, Tiny Meeuwssen-de Boar, Pauline Koopmans, Donald Uges, Wim Sluiter, Anjo Veerman, Willem Kamps, and Siebold de Graaf. Pharmacokinetics of vincristine monotherapy in childhood acute lymphoblastic leukemia. *Pediatr Res*, 52(1):113–8, Jul 2002.
- [316] Jennifer A Smith, Barbara S Slusher, Krystyna M Wozniak, Mohamed H Farah, Gregoriy Smiyun, Leslie Wilson, Stuart Feinstein, and Mary Ann Jordan. Structural basis for induction of peripheral neuropathy by microtubule-targeting cancer drugs. *Cancer research*, 76(17):5115–5123, 2016.
- [317] T Yoshizumi, GE Gondolesi, CA Bodian, Hoonbae Jeon, ME Schwartz, TM Fishbein, CM Miller, and Sukru Emre. A simple new formula to assess liver weight. In *Transplantation proceedings*, volume 35, pages 1415–1420. Elsevier, 2003.
- [318] RD Mosteller. Simplified calculation of body-surface area. *The New England journal of medicine*, 317(17):1098, 1987.
- [319] CV Greenway and RD Stark. Hepatic vascular bed. *Physiological Reviews*, 51(1):23–65, 1971.
- [320] Jennifer B. Dennison, David R. Jones, Jamie L. Renbarger, and Stephen D. Hall. Effect of CYP3A5 expression on vincristine metabolism with human liver microsomes. *J. Pharmacol. Exp. Ther.*, 321(2):553–563, May 2007.
- [321] J Brian Houston and David J Carlile. Prediction of hepatic clearance from microsomes, hepatocytes, and liver slices. *Drug metabolism reviews*, 29(4):891–922, 1997.
- [322] Malcolm Rowland, Leslie Z Benet, and Garry G Graham. Clearance concepts in pharmacokinetics. *Journal of pharmacokinetics and biopharmaceutics*, 1(2):123–136, 1973.
- [323] Lawrence D Mayer and Ginette St Onge. Determination of free and liposome-associated doxorubicin and vincristine levels in plasma under equilibrium conditions employing ultrafiltration techniques. *Analytical biochemistry*, 232(2):149–157, 1995.
- [324] Richard A Bender, Manford C Castle, David A Margileth, and Vincent T Oliverio. The pharmacokinetics of [3h]-vincristine in man. *Clinical Pharmacology & Therapeutics*, 22(4):430–438, 1977.
- [325] V Sagar Sethi and Jim C Kimball. Pharmacokinetics of vincristine sulfate in children. *Cancer chemotherapy and pharmacology*, 6(2):111–115, 1981.
- [326] William E Hart, Carl Laird, Jean-Paul Watson, and David L Woodruff. *Pyomo-optimization modeling in python*, volume 67. Springer Science & Business Media, 2012.
- [327] J. Herman and W. Usher. Salib: An open-source python library for sensitivity analysis. *Journal of Open Source Software*, 9(2), 2017.

- [328] Geoffrey C Farrell and Claire Z Larter. Nonalcoholic fatty liver disease: from steatosis to cirrhosis. *Hepatology*, 43(S1):S99–S112, 2006.
- [329] Paul Angulo. Nonalcoholic fatty liver disease. *New England Journal of Medicine*, 346(16):1221–1231, 2002.
- [330] AEA Joseph, SH Saverymattu, S Al-Sam, MG Cook, and JD Maxwell. Comparison of liver histology with ultrasonography in assessing diffuse parenchymal liver disease. *Clinical radiology*, 43(1):26–31, 1991.
- [331] Renata Longo, Piero Pollesello, Claudio Ricci, Flora Masutti, Bjarne J Kvam, Luisa Bercich, Lory S Croce, Piergiovanni Grigolato, Sergio Paoletti, Benedetto De Bernard, et al. Proton mr spectroscopy in quantitative in vivo determination of fat content in human liver steatosis. *Journal of Magnetic Resonance Imaging*, 5(3):281–285, 1995.
- [332] Giovanni Musso, Roberto Gambino, and Maurizio Cassader. Recent insights into hepatic lipid metabolism in non-alcoholic fatty liver disease (nafld). *Progress in lipid research*, 48(1):1–26, 2009.
- [333] Giulio Marchesini, Mara Brizi, Giampaolo Bianchi, Sara Tomassetti, Elisabetta Bugianesi, Marco Lenzi, Arthur J McCullough, Stefania Natale, Gabriele Forlani, and Nazario Melchionda. Nonalcoholic fatty liver disease: a feature of the metabolic syndrome. *Diabetes*, 50(8):1844–1850, 2001.
- [334] Clare Flannery, Sylvie Dufour, Rasmus Rabøl, Gerald I Shulman, and Kitt Falk Petersen. Skeletal muscle insulin resistance promotes increased hepatic de novo lipogenesis, hyperlipidemia, and hepatic steatosis in the elderly. *Diabetes*, 61(11):2711–2717, 2012.
- [335] Shivakumar Chitturi and Geoffrey C Farrell. Etiopathogenesis of nonalcoholic steatohepatitis. In *Seminars in liver disease*, volume 21, pages 027–042. Copyright© 2001 by Thieme Medical Publishers, Inc., 333 Seventh Avenue, New , 2001.
- [336] D Lee Gorden, David S Myers, Pavlina T Ivanova, Eoin Fahy, Mano R Maurya, Shakti Gupta, Jun Min, Nathanael J Spann, Jeffrey G McDonald, Samuel L Kelly, et al. Biomarkers of nafld progression: a lipidomics approach to an epidemic. *Journal of lipid research*, 56(3):722–736, 2015.
- [337] Puneet Puri, Rebecca A Baillie, Michelle M Wiest, Faridoddin Mirshahi, Jayanta Choudhury, Onpan Cheung, Carol Sargeant, Melissa J Contos, and Arun J Sanyal. A lipidomic analysis of nonalcoholic fatty liver disease. *Hepatology*, 46(4):1081–1090, 2007.
- [338] Puneet Puri, Michelle M Wiest, Onpan Cheung, Faridoddin Mirshahi, Carol Sargeant, Hae-Ki Min, Melissa J Contos, Richard K Sterling, Michael Fuchs, Huiping Zhou, et al. The plasma lipidomic signature of nonalcoholic steatohepatitis. *Hepatology*, 50(6):1827–1838, 2009.
- [339] Zhaoyu Li, Luis B Agellon, and Dennis E Vance. Phosphatidylcholine homeostasis and liver failure. *Journal of Biological Chemistry*, 280(45):37798–37802, 2005.

- [340] Zhaoyu Li, Luis B Agellon, Theresa M Allen, Masato Umeda, Larry Jewell, Andrew Mason, and Dennis E Vance. The ratio of phosphatidylcholine to phosphatidylethanolamine influences membrane integrity and steatohepatitis. *Cell metabolism*, 3(5):321–331, 2006.
- [341] Carlos Minahk, Kyung-Wook Kim, Randy Nelson, Bernardo Trigatti, Richard Lehner, and Dennis E Vance. Conversion of low density lipoprotein-associated phosphatidylcholine to triacylglycerol by primary hepatocytes. *Journal of Biological Chemistry*, 283(10):6449–6458, 2008.
- [342] Julie C Robichaud, Jelske N van der Veen, Zemin Yao, Bernardo Trigatti, and Dennis E Vance. Hepatic uptake and metabolism of phosphatidylcholine associated with high density lipoproteins. *Biochimica et Biophysica Acta (BBA)-General Subjects*, 1790(6):538–551, 2009.
- [343] René L Jacobs, Jelske N van der Veen, and Dennis E Vance. Finding the balance: The role of s-adenosylmethionine and phosphatidylcholine metabolism in development of nonalcoholic fatty liver disease. *Hepatology*, 58(4):1207–1209, 2013.
- [344] Maida Duric, Sugas Sivanesan, and Marica Bakovic. Phosphatidylcholine functional foods and nutraceuticals: A potential approach to prevent non-alcoholic fatty liver disease. *European journal of lipid science and technology*, 114(4):389–398, 2012.
- [345] Karen D Corbin and Steven H Zeisel. Choline metabolism provides novel insights into non-alcoholic fatty liver disease and its progression. *Current opinion in gastroenterology*, 28(2):159, 2012.
- [346] STEVEN H Zeisel, KA Da Costa, PETER D Franklin, EDWARD A Alexander, J THOMAS Lamont, NANCY F Sheard, and ALEXA Beiser. Choline, an essential nutrient for humans. *The FASEB journal*, 5(7):2093–2098, 1991.
- [347] Alan L Buchman, Mark D Dubin, Adib A Moukarzel, Donald J Jenden, Margaret Roch, Kathleen M Rice, Jeff Gornbein, and Marvin E Ament. Choline deficiency: a cause of hepatic steatosis during parenteral nutrition that can be reversed with intravenous choline supplementation. *Hepatology*, 22(5):1399–1403, 1995.
- [348] Yoshikazu Sakakima, Akemi Hayakawa, Tetsuro Nagasaka, and Akimasa Nakao. Prevention of hepatocarcinogenesis with phosphatidylcholine and menaquinone-4: in vitro and in vivo experiments. *Journal of hepatology*, 47(1):83–92, 2007.
- [349] Yoshikazu Sakakima, Akemi Hayakawa, and Akimasa Nakao. Phosphatidylcholine induces growth inhibition of hepatic cancer by apoptosis via death ligands. *Hepato-gastroenterology*, 56(90):481–484, 2009.
- [350] Lucia Satiko Yoshida, Teruo Miyazawa, Ichiro Hatayama, Kiyomi Sato, Ken-shiro Fujimoto, and Takashi Kaneda. Phosphatidylcholine peroxidation and liver cancer in mice fed a choline-deficient diet with ethionine. *Free Radical Biology and Medicine*, 14(2):191–199, 1993.
- [351] Alexandra K Leamy, Robert A Egnatchik, and Jamey D Young. Molecular mechanisms and the role of saturated fatty acids in the progression of non-alcoholic fatty liver disease. *Progress in lipid research*, 52(1):165–174, 2013.

- [352] Alexandra K Leamy, Robert A Egnatchik, Masakazu Shiota, Pavlina T Ivanova, David S Myers, H Alex Brown, and Jamey D Young. Enhanced synthesis of saturated phospholipids is associated with er stress and lipotoxicity in palmitate treated hepatic cells. *Journal of lipid research*, 55(7):1478–1488, 2014.
- [353] Benjamin T Bikman and Scott A Summers. Sphingolipids and hepatic steatosis. In *Sphingolipids and Metabolic Disease*, pages 87–97. Springer, 2011.
- [354] Bungo Shirouchi, Koji Nagao, Nao Inoue, Kenta Furuya, Shinji Koga, Hideyuki Matsumoto, and Teruyoshi Yanagita. Dietary phosphatidylinositol prevents the development of nonalcoholic fatty liver disease in zucker (fa/fa) rats. *Journal of agricultural and food chemistry*, 56(7):2375–2379, 2008.

A. SUPPLEMENTARY MATERIAL FOR CHAPTER 2

A.1 Metabolite selection

In this section, we have provided details on feature selection by recursive feature elimination (RFE). Supplementary Table A.1 describes the model accuracy along with sensitivity and specificity for each time point.

After the final feature selection preceded by manual peak integration, models were evaluated using cross validation. Subsequently, models were trained using the complete data and then the threshold for probability was selected. For this selection, various thresholds were tried and specific metrics were evaluated. See Figure A.1 for model performance upon changing the probability threshold. Threshold of 0.7, 0.65, and 0.7 was chosen for day 8, day 29, and month 6 models respectively.

After selection of probability threshold, model accuracy was estimated based on the confusion matrices. Confusion matrices for the three time points are shown in Table A.3.

Following are the definitions of the terms used, based on the sample confusion matrix shown in Supplementary Table A.2.

$$Sensitivity = \frac{A}{A + C}$$

$$Specificity = \frac{D}{B + D}$$

$$Prevalence = \frac{A + C}{A + B + C + D}$$

$$PPV = \frac{sensitivity \times prevalence}{((sensitivity \times prevalence) + ((1 - specificity) \times (1 - prevalence)))}$$

$$NPV = \frac{specificity \times (1 - prevalence)}{((1 - sensitivity) \times prevalence) + ((specificity) \times (1 - prevalence))}$$

$$Detectionrate = \frac{A}{A + B + C + D}$$

Table A.1.: Metrics obtained by performing recursive feature elimination on the data sets at the three time points. A: Set of metabolites found that can accurately predict overall neuropathy susceptibility at these time points before manual integration of peaks. B: Set of metabolites found that can accurately predict TNS \odot -PV intensity at that specific time point. C: Set of metabolites that can accurately predict overall neuropathy susceptibility at the time points after manual integration of peaks. AUROC: Area Under Receiver Operating Characteristics Curve, Sens: Sensitivity, Spec: Specificity, AUROCSD, SensSD, SpecSD are standard deviations for AUROC, sensitivity and specificity. Sensitivity and specificity are calculated by keeping 0.5 probability as the threshold. Note: positive class is overall susceptibility to high neuropathy (HN) for A and C, and TNS \odot -PV greater than 8 for B.

	Time point	Predictors	AUROC	Sens	Spec	AUROCSD	SensSD	SpecSD
A	Day 8	5	0.968	0.906	0.793	0.048	0.122	0.255
	Day 29	46	0.946	0.936	0.781	0.060	0.090	0.182
	Month 6	42	0.963	0.900	0.918	0.043	0.076	0.152
B	Day 29	2	0.831	0.464	0.865	0.120	0.259	0.092
	Month 6	1955	0.812	0.776	0.617	0.086	0.206	0.204
C	Day 8	6	0.938	0.883	0.677	0.047	0.130	0.261
	Day 29	46	0.861	0.865	0.618	0.122	0.210	0.208
	Month 6	42	0.923	0.844	0.830	0.069	0.119	0.159

Table A.2.: Sample confusion matrix to explain terms used.

	Reference	
Predicted	Event	No Event
Event	A	B
No Event	C	D

$$DetectionPrevalence = \frac{A + B}{A + B + C + D}$$

$$BalancedAccuracy = \frac{sensitivity + specificity}{2}$$

Table A.3.: Confusion matrix generated after training the final models with the final selected thresholds for each time point.

Time points	Day 8		Day 29		Month 6	
Reference Prediction	High	Low	High	Low	High	Low
	High	411	32	387	85	362
Low	69	128	91	155	118	225

A.2 Metabolite identification

After the metabolites were finally chosen and models were trained using them, we attempted to identify the metabolites based on their m/z, retention time, MS/MS when available, and adduct information. Table A.4 shows m/z, retention time, and adduct information for the final 2 chosen metabolites. Table A.5 shows the aforementioned information along with HMDB ID, when possible, for day 29 metabolites. Table A.6 shows m/z, retention time, adduct information and HMDB ID for month 6 metabolites.

Table A.4.: Mass, retention time, and adduct information for the final set of Day 8 metabolites. None of them could be identified

Mass (Da)	Retention time (min)	Adducts
674.0002	11.99401	Not specified
272.1622	13.85099	M+Na

Table A.5.: Mass, retention time, and adduct information for the final set of day 29 metabolites. 4 of them could be identified.

Mass (Da)	Retention time (min)	Adducts	HMDB ID
174.1012	0.956001	Not specified	HMDB0003357
378.1285	8.478009	Not specified	
188.0794	0.981001	M+H	
228.1216	0.877999	M+H	
508.2309	19.18899	M+Na	
331.3234	19.89402	M+H	
239.2243	18.43899	Not specified	
666.2225	1.045999	M+Na	HMDB0000757
996.6191	19.91397	Not specified	
271.2508	18.65903	M+H	
347.0629	1.77	Not specified	HMDB0000045
320.1222	7.380997	Not specified	
159.0681	4.028006	Not specified	
427.0289	1.273001	2M+H	HMDB0001341

A.3 Pathway analysis

We used Metaboanalyst to perform pathway analysis for the identified metabolites for day 29 and month 6 data. Tables A.7 and A.8 show the results from metaboanalyst for these two time points respectively. None of the pathways were significant.

A.4 Univariate analysis

Univariate analysis was performed by keeping age, gender, BMI as control. ANCOVA was used to perform the analysis. P-value adjustment was done using FDR as the method. 9 metabolites were found to be significant at day 8, however, none of

Table A.6.: Mass, retention time, and adduct information for the final set of month 6 metabolites. 9 of them could be identified.

Mass (Da)	Retention time (min)	Adducts	HMDB ID
147.089	0.8	M+H	
129.0789	0.802	M+Na	HMDB0000716
128.0476	5.724	M+H	
385.2012	20.22098	M+H	
700.5516	20.26798	M+H	HMDB0013464
368.1754	20.22302	M+Na	
188.1267	0.710999	Not specified	HMDB0000670
310.1162	5.135994	M+H	HMDB0001961
301.2614	19.797	Not specified	
523.2933	20.203	M+H	
803.5453	20.15502	Not specified	
493.3173	19.99401	M+Na	HMDB0010383
612.152	3.328002	Not specified	HMDB0003337
496.2249	10.36499	Not specified	
294.1104	19.604	M+H	
428.2253	9.986008	M+Na	
260.1371	6.119996	Not specified	HMDB0011170
177.0788	1.277	Not specified	HMDB0001855
414.2041	19.96998	Not specified	
262.1315	8.763993	Not specified	HMDB0011177
208.1098	19.21399	M+H	

the metabolites were found to be significant at day 29 and month 6 treatment time points. Details of the 9 metabolites are specified in Table A.9.

Table A.7.: Table generated from Metaboanalyst for day 29 metabolites

Pathway Name	Total	Expected	Hits	Raw p	-log(p)	Holm adjust	FDR	Impact
Purine metabolism	65	0.17	2	9.84E-3	4.62	8.27E-1	8.27E-1	0.09
Arginine biosynthesis	14	0.04	1	3.57E-2	3.33	1	1	0

Table A.8.: Table generated from Metaboanalyst for month 6 metabolites

Pathway Name	Total	Expected	Hits	Raw p	-log(p)	Holm adjust	FDR	Impact
Sphingolipid metabolism	21	0.07	1	6.60E-2	2.72	1	1	0
Glutathione metabolism	28	0.09	1	8.72E-2	2.44	1	1	0.03
Glycerophospholipid metabolism	36	0.12	1	1.11E-1	2.20	1	1	0.02
Lysine degradation	25	0.08	1	7.82E-2	2.55	1	1	0

Table A.9.: Mass, retention time, adduct information, and HMDB guesses for the metabolites that were significantly associated with VIPN at day 8 time point of the treatment.

Mass (Da)	Retention time (min)	Adducts	HMDB ID
137.0833	4.648852	M+H	
180.0758	6.138951	M+H	HMDB0001860
674.3345	11.99333	M+H	
674.0003	11.996841	Not specified	
272.1622	13.852877	M+H (Found M+Na in MS/MS Spectra)	
583.3265	18.979704	Maybe M+NH4	
958.6447	20.601473	Not specified	
543.3312	20.601473	Not specified	HMDB0010395/HMDB0010396
437.2916	20.60355	M+H	HMDB0011152
463.3069	20.81195	M+H	

A.4.1 Pathway analysis

Pathway analysis was done using the same procedure as before. Tables A.10 and A.11 show the result obtained from Metaboanalyst for either HMDB0010395 or HMDB0010396 as the potential guess for Mass 543.3312, respectively. Both the results show that caffeine metabolism and glycerophospholipid metabolism are the pathways to which the metabolites belong, although none of these pathways were

significant. Moreover, given that the patients were pediatric, it is unlikely that caffeine metabolism will be of interest. However, glycerophospholipid metabolism might be of interest.

Table A.10.: Pathway analysis with HMDB0010395 as the guess for Mass 543.3312

Pathway Name	Total	Expected	Hits	Raw p	$-\log(p)$	Holm adjust	FDR	Impact
Caffeine metabolism	10	0.012903	1	0.012866	4.3532	1	1	0.69231
Glycerophospholipid metabolism	36	0.046452	1	0.045927	3.0807	1	1	0.01736

Table A.11.: Pathway analysis with HMDB0010396 as the guess for Mass 543.3312.

Pathway Name	Total	Expected	Hits	Raw p	$-\log(p)$	Holm adjust	FDR	Impact
Caffeine metabolism	10	0.012903	1	0.012866	4.3532	1	1	0.69231
Glycerophospholipid metabolism	36	0.046452	1	0.045927	3.0807	1	1	0.01736

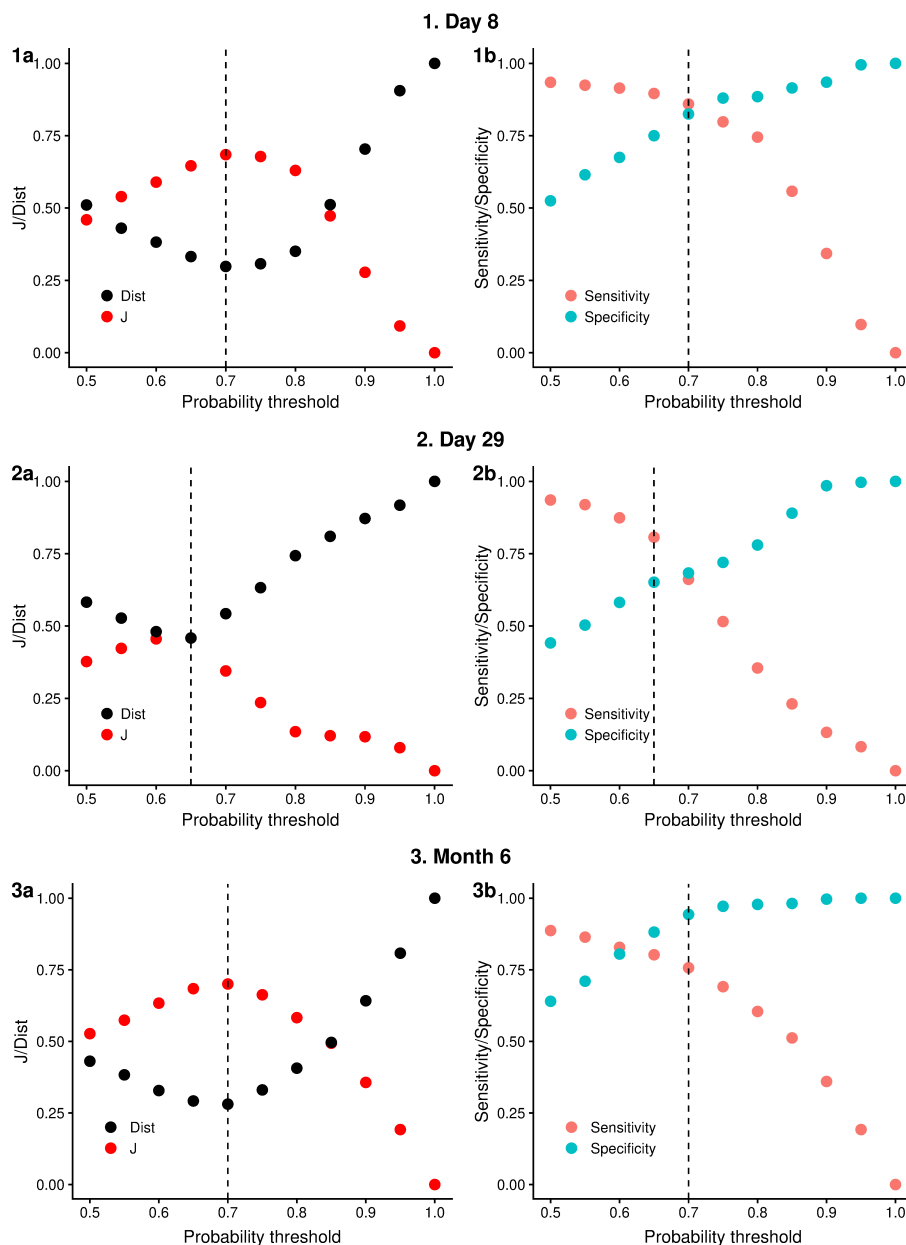


Figure A.1.: The three plots show the metrics evaluated at different probability thresholds. 1a, 2a and 3b show the plot of Youden's J statistic (J) and distance (dist) to best possible cutoff (i.e. sensitivity and specificity equal to 1) at different probability thresholds, at day 8, day 29 and Month 6 data respectively. The probability threshold is for high neuropathy. If the SVM model output is greater than the threshold, the sample is classified as high, and vice versa. 1b, 2b, and 3b show how the sensitivity and specificity varies as a function of probability threshold. Vertical line corresponds to the chosen threshold, based on minimum dist.

B. DESCRIPTION OF MODEL EQUATIONS AND PARAMETER SETTINGS

B.1 XPPAUT settings

Numerical integration and bifurcation analysis were primarily done in XPPAUT [193] and cross checked with MATCONT [213]. In XPPAUT, default settings were used except for the following: `NTST = 100`, `Method = Stiff`, `Tolerance = 1e-7`, `EPSL`, `EPSU`, `EPSS = 1e-7`, `ITMX`, `ITNW = 20`, `PARMIN = 0`, `PARMAX = 300`. In MATCONT, the following settings were kept: `MaxCorrIters = 20`, `MaxTestIters = 20`, `FunTolerance = 1e-6`, `VarTolerance = 1e-7`, `TestTolerance = 1e-7`, `NTST = 300`, `tolerance = 1e-4`, `MaxStepsize = 1` for steady state continuation and 10 for periodic solution continuation. Integration was performed using `ode15s`. Integration option `RelTol` was set to `1e-8`. In MATCONT, the equations were re-scaled as shown in Sec. B.3.

B.2 Model equations

As described in the main text, the equation for voltage can be written as:

$$c \frac{dV}{dt} = \frac{I_{ext}(t)}{A} - (i_{1.7} + i_{1.8} + i_K + i_{KA} + i_l), \quad (\text{B.1})$$

where, A is the membrane surface area, t is time and c is the specific capacitance. $c \frac{dV}{dt}$ is the specific capacitive current, $\frac{I_{ext}(t)}{A}$ is the external current per surface area, and $i_{1.7} + i_{1.8} + i_K + i_{KA} + i_l$ is the ionic current per surface area. The parameter values for this equation are mentioned in Table B.1. The model equations were obtained from literature [186, 187, 292].

The channel specific ionic currents are defined as following:

1. $i_{1.7} = \bar{g}_{1.7} m_{1.7}^3 h_{1.7} s_{1.7} (V - E_{Na})$
2. $i_{1.8} = \bar{g}_{1.8} m_{1.8} h_{1.8} (V - E_{Na})$
3. $i_K = \bar{g}_K n_K (V - E_K)$

Table B.1.: Voltage dynamics equation parameter values

Parameter	Value	Units
A (area)	2168.00	μm^2
C	20.20	pF
E_{Na}	67.10	mV
E_K	-84.70	mV
E_l	-58.91	mV
$\bar{g}_{1.7}$	18.00	mS/cm ²
$\bar{g}_{1.8}$	7.00	mS/cm ²
\bar{g}_K	4.78	mS/cm ²
\bar{g}_{KA}	8.33	mS/cm ²
\bar{g}_l	0.0575	mS/cm ²

$$4. i_{KA} = \bar{g}_{KA} n_{KA} h_{KA} (V - E_K)$$

$$5. i_l = \bar{g}_l (V - E_l)$$

The final equation for voltage is the following:

$$\begin{aligned} c \frac{dV}{dt} = & \frac{I_{ext}(t)}{A} - (\bar{g}_{1.7} m_{1.7}^3 h_{1.7} s_{1.7} (V - E_{Na}) + \bar{g}_{1.8} m_{1.8} h_{1.8} (V - E_{Na}) \\ & + \bar{g}_K n_K (V - E_K) + \bar{g}_{KA} n_{KA} h_{KA} (V - E_K) \\ & + \bar{g}_l (V - E_l)) \end{aligned}$$

For any gating variable x ($x = m_{1.7}, h_{1.7}, s_{1.7}, m_{1.8}, h_{1.8}, n_K, n_{KA}, h_{KA}$), the equation for gating variable dynamics can be written as:

$$\frac{dx}{dt} = \frac{x_\infty(V) - x}{\tau_x(V)}, \quad (\text{B.2})$$

where

$$x_\infty(V) = \frac{\alpha_x(V)}{\alpha_x(V) + \beta_x(V)}, \quad (\text{B.3})$$

and

$$\tau_x(V) = \frac{1}{\alpha_x(V) + \beta_x(V)} \quad (\text{B.4})$$

The general form of $\alpha_x(V)$ and $\beta_x(V)$ is the following:

$$k_1 + \frac{k_2}{1 + \exp\left(\frac{V + k_3}{k_4}\right)}, \quad (\text{B.5})$$

where, k_1, k_2, k_3, k_4 are constants. Most of the variables follow the above form, however, there are some exceptions, which we will mention in the following subsections.

For the rest, the parameter values are mentioned in Table B.2.

B.2.1 Na_v1.8 kinetics

$$\tau_{h_{1.8}}(V) = 1.218 + 42.043 \exp\left(-\frac{(V + 38.1)^2}{2 \times 15.19^2}\right) \quad (\text{B.6})$$

$$h_{1.8\infty}(V) = \frac{1}{1 + \exp\left(\frac{V + 32.2}{4}\right)} \quad (\text{B.7})$$

Table B.2.: Gating variables parameters

Parameter	k_1 (ms ⁻¹)	k_2 (ms ⁻¹)	k_3 (mV)	k_4 (mV)
$\alpha_{m_{1.7}}$	0	15.5	-5	-12.08
$\beta_{m_{1.7}}$	0	35.2	72.7	16.7
$\alpha_{h_{1.7}}$	0	0.38685	122.35	15.29
$\beta_{h_{1.7}}$	-0.00283	2.00283	5.5266	-12.70195
$\alpha_{s_{1.7}}$	0.00003	0.00092	93.9	16.6
$\beta_{s_{1.7}}$	132.05	-132.05	-384.9	28.5
$\alpha_{m_{1.8}}$	2.85	-2.839	-1.159	13.95
$\beta_{m_{1.8}}$	0	7.6205	46.463	8.8289

B.2.2 K/KDR kinetics

$$\alpha_{n_K}(V) = \frac{0.001265 (V + 14.273)}{1 - \exp\left(-\frac{V + 14.273}{10}\right)} \quad (\text{B.8})$$

If $V = -14.273$, $\alpha_{n_K}(V) = 0.001265 \times 10$

$$\beta_{n_K}(V) = 0.125 \exp\left(-\frac{V + 55}{2.5}\right) \quad (\text{B.9})$$

$$n_{K_\infty}(V) = \frac{1}{1 + \exp\left(-\frac{V + 14.62}{18.38}\right)} \quad (\text{B.10})$$

$$\tau_{n_K}(V) = \frac{1}{\alpha_{n_K} + \beta_{n_K}} + 1 \quad (\text{B.11})$$

B.2.3 KA kinetics

$$n_{KA_\infty}(V) = \left(\frac{1}{1 + \exp\left(-\frac{V + 5.4}{16.4}\right)} \right)^4 \quad (\text{B.12})$$

$$\tau_{n_{KA}}(V) = 0.25 + 10.04 \exp\left(-\frac{(V + 24.67)^2}{2 \times 34.8^2}\right) \quad (\text{B.13})$$

$$h_{KA_\infty}(V) = \frac{1}{1 + \exp\left(\frac{V + 49.9}{4.6}\right)} \quad (\text{B.14})$$

$$\tau_{h_{KA}}(V) = 20 + 50 \exp\left(-\frac{(V + 40)^2}{2 \times 40^2}\right) \quad (\text{B.15})$$

If $\tau_{h_{KA}}(V) < 5$, $\tau_{h_{KA}}(V) = 5$.

B.3 Non-dimensional equations

To non-dimensionalize, let us introduce some constants k_v, k_t, g, T_x ($x = m_{1.7}, h_{1.7}, s_{1.7}, m_{1.8}, h_{1.8}, n_K, n_{KA}, h_{KA}$). The non-dimensional variables will be: $V = k_v \cdot v$,

$E_X = k_v \cdot \tilde{E}_X$, ($X = Na, K, l$), $t = k_t \cdot \tilde{t}$, $\bar{g}_y = g \cdot \tilde{g}_y$ ($y = 1.8, 1.7, K, KA, l$),
 $I_{ext} = \tilde{I}_{ext}/(k_v \cdot g \cdot A)$, $\tau_x = T_x \cdot \tilde{\tau}_x$. Then, the equations will be:

$$\begin{aligned} \frac{dv}{d\tilde{t}} = \frac{k_t \cdot g}{c} & [\tilde{I}_{ext} - (\tilde{g}_{1.7} m_{1.7}^3 h_{1.7} s_{1.7} (v - \tilde{E}_{Na}) + \tilde{g}_{1.8} m_{1.8} h_{1.8} (v - \tilde{E}_{Na}) \\ & + \tilde{g}_K n_K (v - \tilde{E}_K) + \tilde{g}_{KA} n_{KA} h_{KA} (v - \tilde{E}_K) \\ & + \tilde{g}_l (v - \tilde{E}_l))] \end{aligned} \quad (\text{B.16})$$

$$\frac{dm_{1.7}}{d\tilde{t}} = \frac{k_t}{T_{m_{1.7}}} \frac{(m_{1.7\infty}(v) - m_{1.7})}{\tilde{\tau}_{m_{1.7}}(v)} \quad (\text{B.17})$$

$$\frac{dh_{1.7}}{d\tilde{t}} = \frac{k_t}{T_{h_{1.7}}} \frac{(h_{1.7\infty}(v) - h_{1.7})}{\tilde{\tau}_{h_{1.7}}(v)} \quad (\text{B.18})$$

$$\frac{ds_{1.7}}{d\tilde{t}} = \frac{k_t}{T_{s_{1.7}}} \frac{(s_{1.7\infty}(v) - s_{1.7})}{\tilde{\tau}_{s_{1.7}}(v)} \quad (\text{B.19})$$

$$\frac{dm_{1.8}}{d\tilde{t}} = \frac{k_t}{T_{m_{1.8}}} \frac{(m_{1.8\infty}(v) - m_{1.8})}{\tilde{\tau}_{m_{1.8}}(v)} \quad (\text{B.20})$$

$$\frac{dh_{1.8}}{d\tilde{t}} = \frac{k_t}{T_{h_{1.8}}} \frac{(h_{1.8\infty}(v) - h_{1.8})}{\tilde{\tau}_{h_{1.8}}(v)} \quad (\text{B.21})$$

$$\frac{dn_K}{d\tilde{t}} = \frac{k_t}{T_{n_K}} \frac{(n_{K\infty}(v) - n_K)}{\tilde{\tau}_{n_K}(v)} \quad (\text{B.22})$$

$$\frac{dn_{KA}}{d\tilde{t}} = \frac{k_t}{T_{n_{KA}}} \frac{(n_{KA\infty}(v) - n_{KA})}{\tilde{\tau}_{n_{KA}}(v)} \quad (\text{B.23})$$

$$\frac{dh_{KA}}{d\tilde{t}} = \frac{k_t}{T_{h_{KA}}} \frac{(h_{KA\infty}(v) - h_{KA})}{\tilde{\tau}_{h_{KA}}(v)} \quad (\text{B.24})$$

k_v is set to 150 mV (approximately the difference between E_{Na} and E_K), k_t as 30 ms (approximately the time covered by one action potential) and g as the $\bar{g}_{1.7} = 18$ mS/cm² (largest value of maximal conductance). Approximate values of the remaining constants can be set as: $T_{m_{1.7}} = 0.2$, $T_{h_{1.7}} = 40$, $T_{s_{1.7}} = 9000$, $T_{m_{1.8}} = 1$, $T_{h_{1.8}} = 40$, $T_{n_K} = 300$, $T_{n_{KA}} = 10$, $T_{h_{KA}} = 70$ ms. The approximate time scale of

evolution of the variables $v, m_{1.7}, h_{1.7}, s_{1.7}, m_{1.8}, h_{1.8}, n_K, n_{KA}, h_{KA}$ can be calculated from the constants on the right hand side of each of these equations, which are equal to 580, 150, 0.75, 0.0033, 30, 0.75, 0.1, 3, 0.42 respectively. The order of magnitude provides insight into the speed of each of these variables. v and $m_{1.7}$ are the fastest and $s_{1.7}$ the slowest.

The XPPAUT and MATLAB codes for these equations are publicly available on ModelDB (<http://modeldb.yale.edu/264591>).

C. MATHEMATICAL MODELING OF INOSITOL 1,4,5-TRIPHOSPHATE MEDIATED CALCIUM DYNAMICS: UNDERSTANDING PERTURBATIONS DUE TO EXTERNAL TOXICITY

Inositol 1,4,5-triphosphate (IP3) mediated calcium ions (Ca^{2+}) release is an essential phenomenon observed in the neurons. Due to an external stimulation by Adenosine Triphosphate (ATP), IP3 gets activated and releases Ca^{2+} from the endoplasmic reticulum to the cytosol. Ca^{2+} ions concentration reaches a peak in the cytosol, and the ions are then transferred back to the endoplasmic reticulum via pumps. The peak Ca^{2+} concentration is lower when the cell is subjected to a chemotherapeutic drug (Paclitaxel), which induces cytotoxicity [73]. A mathematical modeling approach is used to explore the parameters responsible for the decrease in the peak. Sensitivity analysis showed that a parameter related to pump dynamics affects the peak concentration.

C.1 Introduction

Chemotherapy-induced peripheral neuropathy (CIPN) affects both pediatric and adult cancer patients, and affects their daily life in a severe manner. Currently, there are no predictors or cure for CIPN. Doctors usually reduce dosage of drugs, or terminate the treatment altogether, depending on severity of the toxicity [293]. The mechanism underlying CIPN is still unknown, but it has been shown that calcium signaling in neurons is involved in CIPN incidence [294]. A recent study showed deregulation of inositol 1,4,5-triphosphate (IP3) mediated calcium signaling induces a cascade of events, which finally leads to CIPN [73].

IP3 is an essential receptor present in endoplasmic reticulum (ER), responsible for release of Ca^{2+} , a second messenger ion. Agonists like Adenosine Triphosphate (ATP) enable activation of Phospholipase C (PLC) via G-protein-coupled receptor (GPCR). This leads to hydrolysis of Phosphatidylinositol 4,5-bisphosphate (PIP2), and produces IP3. IP3 leads to release of Ca^{2+} from endoplasmic reticulum (ER). Following the release, sarcoendoplasmic reticulum (SR) calcium transport ATPase (SERCA) pumps bring Ca^{2+} back to the the ER. Without any external toxic agent, ATP stimulation leads to a peak Ca^{2+} release and then back. However, when a neuron is exposed to paclitaxel, a chemotherapy drug, the Ca^{2+} spike upon ATP activation lowers down [73]. It is of interest to identify factors leading to a lowering down of the peak. Such factors can provide potential cures to CIPN. In this study, a mathematical model is used to explore parameters sensitive to the peak. Raw Ca^{2+} signaling data is processed, and then fit to a model to estimate model parameters. Then, sensitivity analysis is performed to identify parameters sensitive to Ca^{2+} peak.

C.2 Methods

C.2.1 Data procurement and processing

Raw Ca^{2+} signal data is obtained from Yao and coworkers [295]. Ca^{2+} imaging was performed on nontumorigenic human mammary epithelial cell line (MCF10A) upon stimulation of 10 μM ATP. This was done using a Fluo-4 calcium indicator. Ca^{2+} imaging was done every five seconds. This obtained raw data was processed using a low pass filter with order 5 and cutoff of 0.005 Hz. Butter filter with forward backward filter was used to avoid group delay. Python scipy was used for filtering.

C.2.2 Model development and parameter estimation

Model was based on the simplified version of the system specified in [295]. ATP is assumed to activate a GPCR receptor, which hydrolyzes PIP2 and leads to production of IP3. IP3 stimulates Ca^{2+} out of ER into the cytosol and reaches a peak production.

Following this, Ca^{2+} is sent back to ER using pumps. Buffers are present both in cytosol and ER, and they are incorporated in the model. The model equations are shown below.

$$\frac{d[PLC]}{dt} = K_{on,ATP}[ATP]e^{-K_{ATP}t} - K_{off,PLC}[PLC] \quad (\text{C.1})$$

$$\frac{d[IP3]}{dt} = V_{PLC} \frac{[PLC]^2}{K_{IP3}^2 + [PLC]^2} - K_{off,IP3}[IP3] \quad (\text{C.2})$$

$$\frac{dh}{dt} = a([Ca^{2+}] + d_{inh}) \left(\frac{d_{inh}}{[Ca^{2+}] + d_{inh}} - h \right) \quad (\text{C.3})$$

$$\frac{d[Ca^{2+}]}{dt} = \beta(\epsilon(\eta_1 m_\infty^3 h^3 + \eta_2)(c_0 - (1 + \epsilon)[Ca^{2+}]) - \eta_3 \frac{[Ca^{2+}]^2}{k_3^2 + [Ca^{2+}]^2}) \quad (\text{C.4})$$

$$\beta = \left(1 + \frac{K_e[B_e]}{(K_e + [Ca^{2+}])^2} \right)^{-1} \quad (\text{C.5})$$

$$m_\infty = \left(\frac{[IP3]}{d_1 + [IP3]} \right) \left(\frac{[Ca^{2+}]^2}{d_5 + [Ca^{2+}]} \right) \quad (\text{C.6})$$

Equation (C.1) corresponds to formation of PLC due to activation by ATP. The first term in this equation is associated with activation due to ATP, and second term due to switching off of PLC. Equation (C.2) is written for formation of IP3. The first term in the equation is for formation of IP3 due to PLC following Hill's kinetics. The second term corresponds to switching off of IP3. Equation (C.3) is written for h , the fraction of activated sites on IP3. This is a function of Ca^{2+} and a dissociation constant (d_{inh}). Equation (C.4) is for the formation of Ca^{2+} . This is a function of Ca^{2+} , h , IP3, ER leak, pump permeability constants, total calcium concentration, and constants related to buffers.

Model parameters were estimated using PYOMO [296, 297] and IPOPT [298]. There were 18 unknown parameters in total. Initial guesses for the parameters were used from [295].

C.2.3 Sensitivity analysis

SOBOL sensitivity analysis was performed with sampling 250 times using Saltelli method for sampling. In sensitivity analysis, the peak Ca^{2+} concentration is observed by varying different parameters within specified bounds. If by varying a parameter, the peak concentration varies significantly, it implies that the peak concentration is sensitive to that parameter. Sensitivity analysis was performed for all the 18 parameters and ATP concentration. A heatmap was generated to display sensitivities of parameters to Ca^{2+} spike. Python SALib library was used to perform sensitivity analysis.

C.3 Results

The filtered and raw data is shown in Figure C.1. Low pass filter smoothed the data, which enabled better parameter fitting.

Model fit is shown in Figure C.2. An optimal solution was found using PYOMO and IPOPT. All 18 parameters were estimated within reasonable bounds. The model follows the trend, however, it does not fit very well. This is because the model used is a simplified version. If more rigorous form as mentioned in [299] was used, the fit would have been better. Since the concern was sensitivity of parameters with the peak, a simpler model was used. In this simpler version, stimulation of GPCR was ignored.

The heatmap in Figure C.3 shows the sensitivities of individual (diagonal elements) and paired (non-diagonal parameters) parameters with Ca^{2+} peak. As seen from the heatmap, the most sensitive parameters are c_0 and k_3 . c_0 corresponds to total Ca^{2+} concentration and k_3 corresponds to pump dissociation constant. It is mentioned in [73] that the total Ca^{2+} concentration did not change because of paclitaxel. Hence, k_3 seemed to be a more feasible parameter to vary. Ca^{2+} peak was estimated with k_3 and $k_3/1.1$ as the pump dissociation constants. Figure C.4 shows the Ca^{2+} concentration profile at the estimated value of k_3 and $k_3/1.1$. The peak

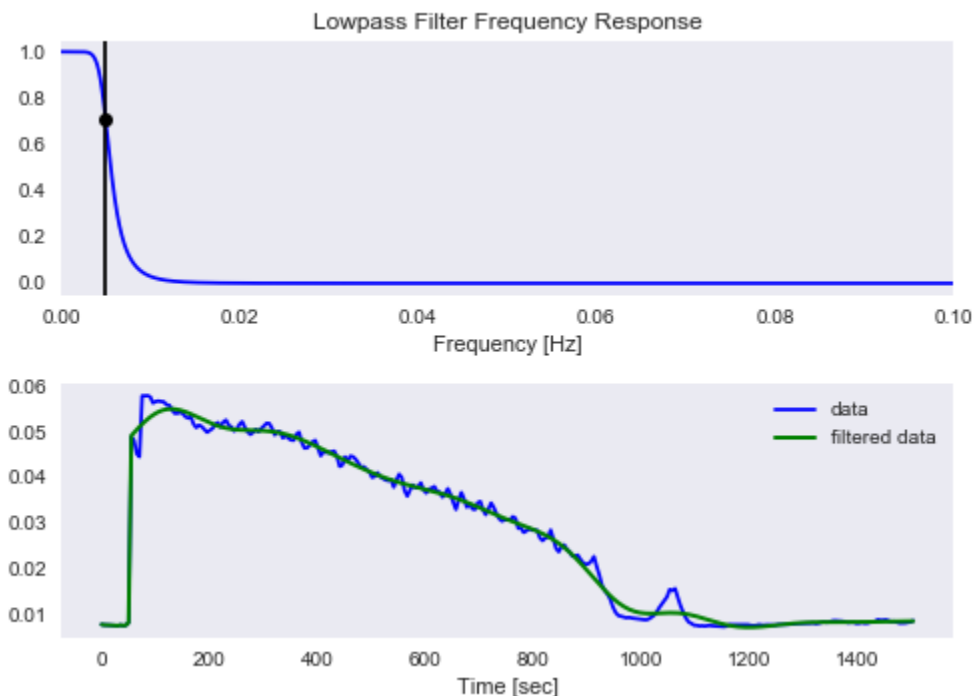


Figure C.1.: First subplot is the frequency plot for the low pass filter. The second subplot shows the raw and the filtered data. Order 5 and cutoff of 0.005 Hz was used.

is lower with lower k_3 . This observation may have biological implications. Through mathematical modeling, we intend to find parameters with therapeutic significance that can be explored as potential cures to CIPN. This implies that the pump may not be functioning well upon administration of paclitaxel.

C.4 Discussions

Agonists such as ATP activate IP₃ in the ER, which leads to release of Ca²⁺ in the cytosol. Ca²⁺ concentration reaches a peak, and then is sent back to ER via a pump. The peak Ca²⁺ release is seen to be lowered when a neuron is subjected to paclitaxel, a chemotherapy drug. This has been associated with axon degeneration, which ultimately leads to peripheral neuropathy. CIPN becomes a hindrance to the

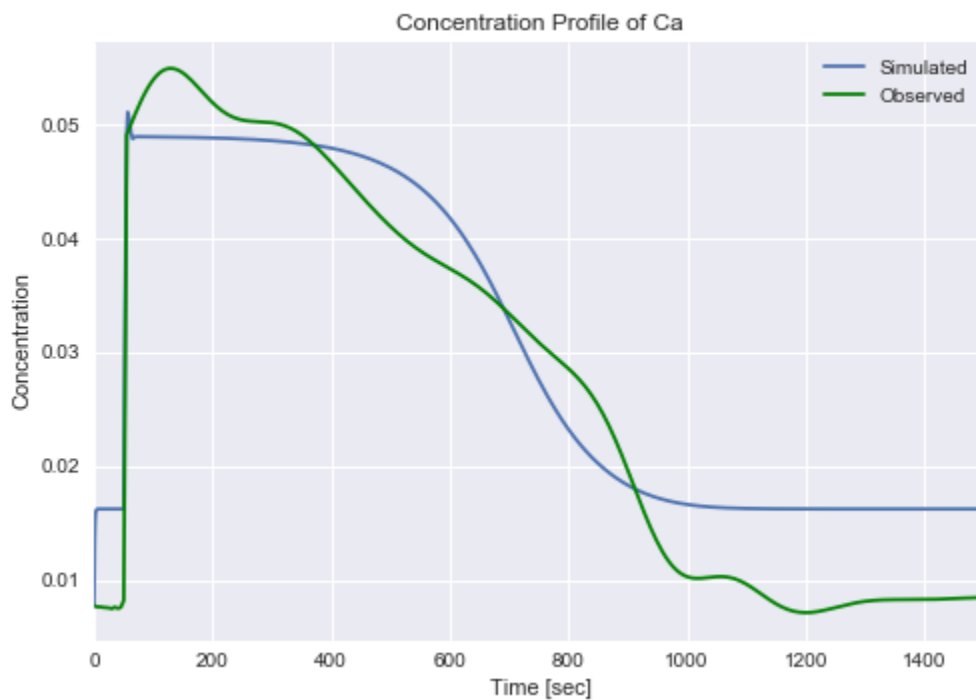


Figure C.2.: Plot of simulated Ca^{2+} concentration (in blue) and the processed Ca^{2+} signal data (in green). Concentration is in μM . Though not evident from the plot, the simulated and observed concentration at time = 0 s is the same.

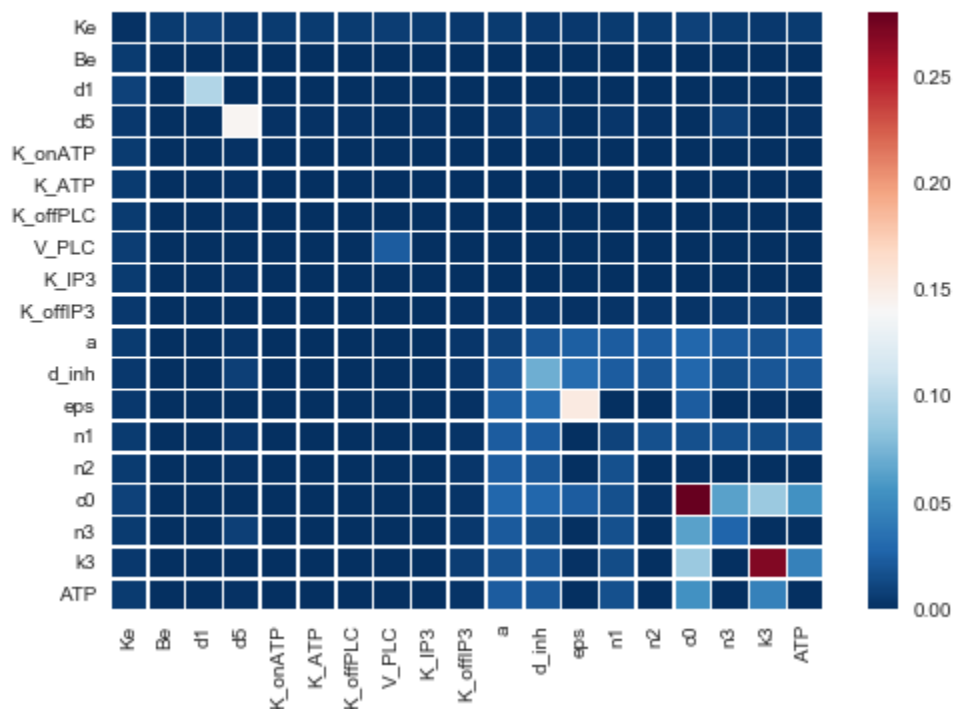


Figure C.3.: A heatmap showing the sensitivity of model parameters with Ca^{2+} peak. The diagonal elements show the sensitivities of individual parameters, and the non-diagonal elements show the sensitivities of paired parameters. Color closer to blue indicates low sensitivity, while color closer to red indicates high sensitivity. From this figure, c_0 and k_3 seem to be most sensitive to Ca^{2+} peak.

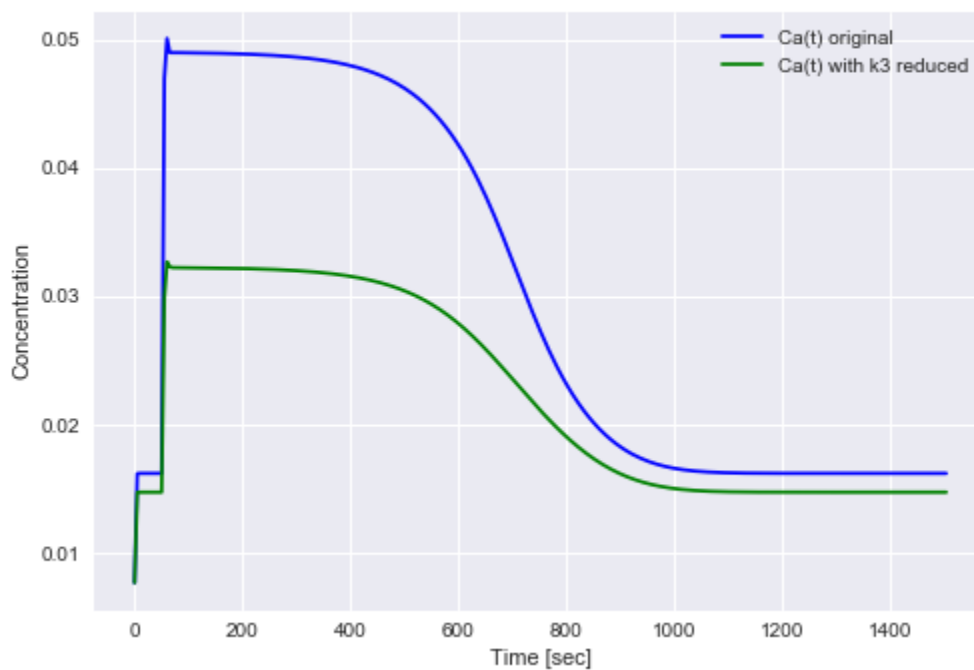


Figure C.4.: Ca^{2+} simulated with estimated model parameters (in blue), and with k_3 reduced by a factor of 1.1 (in green). There is a visible decrease in Ca^{2+} spike.

treatment, and impacts daily life of cancer patients. It is imperative to understand the mechanisms involved in CIPN. In this study, a mathematical model was used to understand the parameters which might be responsible for the lower peak. Sensitivity analysis enabled finding the important parameters. The results of this study show that perturbation of pump dissociation constant might be leading to a lower Ca^{2+} peak. Exploring drugs that can perturb pump's dissociation ability might serve as a therapeutic tool to treat CIPN.

This study used Ca^{2+} signaling data for only one cell. This needs to be repeated for multiple cells, following which a statistical test can be performed to establish a significant difference in the peak by lowering k_3 . Moreover, the Ca^{2+} signaling data used here was obtained from mammary epithelial cell line, rather than from neurons. IP3 mediated Ca^{2+} is similar in both the epithelial cells and the neurons, hence, it is reasonable to perform a sensitivity analysis by using epithelial cells data. It will be of interest to observe the difference in model parameters when neuron cell data is fit to the model. In the future, data from [73] can be used to estimate parameters and estimate the lowered k_3 value.

C.5 Conclusions

In conclusion, pump dissociation constant is sensitive to Ca^{2+} peak concentration. This analysis needs to be repeated on more data and on neurons' Ca^{2+} data. The model needs to be made more rigorous. However, this model along with sensitivity analysis provides a potential tool to explore therapeutic measures to avoid CIPN.

D. OPTIMIZING VINCRISTINE INFUSION RATE

This work was done in collaboration with three undergraduate students: Rohan Sharma, Yuqi Fang, and KS Reshma.

Vincristine (VCR) is a core chemotherapeutic drug administered to pediatric Acute Lymphoblastic Leukemia (ALL) patients. It is administered via an IV bolus injection or via a minibag for approximately 10 minutes. In a subgroup of population, it leads to vincristine-induced peripheral neuropathy (VIPN), which is the dose-limiting toxicity. For few patients, VIPN is severe with long-term effects. Even though VCR has been used as a chemotherapeutic drug for more than 50 years now, predictors and mechanism of VIPN induction are unclear. VIPN incidence seems to be associated with VCR cumulative dosage. Hence, it is of interest to find an optimal infusion time that would lead to a reduction in VCR dosage.

A population balance model is developed to describe the mechanism of VCR in cells in different phases. The model is a function of time and cell age. The mechanism model was combined with pharmacokinetics of VCR. Infusion time was optimized to maximize the number of cancer cells being killed by the end of the induction phase, with VCR being administered weekly.

D.1 Introduction

Vincristine is a cell-cycle specific drug. It implies that VCR kills cells when they are in a particular phase. In the past, it has been shown that VCR attacks cells when they are in the M phase [300–309]. Only recently, it was shown in a cell line that when VCR attacks cells in the G1 phase, it leads to death directly. If it attacks in any other phase, the cells will continue the cycle till the M phase, and then undergo a mitotic arrest first, followed by either death or any other possible fates [310, 311]. A model

was built to describe VCR killing cells in the different phases. G1 phase was kept separately and all other phases were lumped together in the M phase. Quiescent phase was ignored for now. An attempt was made to optimize infusion time of Vincristine during the induction phase, to maximize killing of cancer cells. If the same efficacy can be achieved with lesser amount of drug just by optimizing infusion time, chances of peripheral neuropathy in the patient will be lesser. An optimized infusion time is something the clinicians are interested in as well.

D.2 Model

If vincristine attacks in G1 phase, cells die immediately. If it attacks in any other phase, cells will continue to cycle till the M phase, and then it will lead to mitotic arrest. Followed by mitotic arrest, cells may die, or join the cell cycle back without division. It may also lead to unequal division or interphase arrest, which has been ignored for now. Cells in G1 phase (N_{G1} number of cells with number density n_{G1}) will enter the M phase at a rate of γ_1 . They may die in G1 phase at a rate of $k_1(C)$. Cells in M phase (N_M number of cells with number density n_M) may enter G1 phase at a rate of γ_2 , or die at a rate of $k_2(C)$.

This process has been written in the form of population balance equations [312]. The populations of cells in G1 phase, G2, S, and M phases lumped together, are considered. The number density of cells are modeled as a function of transition and death rates.

The drug concentration is represented by the following equation [313,314]:

For j^{th} dose of i^{th} drug:

$$C_i(t) = \begin{cases} \frac{y_{ij}}{\lambda_i}(1 - e^{-\lambda_i(t-t_{AD,ij})}) + C_{i,residual}(t), & \text{during } j^{th} \text{ application} \\ C_{i,residual}(t) = \sum_{j=1}^{PA} \frac{y_{ij}}{\lambda_i} e^{-\lambda_i(t-t_{AD,ij})} (e^{\lambda_i h_{ij}} - 1), & \text{between applications} \end{cases} \quad (D.1)$$

where,

- $C_i(t)$ (mg) is the amount of i^{th} drug at time t

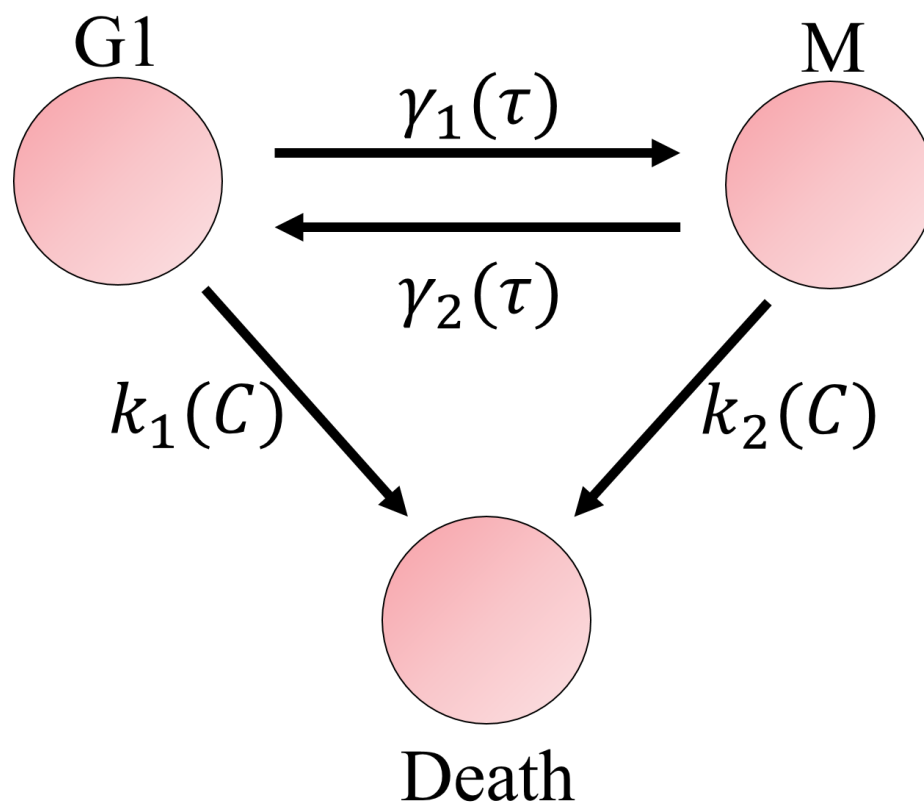


Figure D.1.: Vincristine mechanism in the cell cycle

- y_{ij} is the dose administration rate (mg/m²/h) during the j^{th} dose of i^{th} drug
- h_{ij} (h) is the duration for which the the j^{th} dose of i^{th} drug was administered
- PA stands for previous applications
- $t_{AD,ij}$ (h) is the time when j^{th} dose of i^{th} drug was administered
- λ_i (h⁻¹) is the decay constant of the i^{th} drug

The dose administration rate was multiplied by body surface area. The body surface area was assumed to be 1 m² and volume of blood was assumed as 262 l. The total amount of drug administered was assumed to be 2 mg. It was divided by the body surface area and infusion time to calculate the dose administration rate.

For the model considered in Figure D.1, population balance equations were written. The number density was assumed to be a function of time (t) and cell age (τ), the internal coordinate. The cell age is the time a cell has spent in a particular phase.

$$\frac{\partial n_{G1}}{\partial t} + \frac{\partial n_{G1}}{\partial \tau} + \gamma_1 n_{G1} + k_1(C) n_{G1} = 0 \quad (D.2)$$

$$\frac{\partial n_M}{\partial t} + \frac{\partial n_M}{\partial \tau} + \gamma_2 n_M + k_2(C) n_M = 0 \quad (D.3)$$

Here, n_{G1} and n_M are the number densities of cells in G1 and M phase, respectively. The boundary conditions for the number densities (flux of cells of zero age) will be the following equations.

$$n_{G1}(t, 0) = 2\gamma_2 \int_0^\infty n_M(t, \tau) d\tau \quad (D.4)$$

In equation (D.4), a factor of 2 is incorporated to account for cell division.

$$n_M(t, 0) = \gamma_1 \int_0^\infty n_{G1}(t, \tau) d\tau \quad (D.5)$$

The values of the parameters (transition rates and death rates) were estimated from experimental studies. The transition rates γ_i ($i = 1, 2$) are assumed to be of lognormal distribution form with mean μ_i and standard deviation σ_i [313]. They are described as the following:

Table D.1.: Model parameter and their values

Parameter	Value	Units	Reference
λ	0.0416	h^{-1}	[315]
a	0.1	l/mol	Assumed

Table D.2.: Initial conditions and parameters for the transition and death rates

Parameter	G1 phase	M phase	Units	Reference
μ	1.25	1.25	days	Assumed
σ	0.4	0.3	days	Assumed
$k_{i,max}$	0.1429	0.1845	hr^{-1}	[310]

$$\Gamma_i(\tau) = \sqrt{\frac{2}{\pi}} \frac{1}{\sigma_i \tau} \frac{\exp(-1/2((\log\tau - \mu_i)/\sigma_i)^2)}{1 + \text{erf}((\mu_i - \log\tau)/\sqrt{2}\sigma_i)} \quad (\text{D.6})$$

The rate of cell death k_i are given by the following (for i drugs given in combination) [313]:

$$k_i(C_i) = k_{i,max} \left(1 - \prod_{i=1}^{drugs} SF_i(C_i)\right) \text{in } \text{day}^{-1}, \quad (\text{D.7})$$

where the survival function SF is described as:

$$SF_i(C_i) = \begin{cases} \exp(-a_i C_i(t)) & \text{susceptible phase,} \\ 1 & \text{otherwise} \end{cases} \quad (\text{D.8})$$

Here, $i = 2$ for the two phases. The parameter a_i corresponds to the drug resistance developed due to drug. The larger the value of a_i , the lesser the cell resistance. This value is kept constant at 0.1 l/nmol for both the phases.

The initial number density distributions $g_{G1}(\tau)$ and $g_M(\tau)$ are assumed to be exponential.

$$g_{G1}(\tau) = 0.75 * 10^9 e^{-\tau} \quad (\text{D.9})$$

$$g_M(\tau) = 0.1 * 10^9 e^{-\tau} \quad (\text{D.10})$$

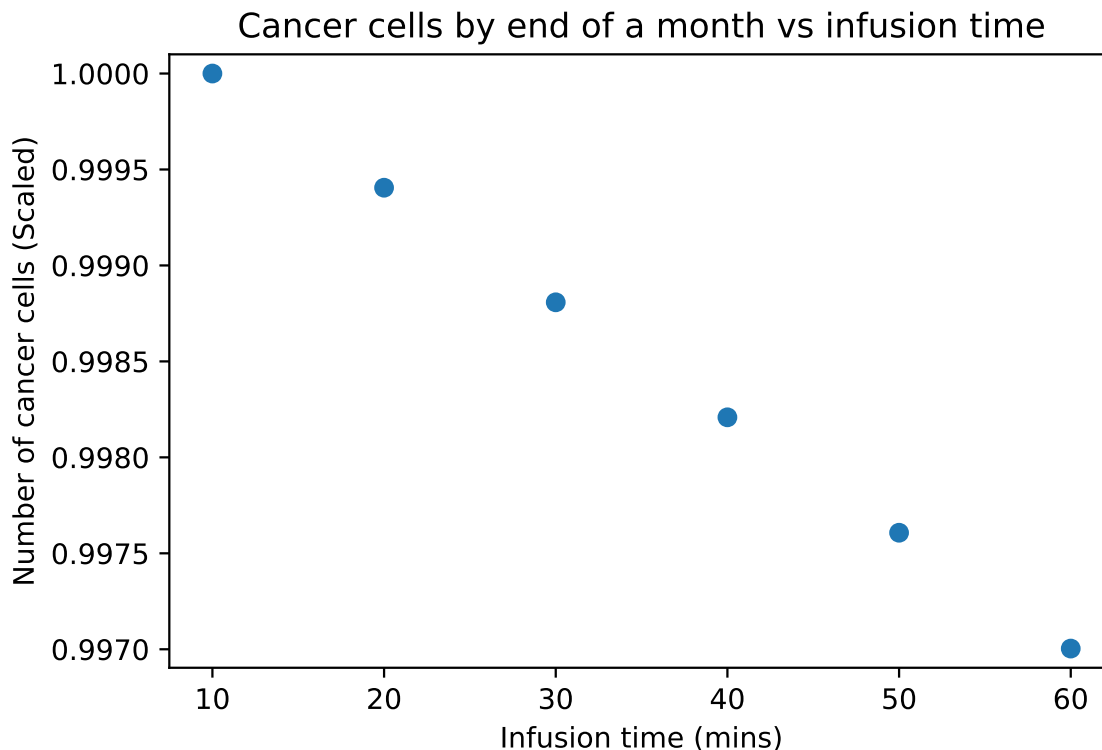


Figure D.2.: Plot of number of remaining cancer cells as a function of infusion time

These equations are solved using method of successive generations, described in [312].

D.3 Results

It is assumed that the treatment regime consists of 2 mg of vincristine administration weekly for one month. The infusion time was varied between 10 to 60 minutes with an interval of 10 minutes. Number of cancer cells by the end of one month was compared. Current infusion time administered to patients is approximately 10 minutes. As shown in Figure D.2, slower infusion time is more effective in killing the cancer cells.

D.4 Discussions

This work can be extended by introducing quiescent phase, dynamics of normal cells, and patient-specific VCR pharmacokinetics parameters. Other chemotherapy drugs that are administered in combination with VCR can also be included.

E. MODELING VINCRISTINE TRANSPORT

E.1 Introduction

Pharmacokinetic (PK) modeling is a prevalent methodology in personalized medicine. The idea is to develop a dynamic model with individualized parameters which can predict drug dynamics in the body. Pharmacodynamics (PD) is further incorporated with PK modeling to take into account the effect of drug on the body (e.g. adverse drug reactions). A PK/PD model can predict the drug effect on a body for a given dose. Further, once individual patient parameters are obtained, the model can be used to suggest individualized dosage of a drug to minimize its side effect. In this work, a PK/PD model is developed, which also takes into account key genotypic information of patients.

Vincristine is administered via an IV bolus injection or infusion mini-bag. From the periphery, it gets transported to the tissues where it kills the cycling cells, including normal as well as cancerous cells. It is transported via the blood to the liver, where it gets metabolized. A transport model as shown in Figure E.1 was developed. It is assumed that the blood transports VCR to the neurons as well, which is speculated to be causing neuropathy if VCR is more than a threshold amount in the neurons [316]. Vincristine gets diffused to tissues, liver and neurons. It is effluxed back via ABC transporter proteins. Vincristine, along with its metabolites, are finally excreted via bile. Elimination and metabolism are lumped together, and liver is not considered as a separate compartment here. This is because V_{max} and K_m for metabolism can be extracted from literature, and, using those values, hepatic clearance can be directly estimated.

E.2 Data available

PK data was provided for the same patients for which metabolomics data was provided. For some patients, PK data was available at 4 time points and for 2 visits. For the rest, it was available for 3 or less time points, and for 2 or less visits. Along with VCR PK, patients' genotypic score was provided for key genes involved. Genotypic score of CYP3A5 (VCR metabolizing enzyme) and MDR1 (transports VCR) was provided. Patient height, weight, and the dose administered was provided as well. Using the data available, the PK-PD model was formulated.

E.3 Model

Reaction differential equations were written for each compartment. The rate constants need to be estimated. The hepatic clearance was estimated based on expression of CYP3A5. Hepatic clearance is a function of intrinsic clearance and liver weight. Liver weight was estimated using the following formula [317], where weight is in grams and body surface area (BSA) is in m^2 :

$$W = \begin{cases} 772 * \text{BSA}, & \text{if } \text{BSA} \geq 1 \\ 772 * \text{BSA} - 38, & \text{otherwise} \end{cases} \quad (\text{E.1})$$

Body surface area is calculated using the Mosteller formula [318]:

$$\text{BSA}(\text{m}^2) = \sqrt{\frac{\text{body weight (kg)} \times \text{height (cm)}}{3600}} \quad (\text{E.2})$$

An estimate of hepatic blood flow (Q) is 104 mL/min per 100 grams of liver mass [319]. Dennison and coworkers [320] estimated V_{max}/K_m for human liver microsomes which were low and high expressers of CYP3A5. The methodology used in [320] was used to calculate intrinsic and hepatic clearance. Average V_{max}/K_m for different genotypic scores are shown in Table E.1.

Table E.1.: V_{max}/K_m (ml/min/g) for different genotypic scores

CYP3A5 genotype	High/Low expresser	V_{max}	K_m	V_{max}/K_m	Number of patients
<i>*1/*1</i>	High	1262	14	90.14	1
<i>*1/*3</i>	High	335.62	19.34	17.35	7
<i>*3/*3</i>	Low	121.8	19.88	6.13	27
<i>*1/*7</i>	Low	50	15.8	3.16	1

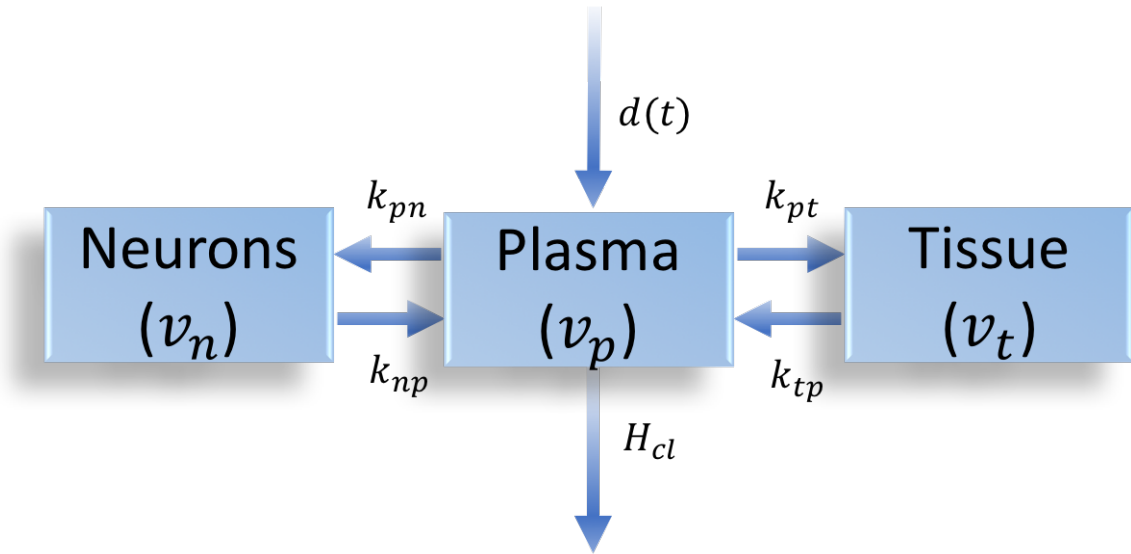


Figure E.1.: Vincristine PK/PD

Intrinsic clearance was calculated according to the following formula [321], where, CL_{int} is the intrinsic clearance:

$$CL_{int} = \frac{V_{max}}{K_m} * W * 45 \text{ mg microsomal protein/g liver} \quad (\text{E.3})$$

Using the intrinsic clearance, hepatic clearance was calculated according to the following formula (well stirred model) [322], where H_{cl} is the hepatic clearance, $f_{u,p}$ is the plasma fraction unbound and ρ is the blood-to-plasma ratio:

$$H_{cl} = \frac{Q * f_{u,p} CL_{int}}{\rho * (Q + \frac{f_{u,p}}{\rho} * CL_{int})}, f_{u,p} = 0.51, \rho = 1.2 \quad (\text{E.4})$$

A microsomal mass of 45 mg per 1 g of liver was assumed as done in the study by Dennison and coworkers [320]. Similarly, $f_{u,p}$ is taken to be 0.51 [323] and ρ is taken to be 1.2 [324].

Using this, a patient's weight, height, and CYP3A5 genotypic information was incorporated to calculate hepatic clearance for each one of them. MDR1 genotypic information was not incorporated into the model as of now.

The rate equations for the model were the following:

$$\frac{dv_p}{dt} = \frac{d(t)}{V_d} - k_{pt}v_p + k_{tp}v_t - k_{pn}v_p + k_{np}v_n - \frac{H_{cl}}{V_d}v_p \quad (\text{E.5})$$

$$\frac{dv_t}{dt} = k_{pt}v_p - k_{tp}v_t \quad (\text{E.6})$$

$$\frac{dv_n}{dt} = k_{pn}v_p - k_{np}v_n \quad (\text{E.7})$$

k_{pt} , k_{tp} , k_{pn} , k_{np} are the rate constants. V_d is the plasma volume. H_{cl} is the hepatic clearance. $d(t)$ is the rate of drug administration. In this case, VCR is administered via a minibag in 10 minutes. v_p is the VCR plasma concentration. v_t and v_n are concentrations in tissue and neurons, respectively.

The value of k_{pt} was taken to be 0.104, average of k_{12} and k_{13} obtained from another PK study done by Sethi and coworkers [325].

E.4 Parameter estimation

For every patient H_{cl} was calculated as shown above. k_{pt} was assumed to be the same for every patient. k_{tp} , k_{np} , k_{pn} and V_d were estimated by optimization, given the PK data. This estimation was done for every patient for which PK data was available at 4 time points, including the initial time point. There were 13 patients for which the data was available at 4 time points. Ideally, 3 parameters should have been estimated using these time points. However, by keeping one of the parameters as constant, the fit generated was not as good. It seems that by letting the optimizer find 4 parameters, it is being given more freedom to fit the model better. At the same time, reasonable constraints were given for all the parameters, hence, the system wasn't fully underdetermined. All the rate constants were constrained to lie between (0,10) (1/min) and the plasma volume was constrained to lie between (1000, 30000) (ml). The parameter estimation was done using pyomo [296, 326] and ipopt [298] in python.

The PK profile and the fit for one patient is shown in Figure E.2. The model fit well with the PK data. For some patients, optimization was difficult since PK data

was available at far-off time points. For most of the patients, PK data was available after around every 15 minutes. For 3 patients, few time points were available at an interval of around 50 minutes or more. For one patient, this might have led to inefficient optimization. The time points need to be confirmed with the clinicians once. Further, a confirmation of the dose infusion time is needed as well.

The next step was to validate the model. We used PK data of the same patients when they came for another round of VCR dose administration. During that round, height and weight were noted down again. Hence, hepatic clearance was calculated again. The parameter values were assumed to be the ones found from optimization. The PK data was available only for two time points, one of them being the initial time point. Furthermore, data was available only for 4 patients. Figure E.3 shows the fit of the model with the validation data points. The model fits reasonably well, except for the patient GW-05.

Next, a first approximation sensitivity analysis was done for all the parameters in the model. The model output was compared only at one fixed time point ($t=30$ minute), for vincristine plasma concentration. The complete time profile was ignored. SOBOL method in python was used [327]. Figure E.4 shows a heat map, with the numbers in the boxes representing the relative variance due to the parameter. The first order variance is due to individual parameters, shown in the diagonal elements, and the remaining variances are due to interaction of two parameters. As seen from the heat map, the model is insensitive to k_{pt} , hence, assuming k_{pt} to be constant for all the patients is reasonable.

E.5 Future work

It has not been completely resolved why estimation of 4 parameters lead to a better fitted model. A steady state VCR concentration time point can be added to enhance model accuracy. Further, infusion time for individual patients need to be confirmed. PK profile of 3 patients need to be confirmed. Upon confirmation and

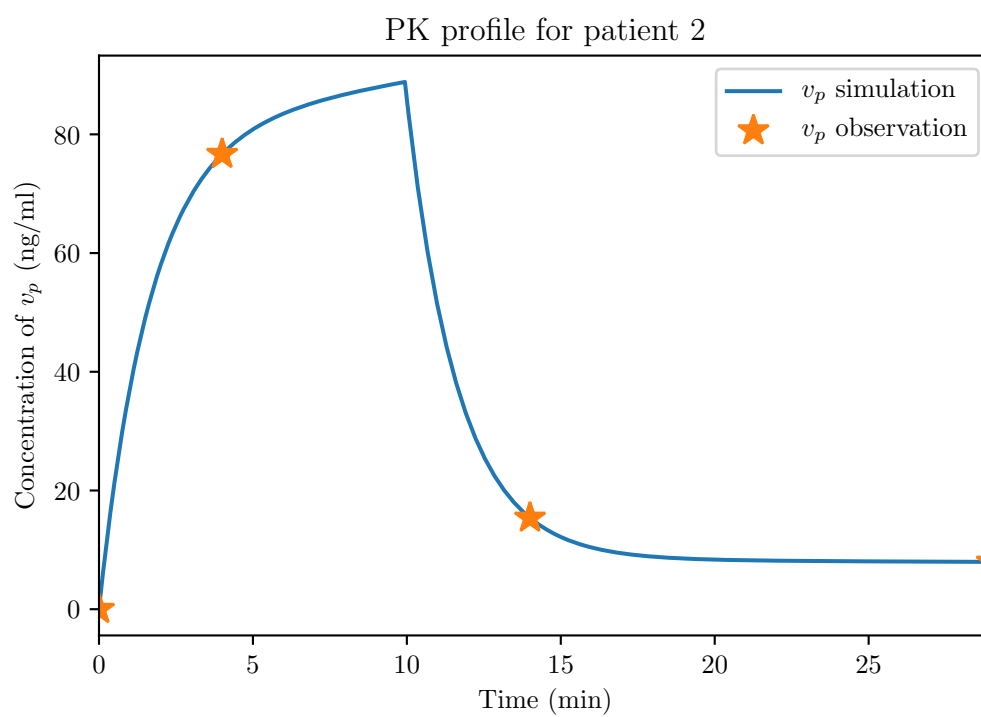


Figure E.2.: PK profile for one patient

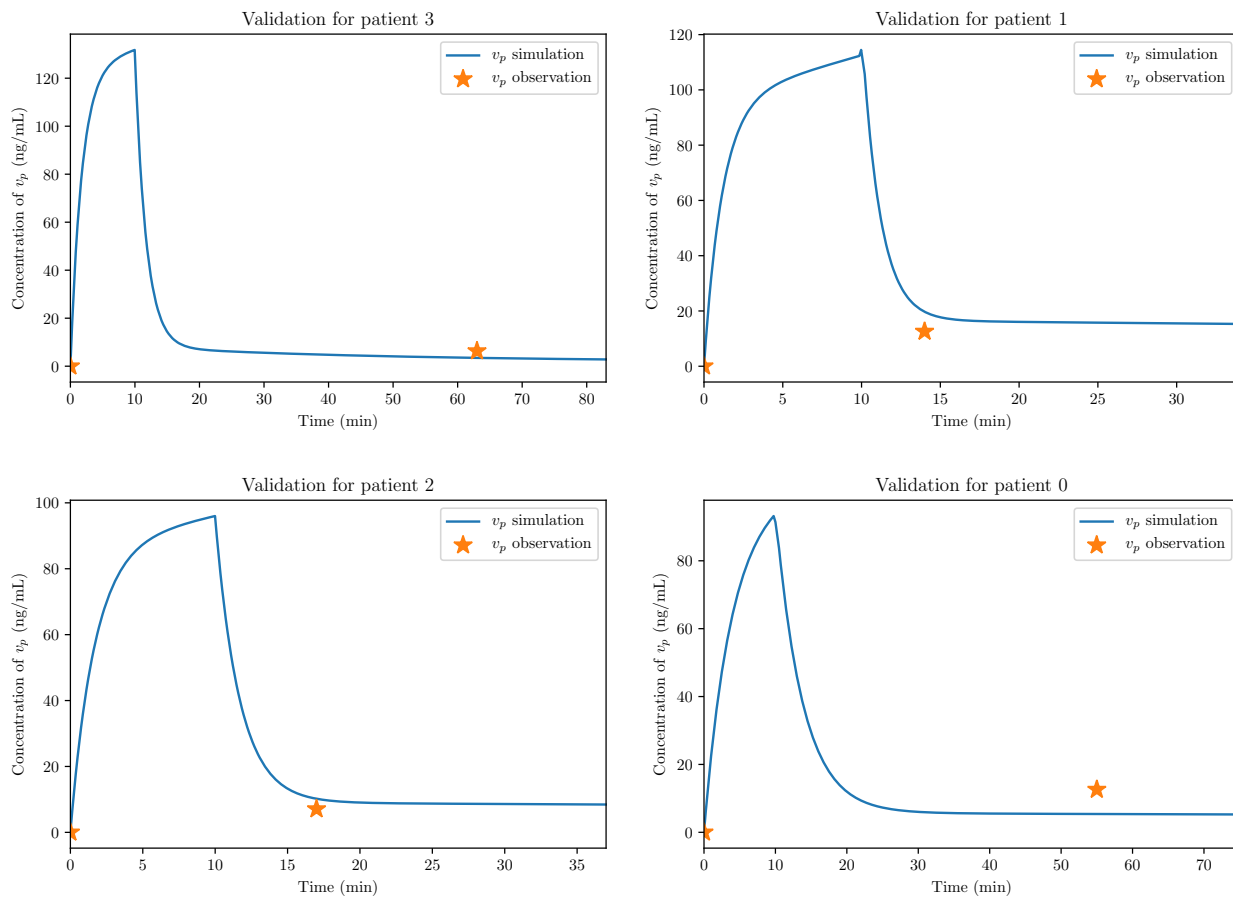


Figure E.3.: PK model validation for patients



Figure E.4.: Heat map showing sensitivity of parameters

incorporation of a steady state time point, parameter estimation can be performed again.

Rigorous sensitivity analysis needs to be done to find important parameters. Then, these parameters will be fixed while the rest can be estimated for the remaining patients (for whom PK data was not available at 4 time points). Further, concentration of vincristine in the neuron compartment can be compared for the low and high neuropathy patients. In the present cohort of patients considered, 12 were high neuropathy and 1 was low neuropathy patient. Once the concentration distribution is available for all the patients, the comparison can be made. Vincristine concentration in neuron compartment can be an indicator of neuropathy. Hence, it is imperative to analyze it.

MDR1 information needs to be included as well. It is unclear as of now on how to incorporate it. Patients can be classified into high and low efflux patients. The drug efflux rate constants can be constrained to lie within a certain range for the two categories of patients. Incorporating these can make the model more comprehensive.

F. A LIPIDOMICS APPROACH TO INVESTIGATE NON-ALCOHOLIC FATTY LIVER DISEASE

This work was done in collaboration with Dr. Wanqing Liu.

Non-Alcoholic Fatty Liver Disease (NAFLD) is a prevalent disease, especially in western countries. It is characterized by substantial accumulation of fat in the hepatocytes. It is similar to alcohol-induced liver damage but in patients who do not over-consume alcohol. NAFLD has a huge spectrum, ranging from mild to a very severe condition. It ranges from simple steatosis, steatohepatitis, fibrosis and to finally advanced fibrosis or even cirrhosis [328]. There is no fixed medication or treatment available. Doctors primarily advise to control diet and reduce weight. Cirrhosis is the final stage of NAFLD when liver tissues get completely scarred. Intermittently at that stage, liver transplantation is the only possible treatment.

Around 10-24% of the general population suffer from NAFLD in different countries [329]. It is also associated with obesity, type 2 diabetes and hyperlipidemia. Most of the patients do not show any typical symptom during diagnosis. They may complain of fatigue or feeling of fullness. Some abnormalities are found in laboratory tests. Elevated serum levels of aspartate aminotransferase or alanine aminotransferase, or both can be found in NAFLD patients [329]. Ultrasonography [330] and magnetic resonance spectroscopy [331] are used to identify fatty infiltration in liver. NAFLD stage can only be identified using liver biopsy. Liver biopsy checks for steatosis, mixed inflammatory-cell infiltration, hepatocyte ballooning and necrosis, glycogen nuclei, Mallory's hyaline, and fibrosis [329].

Pathogenesis of NAFLD is very complex and unclear. The main driving factor is accumulation of lipids within hepatocytes because of an imbalance. Fatty acid uptake and *de novo* synthesis of fatty acid exceeds oxidation and resecretion [332].

Experiments indicate that it is a feature of the metabolic syndrome [333]. It has been shown that insulin resistance may lead to NAFLD [333]. Insulin resistance is associated with *de novo* lipogenesis and hyperlipidemia [334]. It is speculated that increase in intrahepatic levels of fatty acids may be responsible for oxidative stress, which in turn may lead from steatosis to cirrhosis [329]. The transition may also be involving cytochrome P450 activation, lipid peroxidation, increased inflammatory cytokine production, activation of hepatic stellate cells and apoptosis [335]. This transition is not completely clear.

Here, machine learning and statistics are used to analyze role of lipids in NAFLD progression. It was discovered that all significant PCs are negatively associated with NASH. Further, the saturation level was analyzed and it was discovered that unsaturation was negatively associated with NASH. A small set of potential lipid biomarkers was also identified which can accurately classify NASH. All of these were validated using an independent data set.

F.1 Methods and materials

F.1.1 Data acquisition

Two independent data sets (discovery sample size = 120, validation sample size = 106) of liver tissue samples were collected from transplantation donors, and characterized for histology.

F.1.2 Statistical analysis

Samples were divided into classes: no NAFLD and NAFLD belonged to one class, borderline NASH and NASH belonged to another. For all the lipids, logistic regression was performed to find significant association between lipids and class, keeping demographics as control. Benjamini and Hochberg FDR correction was performed and lipids with false discovery (FDR) ≤ 0.05 were kept. These lipids were then segregated based on the lipid family. For every family, fisher test was performed to

determine if the family was significant compared to all other lipids. For validation set, age and sex were kept as control. For discovery set, age, sex and race were kept as control. For serum samples, age, sex, BMI, race were kept as control.

For saturation analysis, logistic regression was performed to find significant association between ratio of lipids within families and class, with demographics as control. An FDR cutoff of 0.1 was kept. Level of saturation was estimated for each lipid based on the number of double or triple bonds. All the ratios were converted such that the numerator was either less or equally saturated. Following this, fisher test was performed to determine if more unsaturation was associated with lower level of NASH within every lipid family. This was repeated for validation data set. MATLAB was used for all the statistical analysis.

To understand if a set of lipids together predict NASH, machine learning was used. Elastic net logistic regression along with 10 fold cross validation, repeated 5 times, was used. Top 10 of those lipids were used to build a model both in discovery and validation set, to confirm predictability. R package CARET was used for this algorithm.

F.2 Results

F.2.1 Clinical profile

In the discovery hepatic lipidomics set, 70 samples belonged to healthy individuals, 6 to individuals with NAFLD, 29 to those with borderline NASH and 15 to those with NASH. Hence, 76 were categorized as no-NASH and 44 were categorized as NASH samples. The age distribution was huge, varying from 0 to 80 years. There were equal number of males and females. However, the population was majorly white, with 111 individuals being white, and 9 being black racially.

In the validation hepatic lipidomics set, none of them were healthy, 52 of them had NAFLD, 9 had borderline NASH, and 22 had NASH. Hence, 52 of them were categorized as no-NASH and 54 were categorized as NASH samples. The age distri-

bution was huge in this data set as well, varying from 0 to 80 years. 57 of them were males and 49 of them were females. All of them were white racially.

F.2.2 Statistical results for hepatic lipids

In discovery set, PC (FDR < 0.15), SM and DSM (FDR < 0.01), ePC (FDR < 10E-6) were found to be significantly associated with NASH, keeping demographics as control. Interestingly, each of them were negatively associated. In validation set, PC (FDR < 0.01) and ePC (FDR < 0.12) were significantly associated with NASH. All of them were negatively associated as well. This implies that hepatic PCs and ePCs are significantly negatively associated with NASH.

Saturation analysis showed that unsaturated PC (FDR < 0.01), PE (FDR < 0.12), and PI (FDR < 0.1) were significantly negatively associated with NASH in discovery set. In the validation set, PC (FDR < 0.01), and PE (FDR < 0.1) were significantly negatively associated with NASH. This implies that hepatic unsaturated PCs and PEs are negatively associated with NASH. Four of these PC ratios and five of these PE ratios were common between discovery and validation sets.

F.2.3 Hepatic lipid signature

Elastic net logistic regression identified a set of 25 lipids which can create a predictive model with an average AUROC of 0.826 in cross validation sets (10 fold CV repeated 5 times). Top 10 of these lipids were finally used. Upon model building with these 10 lipids in discovery set, AUROC of 0.895 was obtained. In validation set, AUROC of 0.861 was obtained. This can be used as a potential strategy to classify NASH, even though invasive, because it can still remove the bias due to sampling error.

Table F.1.: Lipids and FDR value in discovery set, all negatively associated

Lipid family	FDR
PC	0.14
SM and DSM	0.008
ePC	6.33E-6

Table F.2.: Lipids and FDR value in validation set, all negatively associated

Lipid family	FDR
PC	0.002
ePC	0.12

Table F.3.: Significant unsaturated lipid families and FDR value in discovery set

Lipid family	FDR
PC	0.0064
PE	0.11
PI	0.0625

Table F.4.: Significant unsaturated lipid families and FDR value in validation set

PC	0.0021
PE	0.0575
PI	0.213

Table F.5.: List of lipids found as biomarkers (in order of importance)

Lipid	Mass	Formula
SM(18:1)	729.6	C41H81N2O6P
SM(18:0)	731.6	C41H83N2O6P
PI(34:1)	854.5	C43H81O13P
PA(38:4)	742.5	C41H73O8P
PI(34:2)	852.5	C43H79O13P
SM(16:0)	703.6	C39H79N2O6P
LPC(20:0)	552.4	C28H58O7PN
PG(36:1)	794.6	C42H81O10P
ePC(38:2)	800.6	C46H90O7PN
SM(24:1)	813.7	C47H93N2O6P

Table F.6.: Overlapping lipids between discovery and validation set

Lipid
PC(40:8)
PC(40:7)
PC(40:3)
PC(40:2)
PC(42:10)
PC(42:5)
PC(42:4)
PC(42:3)
ePC(34:0)
ePC(36:3)
ePC(38:6)
ePC(38:2)
ePC(40:4)
PG(36:4)

F.3 Discussions

NAFLD is a prevalent disease with a wide spectrum. Pathobiology of NAFLD and its transition to NASH remains elusive. The role of lipids in understanding the pathobiology has been widely discussed. In this study, lipidomics data was analyzed to understand their role at a molecular level. Significant amount of research has focused on lipidomics association with NAFLD and NASH [336–338]. However, only one of them performed the analysis at the molecular level [336]. The study here is focused majorly on liver tissue lipidomics. Moreover, different classes of lipids were analyzed separately. The role of lipid classes in progression from no-NASH to NASH was analyzed. Further, the results were validated in an independent data set.

Role of PC in NAFLD progression has been emphasized extensively [339,340]. It is also shown to be involved in hepatic TG synthesis [341,342], which is associated with NAFLD. The authors in [343] have provided a comprehensive review on role of PC and stress on the importance of a balance of SAME and PC. Importance of choline in diet to prevent NAFLD and NASH has also been discussed [344,345]. In this study, these lipid families were focused on separately. It was observed that all significant PCs are negatively associated with NASH. This supports the observation that choline deficiency can lead to NAFLD [346,347]. There is evidence of role of PC in preventing HCC as well [348–350]. Interestingly, not just the overall amount of PC, but all the significant individual PCs are negatively associated with NASH. This was confirmed in the independent validation set. This implies that synthesis of several PCs is reduced in NASH. There was also an overlap of 8 such PCs in the discovery and validation sets (out of 14 and 20 respectively). Most of them had either 40 or 42 primary carbon chains. The overlap strengthens the conclusion that several PCs are negatively associated with NASH. A similar result was also observed for ePC. All of the significant ones were negatively associated in both the validation and the discovery set. This implies that both PC and ePC follow a similar trend and are similarly synthesized in NASH samples. There was an overlap of 5 of them in the

discovery and validation sets (out of 17 and 10 respectively). They had either 34, 36, 38, or 40 primary carbon chains. To our knowledge, targeted study on ePC and its role in NAFLD progression has not been done. Based on these results, it seems worthwhile to focus on ePC alone as well.

Several studies have shown the role of saturated fatty acids in NAFLD progression. The review article by Leamy et al [351] elucidates on the mechanisms of saturated fatty acids. However, based on our knowledge, only one study has explored the role of saturation in phospholipids [352]. They concluded that increased saturation in phospholipids may lead to lipotoxicity, which can indicate NAFLD. Our findings agree with them, and it was found that increased saturation is associated with NASH. Moreover, it was identified that increased hepatic PC and PE are associated with NASH. A thorough targeted validation on a larger cohort may provide a possible therapeutic solution to reverse NASH. It needs to be noted that the FDR cutoff for this analysis was not stringent ($FDR_{crit} = 0.1$). Hence, there is a need to validate the findings on a larger data set.

Previous studies have come up with different lipids in both liver and serum as potential biomarkers. Here, machine learning was used to identify a 10 lipid signature, and it was validated on the validation set. A set of 10 lipids can accurately discriminate NASH and non-NASH both in discovery and validation set. Although these biomarkers are invasive, they still provide insight into which lipids are important in predicting NASH accurately. From the list of biomarkers, SM seemed to play a major role in a multivariate sense. The role of SM in NAFLD has been discussed in [353]. The exact role of SM is unclear, however. PI also seemed to play a role. PI has been shown to be involved in prevention of NAFLD [354].

This study has limitations because of the demographics. Both the discovery and validation sets consisted primarily of a white race population. However, there is a wide age distribution, and the population consists of almost equal males and females. We performed a rough power calculation for the sample size based on the variance in these populations. An average power of 90% was estimated for the discovery set.

However, power for the validation set was low and highly varied, varying between 70-99%. A larger sample size may help in better validation. Further, BMI was not available for all the samples in the discovery set. Hence, we did not include it in our analysis for both the discovery and validation sets. A rough estimate showed that BMI varied from approximately 7 to 65 in both the sets. BMI needs to be included in future studies to arrive at a stronger conclusion. Another major limitation is the identification of lipids. Lipids were analyzed using MS, and the true structures are unknown. In spite of the limitations, this study shows some interesting trends regarding the association of lipids with NASH, and the role of level of saturation with respect to NASH. Focused molecular level analysis of PCs, ePCs, PEs, and PIs will provide further biological insights.

In conclusion, all significant hepatic PC and ePC were identified to be negatively associated with NASH. A 10 hepatic lipid signature was found that can accurately discriminate NASH and no-NASH. Hepatic lipidomics analysis was validated in an independent data set. This analysis indicates individual hepatic phospholipids and their saturation level may play a role in progression to NASH. Further, the lipid signature indicates that few phospholipids may together play a role in progression to NASH. Lastly, various classes of saturated phospholipids liver tissue were positively associated with NASH.

VITA

EDUCATION

Purdue University May 2020
 Doctor of Philosophy, Chemical Engineering GPA: 3.79/4.00
 Concentration in Computational Life Sciences (CLS)

Indian Institute of Technology, Bombay May 2014
 Bachelor of Technology, Chemical Engineering GPA: 3.47/4.00
 Honors in Chemical Engineering
 Minors in Probability and Statistics

RESEARCH EXPERIENCE

Max Planck Institute, Magdeburg August 2018, May 2019
Visiting Researcher *Advisors: Achim Kienle, Dietrich Flockerzi*
 Title: Computational analysis of a 9D small DRG neuron model

Indian Institute of Technology, Bombay July 2013 - May 2014
Undergraduate Research Assistant *Advisor: Ganesh Viswanathan*
 Title: Moment closure technique for estimation of noise propagation

Purdue University May - June 2012
Undergraduate Visiting Scholar *Advisor: Doraiswami Ramkrishna*
 Title: Modeling and control of crystal morphology

HONORS AND AWARDS

- OCNS trainee poster award (*Organization For Computational Neurosciences*)
2019
- Schmidt Science Fellows Award Nominee (*Purdue Graduate School*, one of the
five selected graduate students, media coverage) 2018

- Best Oral Presentation in Computational Chemical Engineering (*Purdue Chemical Engineering*) 2017
- Lynn Fellowship (*Purdue Graduate School*) 2014-2015
- All India rank 642 in IIT Joint Entrance Exam, out of more than 450,000 students 2010

Travel Awards

- Student travel grant (*Purdue Institute for Integrative Neuroscience*, \$750) 2019
- Travel support for MBI Summit on Rules of Life (*Mathematical Biosciences Institute, Ohio State University*) 2019
- Travel support for Annual Computational Neuroscience Meeting (*Organization For Computational Neurosciences*, \$800) 2019
- The Marcy and Bob Ziek Student Travel Fund (*Purdue Chemical Engineering*, \$1000) 2018
- Graduate Conference Travel Grant (*Purdue Graduate Student Government*, \$250) 2017, 2019
- Travel support for Big Data Neuroscience Workshop in Indiana University, Bloomington (*Advanced Computational Neuroscience Network*) 2017

PUBLICATIONS

1. **Verma, P.**, Kienle, A., Flockerzi, D., & Ramkrishna, D. (2019). Using Bifurcation Theory for Exploring Pain. *Industrial & Engineering Chemistry Research*. DOI: 10.1021/acs.iecr.9b04495
2. Singh, M. R., **Verma, P.**, Tung, H. H., Bordawekar, S., & Ramkrishna, D. (2013). Screening crystal morphologies from crystal structure. *Crystal Growth & Design*, 13(4), 1390-1396. DOI: 10.1021/cg400009m

*Article was recognized with *AICHE Process Development Division Student Paper Award, 2013*

3. **Verma, P.**, Devaraj, J., Skiles, J. L., Sajdyk, T., Smith, E., Ho, R. H., Hutchinson, R., Wells, E., Li, L., Renbarger, J. L., Cooper, B., & Ramkrishna, D. A Metabolomics Approach for Early Prediction of Vincristine-Induced Peripheral Neuropathy. (submitted to *Scientific Reports*). Preprint at <https://doi.org/10.1101/19013078>
4. **Verma, P.**, Kienle, A., Flockerzi, D., & Ramkrishna, D. Computational analysis of a 9D model for a small DRG neuron. (submitted to *Journal of Computational Neuroscience*). Preprint at <https://arxiv.org/abs/2001.04915>
5. **Verma, P.**, Eaton, M., Kienle, A., Flockerzi, D., Yang, Y., & Ramkrishna, D. A Mathematical Investigation of Chemotherapy-Induced Peripheral Neuropathy. (submitted to *elife*). Preprint at <https://www.biorxiv.org/content/10.1101/2020.04.23.057851v1>
6. **Verma, P.**, Eaton, M., Yang, Y., & Ramkrishna, D. Exploring interactions in chemotherapy-induced peripheral neuropathy mechanisms. *In preparation*